In vitro Reconstitution of Collective Effects in Microtubule Transport and Dynamics

A thesis
Submitted in partial fulfillment of the requirements

Of the degree of

Doctor of Philosophy

By

Kunalika Jain

20133246

Indian Institute of Science Education and Research Pune

2019

Declaration

I declare that this written submission represents my ideas in my own words and where others' ideas have been included, I have adequately cited and referenced the original sources. I also declare that I have adhered to all principles of academic honesty and integrity and have not misrepresented or fabricated or falsified any idea/data/fact/source in my submission. I understand that violation of the above will be cause for disciplinary action by the Institute and can also evoke penal action from the sources which have thus not been properly cited or from whom proper permission has not been taken when needed.

(Signature)
(Kunalika Jain)
20133246

Date: 18 June, 2019

Indian Institute of Science Education and Research
(IISER – Pune)
Dr. Homi Bhabha Road, Pashan, Pune 400 008.

Dr. Chaitanya Athale, Ph.D.
Associate Professor

CERTIFICATE

This is to certify that the work incorporated in the thesis entitled "*In vitro* Reconstitution of Collective Effects in Microtubule Transport and Dynamics", submitted by Kunalika Jain was carried out by the candidate, under my supervision. The work presented here, or any part of it, has not been included in any other thesis submitted previously for the award of any degree or diploma from any other University or institution.

Date: *18/06/2019*

(Supervisor)
Dr. Chaitanya Athale,
Associate Professor,
Division of Biology
IISER Pune

Tel.: +91 020 2590 8050 Fax: +91 020 2589 9790 Web: www.iiserpune.ac.in

Acknowlegement

I would like to begin this acknowledgment by thanking my Ph.D. supervisor Dr. Chaitanya Athale, for providing me a platform to work on multiple systems in his lab, motivating me in times of distress and inculcating the value of quantitative analyses while addressing a problem. I would like to thank my research advisory committee- Dr. Richa Rikhy, Dr. Roop Mallik and Dr. Thomas Pucadyil for their timely guidance, suggestions and evaluations. I would also like to thank Dr. Gayathri Pananghat for her time to discuss various aspects of the work whenever I needed.

I am grateful to the following people who willingly extended their help for the different projects I worked on. I would like to begin by thanking Neha Khetan, my lab mate and a good friend, for performing the *in silico* work on gliding assays. I am grateful to Dr. Saravanan Palani for the time-lapse movies of the growing *S.cerevisiae* strains, and Dr. Shivaprasad Patil for providing me the access and help with the AFM facility. The help received in acquiring data by Jyoti Yadav, Shatrughan Rajput is acknowledged. I would like to thank Kaveri Vaidya and Tanmaya Sethi for the initial tiresome optimizations with plant tubulin preparations. I would also like to thank Kiran Nilangekar and Yash Jawale for helping with the brain tubulin preparations whenever I needed.
The support from the microscopy facility at IISER Pune is greatly acknowledged especially the training received from Vijay Vittal. The shared lab facility at IISER provided hassle free interactions and promoted easier discussions. I would like to thank all of my lab members who witnessed the lab transition to CyCel (Cytoskeleton and cell shape) from SOCM (Self organization and cell morphogenesis). I would like to thank Abhishek, Anushree, Dhruv, Manasi, Megha, Neha, Snehal, Tanmaya and Yash for the pleasant times we had during various lab lunches and dinners, and the intense but delightful lab meets and journal clubs discussions. I am grateful to Anushree, Neha and Prangya for making me comfortable with the MATLAB scripts. A special thanks to my mentor, Dr. Chaitanya, for creating a good-humored work space, and introducing me to *in vitro* reconstitutions, quantitative image analysis, Matlab, latex and inkscape, during my Ph.D., all of which are my favourites now.

I have a long list of friends who deserve a special acknowledgement. Evening walks

with Jyoti and Shrikant, late night discussions with Shalini and Raunaq, home stays at Tanushree's place, visits to Dhanashree and Abhijit, and fun trips planned with Neha, Neelesh, Shrikant, Kriti, Raunaq and Lokesh were always a delight. The chats in the lab corridors with Dr. Priyanka, Dr. Anand, and Dr. Ramana Athreya sparked the days when experiments couldn't. My friends Alka and Shruthi deserve a special mention here for being constant sources of motivation and great emotional support in times of distress.

I would like to thank the funding agency- DST INSPIRE, for the financial support throughout my Ph.D tenure. Travel support from CSIR, Infosys, Gordon and EMBL that enabled my participation to various international conferences is acknowledged. I am grateful to Tushar Kurulkar and Sayali Damle for their help and support with the numerous administrative procedures. The ordering of materials from the stores was easier with the help of Mrinalini, Shabnam, Rupali, Kalpesh and Piyush.

This acknowledgement section would be incomplete without a special mention to my family. My parents and brother have been a great source of support, strength and motivation. The calls that I missed from them were far more than my failed experiments (and that aren't few) and their patience for me is remarkable. I would also like to thank my in-laws for providing me a very comfortable space, love, warmth and encouragement to pursue my work. A special thanks to my best friend and life partner- Shrikant Harne, who has witnessed my Ph.D journey. He has been with me through all the ups and downs, supported me through all the emotional turmoils and beared the consequences of all the successful and failed experiments. This Ph.D. would have not been possible without the love, encouragement and support of my family.

Contents

List of Figures

List of Tables

Synopsis

Microtubules (MTs) are dynamic cytoskeletal polymers that are involved in regulating cell physiology and mechanics. They are kinetically polar with two distinct ends: rapidly growing plus-ends and slow growing minus-ends. Based on MT polarity, motor protein network is broadly categorized as plus-end directed (Kinesins) and minus-end directed (Dyneins). While single molecule properties of the motors have been studied extensively, cellular processes typically involve collective effects of multiple motors as seen in filament and vesicle transport [Adames and Cooper, 2000b; Shubeita et al., 2008].

Microtubule transport by dynein is essential for nuclear positioning in *Saccharomyces cerevisiae* mitosis. Dyneins are anchored to the bud-cell cortex at the onset of anaphase and pull astral MTs, resulting in nuclear positioning at the bud neck which is critical for DNA segregation [Estrem et al., 2017; Maddox et al., 2000]. During this 'search and capture' of yeast nuclear MTs in mitosis, both motor numbers and MT lengths are dynamic. In *Schizosaccharomyces pombe*, the combined effect of MT lengths and motor-numbers results in nuclear oscillations [Yamamoto et al., 2001b]. This suggests that motor numbers as well as MT lengths play a role during *in vivo* MT transport. A motor number dependence has also been reported in the lab in simulations of radial MT arrays transported by dynein [Athale et al., 2014b]. The work demonstrates the role of MT dynamic instability in directional transport of complex arrays of MTs. However, a minimal system that quantitatively addresses the collective effects of dynein numbers and MT lengths in filament transport is yet to be investigated. Here, I proceed to describe the work done as a part of my Ph.D. project that separately examined the two parts: (a) understanding the length and motor number dependence of microtubule transport by dyneins, (b) understanding the comparative dynamics of tubulin. The work is summarized in the following chapters:

Chapter 1 Introduction

This chapter gives a brief introduction to the general properties of microtubules and the motor proteins associated with it. It summarizes the current literature on microtubule structure, dynamics and kinetics from *in vitro and in vivo* approaches for the available tubulin sources. It discusses various mechanisms by which the filament overcomes kinetic barriers during polymerization for limiting tubulin concentration *in vivo*. Along with MT polymerization, this chapter also gives an overview to the single motor and multi-motor transport by kinesins and dyneins. It then focuses on the collective effects of multi-motor transport for the two scenarios- when they are transporting cargo over static filaments, versus when they are transporting the filaments. The combined effects of the collective role of MT dynamics and filament transport by motors are then highlighted in cellular contexts giving way to the questions raised in my thesis. The last section briefly introduces the caveats of fluorescence imaging and automated tracking, necessitating the need for calibrations in quantitative image analysis, discussed in the following chapter.

Chapter 2 Estimating mechanical noise for motion stability and calibrating intensity by quantitative fluorescence microscopy

This chapter consists of the calibrations performed to estimate the noise in positional accuracy due to the acquisition setup, validate the accuracy of tracking algorithm and build a calibration curve based on epi-fluorescence to estimate the number of molecules. The results of these calibrations have been used to determine both the lower-bound of mobility and estimate the number of unknown motors for the gliding assay. These methods are used for the quantitative analysis of the dynein based gliding assay in the subsequent chapter.

Chapter 3 Collective effects of yeast cytoplasmic dynein in *in vitro* Microtubule transport

This chapter examines the collective effects of microtubule transport by minimal yeast dyneins in an *in vitro* gliding assay. It assesses the effects of MT lengths and dynein number dependence of dynein on microtubule transport properties- speeds, velocity, diffusivity and directionality. The quantitative trends in microtubule transport observed experimentally is explained by stochastic simulations based on single motor parameters. The chapter concludes with the *in vivo* implications of a threshold number dependence observed in directionality of MT transport for spindle positioning in *S.cerevisiae* mitosis.

Chapter 4 Implications for dynein number dependent transitions on spindle pole body transport via microtubules in yeast mitosis

This chapter discusses the potential of a dynein number based switch in directionality of microtubule based transport of *S.cerevisiae* nucleus. Time lapse images of budding cells are analyzed to track the spindle pole body (SPB) movement, a structure that nucleates microtubule. The change in transport directionality of SPB is evaluated for the cells in different growth stages, before and after SPB duplication. The results are then reviewed to observe the trends in diffusivity and directionality of SPB movement. The chapter concludes with the optimizations performed to obtain the yeast nuclei with intact SPB's and alternate source of microtubule nucleator- centrosomes, in order to obtain complex filament geometries. The goal is to unambiguously identify the motor number dependence seen in linear filament transport for more complex geomtries such as spindles.

Chapter 5 Comparative polymerization kinetics of tubulins explains differences between plant and animal microtubule (MT) lengths

This chapter compares the polymerization kinetics of tubulin isolated from a plant source, and a more routinely used animal source- brains. This is a first report which systematically assess tubulin kinetics of germinated mung bean seedling across different tubulin concentrations and estimates the critical concentration (c*). The chapter examines the differences in critical concentrations estimated from kinetics and the potential role it might play in determining filament length distributions between two sources of tubulin. It also assesses the role of a phenomenological scaling model of nucleation dependent polymerization kinetics for mung beans, known to play a role for brain tubulin sources.

The chapter concludes with a simple conceptual model to explain the observed differences based on the observed results.

Chapter 6 Future perspective

This chapter summarizes the key results and the ongoing state of the various experiments discussed in the above chapters. It concludes with the future directions for these results to better understand the collective roles of motor driven microtubule transport, and MT dynamics.

Publications

ACCEPTED

- **Kunalika Jain**, Neha Khetan and Chaitanya A. Athale, "Collective effects of yeast cytoplasmic dynein based microtubule transport", Soft Matter 15, 1571–1581.
- Anushree R. Chaphalkar, **Kunalika Jain**, Manasi S. Gangan, and Chaitanya A. Athale, "Automated Multi-Peak Tracking Kymography (AMTraK):A Tool to Quantify Sub-Cellular Dynamics with Sub-Pixel Accuracy", PLoS One, vol. 11, no. 12, p.e0167620, 2016

IN REVIEW

- Kunalika Jain, Jyoti Yadav and Chaitanya A. Athale, Comparative Polymerization Kinetics of Tubulins Explain Differences between Plant and Animal Microtubules (MTs).

IN PREP

- Kunalika Jain, Saravanan Palani and Chaitanya A. Athale, Transitions in the directionality of transport in budding yeast durin spindle positioning.

Abstract

The transport of dynamic microtubules (MTs) driven by dyneins is essential for spindle assembly, asymmetric cell division, axonal growth and organelle positioning. While the single-molecule mechano-chemistry of dyneins has advanced extensively, their role in collective MT transport, remains unclear. Additionally, MTs in animal somatic cells are typically nucleated by centrosomes forming radial arrays or asters. MT aster transport in oocytes and single-cell embryos involves a tug-of-war of dyneins that is resolved by a combination of MT polymerization dynamics regulation, motor localization and self-organized clustering. This work encompasses (a) the length and motor number dependence of microtubule transport by yeast dyneins, (b) aster-based transport of nuclei in *Saccharomyces cerevisiae* and (c) compares polymerization dynamics of MTs from plant and animal sources. The work shows that microtubules transported by teams of immobilized *S. cerevisiae* dynein transits from random to directed motion with increasing MT lengths and motor densities, both *in vitro* and *in silico*. Velocity, diffusivity and directionality, all reflect a coordination of transport above a threshold motor numbers. Our analysis of *in vivo* data of astral MTs transported by dynein during *S. cerevisiae* mitosis supports a functional role for such a transition. Based on these findings, a general 'search and orient' mechanism is proposed for organelle positioning by MT asters.
The comparative study on the role of MT polymerization dynamics from multiple sources: goat, porcine and plant (mung beans) demonstrates nucleation limited polymerization in all these diverse species, suggesting a central role of nucleators such as centrosomes in determining MT filament distributions. The model proposed highlights the importance of critical concentration in determining filament length distributions. Optimizations with *ex vivo* reconstitutions of nucleators such centrosomes and spindle pole body will advance our understanding of the collective effects of motor numbers, MT length dynamics and transport of complex geometry in eukaryotic cells.

Abbreviations

MT Microtubule

c* Critical concentration

CHO Chinese hamster ovarian

DTT Dithiothreitol

EB End binding

ECT Electron cryotomography

EM Electron microscopy

MAPs Microtubule associated proteins

MSD Mean square displacement

MTOC Microtubule organizing center

PCM Pericentriolar matrix

RPM Revolutions per minute

RT Room temperature

SNR Signal to noise ratio

SPB Spindle pole body

Chapter 1

Introduction to microtubule polymerization and motor systems

KEYWORDS: COLLECTIVE TRANSPORT, DYNEIN, KINESIN, KINETICS, MICROTUBULES, MOTOR TRANSPORT, NUMBER DEPENDENCE, NOISE, NUCLEATION KINETICS, SIGNAL TO NOISE

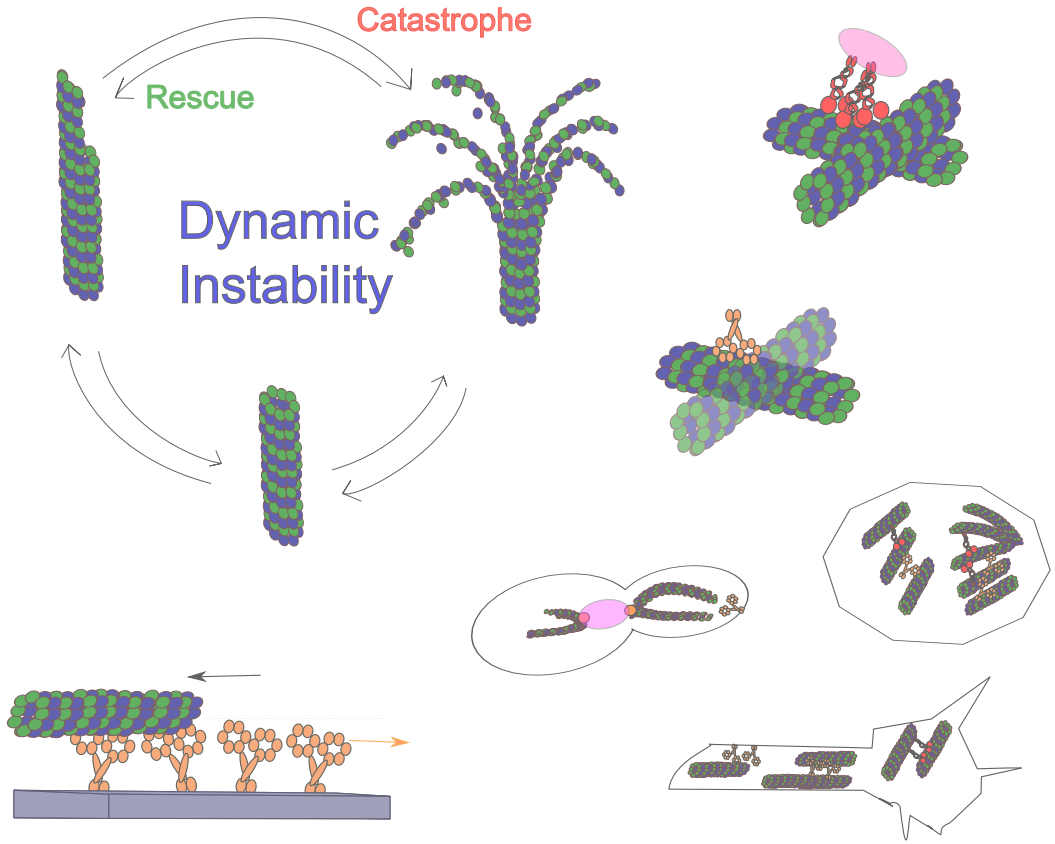

Microtubules (MT) form one of the most important and well-studied cytoskeletal networks within a cell. They are composed of repeating units of α and β tubulin dimers that assemble in a head-to-tail fashion to form protofilaments. Lateral interactions among 13 protofilaments form a dynamic microtubule structure that are stiff, hollow and cylindrical with a diameter of 24 nm. MTs are essential for several vital cellular processes such as cell division, meiotic nuclear oscillations, cargo transport, ciliary movements and cell-polarization. In spite of their functional diversity, the basic units (α and β tubulin) of MTs exhibits rapid transitions between growing and shrinking phases, giving rise to dynamic lengths of MTs. This process, referred to as 'dynamic instability' of a filament, is the most conserved and fundamental property of MTs across different species. The dynamic nature of MTs allows filament remodeling within minutes during cell cycle, explore cell space that serve as tracks during intracellular trafficking and generate mechanical forces to position spindle and various organelles.

1.1 Dynamic Instability: GTP dependent switches in polymerization

The initial reports of dynamic instability came from *in vitro* experiments with pure tubulin, salts and GTP [Mitchison and Kirschner, 1984b]. Video enhanced light microscopy experiments that were conducted to study dynamic instability of microtubules revealed that microtubule growth rate scales linearly with tubulin concentration in a temperature dependent manner whereas shrinkage rate was independent of both [Dogterom et al., 1996; Walker et al., 1988]. The alternating phases of growth and shrinkage exhibited during dynamic instability are characterized by following parameters- growth rate, shrinkage rate, catastrophe frequency (transition from growing to shrinking state) and rescue frequency (transition from shrinking to growing state) [Dogterom and Leibler, 1993]. More recent *in vitro* experiments reconstituted with *Drosophila* proteins showed an additional 'pause' phase during MT polymerization where filaments neither exhibited growth nor shrinkage [Moriwaki and Goshima, 2016]. This suggests that a dynamic filament exhibits three phases during polymerization- growth, shrinkage and pause (**Figure 1.1**).

The energy to drive this process comes from the GTP hydrolysis. In the absence of GTP hydrolysis, dynamic instability in MTs is not observed. This has been shown by

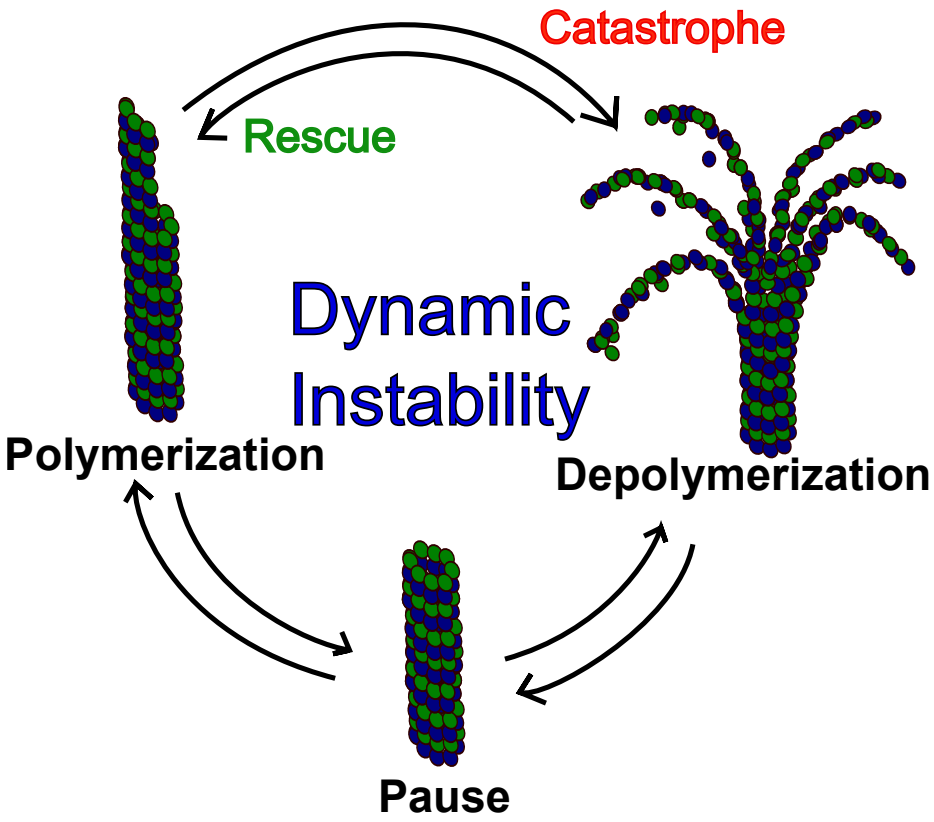

Figure 1.1: **Emerging view of dynamic instability of microtubules**. The schematic represents different phases that a microtubule exhibits during dynamic instability. Polymerization represents a growing microtubule whereas depolymerization represents a shrinking microtubule. The point where a polymerizing filament starts to shrink is termed as 'catastrophe' whereas the point where a shrinking filament resumes polymerization is termed as 'rescue'. Microtubule can transit between the two phases based on the availability og GTP and tubulin dimers. A third phase where the filament neither grows nor shrinks has been identified and is termed as 'Pause'.

experiments performed with GMPCPP, a non-hydrolyzable analogue of GTP, suggesting a role of GTP hydrolysis for switching between growth and shrinking phases [Hyman et al., 1992]. In fact, microtubule stability has been attributed to the presence of GTP caps/islands at the growing end of the polymer that are formed by the addition of GTP tubulin subunits [Mitchison and Kirschner, 1984b]. Direct evidence in support of the idea that longer GTP caps increase microtubule stability [Howard and Hyman, 2009; Schek III et al., 2007] has been shown using end binding (EB) proteins by high resolution

imaging in total internal reflection microscopy (TIRF) [Duellberg et al., 2016]. The study shows that faster growing microtubules accumulate longer GTP caps (observed in the form of fluorescent EB comets), leading to a reduction in the frequency of catastrophes. Although the study provides a breakthrough about the relation of MT growth rates to the size and nature of GTP caps, the conformational and biochemical transitions that the heterodimers undergo during the process cannot be explained.

1.2 Conformational transition in tubulin dimers: GTP dependent switches in polymerization

Crystallography and cryo-electron microscopy studies have revealed that tubulin dimers often undergo conformational transitions from curved state to compact and relaxed states during polymerization. The predominance of each of these states is dependent on the nature of GTP bound dimer present freely in solution or bound to MT lattice (**Figure 1.2**).

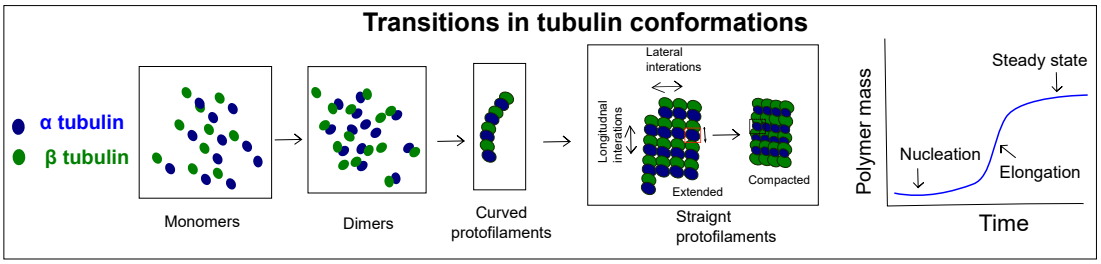

Figure 1.2: **Conformational transitions in filament growth.** The α tubulin (blue) and β tubulin (green) monomers associate to form a heterodimer. These dimers associate with each other to form curved protofilaments. Multiple protofilaments associate with each other by lateral interactions for the formation of microtubule structure. In the process, the curved protofilaments straighten up that induces a strain in the structure, leading to GTP hydrolysis. The hydrolysis of GTP releases the strain built in the lattice structure and compacts it or further forms curved protofilaments destabilizing the lattice. The curved conformations are preferred for unpolymerized dimers and the single protofilaments formed by the incorporation of these dimers. The process of microtubule growth kinetics is identified by three phases- an initial lag phase, followed by elongation and steady state.

Curve state predominates in case of a non-polymerized, GTP-bound tubulin het-

erodimer [Buey et al., 2006]. When this dimer integrates at a growing end of microtubule, it straightens [Nawrotek et al., 2011] to an expanded conformation which compacts on GTP hydrolysis, as seen with bovine tubulins [Alushin et al., 2014]. The compaction releases the strain induced by the lateral interactions within the microtubules that caused it to adopt a straight conformation. However, yeast tubulins do not show such compaction [Howes et al., 2017] inspite of high sequence similarity, suggesting divergence of tubulins across species. Moreover, dynamic instability is intrinsic to MTs as it can be reconstituted with just tubulin dimers and GTP. Our knowledge with respect to dynamic instability and structural characterization of MTs have largely depended on mammalian brain tubulin. However, more recent investigations with yeast tubulins, have shown different behavior of MTs as compared to mammalian brain tubulin [Howes et al., 2018]. This calls for a rigorous understanding of tubulin dynamics from different species. While the sequences of tubulin might be highly conserved, our knowledge of MT dynamics obtained from one species might not be applicable to others. This needs assessment of tubulin properties from different species at the various levels starting from evaluation of microtubule assembly to observing the native kinetics and structural conformations and more importantly their *in vivo* behavior.

1.3 Kinetics of microtubule assembly

During polymerization, the kinetics of filament growth exhibits three phases- nucleation, elongation and steady state. The initial phase of growth termed as 'nucleation' is characterized by a lag period and proceeds via formation of several oligomeric assemblies to form a tubular filament [Erickson and Pantaloni, 1981; Fygenson et al., 1995; Voter and Erickson, 1984]. This spontaneous nucleation of filaments is kinetically unfavourable and a rate limiting step in filament polymerization [Erickson and Pantaloni, 1981]. The efficiency of spontaneous nucleation increases non-linearly with an increase in tubulin concentration. The concentration above which tubulin polymerization overcomes this kinetic barrier to form polymers is termed as critical concentration (c*), and the formation of polymers is represented by the 'elongation phase'. The tubulin concentration required for *de novo* nucleation has been reported to be higher than that required for persistent elongations with bovine brain tubulin [Wieczorek et al., 2015b]. Apart from c* of the polymer, the state of the bound nucleotide- GTP or GDP also governs growth

and shrinkage of the polymer. β tubulin contains exchangeable GTP that undergoes hydrolysis leading to a faster polymerization as compared to the unexchangeable GTP at α tubulin that remains buried at the dimer interface [Allen and Borisy, 1974; Cote and Borisy, 1981; Lowe et al., 2001; Mitchison, 1993]. This gives rise to kinetically polar filament ends during polymerization with a fast growing plus ends and a slow growing minus ends. Single molecule assays have shown that GTP hydrolysis in the microtubule lattice destabilizes spontaneous nucleation at plus ends and slowly hydrolyzable GTP analogues promote spontaneous nucleation [Hyman et al., 1992; Wieczorek et al., 2015b]. Since the *in vivo* concentration of tubulin is usually limiting, spontaneous nucleation is not favored. Hence, cells have evolved mechanisms to overcome these kinetic barriers as discussed below. (**Figure 1.3**).

1.4 Mechanisms to overcome kinetic barriers in polymerization

The kinetic barrier of nucleation is surpassed either by template-based nucleation that stabilizes one of microtubule ends by promoting lateral interactions **(Figure 1.3a-b)** or by non-template based nucleation that stabilizes the longitudinal and lateral interaction within a growing microtubule [Tovey and Conduit, 2018; Wiese and Zheng, 2006] **(Figure 1.3b-c)**. Both these mechanisms operate within a cell to nucleate microtubules as the dimeric pool of tubulin is in limiting concentrations to initiate spontaneous nucleations. Microtubule oraginizing centres (MTOC), more commonly known as centrosomes, are the most studied nucleators till date. They are embedded in a matrix of proteins that contain two barrel shaped structures called centrioles. Electron microscopy (EM) studies performed with the lysates of Chinese hamster ovarian (CHO) cells identified that microtubule nucleation occurs largely in the matrix rather than centrioles [Gould and Borisy, 1977]. The matrix known as pericentriolar matrix (PCM) is composed of dynamic protein network that defines its cell boundary and enriches tubulin locally during MT nucleations [Woodruff et al., 2017]. Electron cryotomography (ECT) studies accompanied by immunolabelling of *Drosophila* centrosomes show that microtubule nucleation occurS from 25 nm sized ring complexes within PCM. These are composed of γ tubulin and anchor minus ends of MTs, thus stabilizing the structure [Keating and Borisy, 2000; Moritz

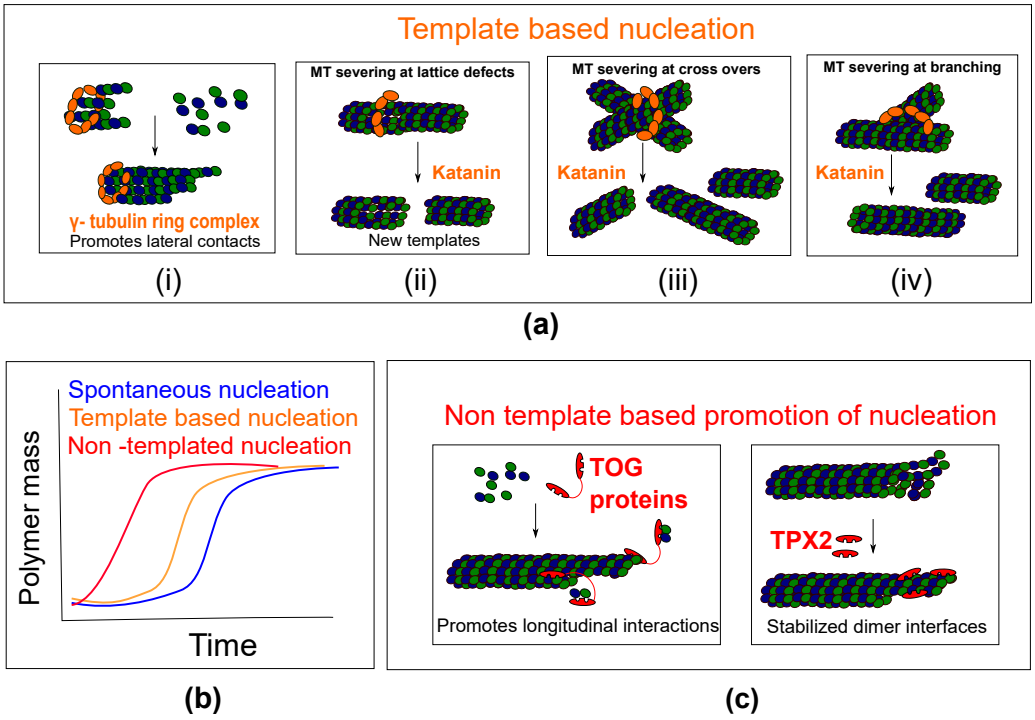

Figure 1.3: **Enhancing microtubule nucleation kinetics by different mechanisms.** (a) γ tubulin ring complexes (orange) (i) act as microtubule nucleators by enhancing lateral contacts in the formation of MT lattice, acting as a template for nucleations by enriching the local tubulin concentration. (ii) Severing enzymes like katanins (orange) cut the pre-existing filaments at (ii) lattice defects, (iii) crossovers, and (iv) branching points in order to generate additional microtubule templates, reducing the lag in polymerization due to nucleation. (b) The three phases in polymerization kinetics are represented here for spontaneous nucleation (blue), template based nucleation (orange), and non-template based nucleation (red). The lag phase observed in spontaneous nucleation is reduced in the presence of template and non-templated nucleation. (c) Non-template based nucleations by TOG proteins promote polymerization by enhancing longitudinal interactions of dimers, by acting as MT polymerases that add curved dimers across the straightened MT lattice, overcoming the kinetic barrier. Apart from stabilizing longitudinal interaction, lateral interactions can also be stabilized by TPX2 protein that stabilize dimer interfaces by preventing MT depolymerization.

et al., 2000, 1995]. The size of the stable intermediates from centrosomal nucleations that undergo persistent elongations is suggested to be 250 dimers by fluorescent intensity measurement of bovine tubulin [Wieczorek et al., 2015b]. It is much higher than the critical nuclei size of $\sim$ 20 dimers reported by turbidity measurements of spontaneous

nucleation [Flyvbjerg et al., 1996b]. This suggests that template based nucleation from centrosomes when compared to *de novo* are also kinetically unfavourable, although templates can nucleate microtubules at much lower concentrations by promoting lateral interactions. In fact, centrosomes are absent in yeast and land plants altogether, suggesting additional mechanisms can overcome kinetic barriers during microtubule growth.

Genetic studies and live imaging performed on *Arabidopsis* cortical arrays have been shown to generate templates for MT nucleation by severing microtubules at cross overs [Wightman et al., 2013; Wightman and Turner, 2007] and branching nucleation sites [Nakamura et al., 2010] by MT severing enzymes like katanins (Figure 1.3a (ii-iv)). *In vitro* observations along with simulated models showed that katanin also sever along the lattice defects on MTs to generate new templates for polymerization [Davis et al., 2002]. In addition to template based nucleations, several proteins have been implicated to assist nucleation without a template. TOG (Tumor over-expressed genes) proteins and TPX2 homologues (Targeting protein for Xklp2) assist MT nucleations in the absence of templates either by promoting longitudinal interaction between dimers, acting as a MT polymerase or by decreasing the frequency of catastrophe of the MTs, thus helping in the formation of stable nuclei assemblies [Reid et al., 2016b; Roostalu et al., 2015; Thawani et al., 2018; Zhang et al., 2017]. Infact, the crystal structure of TOG bound to α-β dimers revealed that the TOG1 domains can differentiate between an unpolymerized dimer and the growing ends of the MT lattice, and thus help incorporate curved dimers at the straightened ends of the filament [Ayaz et al., 2012]. In cellular environments, multiple proteins regulate the dynamics of the filament. With the recent progress in non-template based MT nucleations, the possibilities of discovering additional proteins and mechanisms that assist MT nucleations independent of a template have increased. Since these mechanisms operate in a diverse range of organisms, it necessitates advancement in our understanding of tubulin dynamics from different organisms.

1.5 Microtubule motors: Overview of kinesin and dynein

Molecular motors that walk along microtubules are categorized as either plus end directed-kinesins, or minus end directed- dyneins. Based on the phylogenetic analyses, kinesins have been grouped into 14 subfamilies starting from kinesin-1 to kinesin-14 [Hirokawa,

1998; Lawrence et al., 2004]. Each of this is further sub-grouped into three types depending on the position of the motor domains in the molecule: (i) N-type kinesin, where the motor domain is located at the amino terminal with plus end directed movement, (ii) C-type kinesin, where the motor domain is located at the carboxyl terminal with minus end directed movement, and (iii) M-type kinesin, motor domain is located between the amino and carboxyl terminal, and majorly causes MT depolymerization. In contrast, dynein have been categorized as either axonemal dynein or cytoplasmic dynein based on their functions [Pfister et al., 2005; Wickstead and Gull, 2007]. While axonemal dyneins are involved in cilia and flagellar beating, cytoplasmic dyneins are involved in a wide range of cellular processes like cargo transport, mitosis, migration and polarization (reviewed in [Cole, 2003; Gibbons, 1996; Hirokawa, 1998; Holzbaur and Vallee, 1994]). Unlike kinesins that have a single globular motor domain, dyneins have a large motor domain formed by hexameric rings of AAA+ superfamily (ATPase assocaited with diverse activities) [Kon et al., 2004]. The motor domains generate power by ATP hydrolysis for cargo trafficking. Various studies have been performed to understand the properties of motors like- nature of transport, the mechanism for generating power, stepping kinetics and load dependence, briefly summarized below.

1.5.1 Collective transport by molecular motors

Molecular motor driven cytoskeleton transport was first shown in early experiments on actin moved by myosin fixed to a glass surface [Simmonst et al., 1993]. The invention of optical tweezers [Ashkin et al., 1986] provided the opportunity to measure the force exerted by myosin motors immobilized on a surface acting on an actin filament, complexed to a polystyrene bead [Simmonst et al., 1993]. Experiments where the motor was complexed to the bead and a force was measured against the load, began to reveal single-molecule properties of motors, opening up a whole era of single-molecule force spectroscopy (Newman and Nagy, 2008). More recently quantum dots complexed with dyneins [Reck-Peterson et al., 2006b] and kinesins [Leduc et al., 2010b] were used to measure the processivity of these motors, revealing similar step sizes. Insights from such single molecule approaches have shown that kinesin velocity decreases with an increase in opposing load [Svoboda and Block, 1994b] while in the case of dynein, increasing opposing load on motors reduces their step size from 30 nm (load-free) to 8

nm (high-load) referred to as gear-like behavior [Mallik et al., 2004b; Rai et al., 2013b].

Collective mechanics of motor numbers on cargo transport have been extensively studied. *In vivo* studies using kinesin1 and cytoplasmic dynein hauling lipid droplets in *Drosophila* embryos have been used to understand the bidirectional nature of transport of the cargoes. The two different models that have been proposed for bidirectional movement during transport are:- Tug of war and Regulation. **Tug of war model** proposes that opposite polarity motors bound to the microtubule are equally active resulting in a fight that leads to stochastic detaching of motors of one polarity under the opposing force of other [Lipowsky et al., 2010; Müller et al., 2008, 2010; Soppina et al., 2009] whereas the **Regulation model** proposes that although both polarity motors can bind to cargo, only one is active at any point of time and the activity reversal takes place only in the presence of some cofactor [Leidel et al., 2012]. The studies on ensemble of opposite polarity motors have revealed that while kinesin detaches rapidly in the presence of increasing loads [Leidel et al., 2012], dyneins detachment rate decreases *in vivo* [Nicholas et al., 2015b; Rai et al., 2013b]. It suggests that dynein's interaction with microtubules behaves like a catch bond [Mallik et al., 2004b; Rai et al., 2013b]. The mechanisms responsible for regulating bidirectional cargo transport by opposite polarity motors are not very clear. Given that the function of motors in cells is usually in ensembles, there is a need to understand the collective mechanics of microtubule- motor systems, in light of the new insights obtained from single molecule approaches.

1.5.2 Motor number dependence in cargo transport

A combination of electron microscopy studies, and force measurements have shown that typically vesicles, melanosomes [Vancoillie et al., 2000], mitochondria [Habermann et al., 2001], and lipid droplets [Gross et al., 2002; Shubeita et al., 2008] are engaged by one to seven motors (reviewed in [Gross et al., 2007b; Holzbaur and Goldman, 2010]). The effect of motor numbers while transporting a cargo have been examined at MT intersections with GFP labeled motors **(Figure 1.4)**. While kinesin crossed all the intersections along MTs irrespective of the motor numbers that were involved in cargo transport, dyneins exhibited variable stepping behavior like reversals or switches, and paused as the numbers increased, acting as an anchor for the cargo [Ross et al., 2008]. Such dynein dependent anchorage is observed for golgi apparatus located near the MTOC, where

absence of dynein leads to golgi dispersion, by kinesin [Caviston et al., 2007].

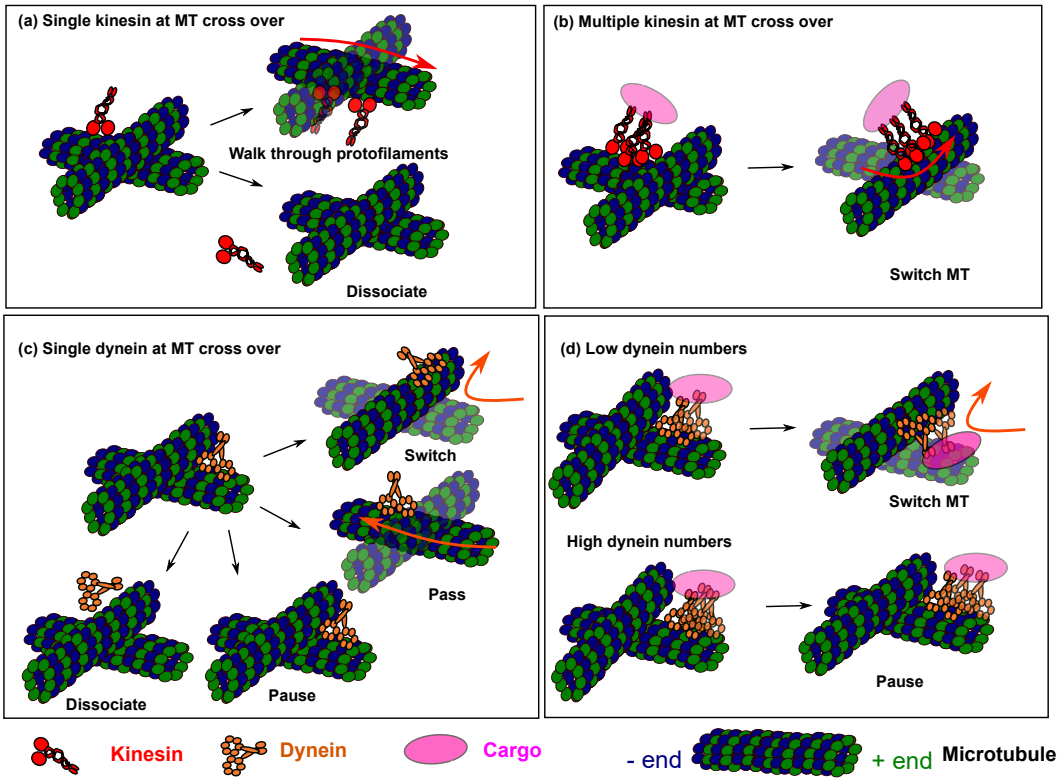

Figure 1.4: **Effect of motor numbers in cargo transport along MT networks.** (a) Kinesin walking along a microtubule intersection can either cross the protofilament at the junction or dissociate from the filament. (b) When multiple kinesins transporting a cargo arrive at MT crossover, they switch the filament. (c) Unlike kinesin, dynein exhibits multiple stepping behavior. They either switch and follow a new MT, or pass through the same one, or halt at the junction or dissociate from the filament. (d) When multiple dyneins are transporting a cargo they either change the MT track during cargo transport for low dynein numbers and, anchors the cargo without stepping for high dynein numbers.

Microtubules as cargo: Apart from transporting and anchoring cargoes, the motor proteins are also known to transport their tracks, microtubules. This is observed especially at the time of formation of spindle assembly where the forces generated by kinesins are counteracted by dynein to maintain a stable spindle structure [Tanenbaum et al., 2008, 2009; Walczak and Heald, 2008]. Dynein have been shown to organize MT networks using cell extracts by sliding them to form focused spindles [Gaglio et al., 1996; Heald

et al., 1996], clustering them to form asters [Verde et al., 1991], and cause fusion of spindles to form a bipolar spindle [Gatlin et al., 2009]. Although the stepping behavior of dynein motor domains during cargo transport has become clearer in the recent years, the mechanisms involved in formation of such networks are yet to be understood. Different possibilities have been suggested for the formation of such networks like exerting forces on the MTs while being anchored to cortex or membranes, transport MTs as cargo via MT binding domain, and sliding MTs relative to each other by forming complexes with other proteins or using both the motor domains **(Figure 1.5)**.
MT sliding via the cargo binding domain of motors is observed during cilia and flagellar beating by axonemal dyneins and several classes of kinesin [Fink et al., 2009; Seeger and Rice, 2010; Weaver et al., 2011]. Such movements are not reported for cytoplasmic dyneins as they lack a separate MT binding site outside the motor domain. *In vitro* studies on rat dynein and recombinant yeast dynein have however shown that cytoplasmic dynein can use both the motor domain to walk independently on antiparallel MTs, causing MTs to slide past each other [Tanenbaum et al., 2013]. These results are also validated *in vivo* using tailless dynein that counteract the outward forces generated by kinesin by sliding MTs using only motor domains, thus maintaining a stable spindle structure.

Search and capture of microtubules in transport: Microtubule nucleation from centrosomes, their dynamics and pivoting in the cell during spindle assembly led to the proposal of a pioneering idea of 'search and capture' of microtubules by Kirschner and Mitchison [Kirschner and Mitchison, 1986]. The dynamically unstable microtubules emanating from the centrosomes searches the cellular space and are captured by kinetochores on chromosomes, leading to the formation of mitotic spindle [Holy and Leibler, 1994]. Several groups have shown using *Xenopus* egg extracts that the presence of RanGTP gradients around the chromosomes stabilize MT lengths [Carazo-Salas et al., 2001; Clarke and Zhang, 2008; Ohba et al., 1999; Zhang et al., 1999]. A theoretical study efficiently recapitulates the capture times of kinetochores by Mts, with a biased spatial gradient around the chromosomes [Athale et al., 2008; Wollman et al., 2005]. Although, the search and capture of MTs is well-known for spindle assembly formation, it relies on probing cellular space by dynamic MTs and can be extended to spindle transport scenarios where MT in the spindle are captured by molecular motors.
Cortically anchored dynein dependent pulling of MTs have been shown to be essential

for spindle positioning in mammalian cells [Kotak et al., 2012], fission yeast [Yamamoto et al., 1999] and budding yeast [Adames and Cooper, 2000b] by genetic studies and live imaging. During this 'search and capture' of MTs, both motor numbers and MT lengths are dynamic. In *Schizosaccharomyces pombe*, the combined effect of MT lengths and motor-numbers results in nuclear oscillations [Yamamoto et al., 2001b]. This suggests that both, motor numbers and MT lengths, play a role during *in vivo* MT transport. A motor number dependence was reported in the lab in simulations of radial MT arrays transported by dynein [Athale et al., 2014b]. The work also demonstrated the role of MT dynamic instability in directional transport of complex arrays of MTs. A minimal system that quantitatively addresses the collective effects of dynein numbers and MT lengths in filament transport is yet to be investigated. *In vitro* reconstitution has become a popular approach to understand the ensemble behavior of MT-motor systems. **Gliding assays**, where the filaments are pulled by motors anchored to the surface, are usually performed in *in vitro* to assess the collective motor behavior in transporting MTs. Combined with quantitative live imaging, they help to dissect the role of individual proteins in a minimal system and re-construct the picture at cellular level.

1.6 Optical Imaging, Image Analysis and Noise

Fluorescence microscopy has been widely used to observe MT dynamics, transport, localization of motor proteins in the cell and cargo trafficking by motors both in an *in vitro* set up and in *in vivo* scenarios. Quantification based on microscopic visualizations is the most direct and powerful approach to understand the dynamics of any process in a cellular system. In order to obtain quantitative spatial and temporal information, the molecule of interest is conjugated to a fluorescent dye. The fluorescence signal is detected and measured in a manner that maximizes signal to noise ratio (SNR) and minimizes background fluorescence. There is a vast choice of imaging modalities ranging from widefield fluorescence, confocal imaging, to total internal reflection and super resolution microscopy. However, the best choice of modality dependes on the type of specimen and the kind of quantitative measures one is interested in. For example, confocal microscopy is the preferred choice for samples with high background fluorescence, as it gets rid of the out of focus light by reducing the point spread function [Murray et al., 2007; Pawley,

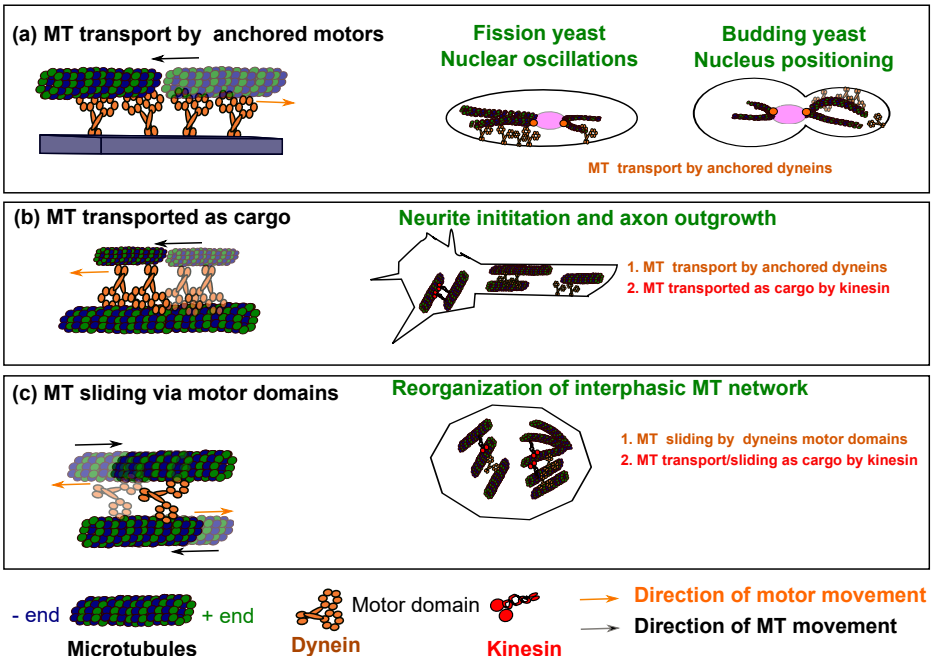

Figure 1.5: **Microtubule transport mechanisms by molecular motors.** The schematic represents different mechanisms of microtubule transport by molecular motors in various cellular systems. (a) Microtubule movement occurs by the forces exerted by surface immobilized motors or cortically anchored motors. In this example, dynein is exerting a force on the minus end of the microtubule (orange arrow). Since it is anchored, it results in the movement of MT in the opposite direction (black arrow). The blurred filament indicates the initial position of the filament. Nuclear oscillation in fission yeast and nuclear positioning in budding yeast results due to the transport of microtubules by cortically anchored dyneins. Axon outgrowth with plus end out MTs also results due to the forces exerted by anchored dyneins on MTs. (b) Microtubules can also be transported by motors as cargo when motors have a MT binding domain in addition to the motor domains. Neurite initiation by kinesin and reorganization of interphasic MT networks during spindle formation are the examples of such movement. (c) Dynein motor domains can move independently on MTs resulting in MT sliding. Such movements occur in the formation of spindle and axon in cellular system.

2010]. But when compared to a sample with low background fluorescence, widefield microscopy is more appreciated than confocal as it generates a high SNR image [Cox and Sheppard, 2004; Murray, 1998; Murray et al., 2007; Pawley, 2006; Swedlow et al., 2002b]. A high signal to noise image is not the same as a high signal to background

image. While the source of background fluorescence usually lies in the specimen preparation conditions (mounting media) and out of focus light from fluorophores, noise in the image can arise from multiple sources like objective, stage, detector and camera [Waters and Wittmann, 2014; Wolf et al., 2007]. Therefore, one needs to carefully assess the signal and the noise components of the image in order to make quantitative interpretations. Apart from optical imaging, noise can also arise at a later step after data acquisition which involves image analysis [Carlton and Englehart, 2005].

With the development of automation in the process of image analysis to detect motion of single particles, filaments or cells and trace morphology of objects, manual bias in the interpretations have been eliminated, making the quantitation faster, reproducible and more reliable, (described in [Chaphalkar et al., 2016; Meijering et al., 2012; Smal et al., 2009]). However, automated measurements are rarely perfect. The multiple sources of errors can still arise from images with- low SNR, high particle density, disappearing objects in the frames, merging and cross over events [Carter et al., 2005; Cheezum et al., 2001]. This requires a visual inspection of the tracks before considering them for further analysis of motility statistics (velocity, diffusion and directionality). While automated tools that claim 'single nanometer precision' have provided an unbiased platform to evaluate the motility statistics of large number of molecules and polymers, it is perfectly fine to view them with some skepticism. The major reason being these tools deviate from the claims of single nanometer precision when tested in low SNR regimes of the images [Cheezum et al., 2001]. In conclusion, the spatial and temporal precision of any quantitative fluorescent measurement is limited by the signal to noise ratio [Churchman et al., 2005; Waters, 2009; Yildiz and Selvin, 2005]. Hence, the analysis should be performed by setting up appropriate controls at the time of pre-processing the image as well as post-processing the trajectories.

With the above background, I will now present the results and findings that have formed the framework of my Ph.D. thesis in the next few chapters. The following chapter will discuss the results obtained from the calibration experiments performed to assess the noise in the acquisition system and tracking algortithm, and fluorescence based calibration to estimate number of molecules in the unknown sample (Chapter 2). The results obtained are then used as cut-offs for the subsequent gliding assay experiments

where the number dependence of dynein is assessed in microtubule transport (Chapter 3). The findings obtained from *in vitro* experiments are extended to *in vivo* measurements of nuclear positioning in budding yeast where cortically anchored dyneins drives nucleus positioning (Chapter 4). Along with assessing dynein number-dependent dynamics of MT transport, my thesis also reports the findings obtained from polymerization kinetics of tubulin using a plant source (mung) and contrast it with the most routinely used tubulins from brains (goat and porcine) (Chapter 5). The final chapter of my thesis concludes these findings with the future implications for biochemical, biophysical and structural insights that can be obtained in MT dynamics and transport networks.

Chapter 2

Estimating mechanical noise for motion stability and calibrating intensity by quantitative fluorescence microscopy

KEYWORDS: MICROTUBULES, GLIDING, KINESIN, BEADS,CUT-OFFS, TRANSLATIONS, MICROSCOPIC NOISE, PSF, TRACKING, Z-PROFILE, EGFP CALIBRATION, LENGTH TRUNCATIONS

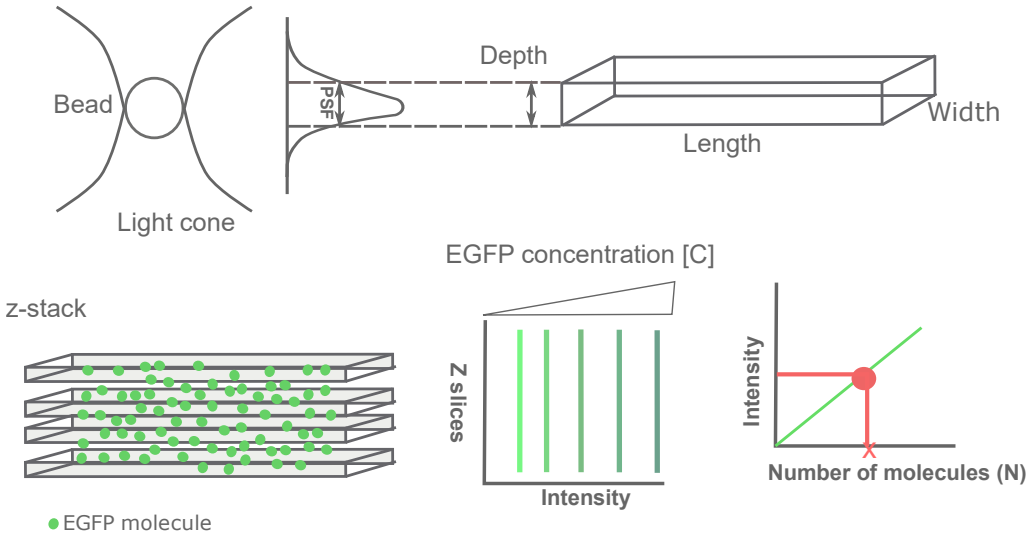

2.1 Introduction

Filament assays, popularly known as 'gliding assays' in MT-motor systems, involve studying of filament transport on sheets of immobilized motors in an *in vitro* system. In order to understand the collective behavior of motors on filament transport, the filaments are tracked and their motility statistics (speed, displacement, orientation) are quantified as a function of motor density. Automation in the tracking process has accelerated the tedious and iterative process of multiple measurements to generate unbiased and reliable data. A more important aspect of "computational imaging" based approaches, is the objective nature of the method. Careful quantification of MT transport are limited by the following factors: (a) limitations of the method for motor number estimation, (b) position detection accuracy and (c) motion detection accuracy. Motor density estimations become a critical factor while evaluating the collective behavior during filament transport.

Previous studies involved motor density estimations in a gliding assay based primarily on one of the following three approaches: i) colorimetric measurements of phosphate release by motors in free solution and on coverslips [Chalovich and Eisenberg, 1982], or ii) concentration of the protein and the geometry of the flow chamber [Hancock and Howard, 1998], and iii) extracting motors from flow chamber and performing densitometric scanning on SDS PAGE gel [Rastogi et al., 2016]. While each of these methods estimate the motor numbers with some degree of certainty, they have limitations. For example, colorimetric assays measure the amount of inorganic phosphate (Pi) released during the ATPase cycles of the motors. A calibration curve is built based on the Pi released in solution which is used for estimating motor number based on the Pi released on the surface of flow cell. The limitation of this method lies in the assumption that the phosphate release cycles are identical for motors present freely in solution and bound to surface in the flow cell. In addition, the real time visualization of filament movement cannot occur along with the colorimetric assay due to which a separate reaction needs to be set up, thereby consuming a lot of protein. Similarly, estimations based on the geometry of flow chamber and protein concentration are uncertain as amount of protein adhered to the glass surface can vary and the method assumes that almost all the protein is adhered in a given area of the flow chamber. Hence, estimations based on the concentration and geometry are not precise. On the other hand, SDS based extraction of proteins from

flow chamber estimates protein adhered on the surface [Rastogi et al., 2016], but might lead to protein losses in the form of bubbles and drying. Moreover, these are indirect measures of quantifying motor numbers. A more direct approach to estimate motors is based on quantitative fluorescent measurements. Counting number of molecules on the surface using fluorescence signal have been made using step-wise photo-bleaching [Das et al., 2007], or super resolution localization microscopy [Lee et al., 2012; Nan et al., 2013]. Although these techniques can estimate the number of molecules precisely, their utility is limited to sparse distribution of molecules over surface [Coffman and Wu, 2012; Waters and Wittmann, 2014]. A more robust way of quantifying samples with abundant protein on the surface involves building a standard calibration curve in fluorescence using wide-field microscopy [Swedlow et al., 2002a], described in this chapter.

Quantification based on microscopic visualizations is one of the most powerful tools to understand the dynamics of the process. Quantitative fluorescence microscopy is used extensively to visualize the temporal and spatial localization of molecules in sub-cellular structures. The measurements based on fluorescence are used either to decipher the (i) spatial information in the form of x-y tracks which can be quantified to obtain displacement, velocity or angle of trajectories and (ii) local concentrations of the fluorophores to decipher the numbers of molecules in a given area based on the intensity. However, quantitative microscopy often requires careful examination of possible sources of errors from- acquisition systems, light source, specimen preparation, and tracking algorithm. It involves setting up of controls meticulously that gives reproducible results.

In this chapter, I will be discussing results which involved calibrations for noise from acquisition system, tracking algorithm and motor density estimations based on fluorescence measurements. While precision in single molecule localization methods have increased [Ober et al., 2004], mechanical noise in the form of vibrations on stage or shutter can be misleading when interpretation of results are based on tracking of particles. This necessitates evaluation of the motion stability of the acquisition set up. Mechanical noise has been quantitated here by tracking image time series of fixed beads. In order to distinguish between the noise existing in the acquisition set up and that in tracking algorithm, synthetic translocation with known displacements are performed for single images of fixed beads and microtubules. The values obtained have been implemented as cut-offs

while considering results of tracked filaments from gliding assays. The applicability of motion stability analysis can in principle extend to measurements like diffusion analysis, single particle tracking or step size determination. Calibrations based on epi-fluorescence intensity measurements are also performed to precisely estimate the number of molecules adhered on a glass surface. While the results from these calibrations are utilized for gliding assays performed subsequently, they have a wide range of applicability. These calibrations are robust and direct measures of estimating mechanical noise and number of molecules in a given sample and can be adapted with any acquisition system.

2.2 Materials and Methods

2.2.1 Fluorescent bead microscopy and analysis for stage calibration

The stability of the microscope stage was assessed using 0.2 μm fluorescently labeled fixed beads on a glass slide. A time series of the bead images were acquired at every 1 s interval (comparable to gliding assays) and tracked using molecule function in FIESTA ver.1.04 reported previously [Ruhnow et al., 2011] in MATLAB R2015b (Mathworks Inc., USA) on a Linux platform. The tracks of the centroids were analyzed using Matlab to obtain instantaneous displacements. An inbuilt function of Matlab - *findpeaks* was used to detect peaks in the histogram of instantaneous displacements.
For the bead tranlocations, a single image of the fixed beads was translated synthetically by 1 pixel and 10 pixels in Image J using a macros script and tracked in Fiesta.

2.2.2 Microscopy and Image analysis

The samples were imaged at room temperature ($\approx 22^{\circ}$C) using a fluorescent upright microscope, Zeiss Axio Imager Z1 (Carl Zeiss, Germany) with an EC Plan-Neofluar 40x (NA - 0.75) lens, a mercury short arc lamp (X-cite Series 120, Lumen Dynamics Inc., Canada), Maerzhauser stage and filter sets for rhodamine (520 nm/540 nm excitation and 580 nm/600 nm emission). Images were acquired every second for 10 to 20 minutes using the Zeiss AxioCam MRm digital camera (Carl Zeiss, Germany).

The images acquired were tracked using Fluorescence Image Evaluation Software for Tracking and Analysis (FIESTA) ver.1.04 reported previously [Ruhnow et al., 2011] in MATLAB R2015b (Mathworks Inc., USA) on a Linux platform. Further analysis for quantifying the gliding behavior of MT's was performed using MATLAB. The analysis was performed after pre-processing the data. It included elimination of the trajectories that leave the field of view. Instantaneous displacements were obtained using the successive differences between the x-y positions.

2.2.3 Preparation of Microtubule filaments

Rhodamine-labeled bovine (0.8 μg/μl) and unlabeled porcine tubulin (3.3 μg/μl) (Cytoskeleton Inc., Denver, USA) were mixed at a ratio of 1:4 (labeled:unlabeled) and incubated in BRB-80 buffer (80 mM PIPES, 1 mM $MgCl_2$, 1 mM EGTA) at 37^oC for 15 minutes, followed by the addition of 20 μM taxol containing BRB-80 to obtain fluorescently labeled microtubules. In order to distinguish individual filaments, samples were diluted 10 - 20 fold before microscopy.

2.2.4 Preparation of flow chambers

Flow chambers were assembled from a microscope slide and 22 x 22 mm coverslip (Micro Aid, Pune, India), both of which were cleaned by sequential immersion in acetone for 1 hr and ethanol for 15 min) followed by two washes with milli-Q water (5 mins each) and treatment with 0.1 M KOH for 15 mins and a final rinse with milli-Q water [Bieling et al., 2007]. Double-backed tape was used to create a chamber parallel to the length of the slide with a final volume of $\approx 16\ \mu l$. The flow chamber was filled by capillary action with a micropipette and filter paper at either end.

2.2.5 Kinesin gliding assay

10 μl of human recombinant kinesin. obtained commercially (Cytoskeleton Inc., Denver, USA)(stock 0.41 *mu*g/μl) protein was perfused through one end of the chamber and incubated at RT for 5 minutes followed by addition of blocking solution- 0.5mg/ml BSA (Sigma Aldrich, Mumbai, India). A 10 μl solution of labeled taxol-stabilized MT filaments was perfused into the chamber and incubated for 5 min. The chamber was

washed with a buffer solution (BRB80 containing 0.1 mg/ml casein) to remove unbound motors and MTs. The motility buffer (BRB-80) with 100 mM ATP, 1X antifade was perfused in the chamber to observe gliding motility of filaments.

2.2.6 Imaging EGFP for building calibration standard

The EGFP concentration used for calibration was varied from 0.01 ng/μl- 100 ng/μl. 50 μl of each protein concentration was flowed in a double backed tape chamber and imaged with filter sets of GFP (Ex-480 /Em-510). Images were acquired at an exposure time of 150 ms, with a Z-stack of 40 μm (4 μm/slice). The intensity for each concentration of EGFP were averaged over 5 images each containing 10 slices over a depth of 40 μm (depth of the flow chamber). The number of EGFP molecules were calculated for the available volume of field of view based on the concentration of the protein in the double-back tape chamber described in detail in the Results subsection 2.3.5

2.2.7 Dynein purification

The truncated minimal dynein construct (331 kDa) from the *S. cerevisiae* VY208 strain, was purified as previously described [Reck-Peterson et al., 2006a] by growth, lysis and affinity purification with IgG beads,and flash frozen at -80^{o}C and is briefly summarized here. Cells were grown in 2 litres of yeast peptone dextrose (YPD) medium to an optical density at 600 nm of $\sim$ 3 and induced with 2% galactose. The culture was centrifuged, lysed and incubated with IgG beads to bind the ZZ-tag of the motor protein. The protein was released from the beads by $\sim$ 12 hours treatment with TEV-protease at 4^{o}C, flash frozen and stored at a concentration of 0.06 μg/ml at -80 ^{o}C.

2.2.8 Data Analysis

The data is processed using MATLAB R2015b (Mathworks Inc., USA) on a Linux platform. The tracks from FIESTA are processed to obtain instantaneous displacements using the successive differences between the x-y positions. Filament lengths detected are sum normalized to obtain frequency distribution of lengths. The frequency distribution of MT lengths were fit to an exponential function $f = A \cdot e^{-L/\lambda}$ where A is a scaling constant and λ is the length at which the frequency (f) is half-maximal. To ensure

filaments of constant length were analyzed, the frequency distribution of the change in MT filament lengths over time (dL/dt) were fit to a Gaussian to estimate the standard deviation, σ, as a cutoff of change of lengths in further analysis. The function used was $f = A \cdot e^{-\frac{1}{2}(x-\mu/\sigma)^2}$ where A is a scaling constant, μ is the mean that was fixed at 0, and σ is the standard deviation. Velocities were calculated using the ratio of instantaneous displacement to instantaneous time interval. Velocities as a function of length is obtained by binning the lengths with a 1 μm width. The analyses of motility statistics are based on the trajectories of plus-end tips of the filaments, unless otherwise specified.

2.3 Results

2.3.1 Quantifying mechanical noise of microscopy set up to analyze motion stability with fixed beads

The stability of the microscopy stage and system is assessed using a time series image of 0.2 μm fluorescently labeled fixed beads **(Figure 2.1(a))** as described in the methods subsection 2.2.1. The instantaneous displacements of the fixed beads tracked using 'molecule function' of a nanometer-precision tracking algorithm- Fiesta, is evaluated to analyze motion stability due to mechanical noise of the system. A single peak obtained using an inbuilt matlab function - *findpeaks* coincides with the arithmetic mean (μ) of instantaneous displacements **(Figure 2.1(b))**. Since the beads are fixed, a peak at 4 nm is suggestive of the noise in acquisition system. This could be used as a cut-off in subsequent gliding assays to eliminate tracks with displacements smaller than 4 nm. In order to evaluate if the noise is an artefact of the tracking, we next assess the accuracy of tracking algorithm- FIESTA, by translocating fixed beads with defined steps.

2.3.2 Validating tracking accuracy of FIESTA

The precision with which fiesta can detect positions of filament centerline has been reported to be 2 nm [Ruhnow et al., 2011]. In order to validate if the displacement observed with fixed beads is due to instrument noise or tracking artefacts, a single image of the fixed beads is translated synthetically using an ImageJ macro by 1 pixel (154 nm) and 10 pixels (1540 nm), and tracked (blue lines) using FIESTA **(Figure 2.2(a) and**

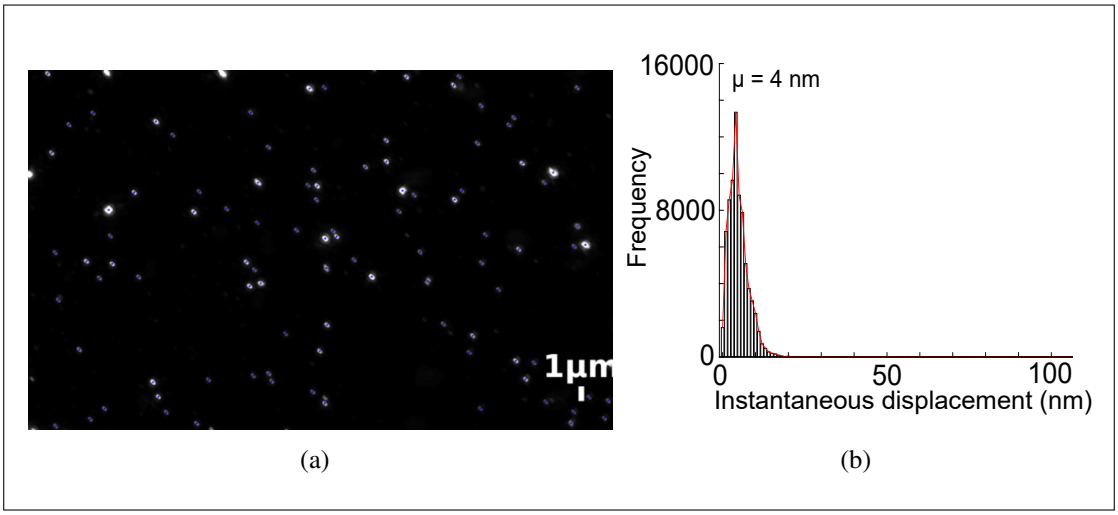

Figure 2.1: **Assessing stability of microscope stage and system with static beads**(a) A time-series of fluorescently labelled 0.2 μm beads immobilized on a glass slide was tracked (blue lines). (b) The histogram of instantaneous displacements (black bars) is overlaid with the output of the peak-finding algorithm (red line). The single peak detected corresponds to 4 nm.

(b)). The frequency distribution of instantaneous displacements shows three peak values for beads translated by 1 pixel at 152 nm, 154 nm, and 158 nm **(Figure 2.2(c))**, and a single peak at 1540 nm for beads translated by 10 pixels **(Figure 2.2(d))**.

In order to evaluate these trends for a filament system, tracks of static filaments translocated synthetically by 1 pixel (154 nm), 2 pixels (308 nm) and 10 pixels (1540 nm) are also analyzed **(Figure 2.3(a) - (c))**. The frequency distribution of the tracked filaments shows peaks at 154 nm, 308 nm and 1540 nm as expected for the respective translocations **(Figure 2.3(d))**.

Although the filaments showed displacement peaks at expected values, a cut- off of 1 pixel is implemented for the filament displacements in subsequent gliding assays based on the bead data translocation. This is to eliminate any artifact that might arise due to the presence of smaller filaments ($\leq$1 μm).

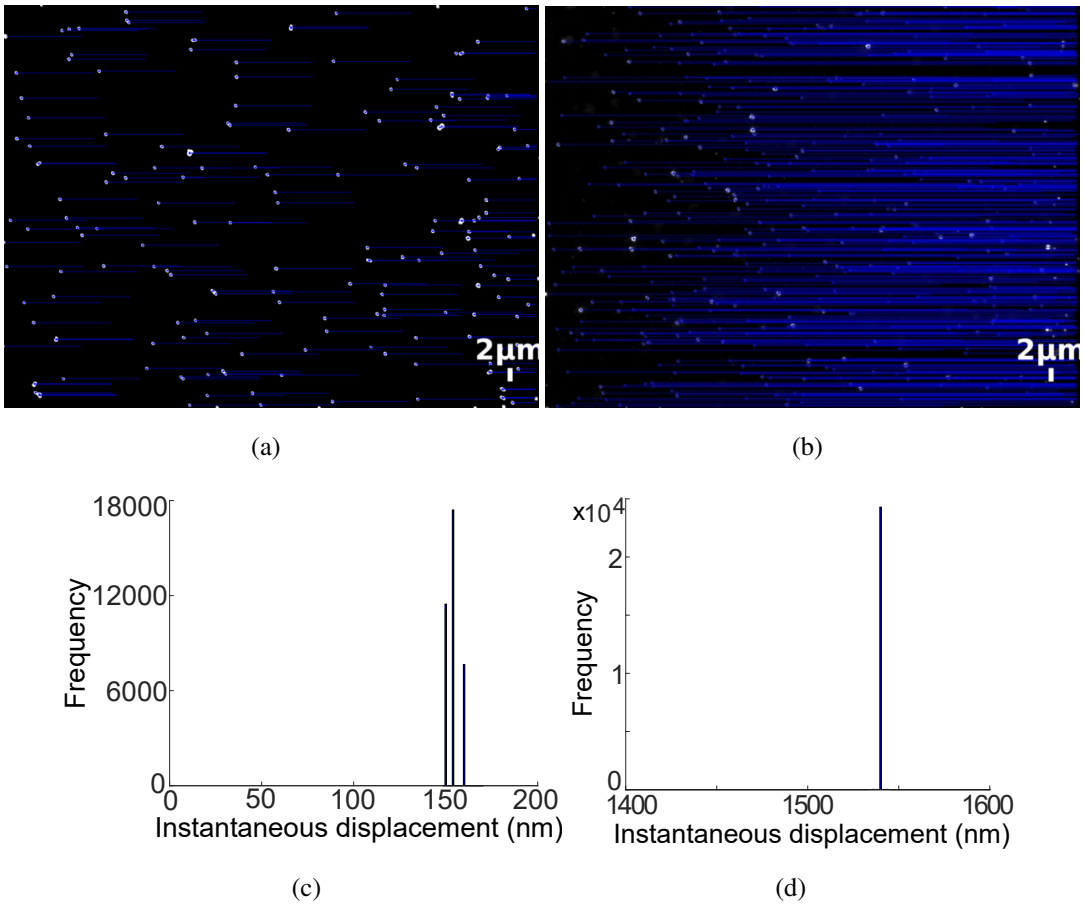

Figure 2.2: **Testing accuracy of tracking algorithm with synthetically translocated beads.** Images of fluorescently labeled immobilized beads (gray) were translocated using ImageJ by (a) 1 and (b) 10 pixels per frame and tracked using FIESTA. The tracks (blue lines) are overlaid on the first frame of the bead image. Frequency distribution of instantaneous displacements (black bars) from synthetically translated beads is shown for (c) 1, and (d) 10 pixels/frame. 1 pixel= 154 nm

2.3.3 Eliminating tracked filaments with fluctuating lengths

A gliding assay with taxol stabilized rhodamine labeled filaments was performed as described in the **Methods subsection 2.2.5** . The length profile of the filaments were fit to an exponential function:- $f = A \cdot e^{-L/\lambda}$ where A is a scaling constant and λ is the length at which the frequency (f) is half-maximal **(Figure 2.4(a))**. The filament

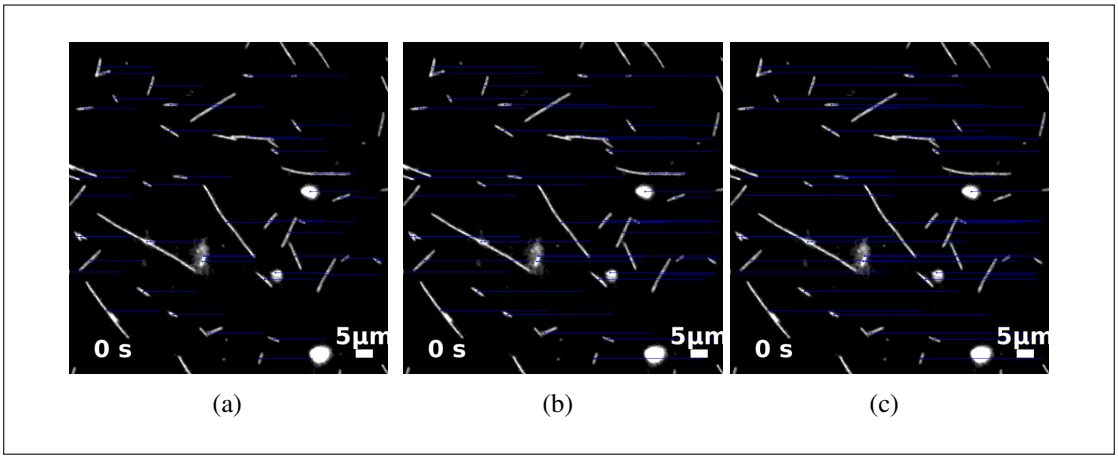

(a) (b) (c)

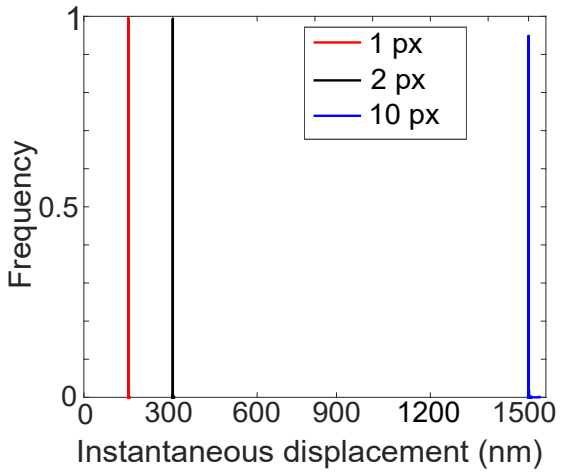

(d)

Figure 2.3: **Testing accuracy of tracking algorithm with synthetically translocated filaments.** A single image of the MT filaments translocated using ImageJ by (a) 1, (b) 2 and (c) 10 pixels per frame and is tracked using FIESTA. The tracks (blue lines) are overlaid on the first frame of the MT image. (d) The bar shows frequency distribution of instantaneous displacements from synthetically translated filaments, where colors indicate the displacements with- 1 pixel (red), 2 pixels (black) and 10 pixels (blue). 1 pixel= 154 nm

lengths follow an exponential distribution (red curve) which is in agreement with the equilibrium models for the polymers [Oosawa, 1970]. The mean value of the filament lengths using the fit is observed to be 4.8 μm. The filament lengths are plotted as a

function of time to observe the length variations during gliding on motors **(Figure 2.4(b))**. These fluctuations in lengths (dL/dt) are also plotted as a function of time for successive intervals **(Figure 2.4(c))**.

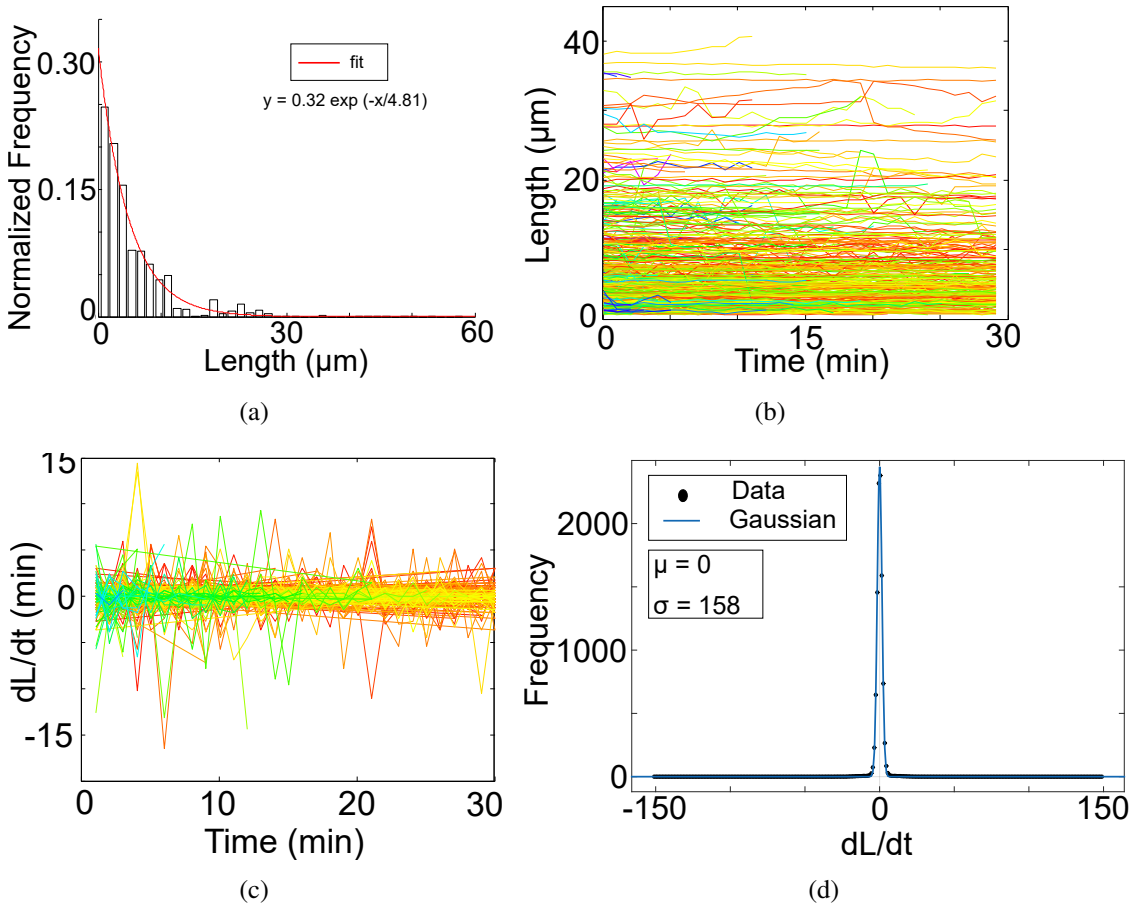

Figure 2.4: **Estimating changes in MT length during tracking from length distribution of MTs.** (a) The exponential fit shows the profile of the frequency distribution of filament lengths after tracking with a mean length of 4.8 μm. (b) Filament lengths are plotted as a function of time to observe length fluctuations. Different colors represent individual filaments. (c) The fluctuations in lengths are quantified and plotted as a function of time. (d) The frequency distribution of the pairwise change in length as a function of time (dL/dt) in nm/s (black circles) was fit to a Gaussian (blue curve) with a mean of 0 nm/s and standard deviation of 158 nm/s.

The tracks with fluctuatating filament lengths are eliminated based on the standard deviation obtained using gaussian fit to frequency distribution of the changes in length

(dL/dt) **(Figure 2.4(d))**. The processed tracks are used for quantitating the filament gliding statistics on motors- kinesin and dyneins.

2.3.4 Quantitating motility statistics of filaments on kinesin motors

The gliding movement of microtubules on kinesin as seen in the montage **(Figure 2.5(a))** is processed to obtain motility statistics as a function of filament length. MT's displacements didn't show any characteristic differences in their profiles when sorted by their lengths **(Figure 2.5(c))**. Also, the velocity profiles show a mean value of ~ 0.5 μ/min as seen from the bins with a bin width of 1 μm. This is in agreement with the published value of velocity for this construct [Stewart et al., 1993]. The gliding assays done on kinesin were also used as control datasets for validating an automated kymography tool-AMTraK, developed in the lab to quantify the sub cellular dynamics with sub-pixel accuracy [Chaphalkar et al., 2016].

Multiple studies have shown that kinesin driven transport of MT filaments doesnot show a length or motor density dependence on quantified motility parameters. In the absence of a systematic study of length and motor number dependence of filament transport on dyneins, gliding assays were performed with a cytoplasmic yeast dynein, discussed in detail in the next chapter. As the motor is tagged to a green fluorescent protein (GFP), motor density estimations involved calibrations with EGFP proteins in flow chambers, as described below.

2.3.5 A standard fluorescent calibration curve to estimate motor density

Motor densities are estimated as illustrated schematically **(Figure 2.6)** [Jain et al., 2019], based on the following three steps: (i) Calculation of Image Volume, (ii) Building a Standard Calibration Curve and (iii)Estimation of Motor Number

(i) **Calculation of Image Volume:** The image volume (V_{img}) is estimated by treating the image as a rectangular cuboid, as a result of which $V_{img} = A_{img} \times h$, with A_{img}: area of the rectangular image, h: height of the image. The area was estimated from x- and y-size of the image (1388 x 1040 pixels) scaled to length units (1 pixel = 0.154 μm) resulting

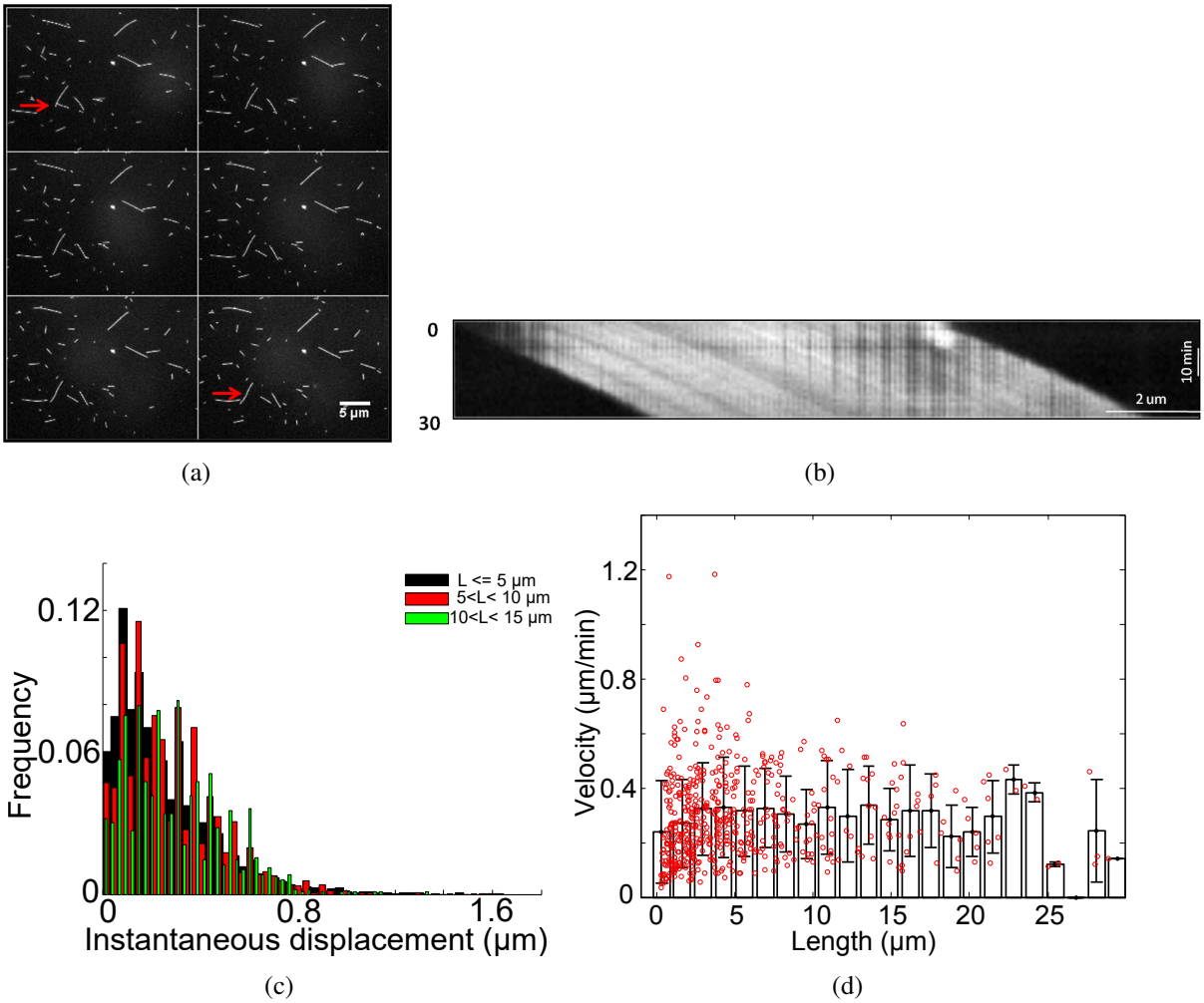

Figure 2.5: **Kinesin gliding assay motility statistics.** (a) Montage represents the motility of rhodamine labeled filaments on kinesin motors. Red arrow denotes the movement of one of the representative filaments in the first and last frames. (b) The kymograph indicates the movement of a single representative filament. (c) The frequency distribution shows the instantaneous displacements of the filaments with lengths (L)- $\leq 5\ \mu$m (black), $5\ \mu\text{m} < \text{L} < 10\ \mu$m (red), and $\text{L} \geq 10\ \mu$m (green). (d) The binned velocity profiles of the filament are indicated for increasing filament lengths where the scatter represents the raw values (o) for a single filament. Bin size = 1 μm

in $A_{img} = 3.4234 \times 10^4\ \mu\text{m}^2$. The height h is estimated from the point spread function (PSF), by analyzing the intensity profile of a z-stack of images of 200 nm diameter FITC labeled fluorescent beads **(Figure 2.6 (i))**. The intensity profile as a function

of z-position is fit to a Gaussian **(Figure 2.7(a))** using the *CurveFitter* tool in Image [Schneider et al., 2012] based on the equation:

$$y = a + (b-a) \cdot e^{[(x-\mu)^2]/[2\cdot\sigma^2]} \tag{2.1}$$

where a and b are scaling factors (a: background grey-value intensity in the image, b: grey-value estimate of the brightest part of the bead), μ is the mean and σ is the standard deviation. By approximating the PSF by the full width at half maximum (FWHM) which is $\approx 2.3548\sigma$ [Pawley, 1995], z-height obtained is 1.77 μm. The resulting V_{img} is 6.02×10^4 μm^3.

(ii) **Building a Standard Calibration Curve:** In a second step, a concentration series of affinity purified 6x-His-tagged EGFP is imaged in the flow chamber **(Figure 2.6 (ii))** and **(Figure 2.7(b)-(c))**. The image intensity corresponding to the concentration series is plotted against the number of EGFP molecules in the image volume (N_{EGFP}) and fit to a straight line. The number of EGFP molecules is calculated as $N_{EGFP} = (c \times V_{img})/m_{EGFP}$, where c: concentration in grams per ml, V_{img}: volume in ml and m_{EGFP}: molecular mass of EGFP in grams. The image-intensity of the GFP-dynein samples (low and high density), is used to estimate the corresponding N_{EGFP} equivalents (x-axis value) from the fit **(Figure 2.6 (iii) and Figure 2.7(d))** To account for the 2-fold brightness of EGFP compared to GFP [Shaner et al., 2005], the N_{EGFP} equivalents are doubled, to obtain the number of dynein molecules in an image (N_{dyn}).

(iii) **Estimation of Motor Number:** The estimated dynein number in a gliding assay is assumed to be localized to a plane, since multiple washout steps are designed to avoid bulk dynein resulting in an estimated 2D density is $\rho_{2D} = N_{dyn}/A_{img}$. Assuming a homogeneous distribution of the motors, the linear density of motors $\rho_{1D} = \sqrt{\rho_{2D}}$. The mean number of motors (N) expected to interact with a microtubule of length L can then be estimated as $N = \rho_{1D} \times L$. The number of dimers (N_{dimers}) are then simply N/2. Unless explicitly stated, N refers to individual motors from experiment in the text, i.e. heads or GFP-equivalents.

This approach of estimating numbers of motors is similar to previous reports [Harris

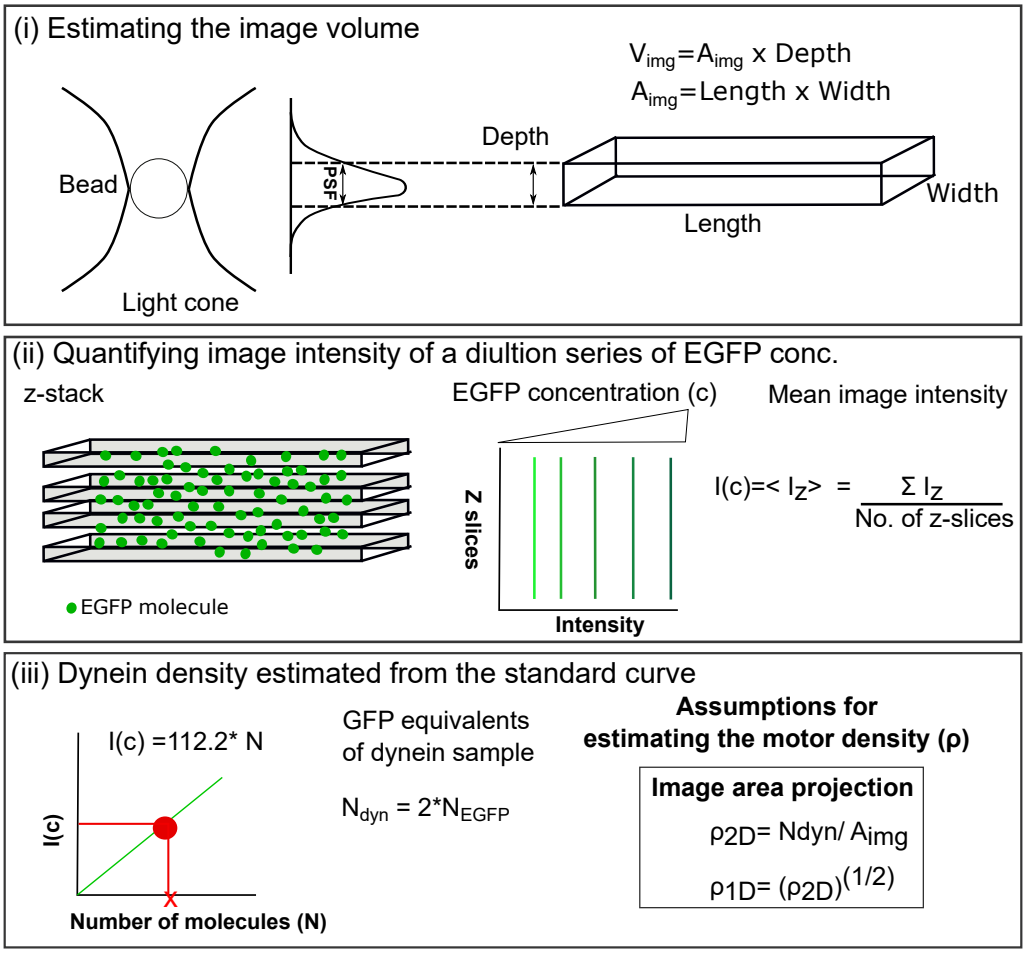

Figure 2.6: **Schematic for estimating motor density using a fluorescence based calibration curve.** The three steps to motor density estimation were: (i) image volume estimation using the area of the field of view and the depth obtained by measuring the psf of the objective , (ii) measuring the image intensities of a dilution series of EGFP solutions to obtain a standard calibration curve and (iii) using the standard curve to quantify dynein numbers. The surface density (ρ_{2D}) is then estimated from the image area.

and Warshaw, 1993; Rastogi et al., 2016; Walcott et al., 2012]. The resulting calibration curve of intensity with EGFP molecules estimates a dynein density of 6.8 motors/μm^2 and 72.4 motors/μm^2 for the low- and high-density experiments respectively **(Figure 2.6(d))**. The uncertainty in the motor number estimates is based on calculating upper and lower

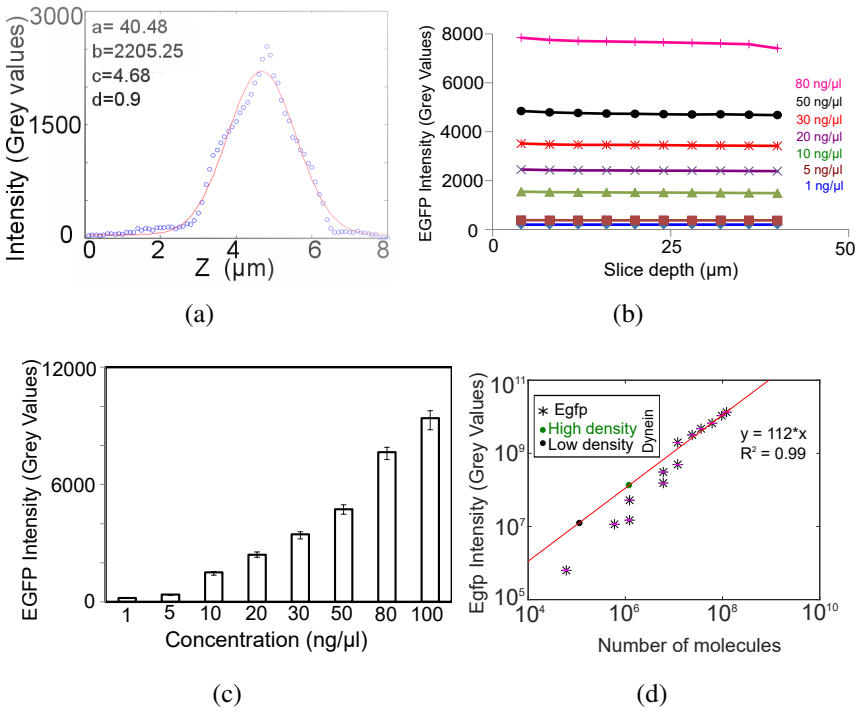

Figure 2.7: **Estimating motor density using EGFP calibration standard.** (a) The z-profile of the fluorescence intensity of 0.2 μm fluorescent beads (blue circles) were fit to a gaussian profile (red line) based on Equation 2.1, and used to estimate the PSF. (b) The plot indicates the intensities profiles of EGFP dilution series in Z with a depth of 40 μm. The EGFP concentrations were varied from 1-80 ng/μl as shown in the legend with different symbols and colors corresponding to each concentration (ng/μl): -:Blue= 1 , □:brown= 5, △:green= 10 , x:purple= 20 , *:red= 30, o:black= 50, +:magenta= 80. (c) The bar shows the intensity profiles of EGFP across increasing concentrations. (d) The standard-curve of total EGFP fluorescence (mean values- *, $\pm$s.d. - magenta, n=3) from an image (y-axis) as a function of number of molecules (x-axis) is used to estimate the number of GFP-dynein molecules on the surface. Slope of the linear fit: 112.7 ± 6 based on 95% confidence interval (Table 2.1).

bounds of the slope. Fit to the EGFP calibration data was used to estimate the 95 % confidence intervals, CI **(Figure 2.7 (b))** which gives upper- (B1) and lower-bounds (B2) of the slope. These are used to estimate upper- and lower-bounds for the two conditions of dynein (unknown sample) that are referred to as high- and low-density (**Figure 2.7(b)**) and (**Table 2.1**). Using a 95% confidence interval, we infer a maximal error of 10% in 2D and 4% in 1D density estimates **Table 2.1**, which translates to an uncertainty

of ± 0.04 motors/μm of MT lengths. The validation of the density estimates are also discussed alongwith the results from gliding assays in the following chapter.

		Surface density, ρ_{2D} ($\mu\mathbf{m}^{-2}$)		**Linear density, ρ_{1D} ($\mu\mathbf{m}^{-1}$)**	
Fit/ Bound	**Slope**	Low density	High density	Low density	High density
Fit	112.7	6.8	72.8	2.62	8.53
B1	118.7	6.5	69.2	2.55	8.31
B2	106.7	7.2	77	2.69	8.77

Table 2.1: **Uncertainty in dynein number estimation.** The table represents the 1D (ρ_{1D}) and 2D (ρ_{2D}) densities of dyneins based on the slope of the fit (Fig. 2.6(b)). Based on a 95% confidence interval, the bounds of the slope B1 and B2 are calculated. Based on these slopes, the corresponding dynein densities are calculated for high- and low-density samples.

2.4 Discussion

This chapter discusses the various cut-offs implemented for the gliding assay set up based on the accuracy and sensitivity of the imaging set up and tracking algorithm. The mechanical noise in the acquisition system quantified from images of fixed beads is used as the lower limit for eliminating any movements observed **(Figure 2.1)**. Synthetic translation of fixed beads showed multiple peaks for 1 pixel when tracked using FIESTA **(Figure 2.2)**. However, this translocation when applied to filaments showed the peaks at desired intervals of 1, 2 and 10 pixels **(Figure 2.3)**. This shows that the algorithm can accurately detect displacements for elongated objects and is sensitive to sub-pixel movement as reported [Ruhnow et al., 2011]. However, it can give discrepant results for sub-pixel movements of sub-micron sized particles. Therefore, one pixel cut-off (154 nm) has been set for considering displacement of filament movement in subsequent gliding assays.

Density estimates are obtained using the calibration curve based on wide field fluorescence **(Figure 2.7)**. Motor densities on surfaces of gliding assay have been estimated in the past by washing out the flow chamber and SDS-PAGE based protein estimation [Rastogi et al., 2016; Sato et al., 2012]. However, the indirect nature of the method and potential losses suggest a more direct approach could improve the reliability of the estimation. Our use of EGFP dilution series as a calibration standard to estimate protein concentration using epi-fluorescence microscopy [Jain et al., 2019] is comparable to previously reported methods using fluorescently tagged proteins to estimate *in vivo* protein copy numbers [Joglekar et al., 2008; Swedlow et al., 2002a]. Indeed, the advantages of wide field microscopy over confocal for such copy-number estimations have been discussed in literature [Swedlow et al., 2002a].

Gliding assay performed with taxol stabilized filaments were analyzed after eliminating tracks with lengths fluctuations **(Figure 2.4)**. This makes certain that length dependent analysis of microtubule transport is accurate. Gliding assays with immobilized kinesin motor show mean speeds comparable to published values [Stewart et al., 1993] **(Figure 2.5)**. This assures that the various cut-offs implemented based on the controls for acquisition set up (Results subsection 2.3.1), tracking algorithm (Results subsection 2.3.2) and post-processing filament lengths (Results subsection 2.3.3) work to give expected outcomes. The motility speeds are constant across the observed MT lengths consistent with previous reports of bovine kinesin [Howard et al., 1989a; Hunt et al., 1994; Imafuku et al., 1996b]. Multiple models that reconcile single motor and collective mechanics have been proposed. For example, the processivity of kinesin based MT transport [Howard et al., 1989a] has been explained by a 'loose coupling' of motors [Oosawa, 2000; Oosawa and Hayashi, 1986] and validated in case of kinesin-1 [Bieling et al., 2008]. Fluctuation based load-sharing [Belyy et al., 2014; Gagliano et al., 2010; Kunwar et al., 2008] and negative cooperativity of detachment [Arpağ et al., 2014; Driver et al., 2011] have also been proposed to enable cooperative transport by multiple motors. More recent studies with kinesin-1 anchored on membranes have shown a density dependence on velocity statistics, suggesting a role of motor diffusivity and density in controlling the efficiency of MT transport [Grover et al., 2016]. However, such studies with dyneins are limited due to a relatively more complex structure and stepping behavior. In order to understand the collective behavior of dyneins in MT transport, we have used a model yeast dynein

and studied the role of motor numbers and MT lengths during filament transport using a minimal *in vitro* system, discussed in the next chapter.

Chapter 3

Collective effects of yeast cytoplasmic dynein in *in vitro* Microtubule transport

KEYWORDS: DIRECTIONAL, DIFFUSION, DYNEIN, FILAMENTS, GLIDING, MINIMAL, MICROTUBULE, MOTOR NUMBER, RANDOM, SINGLE MOTOR, SIMULATIONS, TRUNCATED, YEAST.

Contributions: Simulations were performed in the lab by Ms. Neha Khetan, IISER Pune.

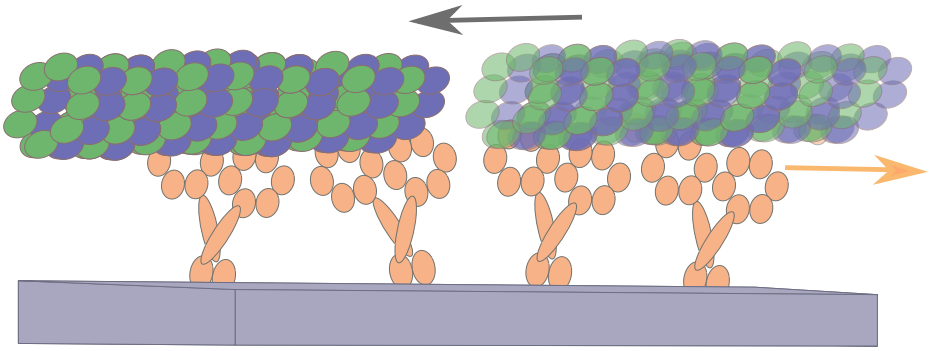

3.1 Introduction

Microtubule (MT) transport by molecular motors plays a vital role in regulating cell physiology and mechanics as seen in eukaryotic cell division [Burbank et al., 2007; Rusan et al., 2002], polarization [Witte et al., 2008] and migration [Wu et al., 2012]. While single-molecule *in vitro* assays have increasingly provided a detailed understanding of the mechanochemistry of kinesins [Coppin et al., 1997; Howard et al., 1989b; Svoboda and Block, 1994a] and dyneins [Mallik et al., 2004a; Reck-Peterson et al., 2006a; Shima et al., 2006], cellular processes typically involve multiple motors acting together. Transport processes involving many motors acting together have been well studied in vesicle transport where motors work in teams to carry cargoes on immobile filaments [Gross et al., 2007a; Rai et al., 2013a]. However, filament transport by immobilized motors, has also been reported in physiologically relevant processes such as such as spindle assembly [Burbank et al., 2007; Cytrynbaum et al., 2003; Walczak et al., 1998], neuronal axon development [Baas and Mozgova, 2012; Goldstein and Yang, 2000], *Caenorhabditis elegans* fertilization [Kimura and Kimura, 2010; Tanimoto et al., 2016], mouse oocyte maturation[Schuh and Ellenberg, 2007], nuclear oscillations in *Schizosaccharomyces pombe* [Ding et al., 1998; Svoboda et al., 1995; Yamamoto et al., 2001a] and mitotic nuclear positioning in *Saccharomyces cerevisiae* [Adames and Cooper, 2000a]. The regulation of the number of motors (N) transporting MTs and their localization result in spindle oscillations in *S. pombe*[Ananthanarayanan et al., 2013; Vogel et al., 2009; Yamamoto et al., 2001a] and *C. elegans*[Pecreaux et al., 2006a]. Thus, understanding the effect numbers of motors (N) on collective transport properties could provide insights into MT transport *in vivo*.

Dyneins play an important role during the *in vivo* transport of filaments. However, they are relatively less well understood at a single molecule level compared to kinesins, due to their greater structural complexity [Oiwa and Sakakibara, 2005]. One such well studied dynein is the highly processive yeast cytoplasmic non-essential dynein. At a single molecule level it has been shown to stochastically step backwards and forwards with variable step sizes ranging from 8 to 32 nm in the absence of load [Reck-Peterson et al., 2006a] and increasing in backward steps under load [Gennerich et al., 2007]. The processivity of the dimeric motor has been attributed to a lack of inter head co-ordination

and asynchronous stepping when the two motor domains are close to each other [DeWitt et al., 2012; Qiu et al., 2012], while coordinated stepping can arise with increasing inter-head separation through linker tension gated release of the motor from MTs [Cleary et al., 2014]. Load sharing between the heads allows dynein to step processively even under large loads [Belyy et al., 2014]. Additionally, single molecule detachment rates for this yeast dynein have asymmetric force dependence - assisting forces increase detachment, while hindering forces result in persistent binding [Cleary et al., 2014; Nicholas et al., 2015a]. The effect of single-molecule dynamics on multi-molecular transport by teams of this dynein is not apparent from current theoretical models of collective transport that are based on 'loose coupling' of motors [Bieling et al., 2008; Oosawa, 2000; Oosawa and Hayashi, 1986], fluctuation based load-sharing [Gagliano et al., 2010; Kunwar et al., 2008] and negative cooperativity of detachment [Arpağ et al., 2014; Driver et al., 2011]. A mathematical model specific to the yeast dynein would thus help better understand the *in vivo* role of this 'model' dynein.

The collective transport velocity of the yeast cytoplasmic dynein has been shown to be comparable to the single molecule velocity in experiments[Reck-Peterson et al., 2006a]. While a DNA-origami cargo has been used to precisely control the effect of increasing dynein team sizes on run lengths and times[Derr et al., 2012], it involved maximally 7 motors moving a cargo on static MTs. Studying the number dependence of MT transport by anchored motors over a wider range, could be more representative of the *in vivo* scenario in *S. cerevisiae* mitosis, where this dynein localizes on the the bud-cell cortex and pulls on astral MTs, driving nuclear positioning [Adames and Cooper, 2000a; Hoepfner et al., 2000a; Moore et al., 2009; Shaw et al., 1997]. At the same time, the astral MTs act as tracks transporting more dynein to the cortex, increasing the local density [Lee et al., 2005]. Thus, 'search and capture' of astral MTs in nuclear positioning involves changes in motor numbers and MT lengths. This suggests, a minimal system which quantitatively address the role of MT lengths and motor numbers, could improve our understanding of nuclear positioning *in vivo*.

Here, the collective transport properties of a *Saccharomyces cerevisiae* cytoplasmic dynein fragment, widely used as a minimal model, are examined by a combination of quantitative MT gliding assays and stochastic simulations. To understand the dependence

of transport on the motor numbers, two variables are analyzed: (a) the motor density and (b) MT lengths. As the length of MTs increase, the movement seems to become more directed. The combined effect of motor density and MT lengths on speed, velocity and directionality of filament transport is best understood in terms of motors per MT. While translocation speeds (scalar, considers only magnitude) decrease and saturate with increasing MT lengths and motor densities, the transport velocity (indicative of vectorial transport) suggests a motor number dependent threshold change at low densities. Increasing motor numbers also results in a switch-like transition in directionality of filament transport from random to directed movement. To better understand this behavior, a gliding assay is simulated based on a model of uniformly distributed immobilized motors transporting semi-flexible MTs. The results of such number dependence in MT transport are discussed in the context of *in vivo* scenario of *S.cerevisiae* mitosis where this dynein is involved in nuclear positioning.

3.2 Materials and Methods

3.2.1 Gliding assay

Double-backed tape based flow chambers were prepared similar to those described previously [Bieling et al., 2007] to create a chamber with a volume of ≈ 16 μl using glass slides and 22 x 22 mm coverslips (Micro Aid, Pune, India) that were cleaned with acteone, ethanol, water, KOH and water. Dynein purification and MT assembly is described in the sections of the previous chapter- Dynein purification, 2.2.7 on page 22 and Preparation of Microtubule filaments, 2.2.3 on page 21 respectively.

Motors were perfused (50 μl of 0.06 μg/ml dynein) through one end of the chamber in lots $\sim$15 μl each, incubated for 5 minutes at room temperature. Blocking solution containing 0.5 mg/ml BSA (Sigma Aldrich, Mumbai, India) was flowed in, followed by the addition of 10 μl of MT filaments (labelled, taxol-stabilized) and the slide incubated for 5 minutes. A wash buffer (also used as lysis buffer- 30 mM HEPES (pH 7.2), 50 mM potassium acetate, 2 mM magnesium acetate, 1 mM EGTA, 10% glycerol, 1 mM DTT, 1 mg/ml casein) was used to remove unbound motors and MTs. Motility buffer (wash buffer supplemented with 1 mM ATP) with 1x Anti-fade (Cytoskeleton Inc., USA)

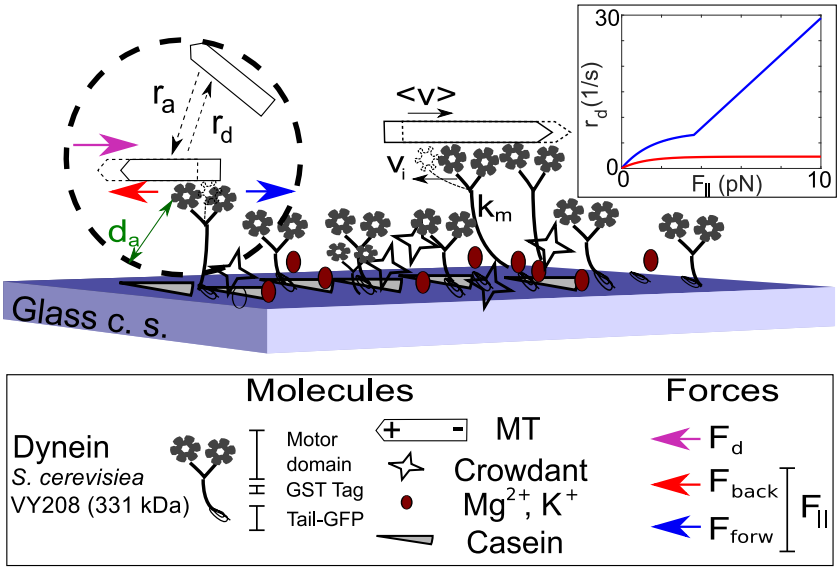

Figure 3.1: **Dynein collective transport.** The molecular components of the *in vitro* reconstituted MT-transport by a truncated minimal form of the *S. cerevisiae* dynein motor on a glass coverslip (c.s.) surface in experiment are schematically represented. A stochastic mechanochemical model to represent key aspects of the system is developed, where motors attach to MTs at a rate 'r_a' if they are within an attachment distance 'd_a', and detach at a rate 'r_d'. Single motors step along the MT with an instantaneous velocity v_i and multiple motors transport MTs with an effective mean effective velocity $\langle v_{eff} \rangle$ (black arrows represent the direction of movement). A drag force F_d (magenta arrow) acts on the MTs due to their motion through the medium with viscosity η. The motors are modeled as Hookean springs with a stiffness k_m. Motor stepping along MTs produces a parallel force $F_{||}$ in forward (blue arrow) and backward (red arrow) directions, affecting the motor detachment rate (inset).

was perfused to observe MT gliding. For the low density experiments, before adding motors, anti-GFP antibody (0.2 μg /μl) (Sigma Aldrich, Mumbai, India) was perfused through one end of the flow chamber and incubated for 5 mins followed by the addition of blocking solution, motors, MTs, wash- and motility-buffer, as described above. The flow chamber was then imaged on an upright microscope.

3.2.2 Image and data analysis

Image time series of gliding assays were pre-processed by median filtering using ImageJ ver.1.45s [Schneider et al., 2012] and tracked using a filament tracking tool FIESTA ver.1.04 reported previously [Ruhnow et al., 2011] in MATLAB R2015b (Mathworks Inc., USA) on a Linux platform.

The maximal connecting velocity was set to 1 $\mu m/s$ and FWHM to 500 nm. Only filaments that persisted for 10 or more frames and a permitted angular deviation between successive frames of 1 to 5 degrees were processed. To ensure filaments of constant length were analyzed, the frequency distribution of the change in MT filament lengths over time (dL/dt) were fit to a Gaussian as described in Chapter 2, Section- Data Analysis. The analyses of motility statistics are based on the trajectories of plus-end tips of the filaments, unless otherwise specified.

The gliding velocity of MT filaments, (vector, v_{eff}) (Figure 3.6) was estimated from the magnitude of the vector representing the instantaneous displacement of filament tips at each successive time point as a function of the time interval [Ruhnow et al., 2011]. Mean $\langle v_{eff} \rangle$ was obtained from binning MT lengths every 1 μm.

The measure of directionality of motility (χ) from experiment and simulation was calculated from individual trajectories as the ratio of the magnitude of start to end displacement to the path length of a trajectory as previously described [Khetan and Athale, 2016].

To avoid sampling static filaments, trajectories with displacements less than a cutoff distance of 1 pixel (154 nm) were ignored from the microscope calibration in experiment in previous chapter- Validating tracking accuracy of FIESTA, 2.3.2 on page 24.

To improve our statistics, trajectories of motile filaments which were static between successive frames, were linearly interpolated, until the filament moved a distance greater than the cutoff. Mean directionality was estimated for bin-width of MT lengths of 1 μm and reported for that average length. To obtain a χ value as a function of motors, the same approach was taken as before (product of mean linear density and length). All further data analysis was performed using MATLAB R2014b (Mathworks Inc., USA).

3.2.3 MSD and diffusivity analysis

The mean square displacement (MSD) is calculated from the 2D positional coordinate of the filament (**r**) as previously described [Arcizet et al., 2008; Athale et al., 2014a; Khetan and Athale, 2016] for increasing each time interval (δt) and averaged based on the expression:

$$MSD(\delta t) = \frac{1}{N}\Sigma[\mathbf{r}(t) - \mathbf{r}(t+\delta t)]^2_{t \leq 3T/4} \tag{3.1}$$

where t is the time point, T is the total time and N is the total number of displacements in a time interval. The analysis used $\delta t \leq 0.75 \times T$, based on previous reports for improved statistics [Arcizet et al., 2008; Michalet, 2010]. If the net displacement of a trajectory was 154 nm or less (equivalent to a pixel in these experiments), those trajectories were ignored, assuming the filament did not move.

Experimental MSD profiles were averaged by pooling length classes ranging from 0.5 to 12.5 μm in bins of 3 μm with the mean of that bin representative of the length (Figure 3.4). Both experiment and simulation data were fit to two models of effective diffusion: *(a)* anomalous diffusion and *(b)* diffusion with transport. The anomalous diffusion model allows us to test whether MT length or density resulted in any deviation from diffusive behaviour (super- or sub-diffusive) [Athale et al., 2014a; Saxton, 2007, 2008], while the transport velocity can be extracted from the diffusion-transport model [Arcizet et al., 2008; Grover et al., 2016; Khetan and Athale, 2016]. The *(a)* anomalous diffusion model is:

$$MSD = 4 \cdot D^{'} \cdot t^{\alpha} + c_1 \tag{3.2}$$

where $D^{'}$ is the anomalous diffusion coefficient, t is time, α is the anomaly parameter and c_1 is the error in detection. The *(b)* diffusion with transport model is:

$$MSD = 4 \cdot D_{eff} \cdot t + (v \cdot t)^2 + c_2 \tag{3.3}$$

where D_{eff} is the effective diffusion coefficient, t is time, v is the transport velocity and c_2 is the error in detection.

3.2.4 Simulations

A gliding assay simulation was developed in the lab to model the experiments with single molecule measurements of the yeast dynein [Gennerich et al., 2007; Qiu et al., 2012; Reck-Peterson et al., 2006a] by Ms. Neha Khetan. In the simulation, motors are assumed to be immobilized on a surface by their stalks and the heads can bind MTs based on stochastic attachment-detachment kinetics. The average effective velocity of MT transport ($< v_{eff} >$) results from a combination of (i) attachment and detachment dynamics of individual motors, (ii) stochastic stepping of individual motors at a velocity v_i where i is the index of motors, (iii) the passive stretch force experienced by a static motor bound to a filament, due to the transport of the filament by other motors and (iv) the thermal and drag forces due to the medium (Figure 3.1).

2D simulations were performed using Cytosim [Nedelec and Foethke, 2007], an agent-based simulation engine written in C++. MT and motor dynamics and mechanics were modeled as before [Athale et al., 2008, 2014a; Khetan and Athale, 2016] in a square simulation box of length L_{box} with periodic boundary conditions. The integration time was chosen to be smaller than the fastest time-scale. The system consists of MT filaments of a fixed length (L) and a fixed number of motors determined by the density (ρ_{2D}). Both filaments and motors were randomly distributed in simulation space at the time of initialization. Model structure with motor mechanics is described in great detail in our publication- [Jain et al., 2019].

3.3 Results

3.3.1 Motor density and MT length both affect MT transport

Gliding assays were performed with dyneins immobilized at the surface and the transport properties of MTs were observed **(Figure 3.1)**. The motor densities quantified using fluorescence calibration in the previous **Chapter 2, Section 2.3.5 on page 28** were found to be 6.8 and 72.4 motors/μm^2. At a low motor density **(Figure 3.2a)**, the XY trajectories of MT tips appeared random for short filaments ($< L > \leq 5$ μm) as compared to long filaments($< L >> 5$ μm) **(Figure 3.2b)**. In contrast, in presence of a high-density of

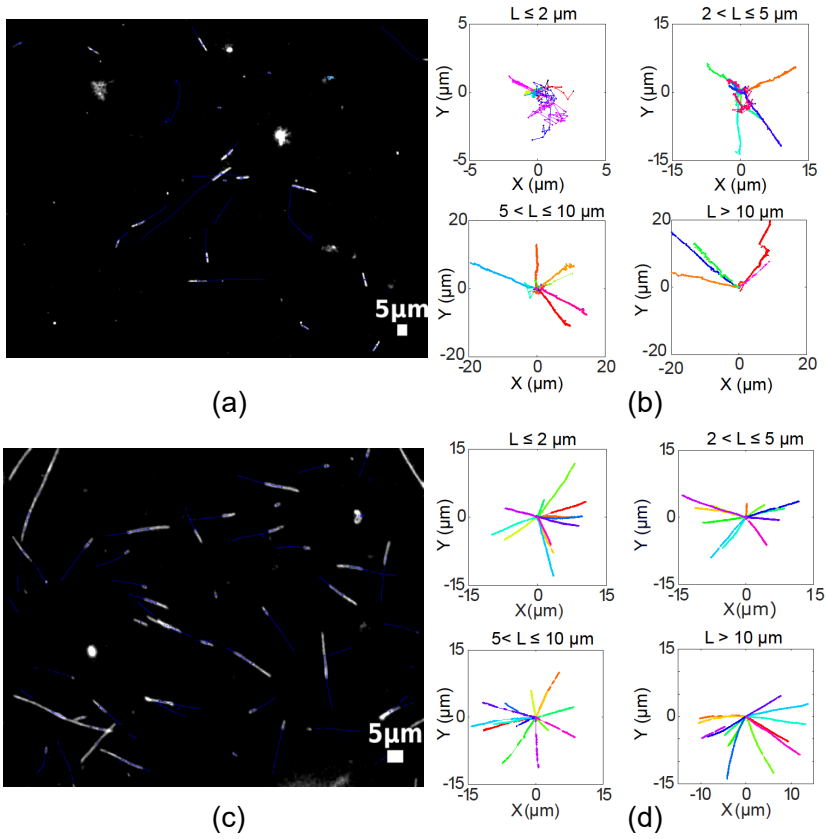

Figure 3.2: **Length dependence of MT transport**. Representative time-series of rhodamine-labelled MTs (grey-scale) gliding in presence of dyneins of densities (a) 6.8 and (c) 72.4 motors/μm^2 are overlaid with tracks of the centroids (blue). XY trajectories of plus tips of filaments transported by motors of density (b) 6.8 and (d) 72.4 motors/μm^2 are plotted for increasing MT lengths. For clarity between 5 and 15 trajectories are plotted per length and density class.

motors **(Figure 3.2c)**, filament transport appeared to be directionally persistent, independent of length **(Figure 3.2d)**. Also, if a particular length range is compared between the two densities, filament tracks appeared more random for the low motor density.

By combining dynein density (ρ_{2D}) and MT length (L) measurements, qualitative differences were observed in MT tip tracks at a low density of motors.

Short MTs of mean length 0.68 μm, swivel or diffuse away. These are expected to encounter 1 to 2 motors whereas in the high density experiments, the same

filament is expected to be bound by 5-6 motors and glides processively **(Figure 3.3(a))**. Intermediate lengths ($\sim$3 μm) of filaments are transported with intermittent changes in direction, possibly interacting with $\sim$7 motors and are directionally persistent when interacting with $\sim$10 motors **(Figure 3.3(b))**. Thus, based on the density estimates, the transition from diffusion and swiveling to persistent MT transport occurs when filaments interact with 2 or more motors on average, consistent with literature on collective motor transport [Imafuku et al., 1996a; Scharrel et al., 2014].

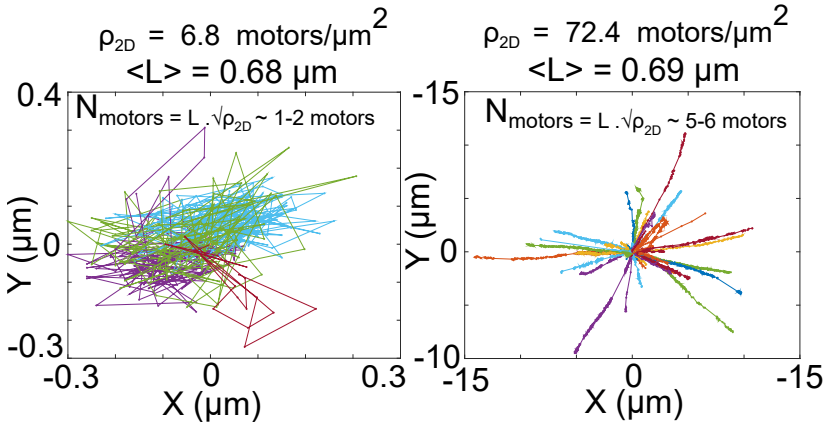

(a)

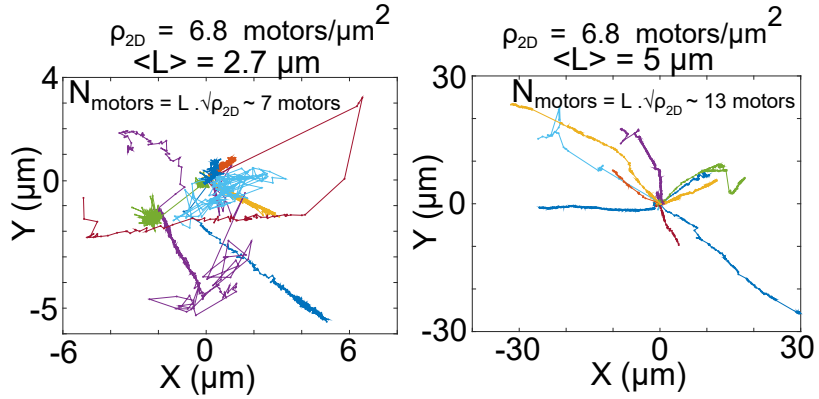

(b)

Figure 3.3: **Motor number (N) dependence of transport characteristics.** Representative XY trajectories of filaments (plus-tips) represent the effect of increasing motor numbers from (a) $< N > \sim 1$ to 2 (n=4) to 5-6 (n=48) for the same length of MTs $\sim$0.7 μm based on motor density (ρ_{2D}). (b) The effect of a change in $< N >$ from 7 (n=8) to 13 (n=17) on XY trajectories is seen for the same motor density, arising from differences in length alone. Colors represent individual trajectories.

Also, MT motility exhibits qualitative differences between the low and high density experiments when similar numbers of motors (5 to 7) are expected to interact for different lengths **(Figure 3.3)**. This appears to suggests that along with N-dependence of MT transport, subtle effects of motor density may also play a role. The observed rapid unbinding of MTs for estimates of 1 to 2 motors resulting in diffusion and swivelling, and the switch to processive transport at higher N serves to validate the motor density

estimate.

3.3.2 Motor number dependence of diffusion and transport velocity

In order to quantitate the qualitative trends of transitions from random to directed transport, mean square displacements (MSD) were analysed. The diffusive filaments were ignored from analysis by sampling only the ones that were present in the plane of imaging. An ensemble average MSD for binned mean lengths appears to confirm the impression of a transition from apparently diffusive to directed transport **(Figure 3.4)**.

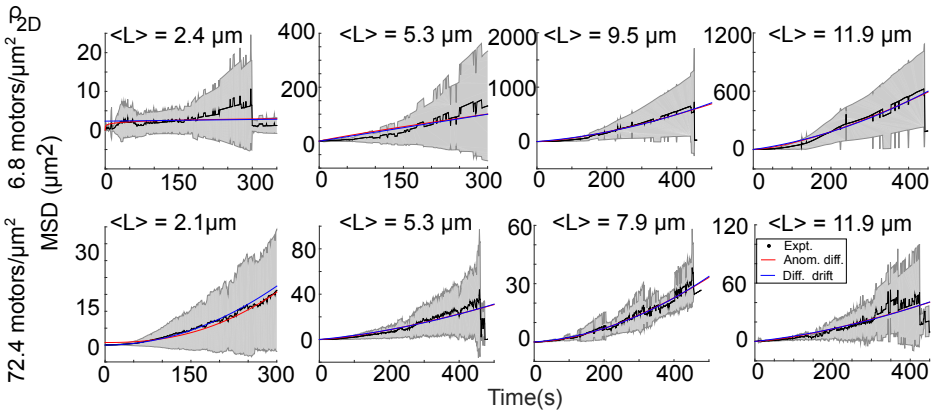

(a)

Figure 3.4: **Mean square displacement (MSD) of filament transport.** (a) The MSD as a function of time (black) for increasing MT filament lengths (L) ranging between 1.46 to 15.5 μm are plotted. The motor density (ρ_{2D}) is 6.8 (upper panel) and 72.4 motors/μm^2 (lower panel). Data was fit to two models: anomalous diffusion (red, Equation 3.2) and diffusion with transport (blue, Equation 3.3). Grey region: standard deviation.

The MSD profiles were fit with two models: (i) a phenomenological anomalous diffusion model (Equation 3.2) with the anomaly parameter α used to distinguish between diffusive, super- and sub-diffusive motility and (ii) a diffusion with transport model (Equation 3.3) to quantify the random and directed components of the motility. The trajectories of short filaments of less than 5 μm in length with low motor density deviate from both model fits, potentially due to a greater heterogeneity in MT motility also seen in XY trajectories. Such filaments, even when bound to just 1 or 2 motors, are expected to undergo frequent changes in direction and swivel, as reported for kinesin

gliding assays [Leduc et al., 2007]. The anomaly parameter obtained from fitting the phenomenological model is $\alpha \sim 1.5$ and greater for all trajectories irrespective of length and motor density, indicative of super-diffusive motility.

The fit parameters of the diffusion and transport model to experimental data, D_{eff} and v, show a higher variability for short filaments at low density as seen in the box plots **(Figure 3.5, upper panel)**.

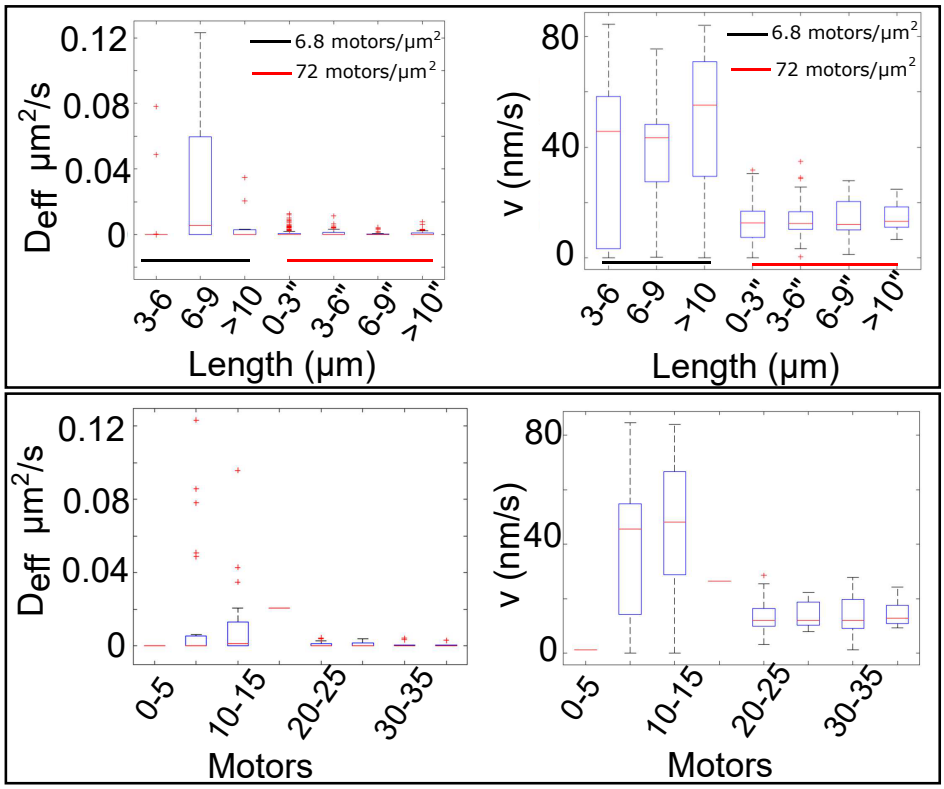

(a)

Figure 3.5: **Motor number dependence of effective diffusion and transport velocity.** Based on the fits to the diffusion with transport model Equation 3.3, box plots for the effective diffusion coefficient (D_{eff}, left) and transport velocity (v, right) of MTs are plotted as a function of the lengths (top) and expected number of motors (bottom) x-axis. The datasets for two density are represented by solid lines beneath the box plots in *black*: low density and *red*: high density. The red line inside the box of the box plot marks the median values.

In order to better understand these trends, the fit parameters are plotted as a func-

tion of motor numbers (N). The spread in box plot for D_{eff} appears to decrease with increasing motors, consistent with the higher variability expected from 'stop-and-go' and occasional swivelling of MTs. The nearly immobile filaments ($D_{eff} < 10^{-6}$ μm^2/s) are ignored in this analysis, assuming these to be artefacts due to MTs binding inactive or mis-oriented motors [Scharrel et al., 2014].

The transport velocity as a function of motors obtained from fits to experimental MSD, increases from close to zero to 80 nm/s and then saturates at around 20-40 nm/s, **(Figure 3.5, lower panel)**. This might arise from a combination of effects namely the 2D 'search' by MTs for motors that depends on motor density and increased coordination of multiple motors. However, at a high density the independence of velocity with motor numbers could be explained by saturation effects. The quantitatively lower velocity obtained at high motor densities, could result from crowding effects, as reported previously for kinesin [Grover et al., 2016]. Filament transport velocity is also quantified independent of the MSD fits to assess filament motility characteristics and observe for the number dependent transitions.

3.3.3 Asymmetric detachment model reproduces the trends observed in dynein dependent MT transport

Filament transport is quantified using both the measures of motility- speeds and velocities. While speed (scalar quantity) considers only magnitude of transport, velocity (vector quantity) considers both magnitude as well as direction of transport. The primary reason to evaluate both these quantities is to observe if the motor number dependence extend to measures independent of direction. Although, speeds decrease for the high motor density, they remain constant across the length of MT observed **(Figure 3.6(a), *left*)**. However, velocity ($\langle v_{eff} \rangle$) shows a length dependence at low motor density, consistent with the qualitative changes in transport **(Figure 3.6(a), *right*)**.

Mean gliding velocity $\langle v_{eff} \rangle$ when plotted as a function of motors show a five-fold increase when $\sim$8-10 motors are encountered (Figure 3.6). In order to better understand this process, simulations were performed using single motor mechanics and understand the ensemble role of dynein during MT transport. Interestingly, simulations performed using single motor mechanics could recapitulate the observed trends in filament gliding.

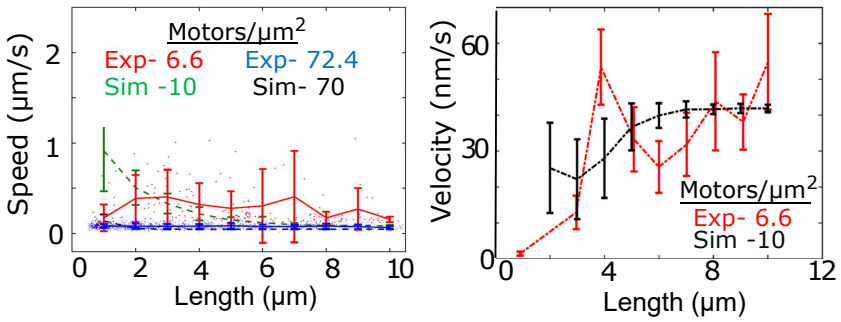

(a)

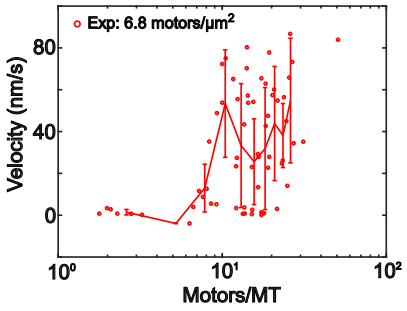

(b)

Figure 3.6: **Effect of motor numbers on gliding velocity**. The mean gliding velocity of filaments, $\langle v_{eff} \rangle$ (red circles), from experiments is plotted as a function of the mean number of motors (N). The motor density is 6.8 motors/μm^2. The dashed line connected binned averages with error bars indicating standard deviations.

Since, the transition in velocity appears to coincide with a transition from random to vectorial transport, a simpler and more robust measure of directionality χ, that is independent of any fitting is evaluated [Athale et al., 2014a; Khetan and Athale, 2016] as described in the methods section.

3.3.4 Directionality shows a threshold number dependence

The mean directionality (χ) shows length dependence for low motor densities but not for high density. A four-fold change in χ is seen when MT lengths increase from 3 to 4 μm at low motor densities **(Figure 3.7(a))**. The high density data for lower lengths

(1 μm) have the values of χ similar to lengths at transition values from low density. Interestingly, motility changes quantified by χ correspond to three qualitative modes of filament transport for increasing lengths at low motor densities: (a) swivelling by short filaments ($\approx$1 μm) when 1-2 motors are expected to interact, (b) transport and intermittent changes in direction of intermediate lengths ($\approx$3 μm), when interacting with $\sim$7 motors and (c) directionally persistent transport of long filaments ($>$5 μm), when interacting with $\sim$10 motors **(Figure 3.7(b))**. When this data is combined for different motor densities and MT lengths, in terms of expected number of motors interacting with a filament, all the data falls onto a trend of increase and saturation of χ above a threshold of 8 to 10 motors **(Figure 3.7(c))**. This motor number threshold above which transport becomes directionally persistent is based on the expected number of motors a filament encounters, while binding-unbinding kinetics would result in a lower number of bound motors, as predicted in simulations. Hence, a model of yeast single-molecule dynamics is further tested to evaluate if it can reproduce our experimental measure of directionality in collective transport.

The directionality, from the same calculations, show a threshold effect increasing abruptly when $\sim$10 or more motors are acting on an MT, an effect also observed in experiments for $\sim$8 to 10 motors (Figure 3.7(c)). The simulations however are based on a model of the motor as a single bead that stochastically steps along an MT, similar to previous work [Arcizet et al., 2008; Athale et al., 2014a; Grover et al., 2016; Imafuku et al., 1996a; Khetan and Athale, 2016], while in experiment the yeast dynein is dimeric. Our result would suggest that the reported uncoordinated stepping of heads of this yeast dynein [Cleary et al., 2014; DeWitt et al., 2012], could explain why the transition in directionality in experiment emerges at 8 to 10 heads, comparable to the 8 to 10 motors in simulations, due to the statistics of independent stochastic stepping and detachment behaviour. Additionally, visualization of the simulation for increasing MT lengths suggests the statistics of directionality can be understood in terms of three qualitatively different MT motility modes, just as in experiment: swivelling and occasional free-diffusion when filaments encounter 1-2 motors, (b) 2D 'search' interspersed with stretches of transport with 3-5 motors and (c) persistent directional transport when the motors encountered exceed 5 **(Figure 3.7(d))**.

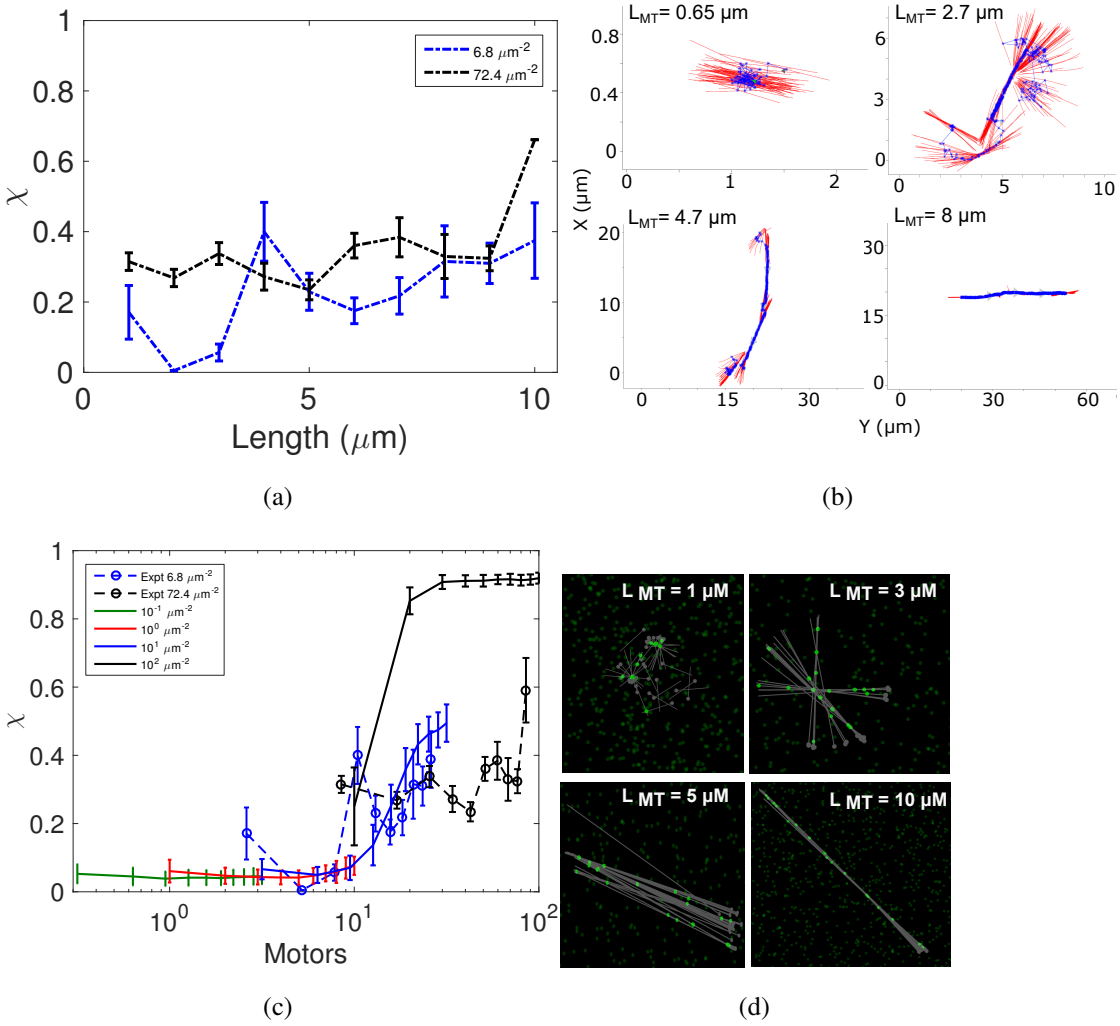

Figure 3.7: **Length and motor-dependence of MT transport directionality in experiment and simulation.**

(a) The mean directionality, χ ($\pm$s.e.) of MT transport is plotted as a function of length in presence of two different motor densities (colors) from experiments. (b) Representative time-projections of filament contours (red lines) are overlaid with trajectories of centroids (blue *) from experiments for a low density of motors (6.8 motors/μm^2) for increasing lengths. The time-interval between frames is 1 s. (c) The value of χ from experiment (o–, mean $\pm$s.e.) and simulation (-, mean $\pm$s.d. from 100 MTs each) are plotted in terms of motors encountered per filament. Colors represent motor density in units of motors/μm^2. (d) Simulation outputs of filaments (gray) from 10 s of simulations at 0.25 s per frame for a motor density of 10 motors/μm^2. Two states of motors are indicated: bright-green: MT-bound, dark-green: free

While the directionality of transport over three orders of magnitude from simulations of motor density appears to fall on one curve resembling saturation kinetics, the transition is not 'smooth' as a function of motors per MT. For instance, the directionality of filaments of increasing lengths in presence of 10 motors/μm^2 do not appear to increase above 0.4, while higher values of directionality are only seen in case of an order of magnitude higher motor density. This could be due to the fact that increasing MT lengths for a given motor density could result in filament bending and defects in motion (kinks, spiral etc.) as previously reported for myosin and kinesin [Bourdieu et al., 1995], thus reducing directionality. Additionally, simulations also predict the point of inflection of directionality as a function of motors (N-dependence) will be seen even if as little as half the motors are active [Jain et al., 2019], suggesting a potential experimental test of the model. To test the specificity of the asymmetric detachment model, effect of alternative models of detachment on MT collective transport were also tested in simulations. The alternate models tested were: a) force independent model, where the detachment rate is constant ($r_d = r^0{}_d$). (r_d: detachment rate; $r^0{}_d$: basal detachment rate) (b) force dependent model, where load dependence was symmetric in nature based on kramers law ($r_d = r^0{}_d.e^{|F_{ll}/F_s|}$) [Kramers, 1940]. (F_{ll}: magnitude of the force parallel to load; F_s: stall force of dynein motor). None of the alternative models could reproduce the value of the threshold number of motors encountered that results in a change in χ comparable to experimental data [Jain et al., 2019]. This may point to a property of switch in transport by this yeast dynein from random to persistent motion of MTs through an N-dependent (collective) mechanical coupling, rather than a simple 2D 'search'. It would suggest that such a motor number based threshold dependence of persistent filament transport might differ for a full length dynein construct, due to a quantitative difference in the load dependence as compared to the truncated dynein used in this study, acting as a test of our model predictions.

3.4 Discussion

In this work, the collective transport by dyneins reveal a threshold number depedence for persistent transport. The transport velocity and 2D directionality undergo a steep increase both in simulation and experiment with increasing motor numbers. Modeling can explain such threshold dependent behavior as an emergent property of the collective effect of

motor detachment dependence on the direction of the load force and a 2D 'search' by MTs for motors. This number-dependence of directionality of MT transport, arising from the coordination of multiple *S. cerevisiae* dyneins at a low density comparable to the *in vivo* scenario, could help us better understand the 'search and capture' of astral MTs in mitosis during nuclear positioning.

The observations of the reduction in mean D_{eff} with the number of motors (1/N dependence) resembles the inverse length dependence, $1/L$ of diffusivity of MTs transported by kinesins reported previously [Imafuku et al., 1996a]. This suggests the the motor-number dependence of randomness in collective MT transport might be similar for kinesin and dynein. This threshold could be smaller, based on the assumptions inherent in the motor number estimation and the expectation that the number of bound motors will always be lower than those encountered, as seen in simulations [Jain et al., 2019]. Additionally, the mean velocity of MTs for a saturating number of motors encountered is $\sim$40 nm/s, in qualitative agreement with the reported velocity of 41 nm/s of yeast spindle translocation during mitosis [Markus et al., 2011]. Thus, the velocity and directionality of MT transport by yeast dyneins depends on both the motor density and MT length.

The effect of increasing motor density on collective transport of MTs has also been shown for kinesins in a gliding assay, when the motors were anchored in a lipid bilayer but not when anchored on glass [Grover et al., 2016]. The similarity in trends with increased density despite the glass immobilization of dynein, could relate to the greater flexibility inherent in dynein, thus mimicking the effects of anchorage. This could reveal a general property of filament transport arising from intermolecular spacing and flexibility.

The ensemble mean directionality of transport steeply increases four-fold when the number of motors a filament encounters change from 8 to 10, in experiment. Simulations reproduce both the steepness of change and the N-value of the onset based on single molecule detachment mechanics. The transition in directionality with N$\sim$10 is observed even in the presence of 50% inactive motors that are unable to step [Jain et al., 2019], suggesting the robustness of our result to experimental artefacts such as the active fraction of the motor. This could also serve as a falsifiable test of our model. Our theoretical predictions explain not just our data, but also potentially provide an explanation for the

previous report of a sharp increase in run length and run time with an increase in yeast dynein team sizes from 2 to 7 motors [Derr et al., 2012].

Interestingly, the observation of a sharp transition in gliding velocity (v_{eff}), transport velocity (v) and directionality (χ) from low values of (less efficient transport) to high values above a threshold of motors, in simulations and in experiments, resembles a phase-transition. Phase transitions in directional motility of motor-driven transport, have been predicted in theory for symmetric and asymmetric motors [Badoual et al., 2002; Jülicher et al., 1997; Jülicher and Prost, 1995]. They have also been experimentally demonstrated in the case of antagonistic kinesins transporting anti-parallel MT-doublets [Leduc et al., 2010a]. A simple dynein driven collective MT transport system could also fall into this general category. This finding implies cells could regulate the qualitative nature of multi-motor transport by simply modulating the number of motors.

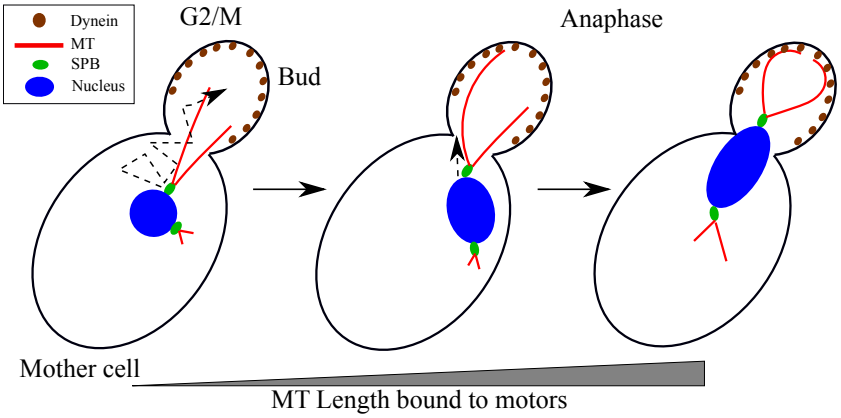

Figure 3.8: **Search and capture of astral MTs during nuclear positioning.** A schematic representation of a yeast nucleus (blue) positioned (dashed arrow) by dynamic astral MTs (red) nucleated from SPBs (green) pulled by cortical dyneins (brown) localized in the bud cell. The scale represents the increasing length of MTs interacting with the motors.

In our work, simulations allow us to explore a much wider range of motor densities than either previous or our own experimental data can approach. The increase in velocity and directionality both saturate rapidly when more than ∼20 motors heads (10 dimers) interact with an MT. This result suggests the motor numbers of this dynein could have

a role to play during *S. cerevisiae* mitosis in pulling MTs *in vivo*. The native yeast cytoplasmic dynein is localized to the daughter cell during mitosis [Markus and Lee, 2011] as part of the machinery that positions the nucleus to the bud neck between the daughter and mother cells [Adames and Cooper, 2000a; Hoepfner et al., 2000a; Shaw et al., 1997]. During the G2/M to anaphase transition, astral MTs emanating from SPB embedded in the nucleus, are thought to 'search' and are 'captured' by dynein motors localized to the bud-cell cortex which then 'reel in' the nucleus [Adames and Cooper, 2000a]. The captured MTs are then transported in a manner reminiscent of a gliding assay, with both MT lengths and motor numbers changing in time. The reported number of dyneins present on cortical foci in budding yeast 6 ± 2 dimers [Markus et al., 2011]. A transition in the directionality of MT transport is observed when $\approx$10 motors are expected to interact with an MT. We speculate that the number dependence of random to directed MT transport, could affect the 'search and orientation' of the nucleus **(Figure 3.8)**. Since the process involves collective motor transport, a transition to directed transport with increasing motor numbers might improve the accuracy and reduce the time taken for spindle alignment during division, while maintaining a constant velocity. Our experimental and theoretical observations suggest that the mechanics of the yeast dynein, might be adapted to ensure robust positioning of the nucleus in anaphase. Further quantitative analysis of yeast nuclear migration will be required to test this hypothesis.

The transport velocity and 2D directionality undergo a steep increase both in simulation and experiment with increasing motor numbers. Modeling can explain such threshold dependent behavior as an emergent property of the collective effect of motor detachment dependence on the direction of the load force and a 2D 'search' by MTs for motors. This number-dependence of directionality of MT transport, arising from the coordination of multiple *S. cerevisiae* dyneins at a low density comparable to the *in vivo* scenario, could help us better understand the 'search and capture' of astral MTs in mitosis during nuclear positioning

Chapter 4

Implications for dynein number dependent transitions on spindle pole body transport via microtubules in yeast mitosis.

KEYWORDS: ASTER, DIRECTIONAL TRANSPORT, CENTROSOME, NUCLEUS, SPINDLE POLE BODY, BUDDING YEAST

Contributions: The time-lapse movies for the growing yeast cells were acquired by Dr. Saravanan Palani, Warwick Medical School, University of Warwick, UK.

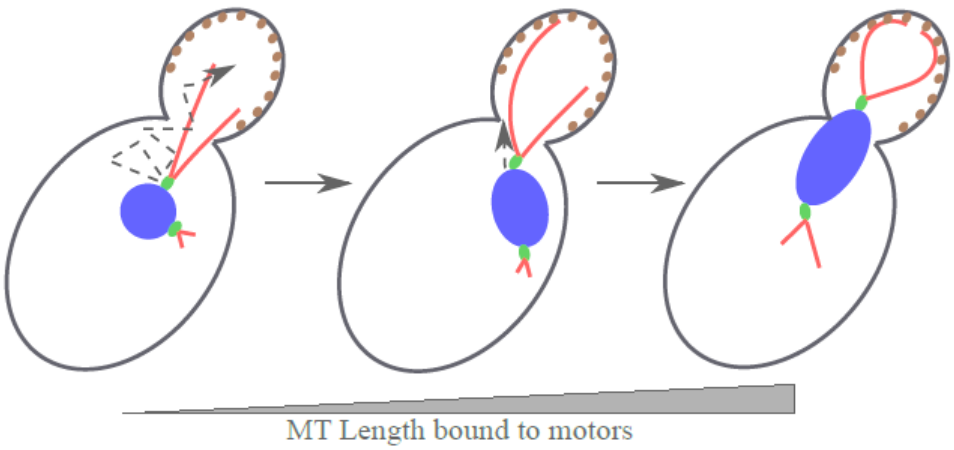

4.1 Introduction

Saccharomyces cerevisiae has been used as a model organism for decades to understand the role of protein networks and cell cycle regulators. It undergoes closed mitosis leading to formation of spindle inside the nucleus with intact nuclear membrane. The site for cytokinesis in *S.cerevisiae* is pre-determined at the position where bud emerges. This necessitates the positioning of nucleus between the mother cell and bud neck in order to ensure equal segregation of chromosomes. Spindle pole body (SPB) involved in the formation of spindle is embedded within the nuclear envelope [Byers and Goetsch, 1975]. This leads to the formation of two kinds of microtubules- (i) nuclear MTs, nucleated from the spindle pole body (SPB) inside the nucleus and (ii) cytoplasmic or Astral MTs, nucleated from the SPB in the cytoplasm.

While nuclear MTs are involved in spindle formation within the nucleus, astral MTs bind to cortically anchored dynein motors on the bud crotex [Adames and Cooper, 2000a; Hoepfner et al., 2000b; Lee et al., 2003; Palmer et al., 1992; Shaw et al., 1997]. The function of dynein in budding yeast is limited to cortical pulling of MTs, unlike in higher eukaryotes where they are also involved in cargo trafficking [Fagarasanu and Rachubinski, 2007]. During *S. cerevisiae* mitosis, dynein is targeted to the daughter cell cortex [Markus and Lee, 2011] through a complex network of transport, anchoring and regulatory co-factors [Moore et al., 2009]. Dynein based pulling is known to cause microtubule sliding along the cortex, eventually leading to nucleus positioning. The null mutants of dynein show cells defective in spindle positioning at the onset of anaphase [Eshel et al., 1993; Li et al., 1993]. A recent study has shown that dynein regulates the plus end dynamics of the microtubules by increasing the frequency of catastrophes as it slides along the MTs [Estrem et al., 2017] . Inhibiting depolymerization of the filaments worsens spindle movement by dyneins and forms cells with abberant spindles. This indicates both- motor numbers and lengths of microtubule, play role during nucleus positioning at the bud neck.

During the ‘search and capture’ of yeast nuclear MTs in mitosis, both motor numbers and MT lengths are changing while the nucleus is being ‘reeled in’ to the bud neck. In the previous chapter, the effect of increasing dynein numbers and MT lengths on directed transport of filaments is shown using a minimal gliding assay system. To

test the relevance of such a qualitative change in directionality of transport in *in vivo* system, the dynamics of nuclear positioning are examined here in *S. cerevisiae* mitosis using a previously described strain with a fluorescently tagged SPB (Spc42-3xmCherry) and GFP labelled tubulin [Caydasi and Pereira, 2009]. The directionality of nuclear transport is assessed by tracking spindle pole body during cell growth. In order to validate the qualitative differences in x-y trajectories of SPB movement during various cell cycle stages, quantitations to measure directed transport are performed based on mean square displacements and tortuosity analysis. The results obtained are compared to the observations from our *in vitro* gliding assays where the same cytoplasmic yeast dynein immobilized on glass surface has been used to assess the number and length effects on transport directionality. Based on our findings, we propose a general 'search and orient' mechanism of organelle positioning by MT asters. To further test this, *ex-vivo* reconstitution of nucleus transport with intacts SPB's is being optimized with the aim of developing a novel nuclear transport assay.

4.2 Materials and Methods

4.2.1 Image analysis of yeast time series

The yeast movies analyzed here were acquired by Dr. Saravanan Palani, Warwick Medical School, University of Warwick, UK using a spinning disk confocal microscope (Andor Revolution XD imaging system, equipped with a 100x oil immersion 1.45 NA Nikon Plan Apo lambda objective, a Confocal Yokogawa CSU-X1 unit, an Andor sCMOS ZYLA detector, and Andor iQ software). Image time series of yeast cells were contrast adjusted, denoised using a median filter (radius-1 pixel), and histogram normalized using Image J ver 1.45s. *Stackreg* plugin with rigid body transformation was used to align stacks of images. The Spc42-3xmcherry (SPB component) channel was tracked using FIESTA ver.1.04 reported previously[Ruhnow et al., 2011] in MATLAB R2015b (Mathworks Inc., USA) on a Linux platform.. The maximal search radius was set to 50 nm/s, with only those molecules considered for further analysis which persisted for 50 or more frames. The x-y co-ordinates of the tracks obtained using Fiesta were processed in Matlab (Mathswork Inc, US) for further data analysis. These tracks were analyzed using matlab scripts to obtain x-y trajectories, MSD estimations and tortuosity estimates

as described in the previous chapter (**Chapter 3, Methods section 3.2 on page 39**). DIC channel was visualized to categorize the cells in either pre-budding or budding stages. Further, in budding stages the analysis was considered with the cells where SPB movement to mother and bud cells was unambiguous with track length $\geq$ 50 time frames.

4.2.2 Isolation of yeast nuclei

Yeast strains were grown on yeast peptone dextrose (YPD) medium at 30^{o}C. The lop phase cells were harvested at 3000xg and resuspended in lysis buffer (Sorbitol- 1.2M, sucrose- 2M, potassium phosphate- 20 mM, $MgCl_2$- 0.5mM). These were flash frozen in liquid nitrogen and lysed with mortar pestle. Lysis was monitored using a bright field microscope. The lysed slurry was thawed at 4^{o}C and different fractions were collected to obtain nuclei.
Alternatively, the cell lysis was also carried out enzymatically using lyticase (Sigma Aldrich, Bangalore, India). The cells were first grown to log phase and harvested at 3oooxg for 5 min at room temperature (RT). The cells were washed in distilled water, harvested and resuspended in buffer 1 (0.1 M Tris- HCl, 10 mM DTT). These were incubated at 30^{o}C, for 30 mins with shaking at 100 rpm, harvested at 3000xg and resuspended in lysis buffer. Lyticase was added to the cell pellet resuspended in buffer 2 and cells were further incubated at 30^{o}C for 1 hour, 150 rpm. Spheroplast formation was monitored on a bright field microscope and the pellet obtained at the end of the incubation was resuspended in lysis buffer. Spheroplast were lysed either using osmotic shock (1:2 in water, 1:4 in water) or homogenized using pestle in a microfuge tube to obtain nuclei from the cells.

4.2.3 Isolation of centrosomes

Centrosomes were isolated using Drosphila embryos and Jurkat cells as described previously by [Moritz and Alberts, 1998], and [Jakobsen et al., 2013] respectively. In brief, Jurkat cells were grown in ATCC modified RPMI 1640 medium (ThermoFisher Scientific, NewYork) supplemented with 10 % heat inactivated fetal bovine Serum (ThermoFisher Scientific, US) and 100 units/ml Penicillin-Streptomycin solution (ThermoFisher Scientific, US) to a density of 5 x 10^6 cells. They were treated with nocodazole (60 ng/ml)

(Sigma Aldrich, Bangalore, India) and cytochalasin-D (1 μg/ml) (Sigma Aldrich, India) for 1 hr at 37^{o}C. Cells were lysed, pelleted, filtered using medical gauze and treated with DNase at 4^{o}C. The lysate was loaded on a sucrose gradient - 3 ml 40%, 3 ml 50% and 5 ml 70% and centrifuged at 116,000 X g for 75 min at 4^{o}C. 0.5 ml fractions were collected using a peristaltic pump and flash frozen. The fractions were loaded on a 10% SDS-Page gel to confirm the presence of centrosomes.

Drosophila embryos were washed, dechorionated using 50% bleach and lysed by homogenizing them with a pestle in a microfuge tube. The lysate was then processed on a sucrose gradient in a similar manner and the fractions were flash frozen and stored at -80^{o}C.

4.2.4 Activity testing of centrosomes to nucleate microtubules

The fractions collected on a sucrose gradient were tested for their ability to form asters by either of the two methods (i) formation of asters in solution, (ii) nucleation of asters on glass.

The In-solution assays involved incubation of 20 μl of centrosomal fractions with 20 μM of goat brain tubulin (1:10 labelled:unlabelled) and 1 mM GTP in BRB-80 buffer (80 mM PIPES, 1 mM $MgCl_2$, 1 mM EGTA) in a microfuge tube. The nucleation temperature for the centrosomes obtained from jurkat cell lines was 37^{o}C and drosophila embryos was 29^{o}C, and was set using a heating block (Thermo mixer, Eppendorf) . The incubation time was varied from 5-30 mins followed by fixing in 1 % glutaraldehyde (Sigma Aldrich, Bangalore, India).

On-glass nucleation assays were done by incubating 20 μl of centrosomal fraction on acid-washed (1 N HCl) glass coverslips. The centrosomes were incubated on the glass surface followed by incubation with 20 μM of goat brain tubulin (1:10 labelled:unlabelled) and 1 mM GTP for 10-30 mins and fixed with 1 % glutaraldehyde. Aster formation was checked using a Zeiss upright fluorescence system with 40 X objective (N.A- 0.75) with Dsred filters (excitation/emission- 550/570).

4.3 Results

4.3.1 Random to directed movement of spindle pole body during *S.cerevisiae* mitosis

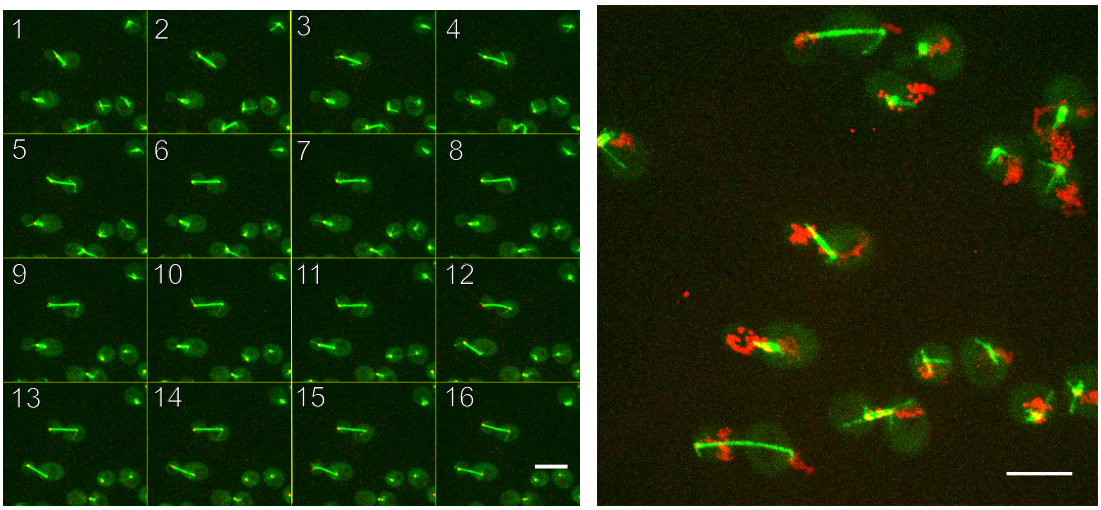

(a) (b)

Figure 4.1: **Visualizing the movement of spindle pole body as yeast cell undergoes budding.** (a) A montage representing growing yeast cells with GFP labeled microtubules (green) and Spc42-3x mCherry (red) labeled spindle pole body (SPB, red) during nuclear positioning. Scale bar - 5 μm, Time stamp- min. (b) SPB is projected in time over the first frame of the corresponding montage to indicate movement in various stages of cells. Scale bar - 5 μm

During *S.cerevisiae* mitosis, the spindle pole body (SPB) associated with the nucleus undergoes duplication and begins to move towards opposite ends of the nucleus at the time of budding (as can be seen in the DIC channel later). The one which moves towards the mother cell is referred here as SPB-M and the other that moves towards the bud cell is referred as SPB-B. A montage corresponding to the image time series as the cells undergo mitosis is shown in **(Figure 4.1(a))**. The time projection of the Spc42-mCherry SPB channel indicates the movement of the SPB in different cells **(Figure 4.1(b))**. For our analyses, SPB movement is considered prior to spindle elongation in order to avoid the complexities in interpretation due to MT pushing forces.

The motility of SPB-GFP puncta in yeast cells is followed using single particle tracking **(Figure 4.2(a))** and XY trajectories are traced. XY tracks shown in **(Figure 4.2)** are normalized with respect to their origin and are observed for the SPB's before and after duplication, as the cell proceeds to bud. The XY movement of SPB's appears to be random **(Figure 4.2(b))** prior to budding and SPB duplication. It seems to become directed after SPB duplication as seen for SPB-M **(Figure 4.2(c))** and SPB-B **(Figure 4.2(d))**. In order to validate the qualitative trends, the randomness in transport is quantitated using the fits to mean square displacements (MSD) as described in the previous chapter.

4.3.2 MSD profiles suggests diffusive SPB movement is highest prior to budding

The MSD profiles of the SPB tracks are fit to two different models to evaluate the degree of diffusion in SPB motion as the cell undergoes budding. (i) Anomalous diffusion model assumes that the inherent nature of transport is diffusive. Anomaly parameter obtained from fit, $\alpha < 1$ indicates diffusive movement. ii) Diffusion with transport model assumes that an active component is driving transport and separates the directed and diffusive component . The equations for both the models are described in the Methods section of Chapter 3, MSD and diffusivity analysis 3.2 on page 42 and 3.3 on page 42.

The fits in our results show linear profiles for the MSD curves of the SPBs prior to duplication indicating diffusive movements **(Figure 4.3(a))**. On the other hand, MSD fits to SPBs after duplication moving to mother cell showed sub-diffusive profiles indicating confined diffusion **(Figure 4.3(b))**, and the bud cell showed super-diffusive profiles indicating active transport **(Figure 4.3(c))**. Box plots of diffusivity (D_{eff}) obtained using anomalous diffusion model for the three categories of SPBs show lowest values of diffusion profiles of the SPB moving towards bud (SPB-B) **(Figure 4.3(d))**.
Measures of anomaly α obtained by fitting anomalous diffusion model to MSD profiles show $\alpha < 1$ for SPB-M and SPB-prior whereas SPB-B has an $\alpha > 1$, further confirming the observations that SPB moving towards the bud has directed movement (**Figure 4.4(a) and (c)**).

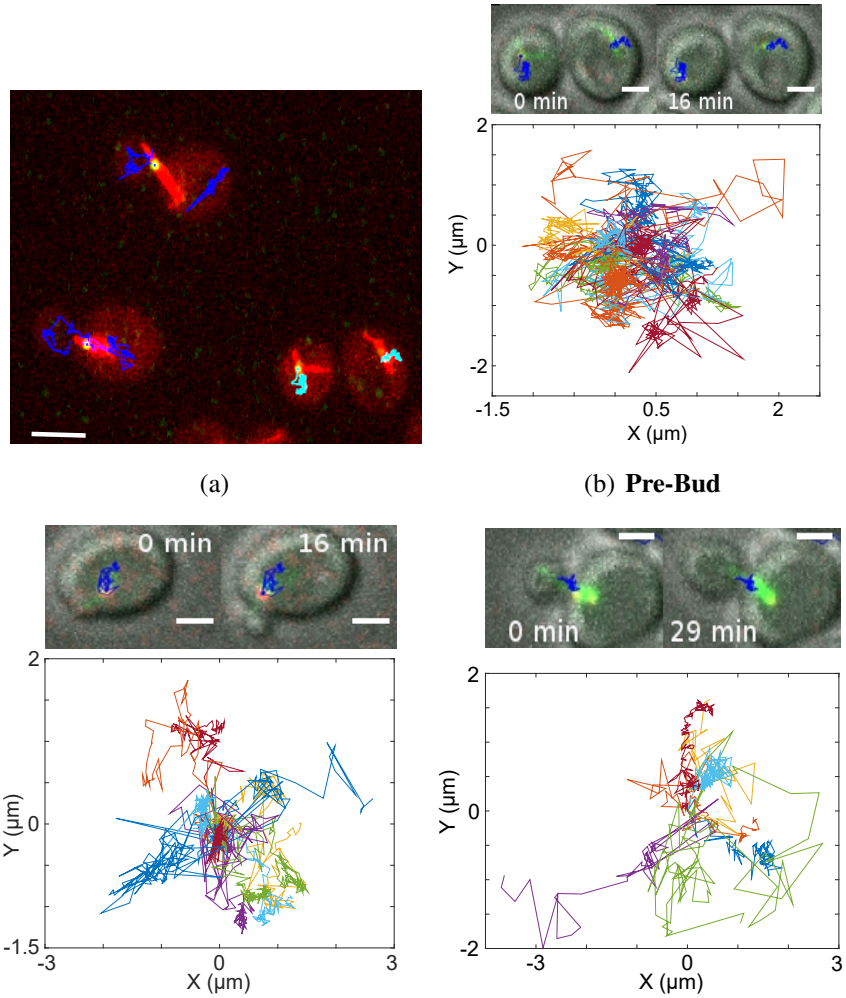

(a)

(b) **Pre-Bud**

(c) **SPB-M**

(d) **SPB-B**

Figure 4.2: **Stage dependence of spindle pole body (SPB) movement during transport of nucleus.** (a) SPB tracks are overlaid on the centroids of SPB (green) tracked using FIESTA. Colors are changed for better visual representation- MTs (red), SPB (green). *Cyan*: Spb tracks in pre-budding cells prior to SPB duplication. *Blue*: Spb tracks in budding cells after spb duplication. Scale: 5 μm. (b)-(d) XY trajectories of SPB movement are plotted for the cells (b) prior to SPB separation before budding and, after SPB separation at the time of budding as the SPB moves either in the (c) mother cell or (d) bud cell. Each XY track is represented in different color. The merged image represent first and last frames of the time-series with DIC (grey) images, Spc42-3xmCherry (red) and GFP-Tub1 (green) channels. Scale: 2 μm.

The transport velocity is the highest for the SPBs moving towards bud indicative of directed movements towards bud **(Figure 4.4(b) and (d))**. In order to estimate the directionality of transport independent of the potential fitting artefacts, tortuosity- an altrnative measure of directionality is estimated.

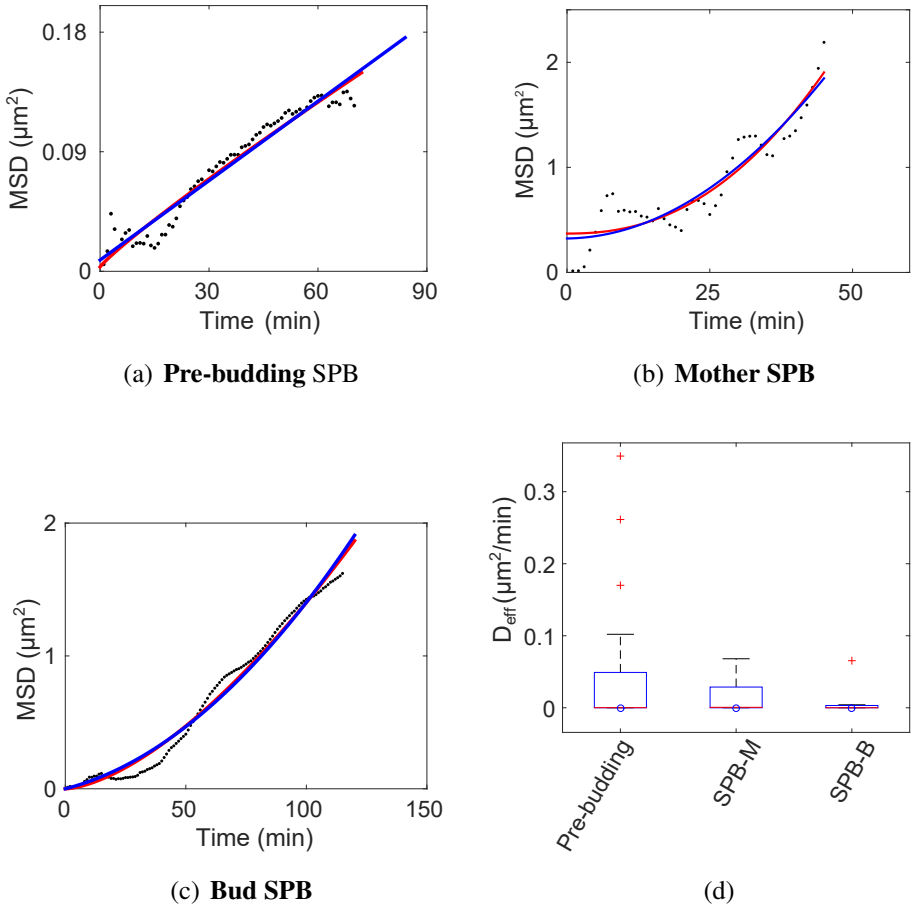

(a) **Pre-budding** SPB

(b) **Mother SPB**

(c) **Bud SPB**

(d)

Figure 4.3: **MSD analysis and estimation of effective diffusion.** MSD profiles for the SPBs (a) Prior to budding (Pre-budding), and after budding as they move to (b) mother cell, or (c) bud cell. The fits to the MSD profiles from anomalous diffusion model (red) and diffusion with drift model (blue) are overlaid on the experimental data (black) from single representative tracks.(d) Box plot represents the diffusivity of the SPB movement estimated by fitting MSD profiles to anomalous diffusion model. Median - red line, Mean- circle, outliers- plus sign.

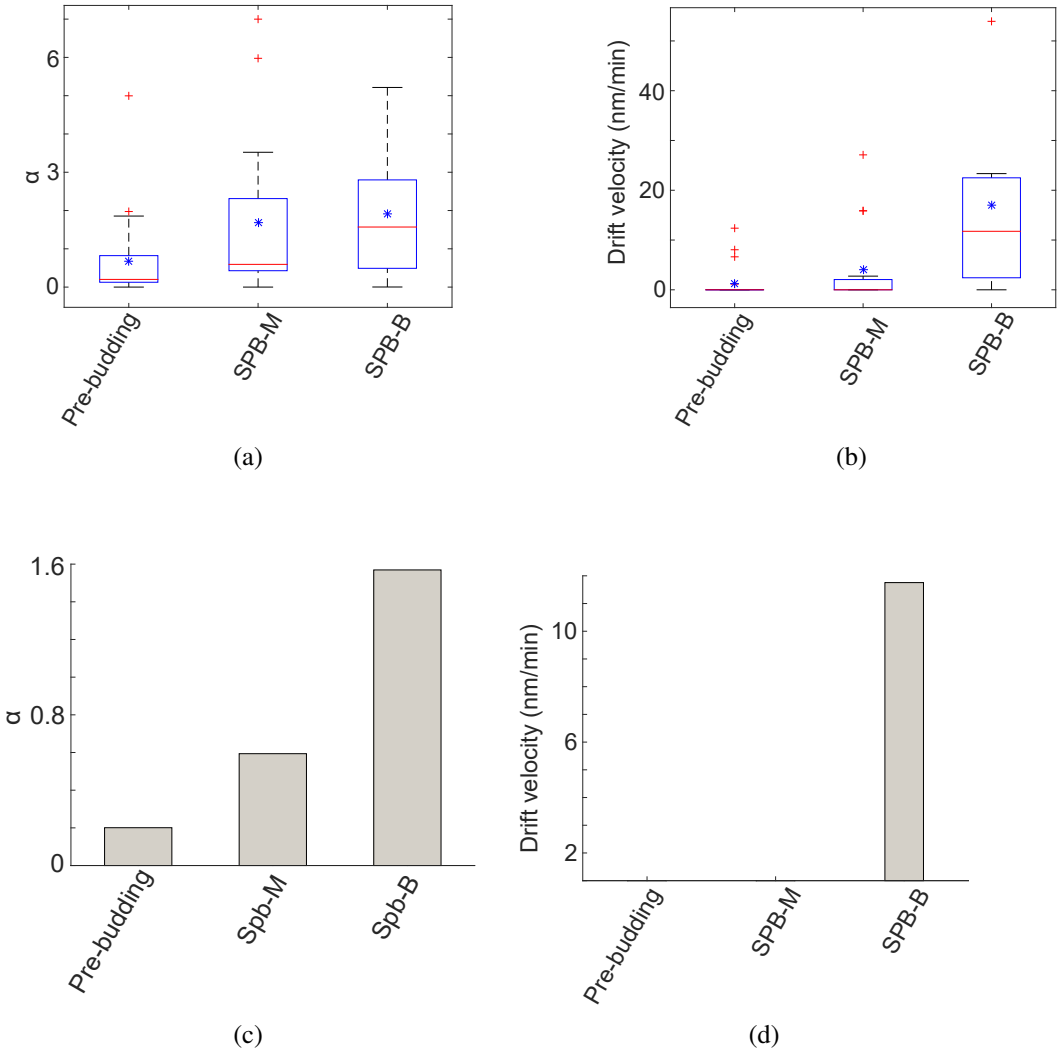

Figure 4.4: **Estimation of anomaly parameter and drift velocity** (a) The box plot shows the measures of (a) anomaly of diffusion ,α and (b) drift velocity of SPB transport estimated by fitting MSD profiles. Bars indicate the medians values for (a) anomaly of diffusion ,α and (b) drift velocity from the box plots. Median - red line, Mean- asterisk, outliers- plus sign.

4.3.3 Directionality increase correlates with prolonged contacts of astral MTs along cortex

Tortuosity (χ) is a measure of directionality, estimated using the ratio of displacement to path length. Quantification of the SPB movement prior to separation shows a mean directionality (χ) of 0.0478 $\pm$0.0238. After separation, the SPB-M shows a mean χ of 0.073 $\pm$0.0420, while the SPB in the bud (SPB-B) has a mean χ of 0.138 $\pm$0.050. This indicates that the tortuosity or directionality of the SPB's after duplication (SPB-M and SPB-B) increases as compared to pre-separated SPB **(Figure 4.5(a))**. The montages represent the time projections of the Spc42-mCherry SPB channel (red) and MTs (green) on the first frame of the DIC image **(Figure 4.5(b))**. It shows SPB and MT profiles for the different stages assessed. It suggests that microtubules emanating from the SPB moving towards the bud (SPB-B) have prolonged contacts along the cortex as compared to other two SPB's . This is further highlighted in the representative images of the cells **(Figure 4.5(c))** prior to budding and **(Figure 4.5(d))** after budding where the MTs are color coded in time for comparable time frames. The prolonged contact of MTs along the bud cortex with an evident sliding behavior and the increase in directionality for the SPB moving towards the bud seems co-related. Since, it is known that dynein drives microtubule sliding along the cortex, such a change in directionality of the SPB moving towards the bud is indicative of a dynein number dependent transition. This is similar to the motor number and length dependent transitions observed in the directionality of linear filament transport in our gliding assay (previous chapter).

Real time quantification of dynein motor numbers is complex as the cell is dynamically varying motors along the cortex. In order to overcome the complexity of *in vivo* measurements for dynein numbers and issues relating to microscopy, the potential to measure transport of nuclei using an *ex vivo* reconstitution system with intact SPBs and astral MTs gliding on immobilized dyneins motors is tested.

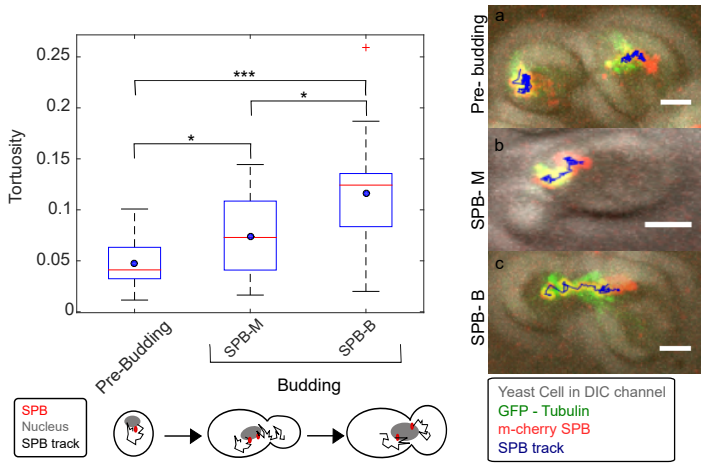

(a) (b)

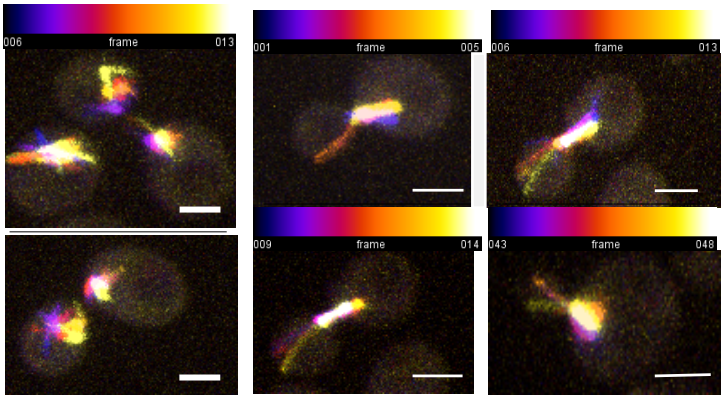

(c) **Pre-budding** (d) **Budding**

Figure 4.5: **Quantitating the change in directionality of SPB transport during different stages.** The box-plot compares the (a) directionality of SPB transport before SPB separation (n = 20), and after SPB separation in the mother cell SPB-M (n = 20) and in the bud cell SPB-B (n = 16). Scale bar: 2 μm. Stage dependent SPB movement analyzed during yeast nuclear positioning in *S.cerevisiae* are represented schematically. (b) Images of yeast cells imaged in DIC (gray) from a single time-point are overlaid with time-projected images of SPBs (Spc42-3xmCherry, red) and tubulin (GFP-Tub1, green), together with the XY tracks of SPB movement (blue lines).(c)-(d) MTs color coded in time (colorbar) are overlaid on the initial frame of the representative images of the pre-budding cells and budding cells, respectively, to observe the cortical interactions. Frame number- Time duration in minutes, Scale bar: 2 μm.

4.3.4 Extracting nuclei with intact SPBs for building an *ex vivo* organelle gliding assay

In order to obtain nuclei with intact SPB's, the yeast strains grown to logarithmic phase are lysed in liquid nitrogen based using mortar pestle as described in **Methods subsection 4.2.2**. Most of the cells remained unlysed when seen in bright field microscopy **(Figure 4.6(a))**. In order to enhance the efficiency of nuclei release from intact cells, an alternative method of enzymatic lysis with lyticase was adopted based on the previous reports [Kiseleva et al., 2007; Mann and Jeffery, 1986].

Lyticase is an enzyme involved in the breakage of peptidoglycan linkages of yeast cell wall forming spheroplasts (cells without cell wall).

The cells treated with lyticase for 20 mins show spheroplasts formation as seen in the DIC channel **(Figure 4.6(b), top panel)**. In order to release nucleus from spheroplast, lysis is carried out using two different methods- i) Osmotic shock in water and ii) homogenization using pestle. Both the methods released few nuclei with intact SPB's as seen in the dual channel images with GFP-SPB and DIC **(Figure 4.6(b), bottom panel)** floating outside the cell. The process of obtaining increased numbers of intact nuclei with SPB's requires further optimization.
In addition to the SPBs with intact nuclei from budding yeast, nucleators from alternate sources were also isolated **Appendix, section 5.4**.

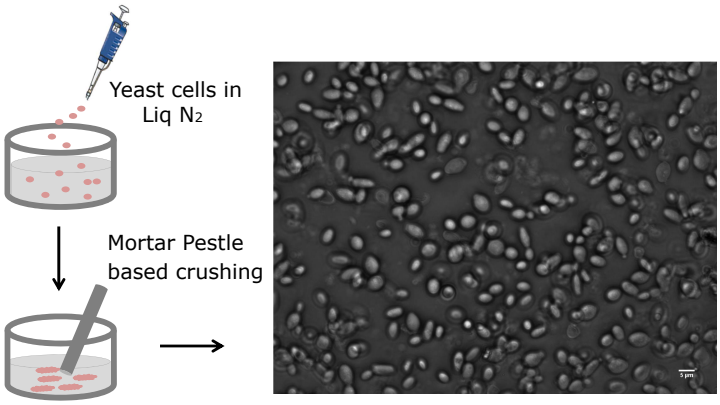

(a)

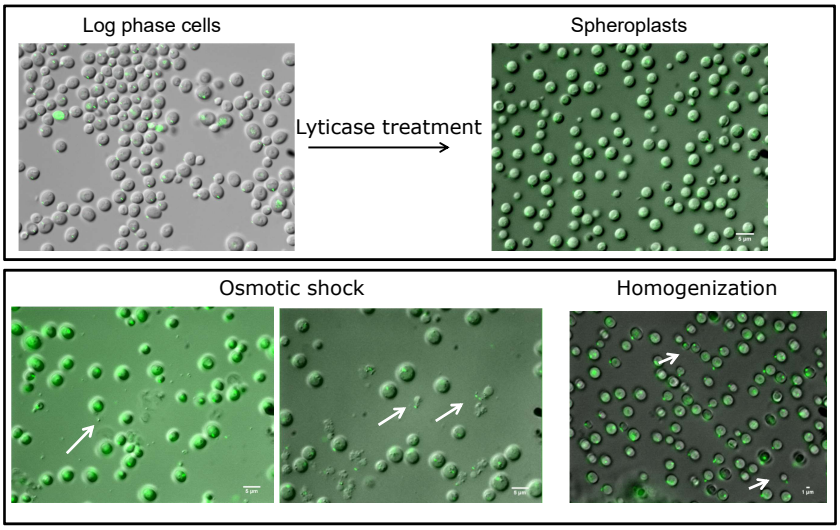

(b)

Figure 4.6: **Extraction of Yeast nuclei** (a) *Left:* The schematic shows the method employed to obtain yeast nuclei using liquid nitrogen based crushing of the cells in a mortar-pestle. *Right:* A bright field image is shown for the cells after liquid nitrogen based crushing on 63 X objective. Scale- 5 μm. (b) DIC and fluorescent labeled GFP-Spc-42 (SPB) images are overlaid for yeast strains that are treated with lyticase to obtain spheroplasts (upper panel). Spheroplasts were subsequently lysed using osmotic shock (*left*-1:2 in water, *middle*-1:4 in water) and *right*- homogenization using pestle.

4.4 Discussion

The dynamics of nuclear positioning is observed in *S. cerevisiae* mitosis using a previously described strain [Caydasi and Pereira, 2009] with a fluorescently tagged SPB (Spc42-3xmCherry) and GFP labeled tubulin. At the time of nuclear positioning, the dynein motors localized to the bud-cell cortex are thought to 'search and capture' MTs emanating from the nucleus, during the G2/M to anaphase transition [Baumgärtner and Tolić, 2014]. Typically, one SPB remains in the mother cell (SPB-M), while the other enters the bud cell (SPB-B). The observations suggests that prior to budding in the G2/M phase transition, the SPB movement appears to be random (**Figure 4.2(b)**). As the cell progresses to anaphase, SPB duplication results in the movement of the SPB-M to the mother cell and of the SPB-B to the bud cell **(Figure 4.2(c) and (d))**. Quantification of these trajectories using mean square displacement analysis confirms the qualitative trends of directed movements observed in the XY trajectories, with a decreasing effective diffusion co-efficient as the cell transits to anaphase **(Figure 4.3)**. The highest values of anomaly parameter, α (> 1) and drift velocity for the SPBs moving towards bud further indicates that the movements become directed for the SPB-B **(Figure 4.3)**. The directionality of SPB-B with a mean χ of 0.14 $\pm$0.050 measured here, is consistent with that predicted by our *in vitro* and *in silico* work for 6 to 8 motors (previous chapter). This value of motors is comparable to the *in vivo* number of cortical dyneins reported in the bud ($\sim$6.3$\pm$2) [Markus et al., 2011], thus potentially validating our model. The difference between the directionality of SPB motility prior to separation and SPB-B (the SPB destined for the bud) most significant ($p < 0.0001$). In this analysis, SPB dynamics are considered prior to the spindle elongation phase, as visible in the tubulin channel. Based on the correlation of SPB-B movement with the appearance of astral-MTs, the more directed movement of SPB-B could be attributed to MT-sliding on the motors in the bud cortex.

Multiple studies have shown that dynein dependent spindle positioning at the onset of anaphase increases shrinkage events at minus ends of the microtubule [Adames and Cooper, 2000b; Carminati and Stearns, 1997; Estrem et al., 2017; Maddox et al., 2000]. This highlights that length dynamics of MT filaments play an important role in nucleus positioning. Our analyses of the increased directionality in SPB-B combined with the

results of *in vitro* gliding assays of dynein mediated transport, further suggest that motor number dependent transitions are involved in the process.

Based on these findings, we propose a general 'search and orient' mechanism of organelle positioning by MT asters. The initial 'search' and attachment of filaments to a few motors could provide the 'noise' necessary for the nucleus to be correctly oriented along the bud-mother axis, due to the low directionality of MTs bound to a few motors. After the 'search and orientation' phase, longer contacts between MTs and motors could then result in more directed motion, which would be required for positioning the nucleus, a form of 'reeling in'.

Cortical dynein mediated microtubule pulling have also been shown to position spindle in *C.elegans* embryo [Grill et al., 2001] and human cells [Kiyomitsu and Cheeseman, 2013]. In *Schizosaccharomyces pombe*, the combined effect of MT lengths and motor-numbers result in nuclear oscillations [Ding et al., 1998; Svoboda et al., 1995; Yamamoto et al., 2001a]. Different models have been proposed for spindle positioning that includes either (i) end-on [Kozlowski et al., 2007] interactions of MTs or (ii) lateral-interactions (sideways pulling) [Adames and Cooper, 2000a] of the MTs with these cortical anchor. The 'search and capture' of MTs in spindle assembly of large cells has been shown to involve additional directional cues such as gradients of regulatory proteins that affect MT growth dynamics in *Xenopus* oocyte meiosis II [Athale et al., 2008, 2014a] or motor gradients in mouse oocyte meiosis I [Khetan and Athale, 2016]. All these processes either involve dynamic rearrangement of motors on the cortex or variations in microtubule lengths. Investigating the motor number and MT length dependence on transport of such complex assemblies might give us a perspective based on the mechanical elements of the cell, different from the usual regulatory networks to understand the collective transport. In this chapter, the results indicate that increased directionality of SPB transport is correlated with the appearance of astral MTs that slide along the bud cortex. However, due to the limitation in imaging for the *in vivo* system, umambiguous detection of lengths or motor numbers cannot be made for a direct assessment of a motor number dependence in nuclear transport. The future implications are discussed later in **Chapter 6** .

In order to overcome the complexity of motor number measurements in an *in vivo*

system, an organelle gliding assay is being optimized with intact nucleus and SPB's from budding yeast. This organelle gliding assay could be used in future to further test the effect of mechanical and biochemical regulators in yeast nuclear positioning. Additional microtubule nucleators that form radial spindle complexes in higher eukaryotes like centrosomes of Drosophila embryos and T-lymphoblastic cell lines have also been isolated **(Figure A1)**. The activity of the centrosomal fractions are confirmed by microtubule nucleations that form asters **(Figure A2)**. Consistent nucleations to observe radial structures reproducibly, is being optimized. This will provide insights whether the number dependence in MT transport by dynein occurs in just linear filament transport or it also extends to more complex spindles observed in higher eukaryotes.

Chapter 5

Comparative polymerization kinetics of tubulins explains differences between plant and animal microtubule (MT) lengths

KEYWORDS: BRAIN TUBULIN, CRITICAL CONCENTRATION, FILAMENTS, KINETICS, MUNG TUBULIN, MICROTUBULE, NUCLEATION, PLANT TUBULIN, POLYMERIZATION.

Contributions: The AFM data was acquired by Jyoti Yadav in the lab of Dr. Shivaprasad Patil, IISER Pune.

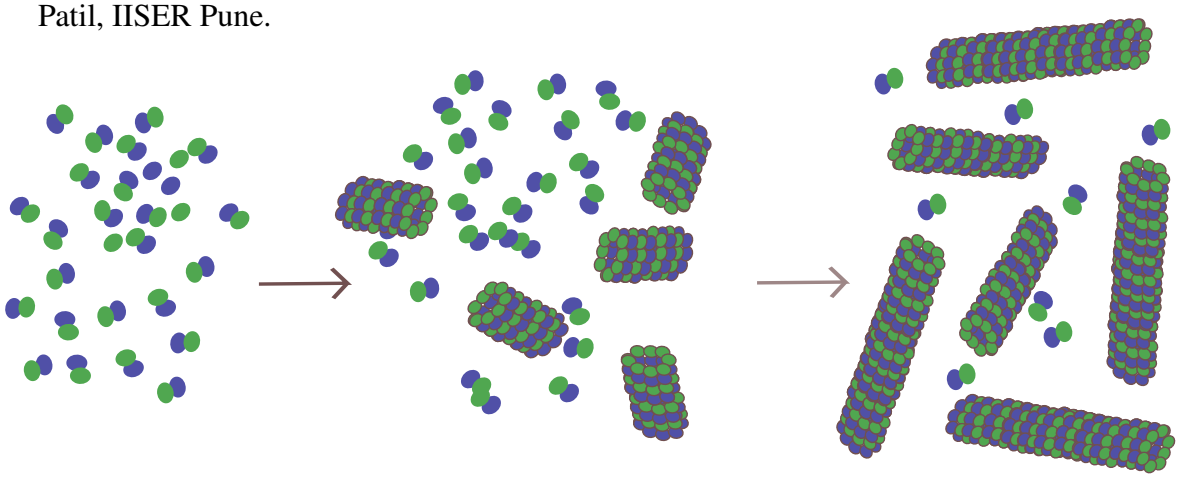

5.1 Introduction

The role of microtubules (MTs) in cell growth and division has led to great interest in developing methods for *in vitro* reconstitution of the polymerization kinetics of tubulin. Indeed, the careful quantification of single filament observations were instrumental in the discovery of dynamic instability of MTs [Kristofferson et al., 1986; Mitchison and Kirschner, 1984a; O'Brien et al., 1987]. Nucleation of MTs in somatic cells of animals is regulated by centrosomes forming radial arrays or asters [Karsenti et al., 1984]. Such nucleators function by lowering the critical concentration for nucleation [Buendia et al., 1992]. Despite the fact that plant cells lack centrosomes, well organized MT arrays are formed in interphase and during mitosis. In such cells, the function of centrosomes appears to be replaced by three pathways as reviewed by Yi and Goshima [Yi and Goshima, 2018]: (a) nucleation from small microtubule organizing centers (MTOCs), (b) MT-dependent MT nucleation and (c) altered minus-end dynamics due to either intrinsic properties of tubulin or by the action of MT-associated proteins (MAPs). Therefore, a better understanding of the nucleation and polymerization dynamics of plant MTs could improve our understanding of their *in vivo* functions.

Plant tubulins have been previously isolated from multiple sources. Some of the earliest reports described tubulin isolation from 'mung' (Azuki) bean (*Vigna radiata*) [Mizuno et al., 1981]. A comparison of filament assembly and drug-binding sensitivity of tubulins isolated from animal brain and cultured cells of multiple higher plants, suggested plant tubulins bind less effectively to colchicine as compared to animal tubulins [Morejohn and Fosket, 1982]. These differences in sensitivity to drug binding could be explained by the divergence of α-tubulin sequences in plants from animals, as compared to the more conserved β-tubulin sequences [Morejohn et al., 1984; Morejohn and Fosket, 1984]. Monoclonal antibodies raised against plant α-tubulin sequences cross-react with plant but not animal tubulins, further supporting the divergence of α-tubulins [Mizuno et al., 1985b]. Indeed, a divergence of α-tubulin sequences was reported even between plants species, based on immuno-histochemistry *in vitro* [Mizuno et al., 1985a] and *in vivo* [Mizuno et al., 1985b] and denaturing gel electrophoresis [Mizuno, 1985]. The tubulin from plant have been shown to consist of multiple isoforms, as seen in case of 'mung' bean tubulin which has two major (MBT1, 2) and one minor sub-unit (MBT3).

These were identified as one β-tubulin (MBT1) and two isotypes of α-tubulin (MBT2, 3) [Hussey and Gull, 1985; Mizuno et al., 1985a; Sen et al., 1987]. MT filaments from a diverse set of plant tubulins- mung bean, pea, zucchini, cucumber seedlings and carrot cell suspensions- were shown to require only GTP, Mg^{2+} ions, EGTA and a crowdant for assembly [Mizuno, 1985]. While the sequence and drug-binding comparison suggests a divergence between plant and animal tubulins, these studies did not examine the consequences of the differences on the kinetics of filament formation.

The purification of MAP enriched tubulins from animal brains has been based on successive cycles of polymerization and depolymerization [Castoldi and Popov, 2003]. However, most isolation methods from plants have reported a combination of affinity and size exclusion chromatography [Mizuno et al., 1981; Morejohn and Fosket, 1982], or a single round of polymerization cycle after precipitating out the protein [Sen et al., 1987]. Recent work has demonstrated the utility of affinity chromatography based on a TOG domain (tumour overexpressed gene domain from *S. cereviseae*), for purifying tubulin from diverse sources [Widlund et al., 2012]. Multiple plant tubulins have been successfully isolated and characterized using this approach [Hotta et al., 2016]. However, most studies on the kinetics of tubulin polymerization so far, have used MAP-enriched animal brain tubulins [Barton and Riazi, 1980; Bonfils et al., 2007; Flyvbjerg et al., 1996a]. A comparison of kinetic properties between MAP-enriched animal and plant tubulins has however not been attempted so far.

Here, a plant tubulin is extracted using mung beans. This is the first study which reports that *Vigna* (mung) tubulin has the lowest critical concentration of microtubule polymerization, based on activity-based isolation of the protein from seedlings. Although epitopes of mung tubulin proteins cross-react with goat and porcine brain tubulins suggesting shared structures, their MT polymerization kinetics are quantitatively different. Further tests using kinetics are performed to observe whether the phenomenological model of nucleation dependent polymerization (NDP) used to explain animal brain MT kinetics [Flyvbjerg et al., 1996a] also applies to mung tubulin. Based on the kinetic results, a novel qualitative model of nucleation and filament elongation is developed, to explain the differences in filament length distributions between plant and animal tubulins.
.

5.2 Material and Methods

5.2.1 Activity-based purification of MAP enriched fraction of tubulin

Tubulin was purified from germinated seedlings of *Vigna radiata* and brains of freshly sacrificed goats. Both purifications involved a temperature based polymerization-depolymerization cycle as described previously [Castoldi and Popov, 2003]. Mung seeds were germinated at 30^{o}C in a commercial 'sprouter', a 2-chamber container to separately soak and sprout, resulting in seedlings after 12 hour of soaking and 36 hours of germination. The manually de-husked seeds were homogenized in a heavy duty Waring blender (Stamford, CT, USA) and the homogenate clarified by high speed centrifugation in a Sorvall Ultracentrifuge (Thermo Scientific, Waltham, MA, USA) at 10^5 g at 4^{o}C for 40 min. The supernatant was processed for subsequent polymerization cycles with polymerization at 37^{o}C for 45 min, followed by centrifugation at 150,000 g at 32^{o}C for 45 min and the pellet was subjected to depolymerization cycle at 4^{o}C and centrifuged at 76,000 g for 30 min. This cycle was repeated and the final pellet was depolymerized and resuspended in BRB 80 buffer (80 mM Pipes, 1 mM EGTA, 1 mM $MgCl_2$). Goat brains from freshly sacrificed animals were cleaned to remove blood clots, homogenized, centrifuged to clarify and the same polymerization-depolymerization cycles in high-molarity PIPES buffer were followed as before.

5.2.2 Fitting and scaling of tubulin polymerization kinetics

The polymerization kinetics of tubulins from different sources were measured by light scattering experiments at 340 nm using a 96-well plate platereader (Varioskan, Thermo Scientific, USA). Plant tubulin concentrations of 0.25 μM, 0.5 μM and 0.75 μM diluted with BRB-80 buffer were incubated with 1 mM GTP, 10% glycerol and 3 mM $MgCl_2$ at 37^{o}C. Absorbance was measured at 340 nm every 10 s for a period of 90 min to obtain the kinetic curves. Similarly, porcine brain tubulin at 15 μM, 20 μM and 30 μM concentrations were incubated with 1 mM GTP, 60% glycerol and 5 mM $MgCl_2$ at 37^{o}C. Kinetic curves were obtained by measuring the absorbance at 340 nm every 10 s for 60 mins.

In order to estimate the polymerization rate, the polymerization kinetics were fit to a model based on the logistic function:

$$P(t) = \frac{P_0 \cdot P_{max}}{P_0 + (P_{max} - P_0) \cdot e^{-r \cdot t}} \tag{5.1}$$

where P_0 is the initial polymer mass (absorbance units), P_{max} is the maximal polymer mass (absorbance units), r is the polymerization rate (1/min) and t is time in minutes.

To examine the nucleation limitation of the mung bean tubulin polymerization kinetics, the curves were rescaled in three steps as described previously [Flyvbjerg et al., 1996a]: (a) converting the time-dependent absorbance A_t into relative absorbance A_{rel}, (b) estimating the half-maximal time of the kinetics $t_{1/2}$, and (c) Rescaling the time $t_{1/2}$. The relative absorbance was estimated by scaling for the difference between the initial A_0 and maximal values A_{max}, using the expression:

$$A_{rel} = \frac{A_t - A_0}{A_{max} - A_0} \tag{5.2}$$

In addition to this scaling of the absorbance, a second scaling is performed for the time based on previous work [Flyvbjerg et al., 1996a; Sabareesan and Udgaonkar, 2014], to estimate the half-maximal time $t_{1/2}$. This estimate was obtained by fitting individual curves to a four parameter kinetic model as follows:

$$S = S_o + \frac{S_{max} - S_o}{1 + e^{-[(t - t_{1/2})/\tau]}} \tag{5.3}$$

where S_o is the initial polymer mass, S_{max} is the maximum polymer mass, $t_{1/2}$ is the half maximal time of polymerization kinetics, t is the time in minutes and τ is the characteristic time constant.

5.2.3 Immunoblotting

The presence of tubulin was detected with anti-tubulin antibodies on a western blot by running the proteins on a 10% SDS Page gel (Mini Protean, BioRad, USA), transferred in methanol containing transfer buffer to a polyvinylidene fluoride (PVDF) membrane (Immobilion-E , GE Healthcare, USA). The PVDF membrane was blocked with 5% milk

powder in TBS-T buffer (w/v) for 1 hour at room temperature, followed by overnight incubation with primary antibody at 4 ^{o}C . The primary antibodies used were either a polyclonal rabbit anti-Arabidopsis α-tubulin antibody (1:5000 dilution)(AS10 680, Agrisera, Sweden) or an anti-*Saccharomyces cerevisiae* α-tubulin (414-422 a.a.) antibody (1:500 dilution) raised in a rat (Ab6161, Abcam, Cambridge, U.K.). Membranes washed in TBS-T buffer (4 washes, each for 15 mins) were incubated with HRP-conjugated secondary antibodies at a dilution of 1:10,000 for 1 hour at room temperature and developed with a chemiluminescent reagent. HRP-conjugated goat anti-rabbit IgG (H&L) (AS09 602 antibody (Agrisera, Sweden) secondary antibody was developed using ECL SuperBright Reagents (Agrisera, Sweden) whereas HRP goat anti-rat secondary antibody was developed using SuperSignal West Femto Maximum Sensitivity Substrate (Thermo Fisher, USA). Blots were imaged using a chemimuminescence imaging system (G-Box, Syngene, Frederick, MD, USA. Dot blot were performed in a similar way after blotting concentrated proteins on a nitrocellulose membrane (Thermo Fisher, USA) beginning with passivation in milk-powder.

5.2.4 Immunofluorescence microscopy of tubulin filaments

Goat brain tubulin (20 μM) was incubated with BRB-80 buffer containing 10 % glycerol at 37^{o}C for 15 min. Taxol buffer (20 μM) was added to the filaments for stabilization, which were used for immuno-fluorescence staining. Filaments stuck passively on the coverslips were incubated with FITC- anti α tubulin antibody at room temperature for 12 hours. Mung tubulin filaments were prepared similarly at a concentration of 1.5 μM. The filaments were incubated with a polyclonal, rabbit, anti-arabidopsis alpha tubulin antibody at room temperature for 12 hours followed by staining with Alexa 568 conjugated- anti rabbit antibody for 1 hours. Coverslips were washed with BRB-80 buffer (2 x 10 min each) and mounted on 60 % glycerol.
Filaments were observed on upright epifluorescence microscope, Zeiss Axiovert Z1 with a 40X lens with 0.75 NA (Carl Zeiss GmbH, Germany) combined with filter sets for rhodamine (520-540 nm excitation and 580-600 nm emission) or FITC (470-490 nm excitation and 510-520 nm emission) for fluorescence.

5.2.5 Visualizing microtubules in atomic force microscopy

MT filaments were prepared using goat and mung tubulin. For the goat sample, 20 μM of unlabelled tubulin was mixed with 5 μM of tubulin tagged with 5,6-carboxy tetramethyl rhodamine (Sigma-Aldrich, India) in BRB-80 buffer containing 10 % glycerol, 1 mM GTP and 5 mM $MgCl_2$ at 37^{o}C for 30 min. Taxol buffer (20 μM) was added to the filaments for stabilization. Mung filaments were similarly prepared with unlabelled tubulin (1.5 μM), and the concentration of $MgCl_2$ was varied: 1 and 2 mM. The AFM imaging was performed using a JPK Nanowizard 2 (JPK Instruments AG, Berlin, Germany). Filament samples were incubated for 5 to 10 min on freshly cleaved mica (18 mm diameter,Electron Microscopy Sciences,U.S.A.), followed by rinsing with Milli-Q water. Taxol stabilized microtubules prepared as described in the previous section, were imaged in contact mode using a silicon cantilever of tip radius 10 nm (stiffness 1.7 N/m). Images of 1024x1024 pixels were acquired at a resonance frequency of 80 kHz with a scan rate of 0.7-1 Hz. The images were processed in the JPK software (JPK Instruments AG, Berlin, Germany).

5.3 Results

5.3.1 Activity based purification of mung bean tubulin

Seedlings are expected to be enriched for tubulin due to rapid growth and have therefore been successfully used in the past as a source for tubulin isolation. One such source for tubulin purification has been seedlings of the legume *Vigna sp.* (mung bean) [Mizuno et al., 1981, 1985a; Sen et al., 1987].

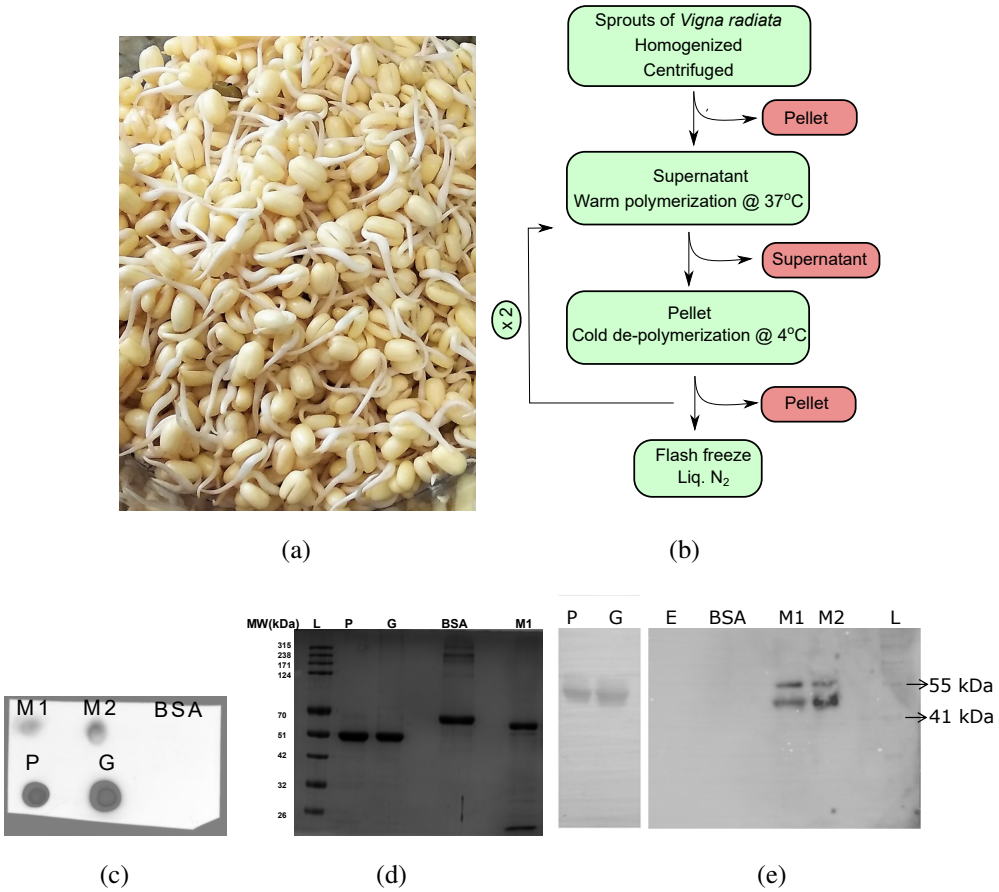

Figure 5.1: **Antibody recognition of activity-based isolation of Mung bean tubulin** (a) The sprouted beans of *Vigna radiata* (mung) were the starting material for (b) polymerization and de-polymerization (activity) based isolation of MTs. (c) A dot blot with 2 μg porcine (P), 1.26 μg goat (G), two independently isolated mung tubulin samples (M1 and M2) and 2 μg BSA was hybridized with polyclonal, anti-Arabidopsis α-tubulin and detected by HRP conjugated anti-rabbit secondary antibodies and developer. (d) Tubulins from porcine (P: 5 μg), goat (G: 5 μg) and mung (M1: 5 μg), alongwith BSA (5 μg) were separated on a 10% SDS-PAGE gel stained with Comassie brilliant blue (CBB). (e) Western blotting of the separated proteins was performed with a polyclonal anti-Arabidopsis α-tubulin primary antibody followed by an HRP-conjugated anti-rabbit secondary antibody and developed. L: molecular weight ladder, mass: kilodaltons.

Mung bean seeds are germinated at 30^{o}C for 48 hours in a commercial sprouter in two steps- soaking and sprouting, as described in detail in the Material and Methods

section, resulting in standardized conditions for seedling growth **(Figure 5.1(a))**. The seedlings were homogenized and the tubulin enriched fraction was isolated using a modification of the method reported for brain tubulin isolation [Castoldi and Popov, 2003], as schematically depicted in **Figure 5.1(b)**. The successive rounds of temperature-based polymerization and depolymerization were concluded with flash freezing the cold-depolymerized sample.

Dot blots analysis of independent isolates of mung protein (M1, M2) tested for polyclonal anti-*Arabidopsis* α-tubulin antibody binding, confirmed that the sample contained tubulin **(Figure 5.1(c))**. The same antibody also recognized goat and porcine brain tubulin, suggesting the epitopes recognize in plants are conserved in animals. A western blot on an SDS-PAGE gel further confirmed the identity of the bands at the expected molecular weights **(Figure 5.1(d)-(e))**

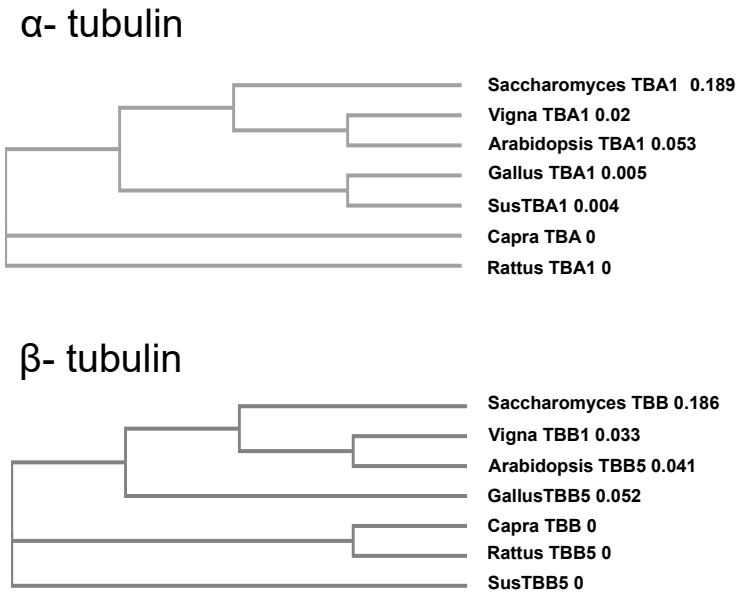

Figure 5.2: **Phylogenetic tree of related α- and β-tubulins.** The phylogenetic tree based on protein sequence differences between the *(top)* α1- and *(bottom)* β-tubulins from *S. cerevisiae*, *Arabidopsis*, *Gallus* (chicken), *Rattus* (rat), *Sus* (pig) and *Capra* (goat) are compared to *Vigna* (mung bean). The tree was generated using Clustal Omega.

The specificity of the results of the dot-blot were confirmed by the lack binding in the BSA and EGFP controls. Taken together, this confirms the presence of tubulin in the

purified sample. Despite the fact that dot blot was loaded with a comparable mass of proteins, the anti-*Arabidopsis* α-tubulin antibody signal was seen to be stronger for goat and pig tubulin, as compared to mung bean tubulin. This could be potentially explained by differences in the proportion of tubulin in the samples, since a phylogenetic tree based on sequence comparison suggests mung and *Arabidopsis* tubulins are more closely related to each other than to animal tubulins **(Figure 5.2)**.

In order to quantify the kinetic activity of isolated mung bean tubulin and compare it with the more commonly used brain tubulins, bulk polymerization kinetics by spectrophotometry have been perfomed.

5.3.2 Activity testing of plant and animal tubulin by bulk polymerization

The polymerization kinetics of mung bean tubulin have been measured using bulk densitometry for increasing tubulin concentrations in order to estimate c*, similar to previous work for estimating the c* of animal tubulin [Bonfils et al., 2007]. Based on reports that $MgCl_2$ plays a role in modulating the polymerization rates [Martin et al., 1987; Schilstra et al., 1991], a range of $MgCl_2$ and EGTA concentrations are tested, in order to optimally capture the early kinetics of polymerization for mung bean tubulin **(Figure 5.3)**. The initial lag phase is reduced and eventually eliminated when the concentration of $MgCl_2$ is increased from 1 to 3 mM (Figure 5.3(a)-(c)), suggesting a potential role in nucleation. This is in contrast to the kinetics of brain tubulin obtained from porcine and goat, where saturation is not observed even in the presence of comparatively higher salt concentrations, 5 mM $MgCl_2$ at 10 % glycerol **(Figure 5.4(a) and (b))**. In order obtain the saturation kinetics of the brain tubulins, crowding is increased to 25 % glycerol **(Figure 5.4(c) and (d))**. These bulk kinetics were then compared to estimate the critical concentrations.

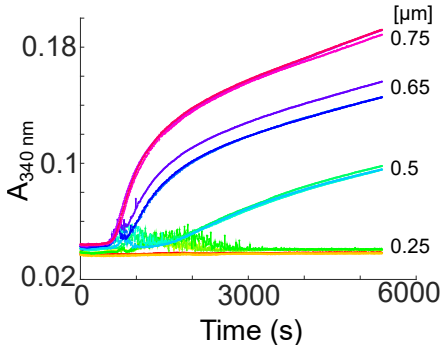

(a) **1 mM $MgCl_2$, 1 mM EGTA**

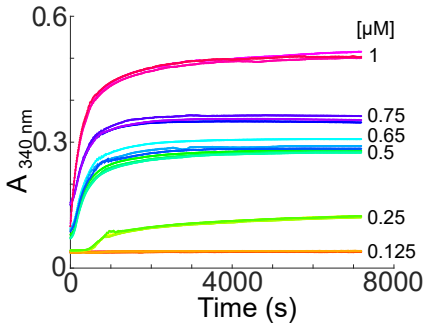

(b) **2 mM $MgCl_2$, 1 mM EGTA**

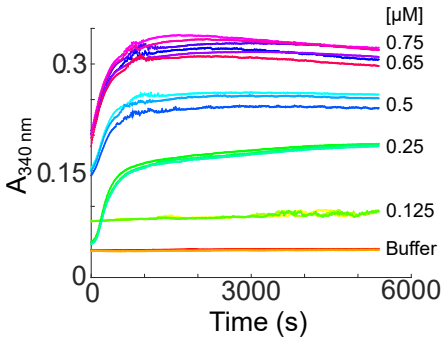

(c) **3 mM $MgCl_2$, 1 mM EGTA**

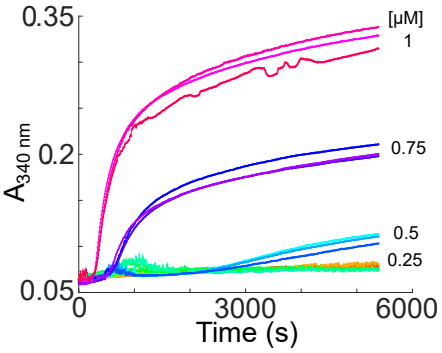

(d) **2 mM $MgCl_2$, 1.6 mM EGTA**

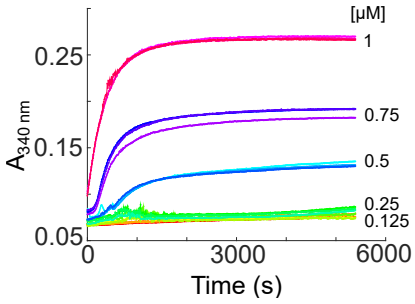

(e) **3 mM $MgCl_2$, 1.6 mM EGTA**

Figure 5.3: **Effect of co-factors on mung tubulin concentration-dependent polymerization kinetics.** The activity of purified tubulin was tested by measuring the absorbance at 340 nm for increasing mung bean tubulin concentrations in the presence of (a)-(c) 1 mM EGTA containing buffer with (a) 1, (b) 2 and (c) 3 mM $MgCl_2$ and compared to the results of (d), (e) 1.6 mM EGTA with (d) 2 and (e) 3 mM $MgCl_2$. Mung bean tubulin concentration was varied between 0.125 and 1 μM with 3 replicates each (indicated by shades of the same color).

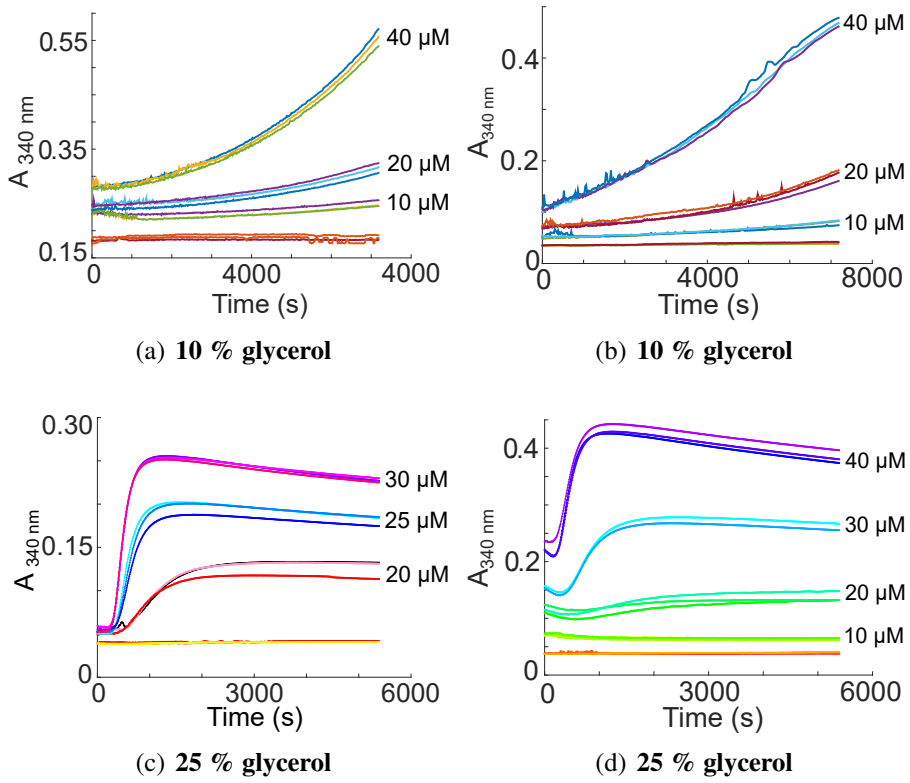

(a) **10 % glycerol** (b) **10 % glycerol**

(c) **25 % glycerol** (d) **25 % glycerol**

Figure 5.4: **Bulk kinetics of brain tubulin in the presence of crowdants** The activity of porcine brain tubulin was tested by measuring the absorbance at 340 nm for increasing tubulin concentrations in the presence of (a) 10 % and (c) 25 % glycerol. This is compared to activity of purified tubulin from goat brain in a similar crowdant concentration of (b) 10 % and (d) 25 % glycerol. Brain tubulin concentration was varied between 10 and 40 μM with 3 replicates each (indicated by shades of the same color).

5.3.3 Comparative kinetics of mung bean tubulin quantified by the critical concentration

The polymerization kinetics of plant tubulin isolated from *Arabidopsis* cell suspension cultures were reported to be rapid at single filament level from previous work, with a minimal tubulin concentration of 7 μM required for filament nucleation [Hotta et al., 2016]. This lower limit of monomer concentration above which polymers form is referred to as the critical concentration (c*).

The polymerization rate, r (min^{-1}) and maximal polymer mass, P_{max} (arbitrary units) for increasing concentrations of tubulin were obtained by fitting the kinetic curves to a model based on the logistic **Equation 5.1**, **(5.5(a)-(f))**. The data of r and P_{max} as a function of tubulin concentration was used to infer the c* values. The critical concentration decreases with increasing $MgCl_2$ concentration and increases with an increase in EGTA concentration. The estimates of c* based on r ranged from 0.03 to 0.421 μM **(Table 5.1)**. The negative values are suggestive of the fact that excess $MgCl_2$ (3 mM) resulted in extremely rapid the kinetics. While the estimates based on P_{max} and r for the same conditions are observed to be comparable, the saturation polymer mass is a more unambiguous variable to estimate, as compared to the initial kinetic rate. Increasing EGTA concentrations resulted in increased c*, potentially due to chelation of ions, consistent with the previously described role for Mg^{2+} ions in early nucleation [Martin et al., 1987; Schilstra et al., 1991] and subsequent elongation.

The kinetics of both animal brain tubulins followed the three phases of growth- lag, elongation and saturation as seen for porcine **(5.6(a))** and goat tubulins **(5.6(b))**. The critical concentration of goat brain tubulin is 4 μM based on polymerization rate (r) **(5.6(c))** and 3 μM based on the maximal polymer mass (P_{max}) (**Figure 5.6(d)**), the first report to our knowledge from this species. Similar estimates for the porcine brain tubulin c* are found to be 4 and $3.6 \pm 4\mu$M, by the two methods respectively **(Table 5.1)**, comparable to previous reports of $\sim$10 μM, that were based on maximal steady state absorbance [Bonfils et al., 2007]. Thus, these observation demonstrates that both sources of brain tubulin exhibit comparable kinetics of bulk polymerization. Interestingly, the critical concentration of of mung tubulin is 50 to 100 fold smaller than goat and porcine brain tubulin, based on similar methods of isolation and kinetic estimations.

The mung bean tubulin critical concentration reported here, is the lowest reported so far **(Table 5.1)**, as compared to non-plant sources such as yeast, bovine brain, porcine brain and *C.elegans* [Bonfils et al., 2007; Chaaban et al., 2018; Davis et al., 1993]. It is even lower than the c* of another plant tubulin, from *Arabidopsis* tubulin (11 μM) [Mao et al., 2005] **(Table 5.2)**.

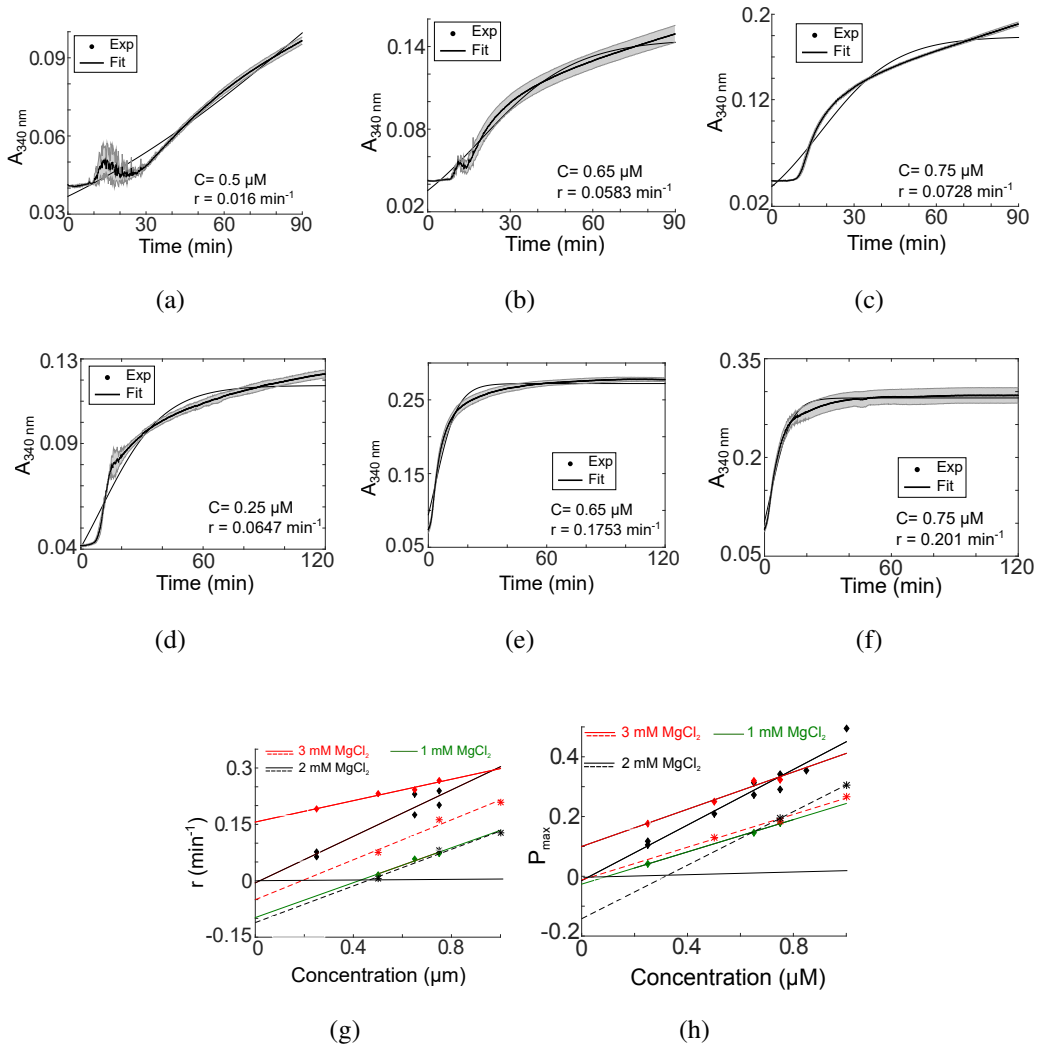

Figure 5.5: **Estimating the critical concentration (c*) of polymerization of mung tubulin.** Absorbance at 340 nm over time was used to measure the kinetics of mung tubulin polymerizationin in presence of (a)-(c) 1 mM $MgCl_2$ and (d)-(f) 2 mM $MgCl_2$ over a range of tubulin concentrations (C) and the fit (black line) of the mean (grey area: $\pm$s.d., n=3) data (-o-) to a saturation model (Equation 5.1) was used to estimate the fit parameter of polymerization rate (r). (g)-(h) The straight line fit to the plot of (g) the polymerization rate, r (min^{-1}) and, (h) maximal polymerization values (P_{max}) as a function of concentration (μM) is used to estimate the critical concentrations (c*) for varying $MgCl_2$ concentrations. $MgCl_2$ concentration: 3 mM (red), 2 mM black, 1 mM (green). Solid lines indicate EGTA concentration of 1 mM in the buffer and dotted lines indicate 1.6 mM EGTA.

.

The sigmoid profile of scattering based measurements for mung bean tubulin kinetics across the range of concentrations, is suggestive of a common process underlying it, similar to that reported for animal brain tubulins. In addition, an increase in tubulin concentration resulted in a reduced 'lag', increased slope of the 'growth phase' and higher saturation value for increasing the monomer concentration **(Figure 5.5)**, demonstrating that monomer concentrations affect nucleation and polymerization rates.

This would suggest that the kinetics of mung tubulin polymerization may follow nucleation dependent polymerization (NDP), as described previously by Flyvbjerg et al. and successfully applied to animal brain MTs [Flyvbjerg et al., 1996a].

Tubulin source	**[$MgCl_2$] (mM)**	**[EGTA] (mM)**	**Critical concentration, c* [μM]]**	
			r	P_{max}
	1	1	0.42	0.09
	2	1	0.018	0.03
Mung bean seedlings	2	1.5	0.45	0.31
	3	1	NA	NA
”	3	1.5	0.189	0.044
Goat brain	5	1	4	3
Porcine brain	5	1	4	3.6

Table 5.1: The critical concentration (c*) estimates of mung bean seedlings are compared to animal brain tubulin from goats isolated by the same method and commercially purified porcine brain tubulin. The c* estimates for mung tubulin vary based on $MgCl_2$ and EGTA concentrations. Estimation of c* is based on either polymerization rates (r) or the maximal polymer mass (P_{max}). NA- Not applicable due to poor fits.

Tubulin source	**c* (μM)**	**Reference**
S.cerevisiae	1.8	[Bode et al., 2003; Davis et al., 1993]
Porcine brain	5	[Walker et al., 1988]
Bovine brain	5.6	[Davis et al., 1993]
Arabidopsis	11	[Mao et al., 2005]
Lily pollen	12	[XU et al., 2005]

Table 5.2: The critical concentration of polymerization for various sources of tubulin are reported in the table.

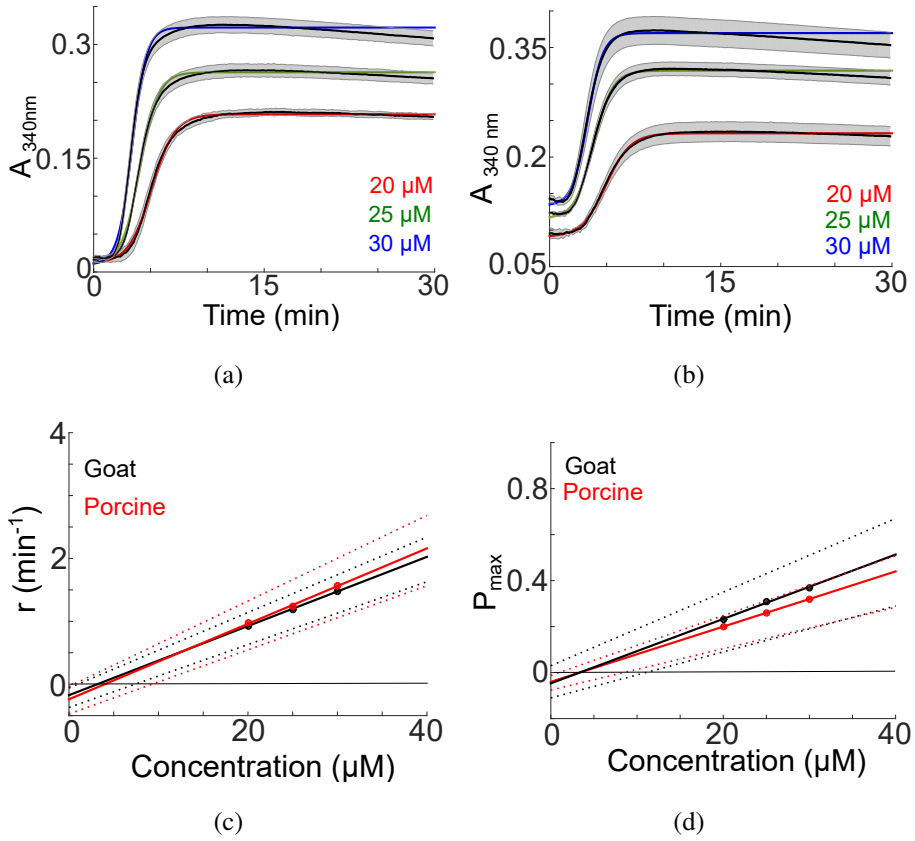

Figure 5.6: **Critical concentration of porcine and goat brain tubulin polymerization.** The 340 nm absorbance (mean ±s.d.: shaded grey area, n=3) were measured to estimate polymerization kinetics of tubulin for a range of tubulin concentrations (20, 25 and 30 μM) from (a) porcine and (b) goat brains in presence of 25 % glycerol and 5 mM $MgCl_2$. The fit to the saturation model (Equation 5.3, colored lines) was used to estimate r and P_{max}. Gray area indicates standard deviation, experimental values are indicated by black lines, and the fits are indicated by the colored lines for the respective concentrations (red: 20 μM, green: 25 μM and blue: 30 μM) (c)-(d) The critical concentration (c*) is estimated from the x-intercepts of the linear fits to porcine (red) and goat (black) brain tubulin kinetics from either (c) r or (d) P_{max} as a function of tubulin concentration.The dashed lines indicate the uncertainty in the slopes and the intercepts as determined from the 95 % confidence interval.

5.3.4 Nucleation dependent polymerization of mung bean tubulin

Nucleation-dependent polymerization (NDP) has been shown to be the predominant mechanism driving *in vitro* animal tubulin polymerization, as determined by a scaling approach to kinetics [Flyvbjerg et al., 1996a]. In order to test this approach, the polymerization kinetic curves were fit to a saturation model **(Equation 5.2)**, to estimate the half-maximal time of the rapid polymerization phase, $t_{1/2}$ **(Figure 5.7)**.

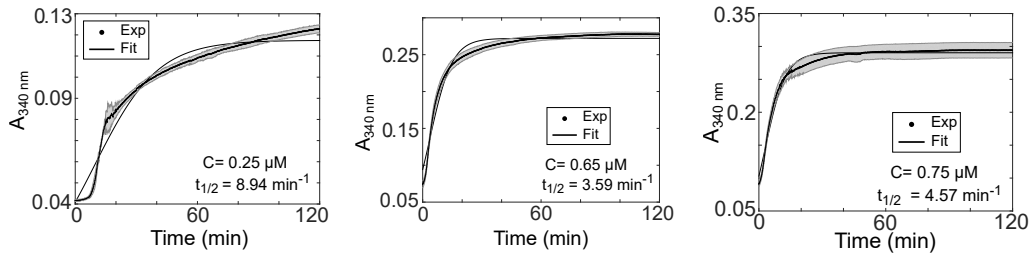

(a) (b) (c)

Figure 5.7: **Estimating the $t_{1/2}$ of mung tubulin polymerization kinetics.** The polymerization kinetics of mung tubulin are measured based on absorbance at 340 nm (black circles) for concentrations (a) 0.25 μM, (b) 0.65 μM and (c) 0.75 μM tubulin in presence of 2 mM $MgCl_2$. The experimental data was fit to a saturation function (black line) based on Equation 5.3, to estimate the value of $t_{1/2}$. Shaded gray region: standard deviation.

Most of the kinetic curves of mung tubulin with 1, 2 and 3 mM $MgCl_2$ collapse onto a single curve **(Figure 5.8(a)-(c))**. The re-scaled plots of the lower tubulin concentrations deviate from the trend since they do not saturate leading to under-estimation of $t_{1/2}$ values. Animal brain tubulin kinetic curves fall on the same curve as seen in case of purified goat **(Figure 5.8(d))** and commercial porcine tubulins **(Figure 5.8(e))**, consistent with previous reports [Flyvbjerg et al., 1996a]. The qualitatively similar behaviour of both mung and animal tubulins demonstrate that the mechanism is qualitatively conserved between mung and brain tubulins. However, quantitatively, mung bean tubulin polymerizes at a critical concentration more than an order of magnitude lower than animal brain tubulins. It is for the first time that such phenomenological analysis of plant tubulin polymerization kinetics has been performed which confirms similar kinetic processes drive both sources of tubulin.

Taken together, the nucleation limitation and extremely low threshold concentration

of mung tubulin for polymerization suggest nucleation might dominate over elongation of filaments, resulting in multiple small filaments at steady state, as compared to the lengths of animal tubulin. In order to test this, filaments were visualized in microsocpe.

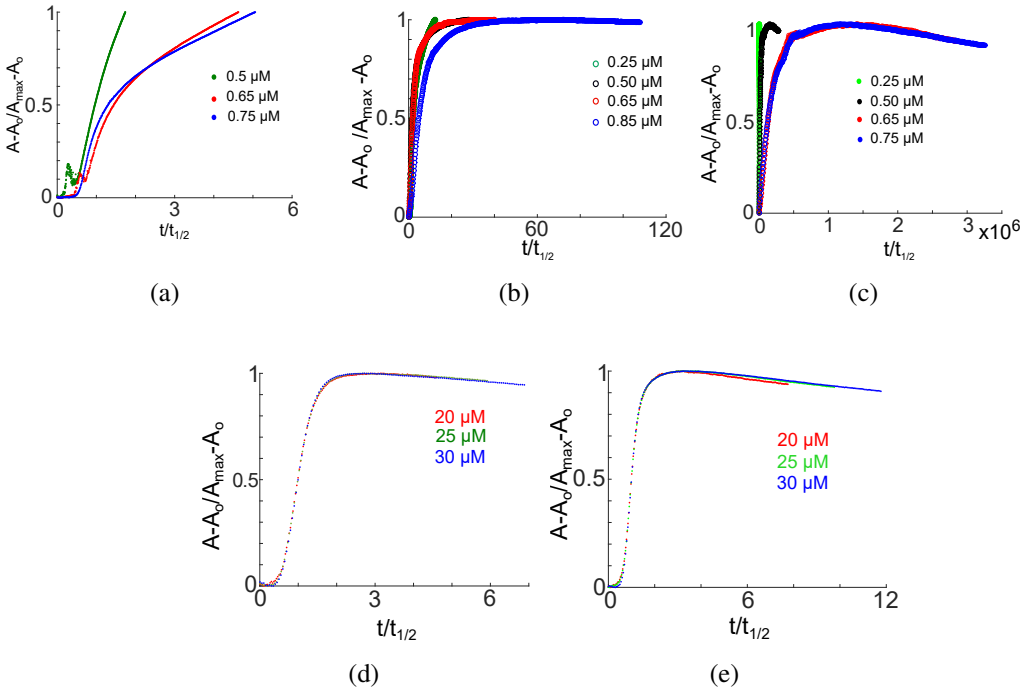

Figure 5.8: **Nucleation dependent polymerization of tubulin from multiple species.** (a)-(c) The relative absorbance of mung tubulin is plotted as a function of scaled time (the ratio of time t, and the half-maximal time, $t_{1/2}$) in presence of increasing concentrations of $MgCl_2$- (a) 1, (b) 2 and (c) 3 mM. Mung tubulin concentration ranges between 0.25 and 0.85 μM. The rescaling parameters were obtained from fitting Equation 5.2 to the unscaled polymerization kinetics data (Figure 5.3). A similar transformation is performed for the polymerization kinetic curves of (d) goat brain tubulin (20, 25 and 30 μM) and (e) porcine brain tubulin (20, 25 and 30 μM) in presence of 5 mM $MgCl_2$.

5.3.5 Mung tubulin polymerization is dominated by short filaments as compared to animal brain tubulin

The comparative study reveals that the kinetics of mung bean and animal brain tubulin polymerization are both nucleation dependent, while quantitative differences are seen

in critical concentrations. Based on the simplest models of polymerization kinetics, the steady state filament length of a tubulin species is expected to depend on both nucleation of 'ends' and their elongation [Edelstein-Keshet, 1998].

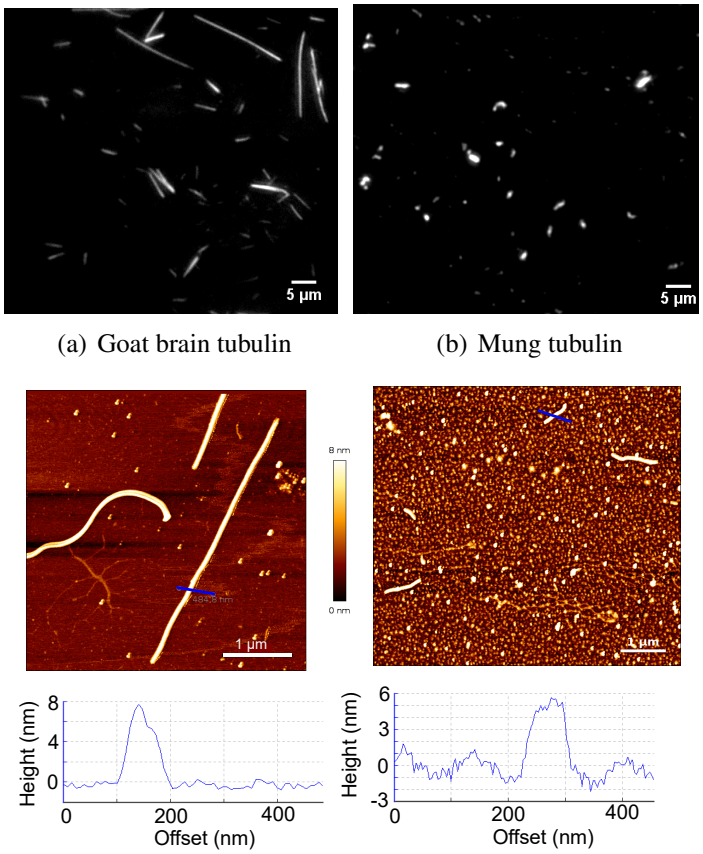

Figure 5.9: **MT filament length distributions of mung bean and pig brain tubulin.** Microtubules stained with (a) FITC- anti α tubulin antibody for goat brain tubulin and (b) Alexa 568 conjugated- anti rabbit α tubulin antibody for mung tubulin are observed in epifluorescence. Scale bar: 5 μM. (c) The AFM images of (left) goat brain tubulin and (right) mung tubulin filaments acquired in imaging mode using air-dried samples. The colour represents the height of the sample (colourbar) in nanometers (nm). A the cross-section of representative goat and mung MTs (blue line in AFM images) is used to plot the height profile of a filament. Scale bar: 1 μm.

Hence, to test whether the difference in critical concentrations would affect filament lengths, taxol stabilized MT filaments were assembled from goat brain and mung bean

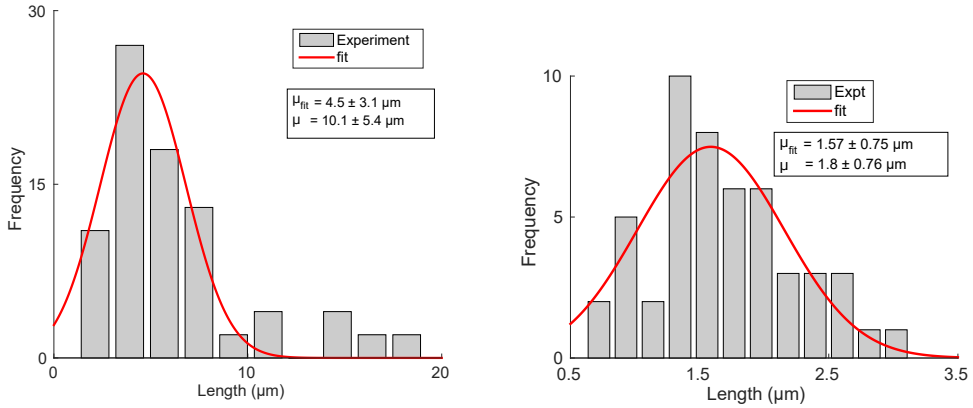

(a) Goat brain tubulin (b) Mung tubulin

Figure 5.10: **Comparing MT length distributions.** The frequency distrubution of MT lengths of (a) goat and (b) mung bean tubulin (grey bars) fit to a log-normal distribution (red line). μ: arithmetic mean, μ_{fit}: log-normal estimate of the mean. N (number of filaments) for goat brain tubulin is 80 and mung tubulin is 65.

tubulin and immuno-stained them as described in detail in the Material and Methods section. Goat brain MTs with a mean length 10$\pm$5.4 μm, were almost ten-fold longer than mung bean (1.8$\pm$0.76 μm) filaments **(Figure 5.9(a)-(b), Figure 5.10)**. The short mung filaments (1 μm and less in length) at times appear ellipsoid, since the lengths and widths are within the diffraction limit of fluorescence light microscopy. In order to unambiguously confirm the presence of filament and confirm the morphology and lengths, an independent label free method is used- atomic force microscopy (AFM) in imaging mode. Steady-state MT filaments of mung tubulin were indeed visible with lengths $\leq$ 1 μm and height profiles comparable to the longer goat MTs **(Figure 5.9(c) and Figure 5.11)**, thus confirming the bonafide filamentous nature of mung MTs.

5.3.6 A model for filament length distribution resulting from a competition between rapid nucleation and filament elongation

Based on these differences in c* and filament lengths, a qualitative model is formulated to better understand these results from comparative kinetics and microscopy. The monomer pool in a given sample is subject to depletion by two competing processes: (a) nucleation

and (b) end-growth (elongation) of previously nucleated oligomers **(Figure 5.12)**. The monomers are expected to rapidly assemble into oligomers (nucleation), by virtue of a lower c* (as seen in mung bean tubulin). This is expected to result in a smaller pool of monomers available for end-growth of the oligomers, resulting in many short filaments, as seen in AFM images with sub-micron structures that have comparable height profiles to long filaments **(Figure 5.11)**. The smaller indentations in the height profiles (< 8 nm) might represent the oligomeric tubulin assembly, protofilament structures or dimeric tubulins. On the other hand, a higher critical concentration (as seen with animal tubulin) will result in slow oligomer formation (nucleation) kinetics, resulting in a relatively fewer ends with a larger pool of free dimers, that elongate by end-growth producing fewer but longer filaments.

Thus, the filament length distribution of mung tubulin appears to be determined by the rapid nucleation kinetics owing to low critical concentrations, which out-competes filament elongation for the same monomer pool.

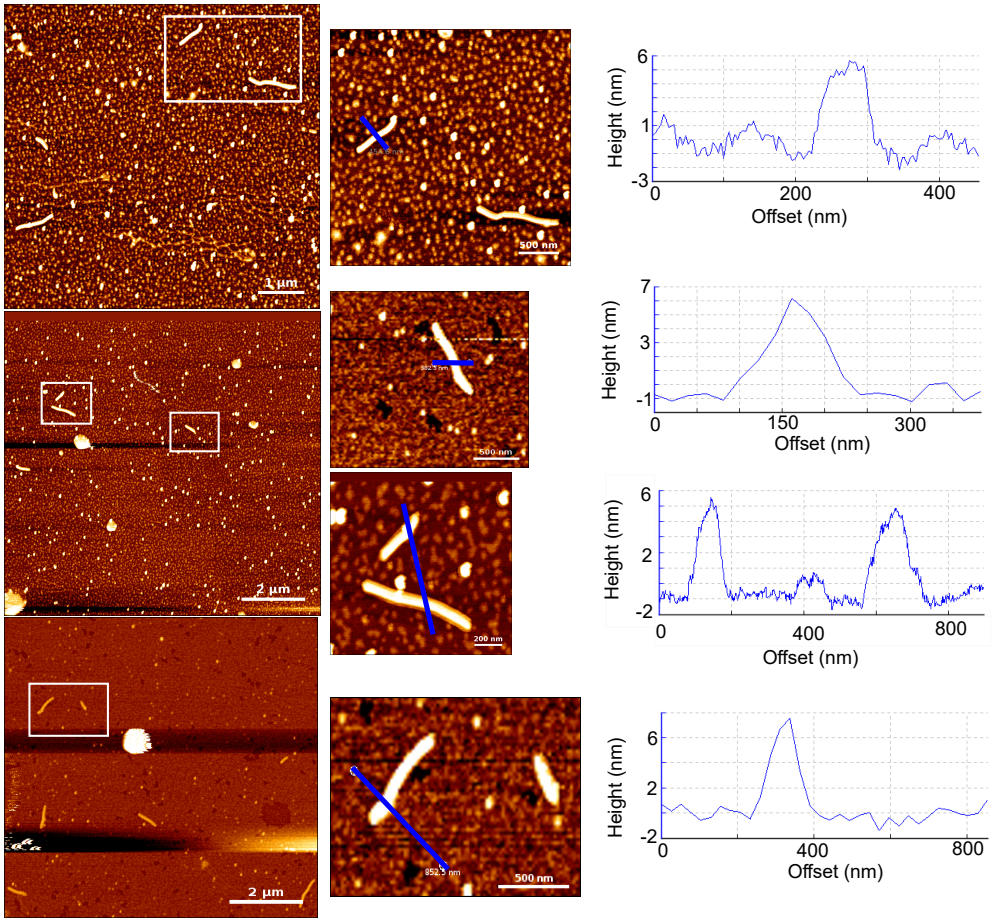

Figure 5.11: **AFM Composite of Mung bean tubulin filaments.** The images (left) represent mung bean tubulin filaments observed in the field of view. The zoomed view of the filaments (center) are represent for the selected filaments (white box on the left images) with the corresponding height profiles on the right (blue lines on zoomed images). Scale bars are indicated in the respective figures.

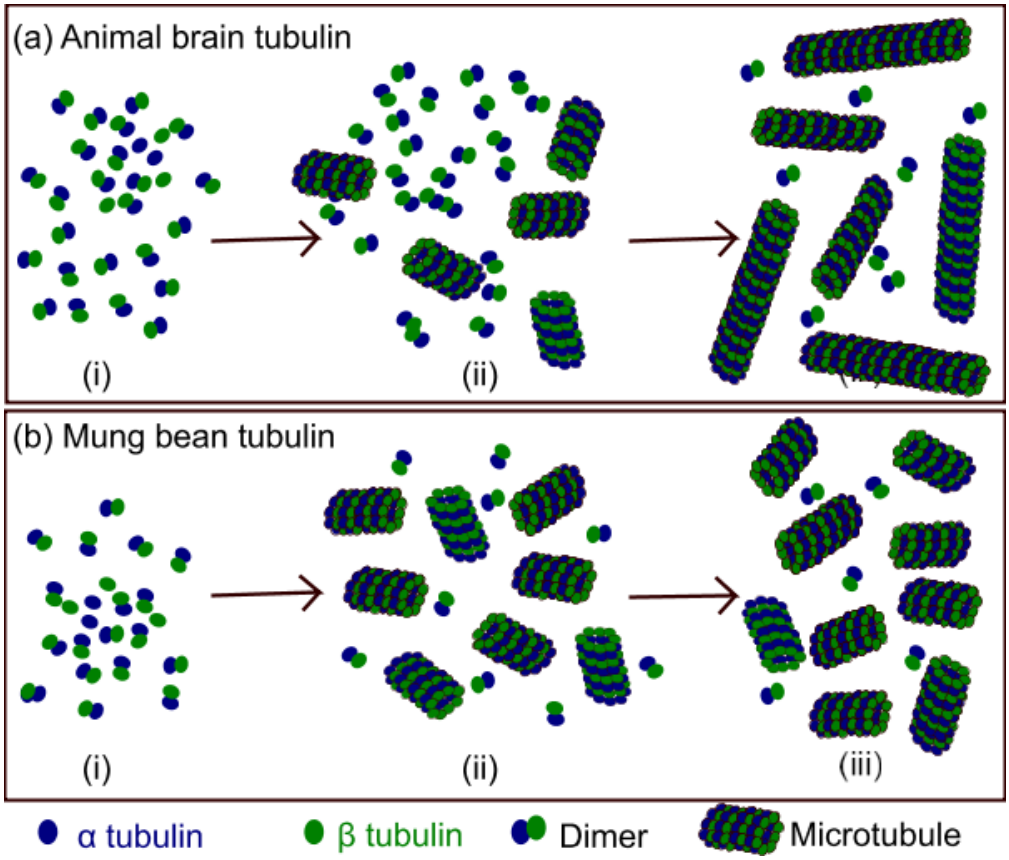

(a)

Figure 5.12: **Schematic interpretation of the effect of c* on microtubule lengths.** The transition between (i) free monomers, (ii) nucleation by oligomers and (iii) end-based filament growth for tubulin from (a) animal brain and (b) mung bean is represented. The c* of animal (goat and porcine) brain tubulin is higher than that of mung bean tubulin. Hence, we expect (a) brain MTs to be longer due to a slower transition of (i) a dimer pool to oligomers leading to the formation of (ii) fewer nuclei with sufficient pool of monomers for (iii) 'end growth' (elongation). (b) Mung bean tubulin with a lower c*, is expected to result in (i) a rapid transition of free tubulin dimers into oligomers. (ii) The oligomers that will serve as nucleators for filament 'end growth' however will have fewer dimers, resulting in (iii) many short filaments at steady state. The circles represent monomers of α- (blue circles) and β-tubulin (green circles).

5.4 Discussion

Studies of tubulin polymerization kinetics have largely focussed on isolates from animal-brains. *In vitro* studies on plant tubulins have been based on isolation from either seedlings or cell suspensions from multiple higher plants. However, these studies have focussed on either identification of the tubulin and microtubule associated proteins (MAPs) or filament assembly, with kinetics used only to demonstrate activity. Here, for the first time, systematic quantification of the concentration dependent polymerization kinetics of plant tubulin using mung bean has been shown. The tubulin is isolated from mung seedlings by a method comparable to that used for animal brain tubulins. Mung bean tubulin's critical concentration of polymerization is lower than any previously reported value of c* for tubulins, and is approximately hundred-fold smaller than goat and porcine brain tubulin values. Despite this quantitative difference, a qualitative similarity exists in the nucleation-dependence of polymerization of mung bean and animal brain tubulins. The assembly of MT filaments at steady state demonstrates mung tubulin forms many but $\sim$10 fold shorter MTs than goat tubulin. A simple model of competition for dimers between nucleation and elongation explains mung bean MT filament polymerization is dominated by nucleation, in contrast to brain tubulin.

Mung bean or *Vigna* tubulin isotypes of α- and β-subunits were first isolated using chromatography [Mizuno, 1985] and identified from whole cell lysates using 2D gel electrophoresis [Hussey and Gull, 1985]. In a subsequent study, two major bands (MBT1 and 2) and a minor band of intermediate size (MBT3) were shown to correspond to β-tubulin isoform, MBT1, and two isoforms of α-tubulin, MBT2, 3 [Mizuno et al., 1985b]. Although, here temperature based polymerization-depolymerization cycles for tubulin isolation is used in contrast to the approach taken by previous studies [Mizuno, 1985; Sen et al., 1987], the isolates reproduce the same electrophoretic pattern on SDS-PAGE reported previously of three bands, two major and one minor (Figure 5.1 (d)). A polyclonal anti-*Arabidopsis* α-tubulin antibody binds to two bands (Figure 5.1(e)), consistent with previous reports of two α-tubulin isoforms in mung tubulin isolates. Interestingly, the plant antibody also recognizes goat and porcine brain tubulins. This further confirms that tubulin epitopes are conserved across plants an animals, consistent with the high degree (80-90%) homology between α- and β-tubulin accross eukaryotes [Breviario et al., 2013]. However, at a functional level, MT organization is distinct

between plants and animals, as seen with plant MT cortical arrays [Allard et al., 2010; de Keijzer et al., 2014; Elliott and Shaw, 2018] that regulate cell wall synthesis [Oda, 2015], that do not form in animal cells. On the other hand, MTs in animal cell are nucleated by centrosomes, that are absent in plant cells [Yi and Goshima, 2018]. Therefore, our findings of a dramatically lower critical concentration of mung tubulin, despite the conservation of sequence, suggests the kinetic divergence plays a functional role of increased nucleation in the absence of well-defined centrosomes. This kinetic divergence could originate from the divergence of α tubulins of higher plants, yeasts and ferns from their animal counterparts, in contrast to the conserved β tubulins, as reported previously [Morejohn and Fosket, 1982]. This has been thought of as one reason why plant MTs are less sensitive to anti-MT drugs such as colchicine as compared to animal MTs [Morejohn and Fosket, 1984]. The apparent correlation between kinetics and drug-sensitivity could in future be addressed by structural and genetic approaches and may have implications for an improved understanding of tubulin-modifications in drug cancer resistance.

The polymerization kinetics of MTs measured by scattering [Shelanski et al., 1973] have been widely used to study the kinetic mechanisms [Barton and Riazi, 1980; Flyvbjerg et al., 1996a] and understand the effect of modulators of MT dynamics such as cellular MAPs [Bonfils et al., 2007; Duan et al., 2017] and drugs [Prinz, 2002]. The observation of dynamic instability of MTs based on single filament kinetics [Kristofferson et al., 1986; Mitchison and Kirschner, 1984a], has been explained by multiple models [Brun et al., 2009; Odde et al., 1995; Sept et al., 2003]. Most recently, a novel model has predicted the co-existence of two polymerization rates at the critical concentration that could explain dynamic instability [Aparna et al., 2017]. Two different critical concentrations of polymerization, one for nucleation and the other for the initiation of filament elongation have been reported in single filament experiments with bovine tubulin [Wieczorek et al., 2015a]. Thus, studying the kinetics of alternatives to animal brain tubulins, could bring us closer to potentially testing the model predictions. Indeed, the recently developed TOG-affinity based method for tubulin purification [Widlund et al., 2012] that has been demonstrated to work for multiple plant systems [Hotta et al., 2016], will accelerate our understanding of the general principles of MT polymerization kinetics and dynamic instability.

Theoretical models of nucleation dependent polymerization (NDP) of protein-based polymeric filaments have been developed to better understand the microscopic events

driving the kinetics [Bishop and Ferrone, 1984; Ferrone et al., 1985]. Early models of diffusion limited growth of microtubules demonstrated how dynamic instability, specifically catastrophe frequencies were regulated in the mitotic to interphase transition of MTs and therefore determined the 'bounded' and 'unbounded' states of growth respectively [Dogterom and Leibler, 1993; Verde et al., 1992]. More recent kinetic models have addressed the role of monomer concentrations on off-rates to explain experimental data [Gardner et al., 2014]. However, most of these assumed a centrosomal nucleation or minus-end immobilization for their models, and were based on animal brain tubulin kinetics. Models of plant MT length distributions have described the role of severing proteins in affecting the qualitative nature of MT length distributions [Tindemans and Mulder, 2010], considered important for the cortical aligment of plant MTs at interphase [Deinum et al., 2017]. The lengths of filaments in our samples are however unlikely to be the result of severing by katanins, due to the need for dense MT networks for the activity [Fan et al., 2018] and the absence of prominent katanin-like proteins in our electrophoresis profile. As a result, a simple model of competition between nucleation and elongation, could explain the observed MT length distributions. Direct single filament dynamics in microscopy, could resolve the question of whether a simple competition between nucleation and end-growth indeed is sufficient to explain the observed differences between mung bean and animal tubulin MT lengths.

While plants lack centrosomes, it does not prevent them from forming complex MT networks [Elliott and Shaw, 2018]. MT associated proteins (MAP) factor interactions are thought to play the role of regulating minus-end dynamics [Yi and Goshima, 2018]. Indeed, TPX2 a prominent mitotic MAP is known to drive centrosome-independent MT nucleation [Gruss et al., 2002] by stabilizing transient tubulin-tubulin interactions [Reid et al., 2016a]. However, our observations of MT nucleation at lower than previously recorded critical concentrations, suggests that along with MAPs, intrinsic nucleation rates of plant tubulins could have evolved to overcome the limitations of the absence of centrosomes.

Thus, the successful purification of a plant tubulin from mung bean (*Vigna sp.*) is demonstrated here with the lowest reported critical concentration of polymerization. Mung tubulin polymerization shows nucleation dependence, similar to goat and porcine brain tubulin. The shared kinetic mechanism could be the result of conserved protein sequence and epitopes. Despite this conservation, the filament length distributions appear

to be dramatically affected by the quantitative differences in critical concentrations. These results are consistent with a qualitative model of a competition for monomers between nucleation and filament elongation, suggesting mung tubulin polymerization is dominated by nucleation. The comparative immuno-staining, polymerization kinetics and microscopy suggests that while the animal brain tubulins share conserved features with *Vigna* tubulin, the kinetics have evolutionary diverged, to address the functional requirement of rapid nucleation of MT's in plants.

Chapter 6

Conclusion and Outlook

The work that I performed during my Ph.D involved quantitative image analysis of large volumes of data for understanding the collective behavior of yeast dyneins in microtubule transport and their *in vivo* implications in *Saccharomyces cerevisiae* nucleus positioning along with comparing the polymerization kinetics of tubulin from two very different sources. Here, I will be discussing the ongoing work and future implications for each of these results that are not discussed in the previous chapters.

Calibrated fluorescence microscopy for protein density estimation

The calibration experiments were performed to estimate the mechanical stability of the acquisition system and the tracking algorithm used. Estimation of protein molecules using a EGFP dilution series as a calibration standard in epi-fluorescence microscopy **Chapter 2, Section 2.3.5 on page 28** is comparable to previously reported methods of counting number of protein molecules *in vivo* using fluorescently tagged proteins [Joglekar et al., 2008; Swedlow et al., 2002b]. Additionally, immuno-staining has been used to independently validate the estimates from calibrated microscopy, in the case of cytoskeletal proteins in fission yeast [Wu and Pollard, 2005]. In fact, wide-field fluorescence based quantification is preferred over confocal microscopy in images with a low background and high signal-to-noise ratio [Cox and Sheppard, 2004; Murray et al., 2007; Pawley, 2006; Swedlow et al., 2002b]. In future, it would be useful to immobilize known amounts of protein on the surface, potentially employing conjugated lipids as

described for kinesin [Grover et al., 2016], to achieve improved density control.

The density estimates obtained from EGFP calibration are used to evaluate the number dependence of motors in microtubule transport properties- mean square displacement (MSD), speeds, velocity and directionality. A threshold motor number dependent transition from low to high values is observed for velocity and 2D directionality **Chapter 3, Section 3.3.3 on page 49 and 3.3.4 on page 50**. While the trends here are observed for homogeneous distribution of surface immobilized dynein, it would be interesting to observe a switch to directional transport on a micro-patterned surface with a precise control over the immobilized motor numbers. A DNA-origami based motor immobilization can serve as one of the approaches to precisely control motor numbers and spacing. Further, experiments with dyneins immobilized on a lipid bilayer can provide mechanistic insights into the functioning of *in vivo* system that recapitulates cortically anchored motors.

Number dependent switch in directionality for *in vivo* transport

Simulations with an asymmetric load dependent detachment in this study indicated that even when 50 % of the motors are inactive, the switch to directional transport occurs at the same threshold motor number [Jain et al., 2019]. It would be interesting to see the results of these predictions experimentally either by using genetic mutants or chemicals that disrupt dynein activity such as ciliobrevin. The results from these experiments might also be important from the view of *in vivo* functioning of this yeast dynein because a number dependent transition might imply a functional team with minimal number of motors. Single molecule studies on yeast dynein have shown that a dimeric motor can step in the presence of one inactive head, indicating that one active head is sufficient to drive the load dependent stepping by this motor [Cleary et al., 2014]. However, this has been shown in a motility assay where motor steps on a static filament, the reverse is yet to be seen.

In order to validate number dependent transitions in directed motility of filaments by this dynein *in vivo* , SPB movement are quantified during *Saccharomyces cerevisiae* nuclear positioning **Chapter 4**. The SPB nucleates astral MTs that are captured and transported by cortical dyneins in a manner similar to a gliding assay, with changes in MT lengths and motor numbers as the time progresses. A threshold number-dependent

transition in nuclear transport might improve the accuracy and reduce the time taken for spindle alignment during division. In fact, it has been shown for *C. elegans* zygote that a threshold number of active force generators results in spindle oscillations during asymmetric cell division [Pecreaux et al., 2006b]. Also, a comprehensive model for nuclear positioning in budding yeasts predicts that timely alignment results with an increase in cytoplasmic MTs or cortical dyneins [Sutradhar et al., 2015].
Our work indicates a directional movement of bud SPB, for the stage where MTs are known to slide along the cortically anchored dyneins. In fact, the increase in directionality value for the SPB to ~ 0.4 **Chapter 4, Section 4.3.3 on page 67** corresponds to the one where number of immobilized motors encountering a filament is $\sim$8-10 in a gliding assay **Chapter 3, Section 3.3.4 on page 50**. To address the complexity of *in vivo* measurements and issues relating to microscopy, we are in the process of optimizing a novel *ex vivo* nuclear transport assay with intact SPBs and astral MTs gliding on immobilized dyneins motors. Currently, the conditions are optimized for obtaining yeast spheroplasts with labeled SPB strains. This 'organelle gliding assay' could be used in future to further test the effect of mechanical and biochemical regulators in yeast nuclear positioning. Additional microtubule nucleators that form radial complexes from alternative sources like centrosomes of *Drosophila* embryos and T-lymphoblastic cell lines have also been isolated. This will provide insights into whether the number dependence in MT transport by dynein occurs in just linear filament transport, or whether it also extends to more complex spindles. This finding implies multi-motor transport at the cellular level might be regulated by a simple modulation of number of motors.

Plant tubulins: Kinetics, dynamics and structure

Along with the collective behavior of dyneins in MT transport, the thesis work also comprised kinetic evaluation and comparison of tubulin polymerization between a plant source and the more routinely used animal source- brains **Chapter 5**. The kinetics indicate that the critical concentration of tubulin isolated from mung is approximately 50-fold lower than that of mammalian tubulin. Tubulin isolation from plant source is based on the protocols similar to the one adopted for mammalian brain tubulin. It is biochemically active fraction enriched with MAPs (microtubule associated proteins). It would be interesting to assess the intrinsic dynamics with pure tubulin fractions isolated using TOG based columns that are known to get rid of MAPS. Single filament dynamics

with labeled tubulin or label free imaging can provide further insights about the polymerization dynamics at varying tubulin concentration. Nucleation dependent polymerization (NDP) confirms that mung tubulin polymerization is limited by nucleation, similar to porcine and goat tubulins. However, the nucleation might be much faster leading to the formation of multiple nuclei and hence short filaments. Immuno-fluorescence and AFM imaging confirms that the distribution of filament lengths for mung tubulin is dominated by very short filaments. However, more precise dynamics with respect to catastrophe's, growth and shrinkage rates can be deciphered from single filament polymerization assays. Further, spectroscopy measurements can be performed to identify the kinetic rates of the initial nucleations stages and verify the conceptual model discussed in the previous chapter.

Previous reports have shown a lower c* for yeast and *C.elegans* tubulins along with a reduction in the number of protofilaments required to assemble a MT filament [Chalfie and Thomson, 1982; Davis and Gull, 1983; Howes et al., 2018]. In order to evaluate the filament structure and the relation of protofilament number to a lower critical concentration of mung tubulin, electron microscopy (EM) and cryo-EM visualizations need to be performed. Currently, our understanding about the polymerization of tubulin comes from mammalian brain, partly due to high yields during purification. Expanding the horizons to other sources might provide insights about the dynamic nature of the filaments that are not yet known. It will be interesting to examine the polymerization kinetics and dynamics of the isolated tubulin in the presence of nucleators. It will also help understand the common mechanisms by which these polymers display drug resistance, template independent nucleation and regulation of dynamic instability despite a high sequence conservation.

Collectively, MT polymerization dynamics, motor localization and self-organized clustering drives MT aster transport in yeasts, animal somatic cells, oocytes and single cell embryos. The 'switch-like' change in transport directionality as a function of MT lengths and motor numbers shown here, could constitute a general 'search and orient' mechanism of organelle positioning. On the other hand, the critical concentration dependent filament length distributions provides evolutionary insights about the MT dynamics across different species. The role of MT polymerization kinetics and motor

collective mechanics on transport could in future be used to better understand their role in spindle pole body (SPB) and centrosome positioning both *in vitro* and *in vivo*, in future. This can help us unify the collective effects of motor numbers, MT length dynamics and complex geometry in organelle positioning and transport in eukaryotic cells.

.

References

Adames, N. R. and Cooper, J. A. (2000a). Microtubule interactions with the cell cortex causing nuclear movements in Saccharomyces cerevisiae. J. Cell Biol. *149*, 863–874.

Adames, N. R. and Cooper, J. A. (2000b). Microtubule interactions with the cell cortex causing nuclear movements in Saccharomyces cerevisiae. The Journal of cell biology *149*, 863–874.

Allard, J. F., Wasteneys, G. O. and Cytrynbaum, E. N. (2010). Mechanisms of self-organization of cortical microtubules in plants revealed by computational simulations. Mol Biol Cell *21*, 278–86.

Allen, C. and Borisy, G. G. (1974). Structural polarity and directional growth of microtubules of Chlamydomonas flagella. Journal of molecular biology *90*, 381–402.

Alushin, G. M., Lander, G. C., Kellogg, E. H., Zhang, R., Baker, D. and Nogales, E. (2014). High-resolution microtubule structures reveal the structural transitions in $\alpha\beta$-tubulin upon GTP hydrolysis. Cell *157*, 1117–1129.

Ananthanarayanan, V., Schattat, M., Vogel, S. K., Krull, A., Pavin, N. and Tolic-Norrelykke, I. M. (2013). Dynein motion switches from diffusive to directed upon cortical anchoring. Cell *153*, 1526–1536.

Aparna, J. S., Padinhateeri, R. and Das, D. (2017). Signatures of a macroscopic switching transition for a dynamic microtubule. Sci Rep *7*, 45747.

Arcizet, D., Meier, B., Sackmann, E., Radler, J. O. and Heinrich, D. (2008). Temporal analysis of Active and Passive Transport in Living Cells. Phys. Rev. Lett. *101*, 248103.

Arpağ, G., Shastry, S., Hancock, W. O. and Tüzel, E. (2014). Transport by populations of fast and slow kinesins uncovers novel family-dependent motor characteristics important for in vivo function. Biophysical Journal *107*, 1896–1904.

Ashkin, A., Dziedzic, J. M., Bjorkholm, J. and Chu, S. (1986). Observation of a single-beam gradient force optical trap for dielectric particles. Optics letters *11*, 288–290.

Athale, C. A., Dinarina, A., Mora-Coral, M., Pugieux, C., Nedelec, F. and Karsenti, E. (2008). Regulation of microtubule dynamics by reaction cascades around chromosomes. Science *322*, 1243–1247.

Athale, C. A., Dinarina, A., Nedelec, F. and Karsenti, E. (2014a). Collective behavior of minus-ended motors in mitotic microtubule asters gliding toward DNA. Phys. Biol. *11*, 016008.

Athale, C. A., Dinarina, A., Nedelec, F. and Karsenti, E. (2014b). Collective behavior of minus-ended motors in mitotic microtubule asters gliding toward DNA. Physical biology *11*, 016008.

Ayaz, P., Ye, X., Huddleston, P., Brautigam, C. A. and Rice, L. M. (2012). A TOG: $\alpha\beta$-tubulin complex structure reveals conformation-based mechanisms for a microtubule polymerase. Science *337*, 857–860.

Baas, P. W. and Mozgova, O. I. (2012). A novel role for retrograde transport of microtubules in the axon. Cytoskel. *69*, 416–425.

Badoual, M., Jülicher, F. and Prost, J. (2002). Bidirectional cooperative motion of molecular motors. Proc. Natl. Acad. Sci. U.S.A. *99*, 6696–6701.

Barton, J. S. and Riazi, G. H. (1980). Evidence for two growth steps in microtubule polymerization. Biochim Biophys Acta *630*, 392–401.

Baumgärtner, S. and Tolić, I. M. (2014). Astral microtubule pivoting promotes their search for cortical anchor sites during mitosis in budding yeast. PloS one *9*, e93781.

Belyy, V., Hendel, N. L., Chien, A. and Yildiz, A. (2014). Cytoplasmic dynein transports cargos via load-sharing between the heads. Nat Commun *5*, 5544.

Bieling, P., Laan, L., Schek, H., Munteanu, E. L., Sandblad, L., Dogterom, M., Brunner, D. and Surrey, T. (2007). Reconstitution of a microtubule plus-end tracking system *in vitro*. Nature *450*, 1100–1105.

Bieling, P., Telley, I. A., Piehler, J. and Surrey, T. (2008). Processive kinesins require loose mechanical coupling for efficient collective motility. EMBO Rep. *9*, 1121–1127.

Bishop, M. F. and Ferrone, F. A. (1984). Kinetics of nucleation-controlled polymerization. A perturbation treatment for use with a secondary pathway. Biophys J *46*, 631–44.

Bode, C. J., Gupta, M. L., Suprenant, K. A. and Himes, R. H. (2003). The two α-tubulin isotypes in budding yeast have opposing effects on microtubule dynamics in vitro. EMBO reports *4*, 94–99.

Bonfils, C., Bec, N., Lacroix, B., Harricane, M.-C. and Larroque, C. (2007). Kinetic analysis of tubulin assembly in the presence of the microtubule-associated protein TOGp. J Biol Chem *282*, 5570–81.

Bourdieu, L., Duke, T., Elowitz, M., Winkelmann, D., Leibler, S. and Libchaber, A. (1995). Spiral Defects in Motility Assays: A Measure of Motor Protein Force. Phys. Rev. Lett. *75*, 176–179.

Breviario, D., Gianì, S. and Morello, L. (2013). Multiple tubulins: evolutionary aspects and biological implications. Plant J *75*, 202–18.

Brun, L., Rupp, B., Ward, J. J. and Nédélec, F. (2009). A theory of microtubule catastrophes and their regulation. Proc Natl Acad Sci U S A *106*, 21173–8.

Buendia, B., Draetta, G. and Karsenti, E. (1992). Regulation of the microtubule nucleating activity of centrosomes in Xenopus egg extracts: role of cyclin A-associated protein kinase. J Cell Biol *116*, 1431–42.

Buey, R. M., Díaz, J. F. and Andreu, J. M. (2006). The nucleotide switch of tubulin and microtubule assembly: a polymerization-driven structural change. Biochemistry *45*, 5933–5938.

Burbank, K. S., Mitchison, T. J. and Fisher, D. S. (2007). Slide-and-cluster models for spindle assembly. Curr. Biol. *17*, 1373–1383.

Byers, B. and Goetsch, L. (1975). Behavior of spindles and spindle plaques in the cell cycle and conjugation of Saccharomyces cerevisiae. Journal of bacteriology *124*, 511–523.

Carazo-Salas, R. E., Gruss, O. J., Mattaj, I. W. and Karsenti, E. (2001). Ran–GTP coordinates regulation of microtubule nucleation and dynamics during mitotic-spindle assembly. Nature cell biology *3*, 228.

Carlton, R. and Englehart, S. (2005). Errors in optical microscope measurements using image analysis. Microscopy and Microanalysis *11*, 1248–1249.

Carminati, J. L. and Stearns, T. (1997). Microtubules orient the mitotic spindle in yeast through dynein-dependent interactions with the cell cortex. The Journal of cell biology *138*, 629–641.

Carter, B. C., Shubeita, G. T. and Gross, S. P. (2005). Tracking single particles: a user-friendly quantitative evaluation. Physical biology *2*, 60.

Castoldi, M. and Popov, A. V. (2003). Purification of brain tubulin through two cycles of polymerization-depolymerization in a high-molarity buffer. Protein Expr Purif *32*, 83–8.

Caviston, J. P., Ross, J. L., Antony, S. M., Tokito, M. and Holzbaur, E. L. (2007). Huntingtin facilitates dynein/dynactin-mediated vesicle transport. Proceedings of the National Academy of Sciences *104*, 10045–10050.

Caydasi, A. K. and Pereira, G. (2009). Spindle alignment regulates the dynamic association of checkpoint proteins with yeast spindle pole bodies. Dev. Cell *16*, 146–156.

Chaaban, S., Jariwala, S., Hsu, C.-T., Redemann, S., Kollman, J. M., Müller-Reichert, T., Sept, D., Bui, K. H. and Brouhard, G. J. (2018). The structure and dynamics of C. elegans tubulin reveals the mechanistic basis of microtubule growth. Developmental cell *47*, 191–204.

Chalfie, M. and Thomson, J. N. (1982). Structural and functional diversity in the neuronal microtubules of Caenorhabditis elegans. The Journal of cell biology *93*, 15–23.

Chalovich, J. M. and Eisenberg, E. (1982). Inhibition of actomyosin ATPase activity by troponin-tropomyosin without blocking the binding of myosin to actin. The Journal of biological chemistry *257*, 2432.

Chaphalkar, A. R., Jain, K., Gangan, M. S. and Athale, C. A. (2016). Automated multi-peak tracking kymography (AMTraK): a tool to quantify sub-cellular dynamics with sub-pixel accuracy. PloS one *11*, e0167620.

Cheezum, M. K., Walker, W. F. and Guilford, W. H. (2001). Quantitative comparison of algorithms for tracking single fluorescent particles. Biophysical journal *81*, 2378–2388.

Churchman, L. S., Ökten, Z., Rock, R. S., Dawson, J. F. and Spudich, J. A. (2005). Single molecule high-resolution colocalization of Cy3 and Cy5 attached to macromolecules measures intramolecular distances through time. Proceedings of the National Academy of Sciences *102*, 1419–1423.

Clarke, P. R. and Zhang, C. (2008). Spatial and temporal coordination of mitosis by Ran GTPase. Nature reviews Molecular cell biology *9*, 464.

Cleary, F. B., Dewitt, M. A., Bilyard, T., Htet, Z. M., Belyy, V., Chan, D. D., Chang, A. Y. and Yildiz, A. (2014). Tension on the linker gates the ATP-dependent release of dynein from microtubules. Nat Commun *5*, 4587.

Coffman, V. C. and Wu, J.-Q. (2012). Counting protein molecules using quantitative fluorescence microscopy. Trends in biochemical sciences *37*, 499–506.

Cole, D. G. (2003). The intraflagellar transport machinery of Chlamydomonas reinhardtii. Traffic *4*, 435–442.

Coppin, C. M., Pierce, D. W., Hsu, L. and Vale, R. D. (1997). The load dependence of kinesin's mechanical cycle. Proc. Nat. Acad. Sci. USA *94*, 8539–8544.

Cote, R. H. and Borisy, G. G. (1981). Head-to-tail polymerization of microtubules in vitro. Journal of molecular biology *150*, 577–599.

Cox, G. and Sheppard, C. J. (2004). Practical limits of resolution in confocal and non-linear microscopy. Microscopy research and technique *63*, 18–22.

Cytrynbaum, E. N., Scholey, J. M. and Mogilner, A. (2003). A force balance model of early spindle pole separation in Drosophila embryos. Biophys. J. *84*, 757–769.

Das, S. K., Darshi, M., Cheley, S., Wallace, M. I. and Bayley, H. (2007). Membrane protein stoichiometry determined from the step-wise photobleaching of dye-labelled subunits. ChemBioChem *8*, 994–999.

Davis, A., Sage, C. R., Wilson, L. and Farrell, K. W. (1993). Purification and biochemical characterization of tubulin from the budding yeast Saccharomyces cerevisiae. Biochemistry *32*, 8823–8835.

Davis, C. and Gull, K. (1983). Protofilament number in microtubules in cells of two parasitic nematodes. The Journal of parasitology *69*, 1094–1099.

Davis, L. J., Odde, D. J., Block, S. M. and Gross, S. P. (2002). The importance of lattice defects in katanin-mediated microtubule severing in vitro. Biophysical journal *82*, 2916–2927.

de Keijzer, J., Mulder, B. M. and Janson, M. E. (2014). Microtubule networks for plant cell division. Syst Synth Biol *8*, 187–94.

Deinum, E. E., Tindemans, S. H., Lindeboom, J. J. and Mulder, B. M. (2017). How selective severing by katanin promotes order in the plant cortical microtubule array. Proc Natl Acad Sci U S A *114*, 6942–6947.

Derr, N. D., Goodman, B. S., Jungmann, R., Leschinzer, A. E., Shih, W. M. and Reck-Peterson, S. L. (2012). Tug-of-war in motor protein ensembles revealed with a programmable DNA origami scaffold. Science *338*, 662–665.

DeWitt, M. A., Chang, A. Y., Combs, P. A. and Yildiz, A. (2012). Cytoplasmic dynein moves through uncoordinated stepping of the AAA+ ring domains. Science *335*, 221–5.

Ding, D. Q., Chikashige, Y., Haraguchi, T. and Hiraoka, Y. (1998). Oscillatory nuclear movement in fission yeast meiotic prophase is driven by astral microtubules, as revealed by continuous observation of chromosomes and microtubules in living cells. J. Cell. Sci. *111 (Pt 6)*, 701–712.

Dogterom and Leibler (1993). Physical aspects of the growth and regulation of microtubule structures. Phys Rev Lett *70*, 1347–1350.

Dogterom, M., Felix, M., Guet, C. and Leibler, S. (1996). Influence of M-phase chromatin on the anisotropy of microtubule asters. The Journal of cell biology *133*, 125–140.

Dogterom, M. and Leibler, S. (1993). Physical aspects of the growth and regulation of microtubule structures. Physical review letters *70*, 1347.

Driver, J. W., Jamison, D. K., Uppulury, K., Rogers, A. R., Kolomeisky, A. B. and Diehl, M. R. (2011). Productive Cooperation among Processive Motors Depends Inversely on Their Mechanochemical Efficiency. Biophys. J. *101*, 386–395.

Duan, A. R., Jonasson, E. M., Alberico, E. O., Li, C., Scripture, J. P., Miller, R. A., Alber, M. S. and Goodson, H. V. (2017). Interactions between Tau and Different Conformations of Tubulin: Implications for Tau Function and Mechanism. J Mol Biol *429*, 1424–1438.

Duellberg, C., Cade, N. I., Holmes, D. and Surrey, T. (2016). The size of the EB cap determines instantaneous microtubule stability. Elife *5*, e13470.

Edelstein-Keshet, L. (1998). A mathematical approach to cytoskeletal assembly. Eur Biophys J *27*, 521–31.

Elliott, A. and Shaw, S. L. (2018). Update: Plant Cortical Microtubule Arrays. Plant Physiol *176*, 94–105.

Erickson, H. and Pantaloni, D. (1981). The role of subunit entropy in cooperative assembly. Nucleation of microtubules and other two-dimensional polymers. Biophysical journal *34*, 293–309.

Eshel, D., Urrestarazu, L., Vissers, S., Jauniaux, J., van Vliet-Reedijk, J., Planta, R. and Gibbons, I. (1993). Cytoplasmic dynein is required for normal nuclear segregation in yeast. Proceedings of the National Academy of Sciences *90*, 11172–11176.

Estrem, C., Fees, C. P. and Moore, J. K. (2017). Dynein is regulated by the stability of its microtubule track. J. Cell Biol. *216*, 2047–2058.

Fagarasanu, A. and Rachubinski, R. A. (2007). Orchestrating organelle inheritance in Saccharomyces cerevisiae. Current opinion in microbiology *10*, 528–538.

Fan, Y., Burkart, G. M. and Dixit, R. (2018). The Arabidopsis SPIRAL2 Protein Targets and Stabilizes Microtubule Minus Ends. Curr Biol *28*, 987–994.e3.

Ferrone, F. A., Hofrichter, J. and Eaton, W. A. (1985). Kinetics of sickle hemoglobin polymerization. II. A double nucleation mechanism. J Mol Biol *183*, 611–31.

Fink, G., Hajdo, L., Skowronek, K. J., Reuther, C., Kasprzak, A. A. and Diez, S. (2009). The mitotic kinesin-14 Ncd drives directional microtubule–microtubule sliding. Nature cell biology *11*, 717.

Flyvbjerg, H., Jobs, E. and Leibler, S. (1996a). Kinetics of self-assembling microtubules: an "inverse problem" in biochemistry. Proc Natl Acad Sci U S A *93*, 5975–9.

Flyvbjerg, H., Jobs, E. and Leibler, S. (1996b). Kinetics of self-assembling microtubules: an" inverse problem" in biochemistry. Proceedings of the National Academy of Sciences *93*, 5975–5979.

Fygenson, D. K., Flyvbjerg, H., Sneppen, K., Libchaber, A. and Leibler, S. (1995). Spontaneous nucleation of microtubules. Physical Review E *51*, 5058.

Gagliano, J., Walb, M., Blaker, B., Macosko, J. C. and Holzwarth, G. (2010). Kinesin velocity increases with the number of motors pulling against viscoelastic drag. Eur. Biophys. J. *39*, 801–813.

Gaglio, T., Saredi, A., Bingham, J. B., Hasbani, M. J., Gill, S. R., Schroer, T. A. and Compton, D. A. (1996). Opposing motor activities are required for the organization of the mammalian mitotic spindle pole. The Journal of cell biology *135*, 399–414.

Gardner, M. K., Charlebois, B. D., Jánosi, I. M., Howard, J., Hunt, A. J. and Odde, D. J. (2014). Rapid Microtubule Self-Assembly Kinetics. Cell *159*, 215.

Gatlin, J. C., Matov, A., Groen, A. C., Needleman, D. J., Maresca, T. J., Danuser, G., Mitchison, T. J. and Salmon, E. (2009). Spindle fusion requires dynein-mediated sliding of oppositely oriented microtubules. Current Biology *19*, 287–296.

Gennerich, A., Carter, A. P., Reck-Peterson, S. L. and Vale, R. D. (2007). Force-induced bidirectional stepping of cytoplasmic dynein. Cell *131*, 952–965.

Gibbons, I. (1996). The role of dynein in microtubule-based motility. Cell structure and function *21*, 331–342.

Goldstein, L. S. B. and Yang, Z. (2000). Microtubule-based transport systems in neurons: the roles of Kinesins and Dyneins. Annu. Rev. Neurosci. *23*, 39–71.

Gould, R. R. and Borisy, G. G. (1977). The pericentriolar material in Chinese hamster ovary cells nucleates microtubule formation. The Journal of cell biology *73*, 601–615.

Grill, S. W., GoÈnczy, P., Stelzer, E. H. and Hyman, A. A. (2001). Polarity controls forces governing asymmetric spindle positioning in the Caenorhabditis elegans embryo. Nature *409*, 630.

Gross, S. P., Vershinin, M. and Shubeita, G. T. (2007a). Cargo transport: two motors are sometimes better than one. Curr Biol *17*, R478–86.

Gross, S. P., Vershinin, M. and Shubeita, G. T. (2007b). Cargo transport: two motors are sometimes better than one. Current biology *17*, R478–R486.

Gross, S. P., Welte, M. A., Block, S. M. and Wieschaus, E. F. (2002). Coordination of opposite-polarity microtubule motors. The Journal of cell biology *156*, 715–724.

Grover, R., Fischer, J., Schwarz, F. W., Walter, W. J., Schwille, P. and Diez, S. (2016). Transport efficiency of membrane-anchored kinesin-1 motors depends on motor density and diffusivity. Proc. Natl. Acad. Sci. U.S.A. *113*, E7185–E7193.

Gruss, O. J., Wittmann, M., Yokoyama, H., Pepperkok, R., Kufer, T., Silljé, H., Karsenti, E., Mattaj, I. W. and Vernos, I. (2002). Chromosome-induced microtubule assembly mediated by TPX2 is required for spindle formation in HeLa cells. Nat Cell Biol *4*, 871–9.

Habermann, A., Schroer, T. A., Griffiths, G. and Burkhardt, J. K. (2001). Immunolocalization of cytoplasmic dynein and dynactin subunits in cultured macrophages: enrichment on early endocytic organelles. Journal of cell science *114*, 229–240.

Hancock, W. O. and Howard, J. (1998). Processivity of the motor protein kinesin requires two heads. J. Cell Biol. *140*, 1395–1405.

Harris, D. E. and Warshaw, D. M. (1993). Smooth and skeletal muscle myosin both exhibit low duty cycles at zero load in vitro. J Biol Chem *268*, 14764–8.

Heald, R., Tournebize, R., Blank, T., Sandaltzopoulos, R., Becker, P., Hyman, A. and Karsenti, E. (1996). Self-organization of microtubules into bipolar spindles around artificial chromosomes in Xenopus egg extracts. Nature *382*, 420.

Hirokawa, N. (1998). Kinesin and dynein superfamily proteins and the mechanism of organelle transport. Science *279*, 519–526.

Hoepfner, D., Brachat, A. and Philippsen, P. (2000a). Time-lapse video microscopy analysis reveals astral microtubule detachment in the yeast spindle pole mutant cnm67. Mol. Biol. Cell *11*, 1197–1211.

Hoepfner, D., Brachat, A. and Philippsen, P. (2000b). Time-lapse video microscopy analysis reveals astral microtubule detachment in the yeast spindle pole mutant cnm67. Molecular Biology of the Cell *11*, 1197–1211.

Holy, T. E. and Leibler, S. (1994). Dynamic instability of microtubules as an efficient way to search in space. Proceedings of the National Academy of Sciences *91*, 5682–5685.

Holzbaur, E. and Vallee, R. (1994). Dyneins: molecular structure and cellular function. Annual review of cell biology *10*, 339–372.

Holzbaur, E. L. and Goldman, Y. E. (2010). Coordination of molecular motors: from in vitro assays to intracellular dynamics. Current opinion in cell biology *22*, 4–13.

Hotta, T., Fujita, S., Uchimura, S., Noguchi, M., Demura, T., Muto, E. and Hashimoto, T. (2016). Affinity Purification and Characterization of Functional Tubulin from Cell Suspension Cultures of Arabidopsis and Tobacco. Plant Physiol *170*, 1189–205.

Howard, J., Hudspeth, A. and Vale, R. (1989a). Movement of microtubules by single kinesin molecules. Nature *342*, 154.

Howard, J., Hudspeth, A. J. and Vale, R. D. (1989b). Movement of microtubules by single kinesin molecules. Nature *342*, 154–158.

Howard, J. and Hyman, A. A. (2009). Growth, fluctuation and switching at microtubule plus ends. Nature Reviews Molecular Cell Biology *10*, 569.

Howes, S. C., Geyer, E. A., LaFrance, B., Zhang, R., Kellogg, E. H., Westermann, S., Rice, L. M. and Nogales, E. (2017). Structural differences between yeast and mammalian microtubules revealed by cryo-EM. J Cell Biol *216*, 2669–2677.

Howes, S. C., Geyer, E. A., LaFrance, B., Zhang, R., Kellogg, E. H., Westermann, S., Rice, L. M. and Nogales, E. (2018). Structural and functional differences between porcine brain and budding yeast microtubules. Cell Cycle *17*, 278–287.

Hunt, A. J., Gittes, F. and Howard, J. (1994). The force exerted by a single kinesin molecule against a viscous load. Biophysical journal *67*, 766–781.

Hussey, P. J. and Gull, K. (1985). Multiple isotypes of alpha- and beta-tubulin in the plant Phaseolus vulgaris. FEBS Letters *181*, 113–118.

Hyman, A. A., Salser, S., Drechsel, D., Unwin, N. and Mitchison, T. J. (1992). Role of GTP hydrolysis in microtubule dynamics: information from a slowly hydrolyzable analogue, GMPCPP. Molecular biology of the cell *3*, 1155–1167.

Imafuku, Y., Toyoshima, Y. Y. and Tawada, K. (1996a). Fluctuation in the microtubule sliding movement driven by kinesin in vitro. Biophys. J. *70*, 878–886.

Imafuku, Y., Toyoshima, Y. Y. and Tawada, K. (1996b). Fluctuation in the microtubule sliding movement driven by kinesin in vitro. Biophysical journal *70*, 878–886.

Jain, K., Khetan, N. and Athale, C. A. (2019). Collective effects of yeast cytoplasmic dynein based microtubule transport. Soft matter *15*, 1571–1581.

Jakobsen, L., Schrøder, J. M., Larsen, K. M., Lundberg, E. and Andersen, J. S. (2013). Centrosome isolation and analysis by mass spectrometry-based proteomics. In Methods in enzymology vol. 525, pp. 371–393. Elsevier.

Joglekar, A. P., Salmon, E. D. and Bloom, K. S. (2008). Counting kinetochore protein numbers in budding yeast using genetically encoded fluorescent proteins. Methods Cell Biol. *85*, 127–151.

Jülicher, F., Ajdari, A. and Prost, J. (1997). Modeling molecular motors. Rev. Mod. Phys. *69*, 2111–2122.

Jülicher, F. and Prost, J. (1995). Cooperative Molecular Motors. Phys. Rev. Lett. *75*, 2618–2621.

Karsenti, E., Kobayashi, S., Mitchison, T. and Kirschner, M. (1984). Role of the centrosome in organizing the interphase microtubule array: properties of cytoplasts containing or lacking centrosomes. J Cell Biol *98*, 1763–76.

Keating, T. J. and Borisy, G. G. (2000). Immunostructural evidence for the template mechanism of microtubule nucleation. Nature cell biology *2*, 352.

Khetan, N. and Athale, C. A. (2016). A Motor-Gradient and Clustering Model of the Centripetal Motility of MTOCs in Meiosis I of Mouse Oocytes. PLoS Comp. Biol. *12*, e1005102.

Kimura, K. and Kimura, A. (2010). Intracellular organelles mediate cytoplasmic pulling force for centrosome centration in the Caenorhabditis elegans early embryo. Proc. Nat. Acad. Sci., USA *108*, 137–142.

Kirschner, M. and Mitchison, T. (1986). Beyond self-assembly: from microtubules to morphogenesis. Cell *45*, 329–342.

Kiseleva, E., Allen, T. D., Rutherford, S. A., Murray, S., Morozova, K., Gardiner, F., Goldberg, M. W. and Drummond, S. P. (2007). A protocol for isolation and visualization of yeast nuclei by scanning electron microscopy (SEM). Nature protocols *2*, 1943.

Kiyomitsu, T. and Cheeseman, I. M. (2013). Cortical dynein and asymmetric membrane elongation coordinately position the spindle in anaphase. Cell *154*, 391–402.

Kon, T., Nishiura, M., Ohkura, R., Toyoshima, Y. Y. and Sutoh, K. (2004). Distinct functions of nucleotide-binding/hydrolysis sites in the four AAA modules of cytoplasmic dynein. Biochemistry *43*, 11266–11274.

Kotak, S., Busso, C. and Gönczy, P. (2012). Cortical dynein is critical for proper spindle positioning in human cells. J Cell Biol *199*, 97–110.

Kozlowski, C., Srayko, M. and Nedelec, F. (2007). Cortical microtubule contacts position the spindle in C. elegans embryos. Cell *129*, 499–510.

Kramers, H. (1940). Brownian motion in a field of force and the diffusion model of chemical reactions. Physica *7*, 284–304.

Kristofferson, D., Mitchison, T. and Kirschner, M. (1986). Direct observation of steady-state microtubule dynamics. J Cell Biol *102*, 1007–19.

Kunwar, A., Vershinin, M., Xu, J. and Gross, S. P. (2008). Stepping, Strain Gating, and an Unexpected Force-Velocity Curve for Multiple-Motor-Based Transport. Curr. Biol. *18*, 1173–1183.

Lawrence, C. J., Dawe, R. K., Christie, K. R., Cleveland, D. W., Dawson, S. C., Endow, S. A., Goldstein, L. S., Goodson, H. V., Hirokawa, N., Howard, J. et al. (2004). A standardized kinesin nomenclature. The Journal of cell biology *167*, 19–22.

Leduc, C., Pavin, N., Jülicher, F. and Diez, S. (2010a). Collective Behavior of Antagonistically Acting Kinesin-1 Motors. Phys. Rev. Lett. *105*, 1–4.

Leduc, C., Pavin, N., Jülicher, F. and Diez, S. (2010b). Collective behavior of antagonistically acting kinesin-1 motors. Physical review letters *105*, 128103.

Leduc, C., Ruhnow, F., Howard, J. and Diez, S. (2007). Detection of fractional steps in cargo movement by the collective operation of kinesin-1 motors. Proc. Nat. Acad. Sci. USA *104*, 10847–10852.

Lee, S.-H., Shin, J. Y., Lee, A. and Bustamante, C. (2012). Counting single photoactivatable fluorescent molecules by photoactivated localization microscopy (PALM). Proceedings of the National Academy of Sciences *109*, 17436–17441.

Lee, W. L., Kaiser, M. A. and Cooper, J. A. (2005). The offloading model for dynein function: Differential function of motor subunits. J. Cell Biol. *168*, 201–207.

Lee, W.-L., Oberle, J. R. and Cooper, J. A. (2003). The role of the lissencephaly protein Pac1 during nuclear migration in budding yeast. J Cell Biol *160*, 355–364.

Leidel, C., Longoria, R. A., Gutierrez, F. M. and Shubeita, G. T. (2012). Measuring molecular motor forces in vivo: implications for tug-of-war models of bidirectional transport. Biophysical journal *103*, 492–500.

Li, Y.-Y., Yeh, E., Hays, T. and Bloom, K. (1993). Disruption of mitotic spindle orientation in a yeast dynein mutant. Proceedings of the National Academy of Sciences *90*, 10096–10100.

Lipowsky, R., Beeg, J., Dimova, R., Klumpp, S. and Müller, M. J. (2010). Cooperative behavior of molecular motors: cargo transport and traffic phenomena. Physica E: Low-dimensional Systems and Nanostructures *42*, 649–661.

Lowe, J., Li, H., Downing, K. and Nogales, E. (2001). Refined structure of ab-tubulin at 3.5 A. J Mol Biol *313*, 1083–1095.

Maddox, P. S., Bloom, K. S. and Salmon, E. (2000). The polarity and dynamics of microtubule assembly in the budding yeast Saccharomyces cerevisiae. Nature cell biology *2*, 36.

Mallik, R., Carter, B. C., Lex, S. A., King, S. J. and Gross, S. P. (2004a). Cytoplasmic dynein functions as a gear in response to load. Nature *427*, 649–652.

Mallik, R., Carter, B. C., Lex, S. A., King, S. J. and Gross, S. P. (2004b). Cytoplasmic dynein functions as a gear in response to load. Nature *427*, 649.

Mann, W. and Jeffery, J. (1986). Yeasts in molecular biology. Spheroplast preparation with Canadida utilis, Schizosaccharomyces pombe and Saccharomyces cerevisiae. Bioscience reports *6*, 597–602.

Mao, T., Jin, L., Li, H., Liu, B. and Yuan, M. (2005). Two microtubule-associated proteins of the Arabidopsis MAP65 family function differently on microtubules. Plant Physiol *138*, 654–62.

Markus, S. M. and Lee, W. L. (2011). Regulated offloading of cytoplasmic dynein from microtubule plus ends to the cortex. Dev. Cell *20*, 639–651.

Markus, S. M., Plevock, K. M., St Germain, B. J., Punch, J. J., Meaden, C. W. and Lee, W. L. (2011). Quantitative analysis of Pac1/LIS1-mediated dynein targeting: Implications for regulation of dynein activity in budding yeast. Cytoskeleton (Hoboken) *68*, 157–174.

Martin, S. R., Butler, F. M., Clark, D. C., Zhou, J.-M. and Bayley, P. M. (1987). Magnesium ion effects on microtubule nucleation in vitro. Biochimica et Biophysica Acta (BBA)-Protein Structure and Molecular Enzymology *914*, 96–100.

Meijering, E., Dzyubachyk, O. and Smal, I. (2012). Methods for cell and particle tracking. In Methods in enzymology vol. 504, pp. 183–200. Elsevier.

Michalet, X. (2010). Mean square displacement analysis of single-particle trajectories with localization error: Brownian motion in an isotropic medium. Phys. Rev. E *82*, 041914.

Mitchison, T. (1993). Localization of an exchangeable GTP binding site at the plus end of microtubules. Science *261*, 1044–1047.

Mitchison, T. and Kirschner, M. (1984a). Dynamic instability of microtubule growth. Nature *312*, 237–42.

Mitchison, T. and Kirschner, M. (1984b). Dynamic instability of microtubule growth. Nature *312*, 237.

Mizuno, K. (1985). In vitro assembly of microtubules from tubulins of several higher plants. Cell Biol Int Rep *9*, 13–21.

Mizuno, K., Koyama, M. and Shibaoka, H. (1981). Isolation of plant tubulin from azuki bean epicotyls by ethyl N-phenylcarbamate-Sepharose affinity chromatography. J Biochem *89*, 329–32.

Mizuno, K., Perkin, J., Sek, F. and Gunning, B. (1985a). Some biochemical properties of higher plant tubulins. Cell Biol Int Rep *9*, 5–12.

Mizuno, K., Sek, F., Perkin, J., Wick, S., Duniec, J. and Gunning, B. (1985b). Monoclonal antibodies specific to plant tubulin. Protoplasma *129*, 100–108.

Moore, J. K., Stuchell-Brereton and Cooper, J. A. (2009). Function of dynein in budding yeast: mitotic spindle positioning in a polarized cell. Cell Motil. Cytoskel. *66*, 546–555.

Morejohn, L. C., Bureau, T. E., Tocchi, L. P. and Fosket, D. E. (1984). Tubulins from different higher plant species are immunologically nonidentical and bind colchicine differentially. Proc Natl Acad Sci U S A *81*, 1440–4.

Morejohn, L. C. and Fosket, D. E. (1982). Higher plant tubulin identified by self-assembly into microtubules in vitro. Nature *297*, 426–8.

Morejohn, L. C. and Fosket, D. E. (1984). Taxol-induced rose microtubule polymerization in vitro and its inhibition by colchicine. J Cell Biol *99*, 141–7.

Moritz, M. and Alberts, B. M. (1998). Drosophila Embryos. Mitosis and Meiosis *61*, 1.

Moritz, M., Braunfeld, M. B., Guénebaut, V., Heuser, J. and Agard, D. A. (2000). Structure of the γ-tubulin ring complex: a template for microtubule nucleation. Nature cell biology *2*, 365.

Moritz, M., Braunfeld, M. B., Sedat, J. W., Alberts, B. and Agard, D. A. (1995). Microtubule nucleation by γ-tubulin-containing rings in the centrosome. Nature *378*, 638.

Moriwaki, T. and Goshima, G. (2016). Five factors can reconstitute all three phases of microtubule polymerization dynamics. J Cell Biol *215*, 357–368.

Müller, M. J., Klumpp, S. and Lipowsky, R. (2008). Tug-of-war as a cooperative mechanism for bidirectional cargo transport by molecular motors. Proceedings of the National Academy of Sciences *105*, 4609–4614.

Müller, M. J., Klumpp, S. and Lipowsky, R. (2010). Bidirectional transport by molecular motors: enhanced processivity and response to external forces. Biophysical journal *98*, 2610–2618.

Murray, J. (1998). Evaluating the performance of fluorescence microscopes. Journal of microscopy *191*, 128–134.

Murray, J. M., Appleton, P. L., Swedlow, J. R. and Waters, J. C. (2007). Evaluating performance in three-dimensional fluorescence microscopy. Journal of microscopy *228*, 390–405.

Nakamura, M., Ehrhardt, D. W. and Hashimoto, T. (2010). Microtubule and katanin-dependent dynamics of microtubule nucleation complexes in the acentrosomal Arabidopsis cortical array. Nature Cell Biology *12*, 1064.

Nan, X., Collisson, E. A., Lewis, S., Huang, J., Tamgüney, T. M., Liphardt, J. T., McCormick, F., Gray, J. W. and Chu, S. (2013). Single-molecule superresolution imaging allows quantitative analysis of RAF multimer formation and signaling. Proceedings of the National Academy of Sciences *110*, 18519–18524.

Nawrotek, A., Knossow, M. and Gigant, B. (2011). The determinants that govern microtubule assembly from the atomic structure of GTP-tubulin. Journal of molecular biology *412*, 35–42.

Nedelec, F. and Foethke, D. (2007). Collective Langevin dynamics of flexible cytoskeletal fibers. New J. Phys *9*, 427.

Nicholas, M. P., Berger, F., Rao, L., Brenner, S., Cho, C. and Gennerich, A. (2015a). Cytoplasmic dynein regulates its attachment to microtubules via nucleotide state-switched mechanosensing at multiple AAA domains. Proc. Natl. Acad. Sci. U.S.A. *112*, 6371–6376.

Nicholas, M. P., Berger, F., Rao, L., Brenner, S., Cho, C. and Gennerich, A. (2015b). Cytoplasmic dynein regulates its attachment to microtubules via nucleotide state-switched mechanosensing at multiple AAA domains. Proceedings of the National Academy of Sciences *112*, 6371–6376.

Ober, R. J., Ram, S. and Ward, E. S. (2004). Localization accuracy in single-molecule microscopy. Biophysical journal *86*, 1185–1200.

O'Brien, E. T., Voter, W. A. and Erickson, H. P. (1987). GTP hydrolysis during microtubule assembly. Biochemistry *26*, 4148–56.

Oda, Y. (2015). Cortical microtubule rearrangements and cell wall patterning. Front Plant Sci *6*, 236.

Odde, D. J., Cassimeris, L. and Buettner, H. M. (1995). Kinetics of microtubule catastrophe assessed by probabilistic analysis. Biophys J *69*, 796–802.

Ohba, T., Nakamura, M., Nishitani, H. and Nishimoto, T. (1999). Self-organization of microtubule asters induced in Xenopus egg extracts by GTP-bound Ran. Science *284*, 1356–1358.

Oiwa, K. and Sakakibara, H. (2005). Recent progress in dynein structure and mechanism. Curr. Opin. Cell Biol. *17*, 98–103.

Oosawa, F. (1970). Size distribution of protein polymers. Journal of theoretical biology *27*, 69–86.

Oosawa, F. (2000). The loose coupling mechanism in molecular machines of living cells. Genes to Cells *5*, 9–16.

Oosawa, F. and Hayashi, S. (1986). The loose coupling mechanism in molecular machines of living cells. Adv. Biophys. *22*, 151–183.

Palmer, R., Sullivan, D., Huffaker, T. and Koshland, D. (1992). Role of astral microtubules and actin in spindle orientation and migration in the budding yeast, Saccharomyces cerevisiae. The Journal of cell biology *119*, 583–593.

Pawley, J. (1995). Handbook of Biological Confocal Microscopy. Cognition and Language, Springer.

Pawley, J. (2010). Handbook of biological confocal microscopy. Springer Science & Business Media.

Pawley, J. B. (2006). Fundamental limits in confocal microscopy. In Handbook of biological confocal microscopy pp. 20–42. Springer.

Pecreaux, J., Roper, J. C., Kruse, K., Jülicher, F., Hyman, A. A., Grill, S. W. and Howard, J. (2006a). Spindle oscillations during asymmetric cell division require a threshold number of active cortical force generators. Curr. Biol. *16*, 2111–2122.

Pecreaux, J., Röper, J.-C., Kruse, K., Jülicher, F., Hyman, A. A., Grill, S. W. and Howard, J. (2006b). Spindle oscillations during asymmetric cell division require a threshold number of active cortical force generators. Current Biology *16*, 2111–2122.

Pfister, K. K., Fisher, E. M., Gibbons, I. R., Hays, T. S., Holzbaur, E. L., McIntosh, J. R., Porter, M. E., Schroer, T. A., Vaughan, K. T., Witman, G. B. et al. (2005). Cytoplasmic dynein nomenclature. The Journal of cell biology *171*, 411–413.

Prinz, H. (2002). Recent advances in the field of tubulin polymerization inhibitors. Expert Rev Anticancer Ther *2*, 695–708.

Qiu, W., Derr, N. D., Goodman, B. S., Villa, E., Wu, D., Shih, W. and Reck-Peterson, S. L. (2012). Dynein achieves processive motion using both stochastic and coordinated stepping. Nat. Struct. Mo. Biol. *19*, 193–200.

Rai, A. K., Rai, A., Ramaiya, A. J., Jha, R. and Mallik, R. (2013a). Molecular adaptations allow dynein to generate large collective forces inside cells. Cell *152*, 172–182.

Rai, A. K., Rai, A., Ramaiya, A. J., Jha, R. and Mallik, R. (2013b). Molecular adaptations allow dynein to generate large collective forces inside cells. Cell *152*, 172–182.

Rastogi, K., Puliyakodan, M. S., Pandey, V., Nath, S. and Elangovan, R. (2016). Maximum limit to the number of myosin II motors participating in processive sliding of actin. Sci Rep *6*, 32043.

Reck-Peterson, S. L., Yildiz, A., Carter, A. P., Gennerich, A., Zhang, N. and Vale, R. D. (2006a). Single-molecule analysis of dynein processivity and stepping behavior. Cell *126*, 335–348.

Reck-Peterson, S. L., Yildiz, A., Carter, A. P., Gennerich, A., Zhang, N. and Vale, R. D. (2006b). Single-molecule analysis of dynein processivity and stepping behavior. Cell *126*, 335–348.

Reid, T. A., Schuster, B. M., Mann, B. J., Balchand, S. K., Plooster, M., McClellan, M., Coombes, C. E., Wadsworth, P. and Gardner, M. K. (2016a). Suppression of microtubule assembly kinetics by the mitotic protein TPX2. J Cell Sci *129*, 1319–28.

Reid, T. A., Schuster, B. M., Mann, B. J., Balchand, S. K., Plooster, M., McClellan, M., Coombes, C. E., Wadsworth, P. and Gardner, M. K. (2016b). Suppression of microtubule assembly kinetics by the mitotic protein TPX2. J Cell Sci *129*, 1319–1328.

Roostalu, J., Cade, N. I. and Surrey, T. (2015). Complementary activities of TPX2 and chTOG constitute an efficient importin-regulated microtubule nucleation module. Nature cell biology *17*, 1422.

Ross, J. L., Shuman, H., Holzbaur, E. L. and Goldman, Y. E. (2008). Kinesin and dynein-dynactin at intersecting microtubules: motor density affects dynein function. Biophysical journal *94*, 3115–3125.

Ruhnow, F., Zwicker, D. and Diez, S. (2011). Tracking single particles and elongated filaments with nanometer precision. Biophys. J. *100*, 2820–2828.

Rusan, N. M., Serdar Tulu, U., Fagerstrom, C. and Wadsworth, P. (2002). Reorganization of the microtubule array in prophase/prometaphase requires cytoplasmic dynein-dependent microtubule transport. J. Cell Biol. *158*, 997–1003.

Sabareesan, A. T. and Udgaonkar, J. B. (2014). Amyloid fibril formation by the chain B subunit of monellin occurs by a nucleation-dependent polymerization mechanism. Biochemistry *53*, 1206–17.

Sato, M. K., Ishihara, T., Tanaka, H., Ishijima, A. and Inoue, Y. (2012). Velocity-dependent actomyosin ATPase cycle revealed by in vitro motility assay with kinetic analysis. Biophys. J. *103*, 711–718.

Saxton, M. J. (2007). A biological interpretation of transient anomalous subdiffusion. I. Qualitative model. Biophysical journal *92*, 1178–1191.

Saxton, M. J. (2008). A biological interpretation of transient anomalous subdiffusion. II. Reaction kinetics. Biophysical journal *94*, 760–771.

Scharrel, L., Ma, R., Schneider, R., Jülicher, F. and Diez, S. (2014). Multimotor transport in a system of active and inactive kinesin-1 motors. Biophys. J. *107*, 365–372.

Schek III, H. T., Gardner, M. K., Cheng, J., Odde, D. J. and Hunt, A. J. (2007). Microtubule assembly dynamics at the nanoscale. Current Biology *17*, 1445–1455.

Schilstra, M. J., Bayley, P. M. and Martin, S. R. (1991). The effect of solution composition on microtubule dynamic instability. Biochemical Journal *277*, 839–847.

Schneider, C., Rasband, W. and Eliceiri, K. (2012). NIH Image to ImageJ: 25 years of image analysis. Nat. Methods *9*, 671–675.

Schuh, M. and Ellenberg, J. (2007). Self-organization of MTOCs replaces centrosome function during acentrosomal spindle assembly in live mouse oocytes. Cell *130*, 484–498.

Seeger, M. A. and Rice, S. E. (2010). Microtubule-associated protein-like binding of the kinesin-1 tail to microtubules. Journal of Biological Chemistry *285*, 8155–8162.

Sen, K., Raha, D., Das, T. and Biswas, B. B. (1987). Purification and characterization of tubulin from mung bean (Vigna radiata). J. Biosci. *12*, 375–381.

Sept, D., Baker, N. A. and McCammon, J. A. (2003). The physical basis of microtubule structure and stability. Protein Sci *12*, 2257–61.

Shaner, N. C., Steinbach, P. A. and Tsien, R. Y. (2005). A guide to choosing fluorescent proteins. Nat. Methods *2*, 905–909.

Shaw, S. L., Yeh, E., Maddox, P., Salmon, E. D. and Bloom, K. (1997). Astral microtubule dynamics in yeast: A microtubule-based searching mechanism for spindle orientation and nuclear migration into the bud. J. Cell Biol. *139*, 985–994.

Shelanski, M. L., Gaskin, F. and Cantor, C. R. (1973). Microtubule assembly in the absence of added nucleotides. Proc Natl Acad Sci U S A *70*, 765–8.

Shima, T., Imamula, K., Kon, T., Ohkura, R. and Sutoh, K. (2006). Head-head coordination is required for the processive motion of cytoplasmic dynein, an AAA+ molecular motor. J. Struct. Biol. *156*, 182–189.

Shubeita, G. T., Tran, S. L., Xu, J., Vershinin, M., Cermelli, S., Cotton, S. L., Welte, M. A. and Gross, S. P. (2008). Consequences of motor copy number on the intracellular transport of kinesin-1-driven lipid droplets. Cell *135*, 1098–1107.

Simmonst, R., Finer, J., Warrick, H., Kralik, B., Chu, S. and Spudich, J. (1993). Force on single actin filaments in a motility assay measured with an optical trap. In Mechanism of Myofilament Sliding in Muscle Contraction pp. 331–337. Springer.

Smal, I., Loog, M., Niessen, W. and Meijering, E. (2009). Quantitative comparison of spot detection methods in fluorescence microscopy. IEEE transactions on medical imaging *29*, 282–301.

Soppina, V., Rai, A. K., Ramaiya, A. J., Barak, P. and Mallik, R. (2009). Tug-of-war between dissimilar teams of microtubule motors regulates transport and fission of endosomes. Proceedings of the National Academy of Sciences *106*, 19381–19386.

Stewart, R. J., Thaler, J. P. and Goldstein, L. (1993). Direction of microtubule movement is an intrinsic property of the motor domains of kinesin heavy chain and Drosophila ncd protein. Proceedings of the National Academy of Sciences *90*, 5209–5213.

Sutradhar, S., Yadav, V., Sridhar, S., Sreekumar, L., Bhattacharyya, D., Ghosh, S. K., Paul, R. and Sanyal, K. (2015). A comprehensive model to predict mitotic division in budding yeasts. Molecular biology of the cell *26*, 3954–3965.

Svoboda, A., Bahler, J. and Kohli, J. (1995). Microtubule-driven nuclear movements and linear elements as meiosis-specific characteristics of the fission yeasts Schizosaccharomyces versatilis and Schizosaccharomyces pombe. Chromosoma *104*, 203–214.

Svoboda, K. and Block, S. M. (1994a). Force and velocity measured for single kinesin molecules. Cell *77*, 773–784.

Svoboda, K. and Block, S. M. (1994b). Force and velocity measured for single kinesin molecules. Cell *77*, 773–784.

Swedlow, J. R., Hu, K., Andrews, P. D., Roos, D. S. and Murray, J. M. (2002a). Measuring tubulin content in Toxoplasma gondii: a comparison of laser-scanning confocal and wide-field fluorescence microscopy. Proc. Natl. Acad. Sci. U.S.A. *99*, 2014–2019.

Swedlow, J. R., Hu, K., Andrews, P. D., Roos, D. S. and Murray, J. M. (2002b). Measuring tubulin content in Toxoplasma gondii: a comparison of laser-scanning confocal and wide-field fluorescence microscopy. Proc. Natl. Acad. Sci. U.S.A. *99*, 2014–2019.

Tanenbaum, M. E., Macrek, L., Galjart, N. and Medema, R. H. (2008). Dynein, Lis1 and CLIP-170 counteract Eg5-dependent centrosome separation during bipolar spindle assembly. The EMBO journal *27*, 3235–3245.

Tanenbaum, M. E., Macrek, L., Janssen, A., Geers, E. F., Alvarez-Fernández, M. and Medema, R. H. (2009). Kif15 cooperates with eg5 to promote bipolar spindle assembly. Current biology *19*, 1703–1711.

Tanenbaum, M. E., Vale, R. D. and McKenney, R. J. (2013). Cytoplasmic dynein crosslinks and slides anti-parallel microtubules using its two motor domains. Elife *2*, e00943.

Tanimoto, H., Kimura, A. and Minc, N. (2016). Shape-motion relationships of centering microtubule asters. The Journal of Cell Biology *212*, 777–787.

Thawani, A., Kadzik, R. S. and Petry, S. (2018). XMAP215 is a microtubule nucleation factor that functions synergistically with the γ-tubulin ring complex. Nature cell biology *20*, 575.

Tindemans, S. H. and Mulder, B. M. (2010). Microtubule length distributions in the presence of protein-induced severing. Phys Rev E Stat Nonlin Soft Matter Phys *81*, 031910.

Tovey, C. A. and Conduit, P. T. (2018). Microtubule nucleation by γ-tubulin complexes and beyond. Essays in biochemistry *62*, 765–780.

Vancoillie, G., Lambert, J., Mulder, A., Koerten, H. K., Mommaas, A. M., Van Oostveldt, P. and Naeyaert, J.-M. (2000). Cytoplasmic dynein colocalizes with melanosomes in normal human melanocytes. British Journal of Dermatology *143*, 298–306.

Verde, F., Berrez, J.-M., Antony, C. and Karsenti, E. (1991). Taxol-induced microtubule asters in mitotic extracts of Xenopus eggs: requirement for phosphorylated factors and cytoplasmic dynein. The Journal of Cell Biology *112*, 1177–1187.

Verde, F., Dogterom, M., Stelzer, E., Karsenti, E. and Leibler, S. (1992). Control of microtubule dynamics and length by cyclin A- and cyclin B-dependent kinases in Xenopus egg extracts. J Cell Biol *118*, 1097–108.

Vogel, S. K., Pavin, N., Maghelli, N., Julicher, F. and Tolic-Norrelykke, I. M. (2009). Self-organization of dynein motors generates meiotic nuclear oscillations. PLoS Biol. *7*, e1000087.

Voter, W. A. and Erickson, H. P. (1984). The kinetics of microtubule assembly. Evidence for a two-stage nucleation mechanism. Journal of Biological Chemistry *259*, 10430–10438.

Walcott, S., Warshaw, D. M. and Debold, E. P. (2012). Mechanical coupling between myosin molecules causes differences between ensemble and single-molecule measurements. Biophys J *103*, 501–10.

Walczak, C. E. and Heald, R. (2008). Mechanisms of mitotic spindle assembly and function. In International review of cytology vol. 265, pp. 111–158. Elsevier.

Walczak, C. E., Vernos, I., Mitchison, T. J., Karsenti, E. and Heald, R. (1998). A model for the proposed roles of different microtubule-based motor proteins in establishing spindle bipolarity. Curr. Biol. *8*, 903–913.

Walker, R., O'brien, E., Pryer, N., Soboeiro, M., Voter, W., Erickson, H. and Salmon, E. (1988). Dynamic instability of individual microtubules analyzed by video light microscopy: rate constants and transition frequencies. The Journal of cell biology *107*, 1437–1448.

Waters, J. C. (2009). Accuracy and precision in quantitative fluorescence microscopy.

Waters, J. C. and Wittmann, T. (2014). Concepts in quantitative fluorescence microscopy. In Methods in cell biology vol. 123, pp. 1–18. Elsevier.

Weaver, L. N., Ems-McClung, S. C., Stout, J. R., LeBlanc, C., Shaw, S. L., Gardner, M. K. and Walczak, C. E. (2011). Kif18A uses a microtubule binding site in the tail for plus-end localization and spindle length regulation. Current Biology *21*, 1500–1506.

Wickstead, B. and Gull, K. (2007). Dyneins across eukaryotes: a comparative genomic analysis. Traffic *8*, 1708–1721.

Widlund, P. O., Podolski, M., Reber, S., Alper, J., Storch, M., Hyman, A. A., Howard, J. and Drechsel, D. N. (2012). One-step purification of assembly-competent tubulin from diverse eukaryotic sources. Mol Biol Cell *23*, 4393–401.

Wieczorek, M., Bechstedt, S., Chaaban, S. and Brouhard, G. J. (2015a). Microtubule-associated proteins control the kinetics of microtubule nucleation. Nat Cell Biol *17*, 907–16.

Wieczorek, M., Bechstedt, S., Chaaban, S. and Brouhard, G. J. (2015b). Microtubule-associated proteins control the kinetics of microtubule nucleation. Nature cell biology *17*, 907.

Wiese, C. and Zheng, Y. (2006). Microtubule nucleation: γ-tubulin and beyond. Journal of cell science *119*, 4143–4153.

Wightman, R., Chomicki, G., Kumar, M., Carr, P. and Turner, S. R. (2013). SPIRAL2 determines plant microtubule organization by modulating microtubule severing. Current Biology *23*, 1902–1907.

Wightman, R. and Turner, S. R. (2007). Severing at sites of microtubule crossover contributes to microtubule alignment in cortical arrays. The Plant Journal *52*, 742–751.

Witte, H., Neukirchen, D. and Bradke, F. (2008). Microtubule stabilization specifies initial neuronal polarization. J. Cell Biol. *180*, 619–632.

Wolf, D. E., Samarasekera, C. and Swedlow, J. R. (2007). Quantitative analysis of digital microscope images. Methods in cell biology *81*, 365–396.

Wollman, R., Cytrynbaum, E., Jones, J., Meyer, T., Scholey, J. and Mogilner, A. (2005). Efficient chromosome capture requires a bias in the 'search-and-capture'process during mitotic-spindle assembly. Current Biology *15*, 828–832.

Woodruff, J. B., Gomes, B. F., Widlund, P. O., Mahamid, J., Honigmann, A. and Hyman, A. A. (2017). The centrosome is a selective condensate that nucleates microtubules by concentrating tubulin. Cell *169*, 1066–1077.

Wu, J. Q. and Pollard, T. D. (2005). Counting cytokinesis proteins globally and locally in fission yeast. Science *310*, 310–314.

Wu, Q. F., Yang, L., Li, S., Wang, Q., Yuan, X. B., Gao, X., Bao, L. and Zhang, X. (2012). Fibroblast growth factor 13 is a microtubule-stabilizing protein regulating neuronal polarization and migration. Cell *149*, 1549–1564.

XU, C.-H., HUANG, S.-J. and YUAN, M. (2005). Dimethyl sulfoxide is feasible for plant tubulin assembly in vitro: A comprehensive analysis. Journal of Integrative Plant Biology *47*, 457–466.

Yamamoto, A., Tsutsumi, C., Kojima, H., Oiwa, K. and Hiraoka, Y. (2001a). Dynamic behavior of microtubules during dynein-dependent nuclear migrations of meiotic prophase in fission yeast. Mol. Biol. Cell *12*, 3933–3946.

Yamamoto, A., Tsutsumi, C., Kojima, H., Oiwa, K. and Hiraoka, Y. (2001b). Dynamic behavior of microtubules during dynein-dependent nuclear migrations of meiotic prophase in fission yeast. Molecular Biology of the Cell *12*, 3933–3946.

Yamamoto, A., West, R. R., McIntosh, J. R. and Hiraoka, Y. (1999). A cytoplasmic dynein heavy chain is required for oscillatory nuclear movement of meiotic prophase and efficient meiotic recombination in fission yeast. The Journal of cell biology *145*, 1233–1250.

Yi, P. and Goshima, G. (2018). Microtubule nucleation and organization without centrosomes. Curr Opin Plant Biol *46*, 1–7.

Yildiz, A. and Selvin, P. R. (2005). Fluorescence imaging with one nanometer accuracy: application to molecular motors. Accounts of chemical research *38*, 574–582.

Zhang, C., Hughes, M. and Clarke, P. R. (1999). Ran-GTP stabilises microtubule asters and inhibits nuclear assembly in Xenopus egg extracts. Journal of cell science *112*, 2453–2461.

Zhang, R., Roostalu, J., Surrey, T. and Nogales, E. (2017). Structural insight into TPX2-stimulated microtubule assembly. Elife *6*, e30959.

Appendix

Part A

Centrosomes nucleate microtubules actively to form asters in an *in vitro* reconstitution

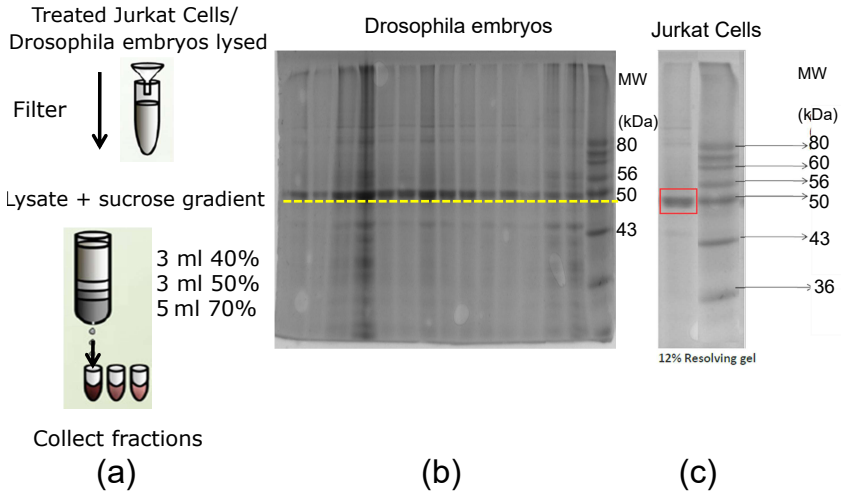

Figure A1: **Centrosome Isolation using sucrose gradients** (a) The schematic indicate the steps carried out to isolate centrosomes using Jurkat cell lysates and Drosophila embryos on a 40-70 % sucrose gradient. The two gel images indicate the purified centrosomal fraction from (b) Drosphila embryos and (c) Jurkat cell lystes on a 12 % SDS Page gel. MW indicates molecular weight of the ladder in kilo Dalton (kDa).

Centrosomes nucleate microtubules in higher eukaryotes and form complex radial structures- asters. Centrosomal proteins were purified on sucrose gradients from two different sources - Jurkat cells (T lymphoblastic cell lines) and *Drosophila* embryos

(Figure A1(a)).

A prominent band observed at 47 kDa, indicative of gamma tubulin (major centrosomal protein) confirms the presence of centrosomes in the purified fractions on a 12 % SDS-Page gel **(Figure A1(b)-(c))**. The band profile on the SDS Page gel is qualitatively comparable to the previous descriptions [Jakobsen et al., 2013; Moritz and Alberts, 1998]. Each of these fractions are tested for their activity to form asters by nucleating microtubules as described in the **Methods subsection 4.2.4**. Epifluorescence microscopy images of the asters confirms the activity of the centrosomes isolated from both the sources **(Figure A2(a)-(b))**. However, nucleation of microtubules from these fractions is inconsistent leading to a need for further optimizations.

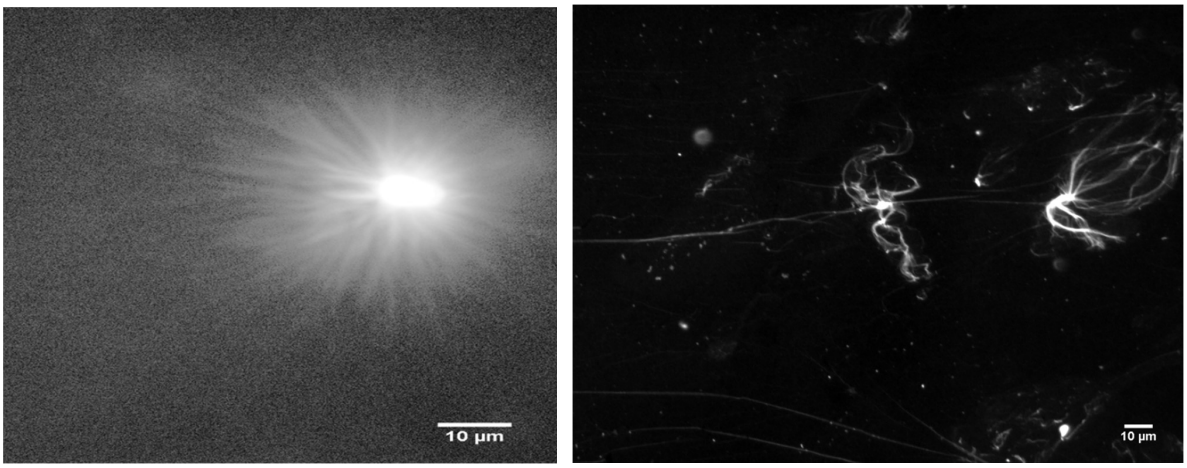

(a) (b)

Figure A2: **Nucleation of Centrosomes** Asters obtained from microtubules nucleated with (a) Jurkat cells and (b) Drosophila embryos in the presence of rhodamine labelled goat tubulin (1 μM) and unlabelled goat tubulin (20 μM) with 1 mM GTP. Scale: 10 μm

Part B

Estimating protein concentration of mung tubulin

The protein concentration was estimated by Bradford assay using two independent standard measurements. Absorbance measurements were made at 595 nm for a range of BSA concentrations and fit it to a straight line **(Figure A3)**. The concentration of the tubulin sample (mung) was then estimated to be 3.2 μM using the approximate molecular weight of the dimer to be 100,000 g/mol.

For comparison, the concentration was also estimated by absorbance measurements at 280 nm using molar extinction coefficients of α and β tubulin based on number of aromating amino acids. The number of aromatic amino acids in mung beta tubulin (accession number -A0A0L9T5L6) is 5 (tryptophan) and 16 (tyrosine). Based on this the molar extincion coefficient for beta tubulin is calculated to be 51,340 M^{-1} cm^{-1}. Similarly, the number of tryptophan (3) and tyrosine (18) residues for alpha tubulin sequence gives a molar extinction of 44,070 M^{-1} cm^{-1}. Using the averaged molar extinction coefficients for α and β mung tubulins, the estimated protein concentration for mung tubulin at 280 nm is 4.5 μM. This is close to the concentration obtained using Bradford assay (3.2 μM).
However, I have chosen to work with the concentration obtained using Bradford assay, as the absorbance at 280 nm might be influenced by the presence of nucleotides in the sample (GTP in this case).

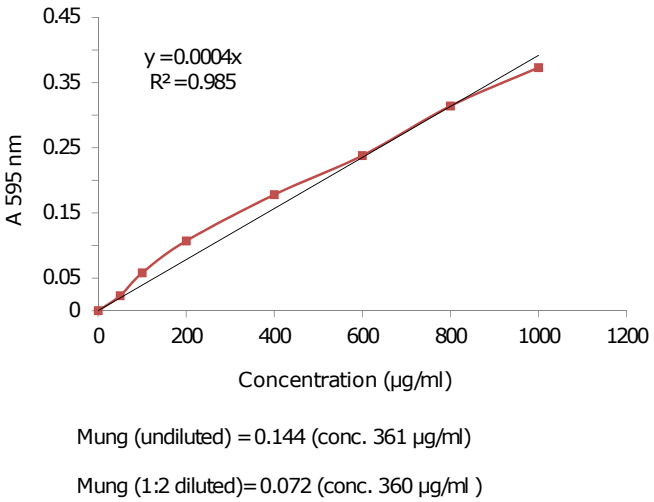

Figure A3: The figure represents the standard curve using BSA (brown line, 0-1000 μg/ml). The straight line fit is indicated with black line. The equation used to calculate the concentrations of the unknown protein is indicated in the legend.

Part C

Atomic force microscopy and aggregation of mung tubulin

The height profiles of the taxol stabilized mung filaments are as expected for micorutbules and are similar to the goat brain microtubules **(Figure A4)**. In the absence of GTP, the filamentous structures are not observed and passive aggregation is observed with pronounced heights **(Figure A5)**. This indicates that the filament assembly is activley driven in the presence of GTP. The kinetics measured at 340 nm show polymerization in the presence of GTP and $MgCl_2$ but not in the absence of GTP and $MgCl_2$ **(Figure A6)**. This further indicates that the sample contains tubulin which undergoes polymerization and it is not just passive aggregation.

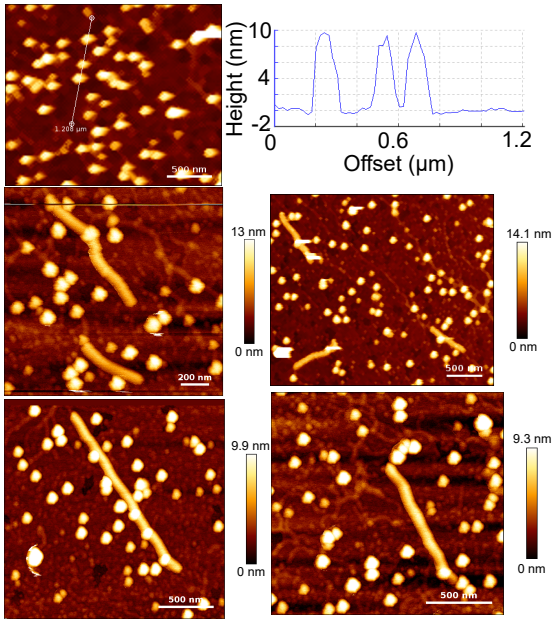

Figure A4: The images represent mung bean tubulin polymerized in the presence of GTP. The corresponding height profiles of the images are indicated by the bar on the right of each image. The height profiles for the topmost image is indicated across the line drawn on the image.

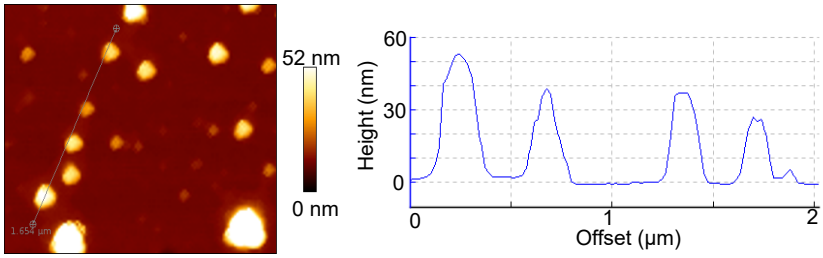

Figure A5: The image (left) represents aggregates of mung bean tubulin formed in the absence of GTP, with the bar indicating the height of the image. The height profile is indicated for the line selected in the image (image).

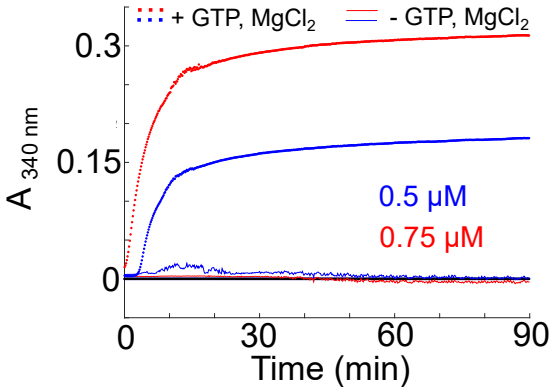

Figure A6: The figure represents the polymerization kinetics of mung tubulin measured at 340 nm in the presence (dots) and absence (solid line) of 2 mM $MgCl_2$, 1 mM GTP with 10 % glycerol. Tubulin concentration compared are 0.5 μM (red) and 0.75 μM (blue)

.

Soft Matter

Accepted Manuscript

This article can be cited before page numbers have been issued, to do this please use: K. Jain, N. Khetan and C. A. Athale, *Soft Matter*, 2019, DOI: 10.1039/C8SM01434E.

ROYAL SOCIETY OF CHEMISTRY

rsc.li/soft-matter-journal

View Article Online
DOI: 10.1039/C8SM01434E

Journal Name

ARTICLE TYPE

Cite this: DOI: 10.1039/xxxxxxxxxx

Collective effects of yeast cytoplasmic dynein based microtubule transport†

Kunalika Jain,[a] Neha Khetan,[a] and Chaitanya A. Athale*[a]

Received Date
Accepted Date

DOI: 10.1039/xxxxxxxxxx

www.rsc.org/journalname

Teams of cortically anchored dyneins pulling at microtubules (MTs) are known to be essential for aster, spindle and nuclear positioning during cell division and fertilization. While the single-molecule basis of dynein processivity is now better understood, the effect of increasing numbers of motors on transport is not clear. Here, we examine the collective transport properties of a *Saccharomyces cerevisiae* cytoplasmic dynein fragment, widely used as a minimal of model, by a combination of quantitative MT gliding assays and stochastic simulations. We find both MT lengths and motor densities qualitatively affect the degree of randomness of MT transport. However, directionality and velocity of MTs increase above a threshold number of motors (N) interacting with a filament. To better understand this behavior, we simulate a gliding assay based on a model of uniformly distributed immobilized motors transporting semi-flexible MTs. Each dynein dimer is modeled as an effective stochastic stepper with asymmetric force dependent detachment dynamics, based on single-molecule experiments. Simulations predict increasing numbers of motors (N) result in a threshold dependent transition in directionality and transport velocity and a monotonic decrease in effective diffusivity. Thus both experiment and theory show qualitative agreement in the emergence of coordination in transport above a threshold number of motor heads. We hypothesize that the phase-transition like property of this dynein could play a role *in vivo* during yeast mitosis, when this dynein localizes to the cortex and pulls astral MTs of increasing lengths, resulting in correct positioning and orientation of the nucleus at the bud-neck.

1 Introduction

Microtubule (MT) transport by molecular motors plays a vital role in regulating cell physiology and mechanics as seen in eukaryotic cell division[1,2], polarization[3] and migration[4]. While single-molecule *in vitro* assays have increasingly provided a detailed understanding of the mechanochemistry of kinesins[5–7] and dyneins[8–10], cellular processes typically involve multiple motors acting together. Transport processes involving many motors acting together have been well studied in vesicle transport where motors work in teams to carry cargoes on immobile filaments[11,12]. However, filament transport by immobilized motors, has also been reported in physiologically relevant processes such as such as spindle assembly[2,13,14], neuronal axon development[15,16], *Caenorhabditis elegans* fertilization[17,18], mouse oocyte maturation[19], nuclear oscillations in *Schizosaccharomyces pombe*[20–22] and mitotic nuclear positioning in *Saccharomyces cerevisiae*[23]. The regulation of the number of motors (N) transporting MTs and their localization result in spindle oscillations in *S. pombe*[22,24,25] and *C. elegans*[26]. Thus, understanding the effect numbers of motors (N) on collective transport properties could provide insights into MT transport *in vivo*.

Dyneins play an important role during the *in vivo* transport of filaments. However, they are relatively less well understood at a single molecule level compared to kinesins, due to their greater structural complexity[27]. One such well studied dynein is the highly processive yeast cytoplasmic non-essential dynein. At a single molecule level it has been shown to stochastically step backwards and forwards with variable step sizes ranging from 8 to 32 nm in the absence of load[9] and increasing in backward steps under load[28]. The processivity of the dimeric motor has been attributed to a lack of inter head co-ordination and asynchronous stepping when the two motor domains are close to each other[29,30], while coordinated stepping can arise with increasing inter-head separation through linker tension gated release of the motor from MTs[31]. Load sharing between the heads allows dynein to step processively even under large loads[32]. Additionally, single molecule detachment rates for this yeast dynein have asymmetric force dependence - assisting forces increase detachment, while hindering forces result in persistent binding[31,33].

[a] *Div. of Biology, IISER Pune, Dr. Homi Bhabha Road, Pune, India. Fax: 91 20 2025 1566; Tel: 91 20 2590 8050; E-mail: cathale@iiserpune.ac.in*

† Electronic Supplementary Information (ESI) available: [Section at the end of this file includes (1) Figures and (2) Videos]. See DOI: 10.1039/b000000x/

View Article Online
DOI: 10.1039/C8SM01434E

The effect of single-molecule dynamics on multi-molecular transport by teams of this dynein is not apparent from current theoretical models of collective transport that are based on 'loose coupling' of motors[34–36], fluctuation based load-sharing[37,38] and negative cooperativity of detachment[39,40]. A mathematical model specific to the yeast dynein would thus help better understand the *in vivo* role of this 'model' dynein.

The collective transport velocity of the yeast cytoplasmic dynein has been shown to be comparable to the single molecule velocity in experiments[9]. While a DNA-origami cargo has been used to precisely control the effect of increasing dynein team sizes on run lengths and times[41], it involved maximally 7 motors moving a cargo on static MTs. Studying the number dependence of MT transport by anchored motors over a wider range, could be more representative of the *in vivo* scenario during *S. cerevisiae* mitosis, where increasing lengths of astral MT are thought to 'glide' on cortically anchored dyneins, driving nuclear positioning[23,42–44]. At the same time, the astral MTs act as tracks transporting more dynein to the cortex, increasing the local density[45]. Thus, 'search and capture' of astral MTs in nuclear positioning involves changes in motor numbers and MT lengths. This suggests, a minimal system which quantitatively address the role of MT lengths and motor numbers, could improve our understanding of nuclear positioning *in vivo*.

Here, we use a combination of a quantitative gliding assay with a computational model of single motor mechanics to address the effect of statistics, i.e. motor numbers (N) of the widely used truncated fragment of the *S. cerevisiae* dynein on MT transport in four steps. (i) First, we quantify the motor density on the surface during a gliding assay. (ii) We then examine the effect of variations in filament length and motor density on MT transport velocity and directionality. We demonstrate that while both motor density and MT lengths affect velocity and directionality of filament transport, the effects can be best understood in terms of numbers of motors (N). (iii) In order to develop a quantitative understanding of the effect of motor numbers (N) on filament motility seen in experiments, we simulate a gliding assay based on a stochastic model of discrete, independent, immobilized, Hookean spring-like motors that bind to and transport semi-flexible MT filaments. The detachment of the motors from MTs is load-dependent and asymmetric for forward and backward loads. The stochastic motor stepping and attachment-detachment dynamics collectively give rise to MT transport velocity, diffusivity and directionality statistics that vary with MT lengths and motor densities. (iv) Finally, we compare MT transport diffusivity, velocity and directionality between experiment and theory and examine the effects of length, motor density and numbers of motors (N) that an MT encounters.

2 Model

2.1 Model of dynein driven collective MT transport

A gliding assay simulation was developed within the framework of a stochastic, discrete particle based simulator Cytosim, that has been extensively used to model collective cytoskeleton-motor mechanics[46–51]. In the simulation, motors are assumed to be immobilized on a surface by their stalks and the heads can bind MTs

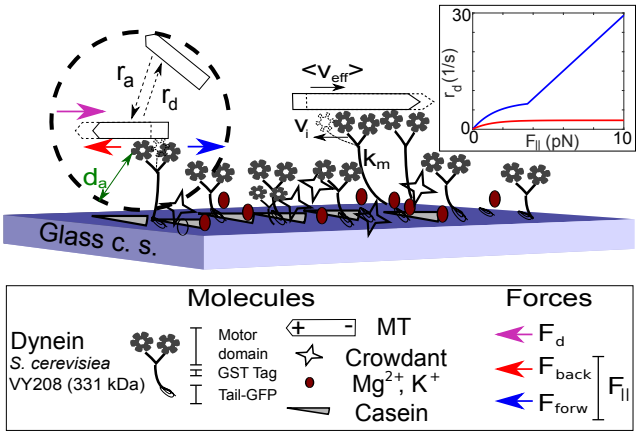

Fig. 1 Dynein collective transport. The molecular components of the *in vitro* reconstituted MT-transport by a truncated minimal form of the *S. cerevisiae* dynein motor on a glass coverslip (c.s.) surface in experiment are schematically represented. A stochastic mechanochemical model to represent key aspects of the system is developed, where motors attach to MTs at a rate r_a if they are within an attachment distance d_a, and detach at a rate r_d. Single motors step along the MT with an instantaneous velocity v_i and multiple motors transport MTs with an effective mean effective velocity $\langle v_{eff} \rangle$ (black arrows represent the direction of movement). A drag force F_d (magenta arrow) acts on the MTs due to their motion through the medium with viscosity η. The motors are modeled as Hookean springs with a stiffness k_m. Motor stepping along MTs produces a parallel force $F_{||}$ in forward (blue arrow) and backward (red arrow) directions, affecting the motor detachment rate (inset).

based on stochastic attachment-detachment kinetics. The average effective velocity of MT transport ($< v_{eff} >$) results from a combination of (i) attachment and detachment dynamics of individual motors, (ii) stochastic stepping of individual motors at a velocity v_i where i is the index of motors, (iii) the passive stretch force experienced by a static motor bound to a filament, due to the transport of the filament by other motors and (iv) the thermal and drag forces due to the medium (Figure 1).

2.2 Attachment-detachment kinetics

Free motors stochastically bind MTs within a distance of attachment, d_a if a random number is less than the probability of attachment given by the attachment rate, r_a (Figure 1). Motors that were already attached are tested for motor detachment by estimating the component of the force acting on the motor along the MT, i.e. the parallel component of the force, $F_{||}$ (Figure 2(a)). When the parallel force acts in the same direction as the direction of motor-motion, towards the minus-end of the MT, it is referred to as the forward force F_{forw} and backward force (F_{back}) when it acts opposite to the direction of motor-motion towards the plus-end of the MT, as previously described[31,33]. Based on measurements of the force-dependent detachment dynamics of individual yeast dynein motors[31,33], we have implemented a novel model parametrized from experiments where the rate of detachment (r_d) changes asymmetrically, depending on the direction of the load force. Thus, r_d with increasing load force has two different forms for forward and backward loads respectively. *(i)* For a backward load, detachment depends on a saturation function (Figure

View Article Online
DOI: 10.1039/C8SM01434E

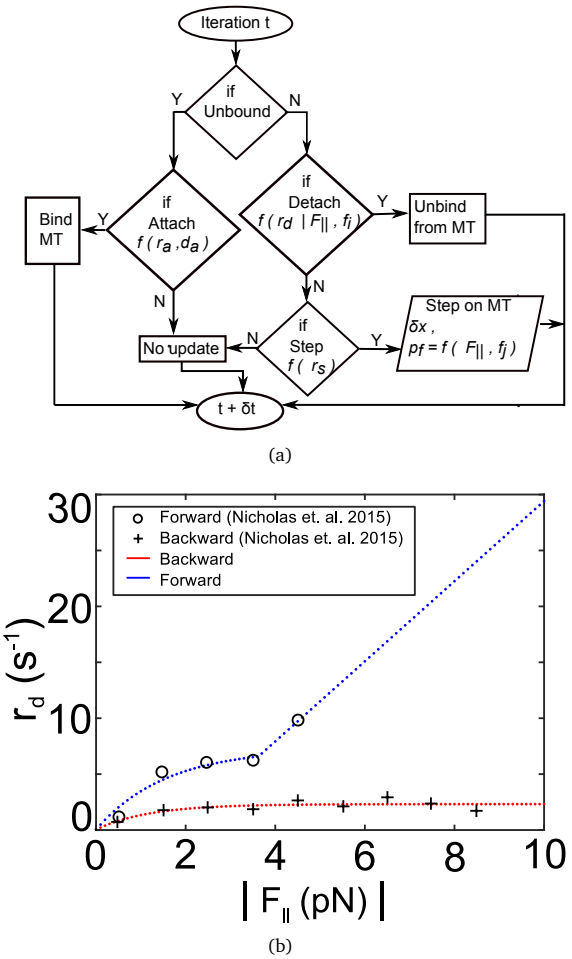

Fig. 2 Motor model. (a) The flow diagram represents the algorithmic sequence of the stochastic model of the motor. The model determines the attachment of free motors, detachment of bound motors, followed by stepping rate and step size. The model description includes detailed expressions for each of the variables. (b) The experimentally measured detachment rate (r_d) with an increase in the parallel load force ($F_{||}$) in forward (o) and backward (+) directions is taken from a previous single-molecule study on yeast dynein[33] and fit by custom functions (Equation 1), that depend on forward (blue) and backward (red) load forces.

2(b)), dependent on the magnitude of the parallel force, $|F_{||}|$, as:

$$r_d(F_{||}) = a + (b-a)\cdot e^{-c\cdot|F_{||}|} \tag{1}$$

with parameters a = 2.3159, b = 0.0400, c = 0.8414. *(ii)* The forward load dependence is determined by a piecewise function determined by a threshold force F_T = 3.51728 pN: below the threshold force ($0 < |F_{||}| < F_T$) detachment saturates according to Equation 1 with a = 7.2768, b = 0.0400, c = 0.6426 (R^2 = 0.90), and above the threshold ($|F_{||}| > F_T$) detachment is linear, $r_d(|F_{||}|) = m\cdot|F_{||}| + c'$, with m = 3.5814, c' = -6.4016 (R^2 = 1) as seen in Figure 2(b). A load free motor detaches according to a basal detachment rate (r_d^0).

2.3 Motor stepping

Motors are modeled to step stochastically, with the probability dependent on the rate of stepping and time interval

$$p_{step} = 1 - e^{-r_{step}\cdot\delta t} \tag{2}$$

where the stepping rate r_{step} is 8 s^{-1} taken from the wild-type yeast dynein construct[31] and δt is the time interval between simulation steps. The motor was simulated to take discrete steps of size δx, with the force-dependent step-sizes based on the predominant peak reported in experiments[9,28] as follows:

$$\delta x(t) = \begin{cases} 8 & \text{nm, if } F_{||} < F_s \\ 4 & \text{nm, if } F_{||} \geq F_s \end{cases} \tag{3}$$

where F_s is the stall force of the dynein motor and $F_{||}$ is the magnitude of the parallel force. The direction of stepping is stochastic and force dependent (both direction and magnitude), determined by probability of forward (p_f) and backward (p_b) stepping, where $p_b + p_f = 1$. The magnitude of the backward force (F_{back}) reduces the likelihood of forward stepping. We model it using multiple thresholds (f_1 to f_4) which are inferred from single molecule level force experiments with this yeast dynein[28] as follows:

$$p_f = \begin{cases} 0.80 & \text{if } F_{back} \leq f_1 \\ 0.74 & \text{if } f_1 < F_{back} \leq f_2 \\ 0.66 & \text{if } f_2 < F_{back} \leq f_3 \\ 0.60 & \text{if } f_3 < F_{back} \leq f_4 \\ 0.48 & \text{if } f_4 < F_{back} < F_s \\ 0.25 & \text{if } F_{back} \geq F_s \end{cases} \tag{4}$$

where f_1 = 0 pN, f_2 = 1 pN, f_3 = 3 pN and f_4 = 4 pN.

Thus, the detachment and stepping behavior of the simulated motors depend on the magnitude and direction of load forces acting on the motors along the MT ($F_{||}$) to which they are bound (Figure 2(b)), resulting in mechanical coupling during collective transport.

Filament transport

The transport of filaments is modeled by numerical integration of a constrained Langevin equation as previously described[47,57] and briefly summarized here. Filaments are divided into i points separated by rigid segments of 0.5 μm (smaller by orders of magnitude than the persistence length). The net force acting on a single MT is calculated by summing all points of each filament and solving a Langevin equation of motion with deterministic and stochastic components to determine the position ($\vec{x}$) based on:

$$d\vec{x} = \mu_i \cdot F(\vec{x},t)\cdot dt + dB_i(t) \tag{5}$$

where the deterministic terms are μ_i: the mobility constant of the i^{th} point and $F(\vec{x},t)$: the matrix of forces acting on every point at time t. The stochastic term is represented by dB_i resulting from random Brownian motion. The mobility (μ) is calculated for a whole filament based on the drag force (F_d) assuming a cylindrical geometry and simplifying the drag term as an average

View Article Online
DOI: 10.1039/C8SM01434E

Symbol	Parameter	Value	Reference
MT and motor mechanics			
κ	MT bending modulus	$2 \times 10^{-23}\ N \cdot m^2$	52
δ	MT diameter	25×10^{-9} m	53
k_m	Motor stiffness	2×10^{-4} N/m	This study
d_a	Attachment distance	2×10^{-8} m	51
r_a	Attachment rate	$5\ s^{-1}$	54
r_d^0	Basal detachment rate	$0.04\ s^{-1}$	9
v_0	Basal motor velocity	1.02×10^{-7} m/s	9
F_s	Stall force	4.8×10^{-12} N	28 55
ρ_m	Motor density	10^{-1} to 10^2 motors/μm^{-2}	This study
Simulation parameters			
δt	Simulation time step	0.01 s	This study
L_{box}	Simulation box length	50 μm	This study
$k_B \cdot T$	Thermal energy	$4.07 \times 10^{-21}\ N \cdot m$	-
η	Viscosity (10 % glycerol)	$1.3 \times 10^{-3}\ Pa \cdot s$	56

Table 1 Simulation parameters of MTs, dynein and the environment.

between the longitudinal and transverse components (a two-fold difference) and is given by:

$$\mu = \log(L/\delta)/3 \cdot \pi \cdot \eta \cdot L \tag{6}$$

where L is the MT length, δ is the diameter of the rod and η is the viscosity of the fluid and the mobility of each point in a filament is approximated as $\mu_i = \mu/p$ for p points per filament. The Brownian term $dB_i = \beta \cdot \theta$, with θ, a uniform random number between 0 and 1 and the diffusive step size is $\beta = \sqrt{2D\tau}$, where D is the diffusion coefficient and τ the time step of integration. The value of D is determined by the Stokes-Einstein relation as $D = \mu_i k_B T$.

The parameters of the system are taken from experimental reports and in the case of motor density varied over a range (Table 1).

3 Experimental Procedures

3.1 Dynein purification and MT filament polymerization

The truncated minimal dynein construct (331 kDa) from the *S. cerevisiae* VY208 strain, was purified as previously described[9] by growth, lysis and affinity purification with IgG beads, released using a TEV protease cleavage of the ZZ-tag and flash frozen at -80^{o}C. The ATPase activity of dynein was assayed in the presence of 1 mM Mg-ATP and 15 μM of pre-assembled goat brain MTs based on malachite green absorbance at 660 nm, as previously described[58]. To obtain fluorescently labelled microtubule filaments rhodamine-labelled bovine (0.8 μg/μl) and unlabelled porcine tubulin (3.3 μg/μl) (Cytoskeleton Inc., Denver, USA) were incubated in BRB80 buffer (80 mM PIPES, 1 mM $MgCl_2$, 1 mM EGTA) at 37^{o}C for 15 minutes followed by adding 20 μM taxol containing BRB80.

3.2 Gliding assay

Double-backed tape based flow chambers were prepared similar to those described previously[59] to create a chamber with a volume of $\approx$ 16 μl using glass slides and 22 x 22 mm coverslips (Micro Aid, Pune, India) that were cleaned with acteone, ethanol, water, KOH and water. Motors were perfused (50 μl of 0.06 μg/ml dynein) through one end of the chamber in lots $\sim$15 μl each, incubated for 5 minutes at room temperature. Blocking solution containing 0.5 mg/ml BSA (Sigma Aldrich, Mumbai, India) was flowed in, followed by the addition of 10 μl of MT filaments (labelled, taxol-stabilized) and the slide incubated for 5 minutes. A wash buffer (also used as lysis buffer- 30 mM HEPES (pH 7.2), 50 mM potassium acetate, 2 mM magnesium acetate, 1 mM EGTA, 10% glycerol, 1 mM DTT, 1 mg/ml casein) was used to remove unbound motors and MTs. Motility buffer (wash buffer supplemented with 1 mM ATP) with 1x Anti-fade (Cytoskeleton Inc., USA) was perfused to observe MT gliding. For the low density experiments, before adding motors, anti-GFP antibody (0.2 μg /μl) (Sigma Aldrich, Mumbai, India) was perfused through one end of the flow chamber and incubated for 5 mins followed by the addition of blocking solution, motors, MTs, wash- and motility-buffer, as described above. The flow chamber was then imaged on an upright microscope.

3.3 Microscopy

The samples were imaged at room temperature ($\approx$ 22°C) using a fluorescent upright microscope, Zeiss Axio Imager Z1 (Carl Zeiss, Germany) with an EC Plan-Neofluar 40x (NA - 0.75) lens, a mercury short arc lamp (X-Cite Series 120, Lumen Dynamics Inc., Canada) and filter sets for rhodamine (520 nm/540 nm excitation and 580 nm/600 nm emission). Images were acquired every second for 10 to 20 minutes using the Zeiss AxioCam MRm digital camera (Carl Zeiss, Germany) with exposure time of 0.7 s.

3.4 Calibrating motor density

Motor densities were estimated as illustrated schematically (Figure 3(a)), similar to previous reports[60 61], based on the following three steps: *(i)* The image volume (V_{img}) was estimated by treating the image as a rectangular cuboid, as a result of which $V_{img} = A_{img} \times h$, with A_{img}: area of the rectangular image, h: height of the image. The area was estimated from x- and y-size of the image (1388 x 1040 pixels) scaled to length units (1 pixel = 0.154 μm) resulting in $A_{img} = 3.4234 \times 10^4\ \mu m^2$. The height h was estimated from the point spread function (PSF) was estimated by analyzing the intensity profile of a z-stack of images of 200

View Article Online
DOI: 10.1039/C8SM01434E

nm diameter FITC labelled fluorescent beads (Invitrogen, ThermoFisher Scientific) and fitting the intensity profile as a function of z-position to a Gaussian (Figure 3(b)) using the *CurveFitter* tool in ImageJ[62] based on the equation:

$$y = a + (b - a) \cdot e^{[(x-\mu)^2]/[2\cdot\sigma^2]} \quad (7)$$

where a and b are scaling factors (a: background grey-value intensity in the image, b: grey-value estimate of the brightest part of the bead), μ is the mean and σ is the standard deviation. By approximating the PSF by the full width at half maximum (FWHM) which is $\approx 2.3548\sigma$[63], we obtain a z-height of 1.77 μm. The resulting V_{img} was 6.02×10^4 μm^3. *(ii)* In a second step, a concentration series of affinity purified 6x-His-tagged EGFP was imaged in the flow chamber and the image intensity corresponding to the concentration series was plotted against the number of EGFP molecules in the image volume (N_{EGFP}) and fit to a straight line (Figure 3(b)). The number of molecules of EGFP were calculated as $N_{EGFP} = (c \times V_{img})/m_{EGFP}$, where c: concentration in grams per ml, V_{img}: volume in ml and m_{EGFP}: molecular mass of EGFP in grams. The image-intensity of the GFP-dynein samples (low and high density), was used to estimate the corresponding N_{EGFP} equivalents (x-axis value) from the fit (Figure 3(b)). To account for the 2-fold brightness of EGFP compared to GFP[64], the N_{EGFP} equivalents were doubled, to obtain the number of dynein molecules in an image (N_{dyn}). *(iii)* The estimated dynein number is assumed to be localized to a plane, since multiple washout steps were designed to avoid bulk dynein resulting in an estimated 2D density is $\rho_{2D} = N_{dyn}/A_{img}$. Assuming a homogeneous distribution of the motors, the linear density of motors $\rho_{1D} = \sqrt{\rho_{2D}}$. The mean number of motors (N) expected to interact with a microtubule of length L can then be estimated as $N = \rho_{1D} \times L$. The number of dimers (N_{dimers}) are then simply N/2. Unless explicitly stated, N refers to individual motors from experiment in the remainder of the text, i.e. heads or GFP-equivalents. This approach of estimating numbers of motors is similar to previous reports[65–67].

3.5 Image and data analysis

Image time series of gliding assays were preprocessed by median filtering using ImageJ ver.1.45s[62] and tracked using a filament tracking tool FIESTA ver.1.04 reported previously[68] in MATLAB R2015b (Mathworks Inc., USA) on a Linux platform. The maximal connecting velocity was set to 1 $\mu m/s$ and FWHM to 500 nm. Only filaments that persisted for 10 or more frames and a permitted angular deviation between successive frames of 1 to 5 degrees were processed. To ensure filaments of constant length were analyzed, the frequency distribution of the change in MT filament lengths over time (dL/dt) were fit to a Gaussian to estimate the standard deviation, σ, as a cutoff of change of lengths in further analysis (Figure S1). The analyses of motility statistics are based on the trajectories of plus-end tips of the filaments, unless otherwise specified.

The gliding velocity of MT filaments, (vector, v_{eff}) (Figure 5) was estimated from the magnitude of the vector representing the instantaneous displacement of filament tips at each successive time point as a function of the time interval[68]. Mean $\langle v_{eff} \rangle$ was

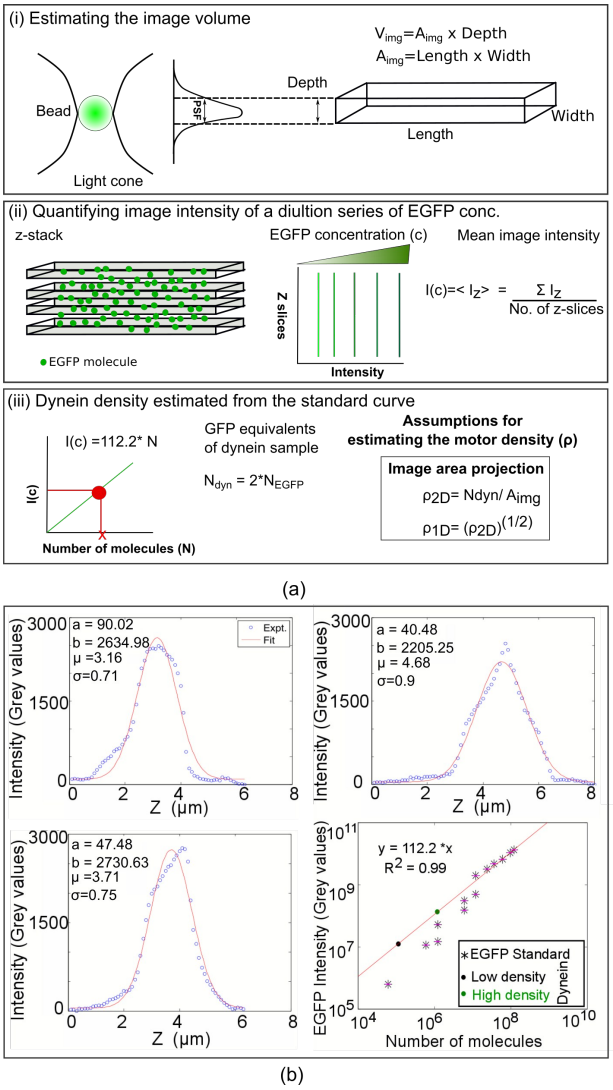

Fig. 3 Estimating dynein density. (a) The three steps to motor density estimation were: (i) image volume estimation, (ii) measuring the image intensities of a dilution series of EGFP solutions and (iii) using the standard curve to quantify dynein numbers. The surface density (ρ_{2D}) is then estimated from the image area area. (b) Three representative graphs of the z-profiles of the fluorescence intensity of 0.2 μm fluorescent beads (blue circles) were fit to a gaussian profile (red line) based on Equation 7, and used to estimate the PSF. The standard-curve of total EGFP fluorescence (mean *, ±s.d. magenta, n=3) from an image (y-axis) as a function of number of molecules (x-axis) is used to estimate the number of GFP-dynein molecules on the surface. Slope of the linear fit: 112.7 ± 6 based on 95% confidence interval (Table S1).

obtained from binning MT lengths every 1 μm.

The measure of directionality of motility (χ) from experiment and simulation was calculated from individual trajectories as the ratio of the magnitude of start to end displacement to the path length of a trajectory as previously described[69]. To avoid sampling static filaments, trajectories with displacements less than a cutoff distance of 1 pixel (154 nm) were ignored. To improve our statistics, trajectories of motile filaments which were static between successive frames, were linearly interpolated, until the filament moved a distance greater than the cutoff. Mean direc-

View Article Online
DOI: 10.1039/C8SM01434E

tionality was estimated for bin-width of MT lengths of 1 μm and reported for that average length. To obtain a χ value as a function of motors, the same approach was taken as before (product of mean linear density and length).

All further data analysis was performed using MATLAB R2014b (Mathworks Inc., USA).

3.6 MSD and diffusivity analysis

The mean square displacement (MSD) is calculated from the 2D positional coordinate of the filament ($\mathbf{r}$) as previously described[51,69,70] for increasing each time interval (δt) and averaged based on the expression:

$$MSD(\delta t) = \frac{1}{N}\Sigma[\mathbf{r}(t) - \mathbf{r}(t+\delta t)]^2_{t\leq 3T/4} \quad (8)$$

where t is the time point, T is the total time and N is the total number of displacements in a time interval. The analysis used $\delta t \leq 0.75 \times T$, based on previous reports for improved statistics[70,71]. If the net displacement of a trajectory was 154 nm or less (equivalent to a pixel in these experiments), those trajectories were ignored, assuming the filament did not move.

Experimental MSD profiles were averaged by pooling length classes ranging from 0.5 to 12.5 μm in bins of 3 μm with the mean of that bin representative of the length (Figure 6). Both experiment and simulation data were fit to two models of effective diffusion: *(a)* anomalous diffusion and *(b)* diffusion with transport. The anomalous diffusion model allows us to test whether MT length or density resulted in any deviation from diffusive behaviour (super- or sub-diffusive)[51,72,73], while the transport velocity can be extracted from the diffusion-transport model[69,70,74]. The *(a)* anomalous diffusion model is:

$$MSD = 4 \cdot D^{'} \cdot t^{\alpha} + c_1 \quad (9)$$

where $D^{'}$ is the anomalous diffusion coefficient, t is time, α is the anomaly parameter and c_1 is the error in detection. The *(b)* diffusion with transport model is:

$$MSD = 4 \cdot D_{eff} \cdot t + (v \cdot t)^2 + c_2 \quad (10)$$

where D_{eff} is the effective diffusion coefficient, t is time, v is the transport velocity and c_2 is the error in detection.

Simulations

2D simulations were performed using Cytosim[47], an agent-based simulation engine written in C++. MT and motor dynamics and mechanics were modeled as before[48,51,69] in a square simulation box of length L_{box} with periodic boundary conditions. The integration time was chosen to be smaller than the fastest time-scale. The system consists of MT filaments of a fixed length (L) and a fixed number of motors determined by the density (ρ_{2D}). Both filaments and motors were randomly distributed in simulation space at the time of initialization.

4 Results and Discussion

4.1 Estimating the density of dynein in a gliding assay

We have used a quantitative gliding assay to examine whether increasing numbers of dynein motors interfere or 'co-operate' with one another in collective transport. The truncated minimal *S. cerevisiae* cytoplasmic non-essential dynein (Dyn 331 kDa) described previously[9,30,41], was surface immobilized and image time-series of the transport of rhodamine-labelled MT filaments were acquired in epifluorescence microscopy. To understand the dependence of transport on the motor numbers, two variables were analyzed: (a) the motor density and (b) MT lengths. The motor density was estimated using calibrated epifluorescence microscopy as described in the Experimental Procedures and in Figure 3(a). The z-profile of sub-micron fluorescent beads was used to estimate the point spread function, PSF (Figure 3(b)) and arrive at the volume of the image cuboid (Figure 3(a))in order to convert from EGFP concentration to molecules in an image. The resulting calibration curve of intensity with EGFP molecules was used to estimate a dynein density of 6.8 motors/μm^2 and 72.4 motors/μm^2 for the low- and high-density experiments respectively (Figure 3(b)). Using a 95% confidence interval, we infer a maximal error of 10% in 2D and 4% in 1D density estimates (Table S1), which translates to an uncertainty of $\pm$0.04 motors/μm of MT lengths. MT lengths were estimated using nanometer-precision single filament tracking.

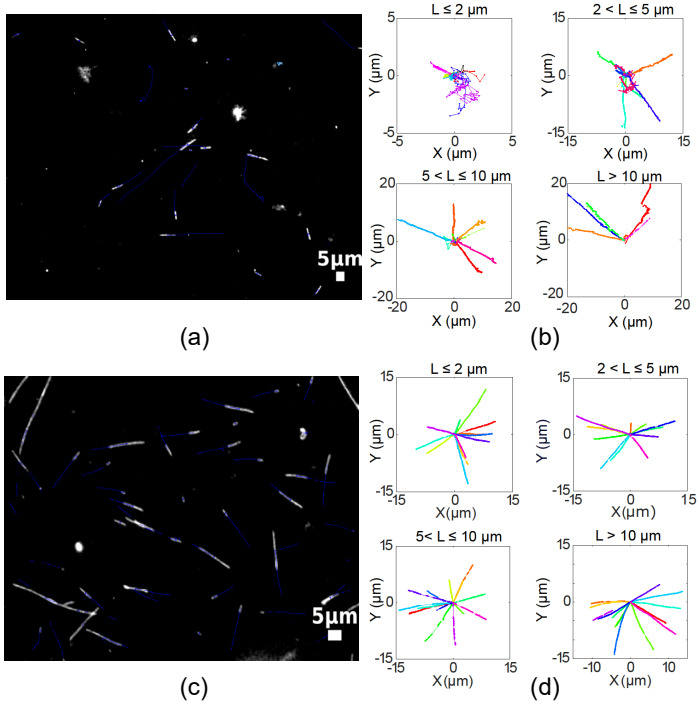

Fig. 4 Length dependence of MT transport. Representative time-series of rhodamine-labelled MTs (grey-scale) gliding in presence of dyneins of densities (a) 6.8 and (c) 72.4 motors/μm^2 are overlaid with tracks of the centroids (blue). XY trajectories of plus tips of filaments transported by motors of density (b) 6.8 and (d) 72.4 motors/μm^2 are plotted for increasing MT lengths. For clarity between 5 and 15 trajectories are plotted per length and density class. Representative time-series are seen in Video SV2(a) ($\rho_{2D} = 6.8$ motors/μm^2) and (b) ($\rho_{2D} = 72.4$ motors/μm^2).

View Article Online
DOI: 10.1039/C8SM01434E

Motor densities on surfaces of gliding assay have in the past been estimated by washing out the flow chamber and SDS-PAGE based protein estimation[67,75]. However, the indirect nature of the method and potential losses suggest a more direct approach could improve the reliability of the estimation. Our use of EGFP dilution series as a a calibration standard to estimate protein concentration using epifluorescence microscopy is comparable to previously reported methods using fluorescently tagged proteins to estimate *in vivo* protein copy numbers[60,61]. Indeed the advantages of wide field microscopy over confocal microscopy for such copy-number estimations have been discussed in literature[60].

4.2 Motor density and MT length both affect MT transport

At a low motor density (Figure 4(a)) the XY trajectories of MT tips appeared random for short filaments ($< L > \leq 5\ \mu$m) as compared to long ($< L >> 5\ \mu$m) (Figure 4(b)). In contrast, in presence of a high-density of motors (Figure 4(c)), filament transport appeared to be directionally persistent, independent of length (Figure 4(d)).

By combining dynein density and MT length measurements, we find qualitative differences in MT tip tracks at a low density of motors (Video SV1(a)). Short MTs of mean length 0.68 μm, swivel and diffuse away in a few frames, when they are expected to encounter 1 to 2 motors (Figure S2(a)). Intermediate lengths (∼3 μm) of filaments are transported with intermittent changes in direction, when interacting with ∼7 motors (Figure S2(b)) and are directionally persistent when interacting with ∼10 motors (Figure S2(b)). Thus, based on our density estimates, we find the transition of MT transport from diffusion and swiveling to transport occurs when filaments interact with 2 or more motors on average, consistent with literature on collective motor transport[76,77]. In contrast, filaments expected to encounter 5 to 6 motors due to a higher motor density, but with the same lengths, are transported in a persistent and directional manner (Video SV1(b), Figure S2(b)). Also, even when similar numbers of motors (5 to 7) are expected to interact with MTs at a low motor density (Figure S2), the MT motility appears to qualitatively different from high density. This appears to suggests that along with N-dependence of MT transport, subtle effects of motor density may also play a role. The observed rapid unbinding of MTs for estimates of 1 to 2 motors and the change to processive transport at higher N serves to validate our motor density estimate.

Since a low density of motors shows qualitative changes in transport with length, we quantified the mean gliding velocity ($\langle v_{eff} \rangle$) of MT motility with increasing numbers of motors (Figure 5), obtained from binning every 1 μm filament and the mean linear motor density (ρ_{1D}). Interestingly, we find the $\langle v_{eff} \rangle$ increases five-fold when the ∼8-10 motors are encountered. This threshold could be smaller, based on the assumptions inherent in the motor number estimation and the expectation that the number of bound motors will always be lower than those encountered, as seen in simulations (Figure S3). Additionally, the mean velocity of MTs for a saturating number of motors encountered is ∼40 nm/s, in qualitative agreement with the reported velocity of 41 nm/s of yeast spindle translocation during mitosis[78]. Since the transition in velocity appears to coincide with a transition from random to vectorial transport, we proceeded to quantify diffusion and transport velocity statistics of filaments based on mean square displacement (MSD) estimation.

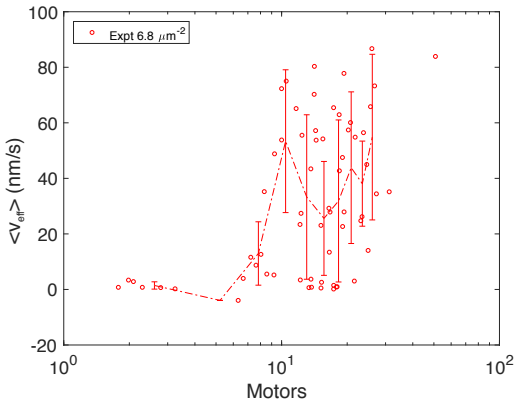

Fig. 5 Effect of motor numbers on gliding velocity. The mean gliding velocity of filaments, $\langle v_{eff} \rangle$ (red circles), from experiments is plotted as a function of the mean number of motors (N). The motor density is 6.8 motors/μm^2. The dashed line connected binned averages with error bars indicating standard deviations.

4.3 Motor number dependence of diffusion and transport velocity

We analyzed MSD statistics to understand the transition from short filaments undergoing a mixture of 'stop-and-go' and swivelling to directed transport of long filaments. By sampling only those filaments in the plane of imaging, we ignore free diffusion of MTs. An ensemble average MSD for binned mean lengths appears to confirm our impression of a transition from apparently diffusive to directed transport (Figure 6). We fit the MSD profiles with two models: (i) a phenomenological anomalous diffusion model (Equation 9) with the anomaly parameter α used to distinguish between diffusive, super- and sub-diffusive motility and (ii) a diffusion with transport model (Equation 10) to quantify the random and directed components of the motility. We find trajectories of short filaments of less than 5 μm in length with low motor density deviate from both model fits, potentially due to a greater heterogeneity in MT motility. Such filaments, even when bound to just 1 or 2 motors, are expected to undergo frequent changes in direction and swivel, as reported for kinesin gliding assays[79]. The anomaly parameter obtained from fitting the phenomenological model is $\alpha \sim 1.5$ and greater for all trajectories irrespective of length and motor density, indicative of super-diffusive motility[51].

The fit parameters of the diffusion and transport model to experimental data, D_{eff} and v, both show a scatter that is higher for short filaments at low density (Figure S4(a), (b)). The spread in experimental D_{eff} appears to decrease with increasing motors, consistent with the higher variability expected from 'stop-and-go' and occasional swivelling of MTs. The nearly immobile filaments ($D_{eff} < 10^{-6}\ \mu$m^2/s) are ignored in this analysis, assuming these to be artefacts due to MTs binding inactive or mis-oriented motors[77]. Thus the trend in effective diffusion from experiments

View Article Online
DOI: 10.1039/C8SM01434E

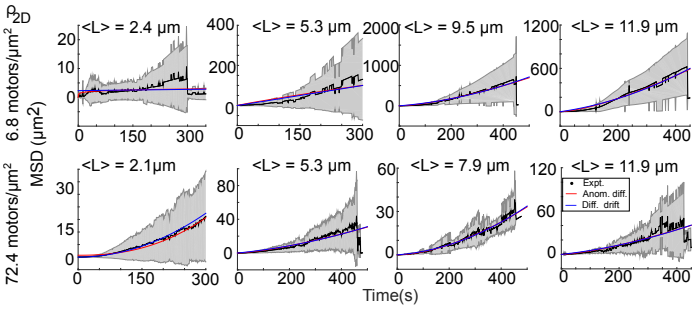

(a)

Fig. 6 Mean square displacement (MSD) of filament transport. (a) The MSD as a function of time (black) for increasing MT filament lengths (L) ranging between 1.46 to 15.5 μm are plotted. The motor density (ρ_{2D}) is 6.8 (upper panel) and 72.4 motors/μm^2 (lower panel). Data was fit to two models: anomalous diffusion (red, Equation 9) and diffusion with transport (blue, Equation 10). Grey region: standard deviation.

with ρ_{2D} of 6.8 and 72.4 motors/μm^2 qualitatively matches the comparable simulations densities of 10^1 and 10^2 motors/μm^2 (Figure S4(a)). Our observations of the reduction in mean D_{eff} with the number of motors (1/N dependence) resembles the inverse length dependence, $1/L$ of diffusivity of MTs transported by kinesins reported previously[76]. This suggests the motor-number dependence of randomness in collective MT transport might be similar for kinesin and dynein.

The transport velocity as a function of motors obtained from fits to experimental MSD, increases from close to zero to 80 nm/s and the low density experiments appear to approximately follow the trend of simulations, increasing with N (Figure S4(b)). Short filaments of lengths $\leq 1\mu$m undergo rapid binding-unbinding motion, filaments with lengths of $\sim$ 2 to 5 μm move with frequent changes in direction and longer filaments ($\geq$ 5 μm) are transported in a directionally persistent manner (Figure S2(a) and S2(b) and Video SV1(a)). Simulations suggest such an effect arises from a combination of effects namely the 2D 'search' by MTs for motors that depends on motor density and increased coordination of multiple motors. However, at a high density the independence of velocity with motor numbers could be explained by saturation effects. The quantitatively lower velocity obtained from experiments as compared to simulations, at high motor densities, could result from crowding effects, as reported previously for kinesin[74]. Such effects are not observed in simulations, since the model does not invoke crowding effects, for simplicity.

Statistical uncertainty in estimating D_{eff} and v from MSD fits, suggests the need for alternative measures of directionally persistent motion. We therefore use a simpler and more robust measure of directionality χ, that is independent of any fitting[51,69] as described in the methods section. We find the mean directionality (χ) is length dependent for low motor densities but not for high density with a four-fold change in χ seen when MT lengths increase from 3 to 4 μm at low motor densities (Figure 7(a)). Interestingly, motility changes quantified by χ correspond to three qualitative modes of filament transport for increasing lengths at low motor densities: (a) swivelling by short filaments ($\approx$1 μm) when 1-2 motors are expected to interact, (b) transport and intermittent changes in direction of intermediate lengths ($\approx$3 μm), when interacting with $\sim$7 motors and (c) directionally persistent transport of long filaments (>5 μm), when interacting with $\sim$10 motors (Figure 7(b)). When we combine this data from different motor densities and MT lengths, in terms of expected number of motors interacting with a filament, we find all the data falls onto a trend of increase and saturation of χ above a threshold of 8 to 10 motors (Figure 7(c)). This motor number threshold above which transport becomes directionally persistent is based on the expected number of motors a filament encounters, while binding-unbinding kinetics would result in a lower number of bound motors, as predicted in simulations (Figure S3). Hence, we proceed to test whether a model of yeast single-molecule dynamics can reproduce our experimental measure of directionality in collective transport.

4.4 Model predictions of coordinated transport

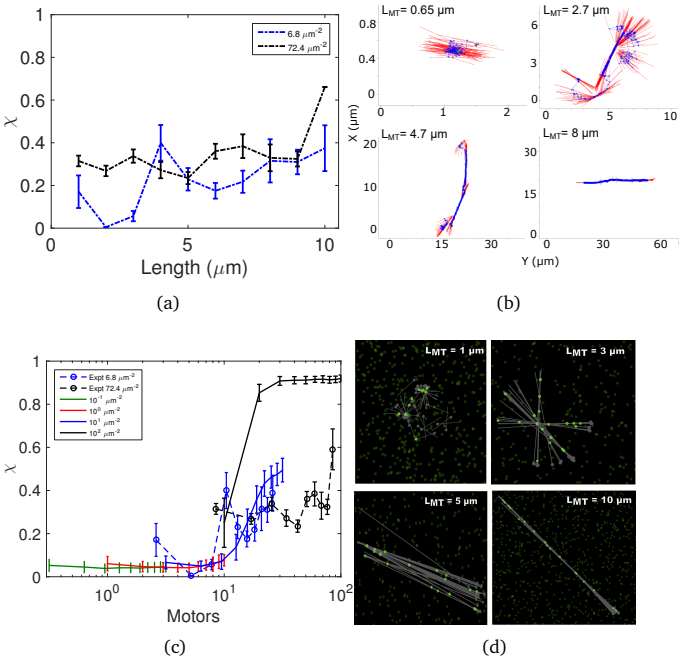

(a) (b) (c) (d)

Fig. 7 Length and motor-dependence of MT transport directionality in experiment and simulation. (a) The mean directionality, χ ($\pm$s.e.) of MT transport is plotted as a function of length in presence of two different motor densities (colors) from experiments. (b) Representative time-projections of filament contours (red lines) are overlaid with trajectories of centroids (blue *) from experiments for a low density of motors (6.8 motors/μm^2) for increasing lengths. The time-interval between frames is 1 s per, corresponding to Video SV1(a). (c) The value of χ from experiment (o–, mean $\pm$s.e.) and simulation (-, mean $\pm$s.d. from 100 MTs each) are plotted in terms of motors encountered per filament. Colors represent motor density in units of motors/μm^2. (d) Simulation outputs of filaments (grey) from 10 s of simulations at 0.25 s per frame for a motor density of 10 motors/μm^2. Two states of motors are indicated: bright-green: MT-bound, dark-green: free. Corresponding Video SV4(a)-(d).

In order to test whether a mathematical model of single-molecules of dynein could explain the observed collective properties in a multi-motor context, a dynein gliding assay simulation was developed (Figure 1 and Model description). Simulations

View Article Online
DOI: 10.1039/C8SM01434E

predict a decrease in diffusion coefficient with increasing motors per MT (Figure S4(a)), with MT lengths ranging from 1 to 10 μm (Video SV3) and densities ranging from 10^{-1} to 10^2 motors/μm^2. The transport velocity and directionality, from the same calculations, show a threshold effect increasing abruptly when ~10 or more motors are acting on an MT (Figure S4(b) and 7(c)), an effect also observed in experiments for ~8 to 10 motors (Figure 7(c)). The simulations however are based on a model of a motor as a single bead that stochastically steps along an MT, similar to previous work[51,69,70,74,76], while in experiment the yeast dynein is dimeric. Our result would suggest that the reported uncoordinated stepping of heads of this yeast dynein[29,31], could explain why the transition in directionality in experiment emerges at 8 to 10 heads, comparable to the 8 to 10 motors in simulations, due to the statistics of independent stochastic stepping and detachment behaviour. Additionally, visualization of the simulation for increasing MT lengths suggests the statistics of directionality can be understood in terms of three qualitatively different MT motility modes, just as in experiment: swivelling and occasional free-diffusion when filaments encounter 1-2 motors, (b) 2D 'search' interspersed with stretches of transport with 3-5 motors and (c) persistent directional transport when the motors encountered exceed 5 (Figure 7(d), Video SV4(a)-(d)).

Simulations predict that while the directionality of transport over three orders of magnitude of motor density appears to fall on one curve resembling saturation kinetics, the transition is not 'smooth' as a function of motors per MT. For instance the directionality of filaments of increasing lengths in presence of 10 motors/μm^2 do not appear to increase above 0.4, while higher values of directionality are only seen in case of an order of magnitude higher motor density. This could be due to the fact that increasing MT lengths for a given motor density could result in filament bending and result in defects in motion (kinks, spiral etc.) as previously reported for myosin and kinesin[80], thus reducing directionality. Additionally, simulations also predict the point of inflection of directionality as a function of motors (N-dependence) will be seen even if as little as half the motors are active (Figure S5), suggesting a potential experimental test of the model.

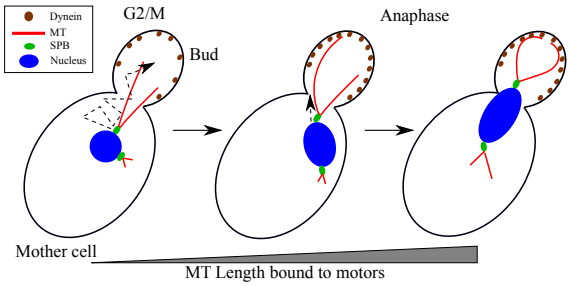

Fig. 8 Search and capture of astral MTs during nuclear positioning. A schematic representation of a yeast nucleus (blue) positioned (dashed arrow) by dynamic astral MTs (red) nucleated from SPBs (green) pulled by cortical dyneins (brown) localized in the bud cell. The scale represents the increasing length of MTs interacting with the motors.

The effect of increasing motor density on collective transport of MTs has also been shown for kinesins in a gliding assay, when the motors were anchored in a lipid bilayer but not when anchored on glass[74]. The similarity in trends with increased density despite the glass immobilization of dynein, could relate to the greater flexibility inherent in dynein, thus mimicking the effects of anchorage. This could reveal a general property of filament transport arising from intermolecular spacing and flexibility.

We find the ensemble mean directionality of transport steeply increases four-fold when the number of motors a filament encounters change from 8 to 10, in experiment. Simulations reproduce both the steepness of change and the N-value of the onset based on single molecule detachment mechanics. The transition in directionality with N~10 was observed even in the presence of 50% inactive motors that are unable to step (Figure S5), suggesting the robustness of our result to experimental artefacts such as the active fraction of the motor. This could also serve as a falsifiable test of our model. Our theoretical predictions explain not just our data, but also potentially provide an explanation for the previously reported of a sharp increase in run length and run time with an increase in yeast dynein team sizes from 2 to 7 motors[41]. To test the specificity of the detachment model, we proceeded to test the effect of alternative models of detachment on MT collective transport. The two alternative models compared for detachment rate (r_d) were: (a) constant ($r_d = r_d^0$), i.e. load-independent detachment, (b) symmetric load-dependent detachment based on Kramers law[81] ($r_d = r_d^0 \cdot e^{|F_\parallel / F_s|}$), keeping all other parameters identical to the asymmetric detachment rate model. We find, none of the alternative models could reproduce the value of the threshold number of motors encountered that results in a change in χ comparable to experimental data (Figure S6). The symmetric models tested also suggest that only a few (1-2) motors with symmetric detachment can result in directionally persistent transport, while the asymmetric detachment model requires a larger 'team' of motors to encounter MTs (Supplementary results). We speculate this may point to a property of this yeast dynein to 'switch' from random to persistent transport of MTs through an N-dependent (collective) mechanical coupling, rather than a simple 2D 'search'. This would suggest that such a motor number based threshold dependence of persistent filament transport might differ for a full length dynein construct, due to a quantitative difference in the load dependence as compared to the truncated dynein used in this study, acting as a test of our model predictions.

In our work, simulations allow us to explore a much wider range of motor densities than either previous or our own experimental data can approach. The increase in velocity and directionality both saturate rapidly when more than ~20 motors interact with an MT.

This result suggests the motor numbers of this dynein could have a role to play during *S. cerevisiae* mitosis in pulling MTs *in vivo*. The native yeast cytoplasmic dynein is localized to the daughter cell during mitosis[82] as part of the machinery that positions the nucleus to the bud neck between the daughter and mother cells[23,42,43]. During the G2/M to anaphase transition, astral MTs emanating from SPB embedded in the nucleus, are thought to 'search' and are 'captured' by dynein motors localized to the bud-cell cortex which then 'reel in' the nucleus[23]. The

View Article Online
DOI: 10.1039/C8SM01434E

captured MTs are then transported in a manner reminiscent of a gliding assay, with both MT lengths and motor numbers changing in time. The reported number of dyneins present on cortical foci in budding yeast 6±2 dimers[78]. We observe a transition in the directionality of MT transport when ≈10 motors are expected to interact with an MT. We speculate that the number dependence of random to directed MT transport, could affect the 'search and orientation' of the nucleus (Figure 8). Since the process involves collective motor transport, a transition to directed transport with increasing motor numbers might improve the accuracy and reduce the time taken for spindle alignment during division, while maintaining a constant velocity. Our experimental and theoretical observations suggest that the mechanics of the yeast dynein, might be adapted to ensure robust positioning of the nucleus in anaphase. Further quantitative analysis of yeast nuclear migration will be required to test this hypothesis.

Interestingly, the observation of a sharp transition in gliding velocity (v_{eff}), transport velocity (v) and directionality (χ) from low values of (less efficient transport) to high values above a threshold of motors, in simulations and in experiments, resembles a phase-transition. Phase transitions in directional motility of motor-driven transport, have been predicted in theory for symmetric and asymmetric motors[83–85]. They have also been experimentally demonstrated in the case of antagonistic kinesins transporting anti-parallel MT-doublets[86]. We believe, a simple dynein driven collective MT transport system could also fall into this general category. Our finding implies cells could regulate the qualitative nature of multi-motor transport by simply modulating the number of motors.

5 Conclusions

Thus, we find the velocity and directionality of MT transport by yeast dyneins depends on both the motor density and MT length. Simulations predict a monotonic decrease in the diffusivity of filaments with increasing numbers of motors. The transport velocity and 2D directionality undergo a steep increase both in simulation and experiment with increasing motor numbers. Modeling can explain such threshold dependent behavior as an emergent property of the collective effect of motor detachment dependence on the direction of the load force and a 2D 'search' by MTs for motors. This number-dependence of directionality of MT transport, arising from the coordination of multiple *S. cerevisiae* dyneins at a low density comparable to the *in vivo* scenario, could help us better understand the 'search and capture' of astral MTs in mitosis during nuclear positioning.

Conflicts of interest

There are no conflicts to declare.

Acknowledgements

We would like to thank Ron Vale and Andrew Carter for the gift of the *S. cerevisiae* VY208 strain and Thomas Pucadyil for the purified EGFP and TEV protease. The help of the microscopy facility in IISER Pune is acknowledged.

Notes and references

1 N. M. Rusan, U. Serdar Tulu, C. Fagerstrom and P. Wadsworth, *J. Cell Biol.*, 2002, **158**, 997–1003.
2 K. S. Burbank, T. J. Mitchison and D. S. Fisher, *Curr. Biol.*, 2007, **17**, 1373–1383.
3 H. Witte, D. Neukirchen and F. Bradke, *J. Cell Biol.*, 2008, **180**, 619–632.
4 Q. F. Wu, L. Yang, S. Li, Q. Wang, X. B. Yuan, X. Gao, L. Bao and X. Zhang, *Cell*, 2012, **149**, 1549–1564.
5 J. Howard, A. J. Hudspeth and R. D. Vale, *Nature*, 1989, **342**, 154–158.
6 C. M. Coppin, D. W. Pierce, L. Hsu and R. D. Vale, *Proc. Nat. Acad. Sci. USA*, 1997, **94**, 8539–8544.
7 K. Svoboda and S. M. Block, *Cell*, 1994, **77**, 773–784.
8 R. Mallik, B. C. Carter, S. A. Lex, S. J. King and S. P. Gross, *Nature*, 2004, **427**, 649–652.
9 S. L. Reck-Peterson, A. Yildiz, A. P. Carter, A. Gennerich, N. Zhang and R. D. Vale, *Cell*, 2006, **126**, 335–348.
10 T. Shima, K. Imamula, T. Kon, R. Ohkura and K. Sutoh, *J. Struct. Biol.*, 2006, **156**, 182–189.
11 S. P. Gross, M. Vershinin and G. T. Shubeita, *Curr Biol*, 2007, **17**, R478–86.
12 A. K. Rai, A. Rai, A. J. Ramaiya, R. Jha and R. Mallik, *Cell*, 2013, **152**, 172–182.
13 E. N. Cytrynbaum, J. M. Scholey and A. Mogilner, *Biophys. J.*, 2003, **84**, 757–769.
14 C. E. Walczak, I. Vernos, T. J. Mitchison, E. Karsenti and R. Heald, *Curr. Biol.*, 1998, **8**, 903–913.
15 L. S. B. Goldstein and Z. Yang, *Annu. Rev. Neurosci.*, 2000, **23**, 39–71.
16 P. W. Baas and O. I. Mozgova, *Cytoskel.*, 2012, **69**, 416–425.
17 K. Kimura and A. Kimura, *Proc. Nat. Acad. Sci., USA*, 2010, **108**, 137–142.
18 H. Tanimoto, A. Kimura and N. Minc, *The Journal of Cell Biology*, 2016, **212**, 777–787.
19 M. Schuh and J. Ellenberg, *Cell*, 2007, **130**, 484–498.
20 A. Svoboda, J. Bahler and J. Kohli, *Chromosoma*, 1995, **104**, 203–214.
21 D. Q. Ding, Y. Chikashige, T. Haraguchi and Y. Hiraoka, *J. Cell. Sci.*, 1998, **111 (Pt 6)**, 701–712.
22 A. Yamamoto, C. Tsutsumi, H. Kojima, K. Oiwa and Y. Hiraoka, *Mol. Biol. Cell*, 2001, **12**, 3933–3946.
23 N. R. Adames and J. A. Cooper, *J. Cell Biol.*, 2000, **149**, 863–874.
24 S. K. Vogel, N. Pavin, N. Maghelli, F. Julicher and I. M. Tolic-Norrelykke, *PLoS Biol.*, 2009, **7**, e1000087.
25 V. Ananthanarayanan, M. Schattat, S. K. Vogel, A. Krull, N. Pavin and I. M. Tolic-Norrelykke, *Cell*, 2013, **153**, 1526–1536.
26 J. Pecreaux, J. C. Roper, K. Kruse, F. Jülicher, A. A. Hyman, S. W. Grill and J. Howard, *Curr. Biol.*, 2006, **16**, 2111–2122.
27 K. Oiwa and H. Sakakibara, *Curr. Opin. Cell Biol.*, 2005, **17**, 98–103.
28 A. Gennerich, A. P. Carter, S. L. Reck-Peterson and R. D. Vale, *Cell*, 2007, **131**, 952–965.

View Article Online
DOI: 10.1039/C8SM01434E

29 M. A. DeWitt, A. Y. Chang, P. A. Combs and A. Yildiz, *Science*, 2012, **335**, 221–5.
30 W. Qiu, N. D. Derr, B. S. Goodman, E. Villa, D. Wu, W. Shih and S. L. Reck-Peterson, *Nat. Struct. Mo. Biol.*, 2012, **19**, 193–200.
31 F. B. Cleary, M. A. Dewitt, T. Bilyard, Z. M. Htet, V. Belyy, D. D. Chan, A. Y. Chang and A. Yildiz, *Nat Commun*, 2014, **5**, 4587.
32 V. Belyy, N. L. Hendel, A. Chien and A. Yildiz, *Nat Commun*, 2014, **5**, 5544.
33 M. P. Nicholas, F. Berger, L. Rao, S. Brenner, C. Cho and A. Gennerich, *Proc. Natl. Acad. Sci. U.S.A.*, 2015, **112**, 6371–6376.
34 F. Oosawa and S. Hayashi, *Adv. Biophys.*, 1986, **22**, 151–183.
35 F. Oosawa, *Genes to Cells*, 2000, **5**, 9–16.
36 P. Bieling, I. A. Telley, J. Piehler and T. Surrey, *EMBO Rep.*, 2008, **9**, 1121–1127.
37 A. Kunwar, M. Vershinin, J. Xu and S. P. Gross, *Curr. Biol.*, 2008, **18**, 1173–1183.
38 J. Gagliano, M. Walb, B. Blaker, J. C. Macosko and G. Holzwarth, *Eur. Biophys. J.*, 2010, **39**, 801–813.
39 J. W. Driver, D. K. Jamison, K. Uppulury, A. R. Rogers, A. B. Kolomeisky and M. R. Diehl, *Biophys. J.*, 2011, **101**, 386–395.
40 G. Arpağ, S. Shastry, W. O. Hancock and E. Tüzel, *Biophysical Journal*, 2014, **107**, 1896–1904.
41 N. D. Derr, B. S. Goodman, R. Jungmann, A. E. Leschinzer, W. M. Shih and S. L. Reck-Peterson, *Science*, 2012, **338**, 662–665.
42 S. L. Shaw, E. Yeh, P. Maddox, E. D. Salmon and K. Bloom, *J. Cell Biol.*, 1997, **139**, 985–994.
43 D. Hoepfner, A. Brachat and P. Philippsen, *Mol. Biol. Cell*, 2000, **11**, 1197–1211.
44 J. K. Moore, Stuchell-Brereton and J. A. Cooper, *Cell Motil. Cytoskel.*, 2009, **66**, 546–555.
45 W. L. Lee, M. A. Kaiser and J. A. Cooper, *J. Cell Biol.*, 2005, **168**, 201–207.
46 F. Nedelec, *J. Cell Biol.*, 2002, **158**, 1005–1015.
47 F. Nedelec and D. Foethke, *New J. Phys*, 2007, **9**, 427.
48 C. A. Athale, A. Dinarina, M. Mora-Coral, C. Pugieux, F. Nedelec and E. Karsenti, *Science*, 2008, **322**, 1243–1247.
49 D. Foethke, T. Makushok, D. Brunner and F. Nedelec, *Mol Syst Biol*, 2009, **5**, 241.
50 R. Loughlin, R. Heald and F. Nédélec, *J. Cell Biol.*, 2010, **191**, 1239–1249.
51 C. A. Athale, A. Dinarina, F. Nedelec and E. Karsenti, *Phys. Biol.*, 2014, **11**, 016008.
52 F. Gittes, B. Mickey, J. Nettleton and J. Howard, *J. Cell Biol.*, 1993, **120**, 923–934.
53 J. Howard, *Mechanics of Motor Proteins and the Cytoskeleton*, Sinauer Associates, Sunderland, MA, 2001.
54 A. Takshak and A. Kunwar, *Protein Sci.*, 2016, **25**, 1075–1079.
55 V. Belyy, M. A. Schlager, H. Foster, A. E. Reimer, A. P. Carter and A. Yildiz, *Nat Cell Biol*, 2016, **18**, 1018–24.
56 O. H. E. Segur J. B., *Ind. Eng. Chem.*, 1951, **43**, 2117–2120.
57 R. Gibeaux, A. Z. Politi, P. Philippsen and F. Nedelec, *Mol. Biol. Cell*, 2017, **28**, 645–660.
58 P. A. Lanzetta, L. J. Alvarez, P. S. Reinach and O. A. Candia, *Analytical Biochemistry*, 1979, **100**, 95 – 97.
59 P. Bieling, L. Laan, H. Schek, E. L. Munteanu, L. Sandblad, M. Dogterom, D. Brunner and T. Surrey, *Nature*, 2007, **450**, 1100–1105.
60 J. R. Swedlow, K. Hu, P. D. Andrews, D. S. Roos and J. M. Murray, *Proc. Natl. Acad. Sci. U.S.A.*, 2002, **99**, 2014–2019.
61 A. P. Joglekar, E. D. Salmon and K. S. Bloom, *Methods Cell Biol.*, 2008, **85**, 127–151.
62 C. Schneider, W. Rasband and K. Eliceiri, *Nat. Methods*, 2012, **9**, 671–675.
63 J. Pawley, *Handbook of Biological Confocal Microscopy*, Springer, 1995.
64 N. C. Shaner, P. A. Steinbach and R. Y. Tsien, *Nat. Methods*, 2005, **2**, 905–909.
65 D. E. Harris and D. M. Warshaw, *J Biol Chem*, 1993, **268**, 14764–8.
66 S. Walcott, D. M. Warshaw and E. P. Debold, *Biophys J*, 2012, **103**, 501–10.
67 K. Rastogi, M. S. Puliyakodan, V. Pandey, S. Nath and R. Elangovan, *Sci Rep*, 2016, **6**, 32043.
68 F. Ruhnow, D. Zwicker and S. Diez, *Biophys. J.*, 2011, **100**, 2820–2828.
69 N. Khetan and C. A. Athale, *PLoS Comp. Biol.*, 2016, **12**, e1005102.
70 D. Arcizet, B. Meier, E. Sackmann, J. O. Radler and D. Heinrich, *Phys. Rev. Lett.*, 2008, **101**, 248103.
71 X. Michalet, *Phys. Rev. E*, 2010, **82**, 041914.
72 M. J. Saxton, *Biophys J*, 2007, **92**, 1178–91.
73 M. J. Saxton, *Biophys J*, 2008, **94**, 760–71.
74 R. Grover, J. Fischer, F. W. Schwarz, W. J. Walter, P. Schwille and S. Diez, *Proc. Natl. Acad. Sci. U.S.A.*, 2016, **113**, E7185–E7193.
75 M. K. Sato, T. Ishihara, H. Tanaka, A. Ishijima and Y. Inoue, *Biophys. J.*, 2012, **103**, 711–718.
76 Y. Imafuku, Y. Y. Toyoshima and K. Tawada, *Biophys. J.*, 1996, **70**, 878–886.
77 L. Scharrel, R. Ma, R. Schneider, F. Jülicher and S. Diez, *Biophys. J.*, 2014, **107**, 365–372.
78 S. M. Markus, K. M. Plevock, B. J. St Germain, J. J. Punch, C. W. Meaden and W. L. Lee, *Cytoskeleton (Hoboken)*, 2011, **68**, 157–174.
79 C. Leduc, F. Ruhnow, J. Howard and S. Diez, *Proc. Nat. Acad. Sci. USA*, 2007, **104**, 10847–10852.
80 L. Bourdieu, T. Duke, M. Elowitz, D. Winkelmann, S. Leibler and A. Libchaber, *Phys. Rev. Lett.*, 1995, **75**, 176–179.
81 H. Kramers, *Physica*, 1940, **7**, 284–304.
82 S. M. Markus and W. L. Lee, *Dev. Cell*, 2011, **20**, 639–651.
83 F. Jülicher and J. Prost, *Phys. Rev. Lett.*, 1995, **75**, 2618–2621.
84 F. Jülicher, A. Ajdari and J. Prost, *Rev. Mod. Phys.*, 1997, **69**, 2111–2122.
85 M. Badoual, F. Jülicher and J. Prost, *Proc. Natl. Acad. Sci.*

View Article Online
DOI: 10.1039/C8SM01434E

U.S.A., 2002, **99**, 6696–6701.

86 C. Leduc, N. Pavin, F. Jülicher and S. Diez, *Phys. Rev. Lett.*, 2010, **105**, 1–4.

PLOS ONE

RESEARCH ARTICLE

Automated Multi-Peak Tracking Kymography (AMTraK): A Tool to Quantify Sub-Cellular Dynamics with Sub-Pixel Accuracy

Anushree R. Chaphalkar, Kunalika Jain, Manasi S. Gangan, Chaitanya A. Athale*

Div. of Biology, IISER Pune, Pashan, Pune, India

* cathale@iiserpune.ac.in

Citation: Chaphalkar AR, Jain K, Gangan MS, Athale CA (2016) Automated Multi-Peak Tracking Kymography (AMTraK): A Tool to Quantify Sub-Cellular Dynamics with Sub-Pixel Accuracy. PLoS ONE 11(12): e0167620. doi:10.1371/journal.pone.0167620

Editor: Jinxing Lin, Beijing Forestry University, CHINA

Received: July 12, 2016

Accepted: November 17, 2016

Published: December 19, 2016

Data Availability Statement: All data is included in the paper. Software that forms an important part of the report has been released as open source and can be downloaded from the author's website (http://www.iiserpune.ac.in/~cathale/SupplementaryMaterial/Amtrak.html) and from GitHub at https://github.com/athale/AMTraK.

Funding: This research was supported by The Department of Biotechnology (DBT), Govt. of India (BT/PR1595/BRB/10/1043/2012), University Grants Commission (F.2-14/2011 (SA-1)), Department of Science and Technology, Ministry of

Abstract

Kymographs or space-time plots are widely used in cell biology to reduce the dimensions of a time-series in microscopy for both qualitative and quantitative insight into spatio-temporal dynamics. While multiple tools for image kymography have been described before, quantification remains largely manual. Here, we describe a novel software tool for automated multi-peak tracking kymography (AMTraK), which uses peak information and distance minimization to track and automatically quantify kymographs, integrated in a GUI. The program takes fluorescence time-series data as an input and tracks contours in the kymographs based on intensity and gradient peaks. By integrating a branch-point detection method, it can be used to identify merging and splitting events of tracks, important in separation and coalescence events. In tests with synthetic images, we demonstrate sub-pixel positional accuracy of the program. We test the program by quantifying sub-cellular dynamics in rod-shaped bacteria, microtubule (MT) transport and vesicle dynamics. A time-series of *E. coli* cell division with labeled nucleoid DNA is used to identify the time-point and rate at which the nucleoid segregates. The mean velocity of microtubule (MT) gliding motility due to a recombinant kinesin motor is estimated as 0.5 μm/s, in agreement with published values, and comparable to estimates using software for nanometer precision filament-tracking. We proceed to employ AMTraK to analyze previously published time-series microscopy data where kymographs had been manually quantified: clathrin polymerization kinetics during vesicle formation and anterograde and retrograde transport in axons. AMTraK analysis not only reproduces the reported parameters, it also provides an objective and automated method for reproducible analysis of kymographs from *in vitro* and *in vivo* fluorescence microscopy time-series of sub-cellular dynamics.

Introduction

Kymographs, or space-time plots, have been extensively used to analyse sub-cellular microscopy time-lapse data with improvements in microscopy. It has been used in the past to characterize organelle transport, cell division and molecular motor motility as reviewed by Pereira et al. [1], and the wide-range of applications could be the result of the reduced spatial

Science and Technology (INSPIRE IF130394), and Indian Council of Medical Research (3/13/WLC/JRF-2011/HRD-156 (51550)).

Competing Interests: The authors have declared that no competing interests exist.

dimensions of complex microscopy time-series. Most often however, kymography has been used as a qualitative readout of movement or dynamics. In studies where kymographs have been quantified, most often this has been manual, as seen in the Multi Kymograph plugin for ImageJ [2]. Most of the existing tools such as the automated kymography tool [3] and 'guided' kymography [1] focus on automating the process of kymograph building. Few methods for the automated quantification of kymographs exist, such as 'Kymomaker' [4] and a curvelets based tool [5]. Both these tools automate quantification, but cannot deal with merging and spitting events. Despite the ubiquitous nature of merging and splitting events in typical sub-cellular processes, none of the existing tools for the automated quantification of kymographs include a feature to handle budding and coalescence.

Genome segregation is conserved across cellular systems and has been extremely well studied in the rod-shaped Gram-negative bacterium *Escherichia coli* [6,7]. However microscopic analysis of DNA segregation has only recently been made possible with improvements in microscopy and image-analysis [8–10]. Given the almost 1D geometry of segregation of the genome along the long axis of the cell, kymography is a convenient way to analyze the process of nucleoid DNA segregation. Recent studies using explicit 3D over time tracking have found compaction waves are associated with *E. coli* genome segregation [11]. Based on a reduction in dimensions to 1D over time, a quantitative kymograph-based analysis could be used to screen for changes and defects in segregation, without the need for more complex datasets and their analysis.

The process of microtubule transport by molecular motors reconstituted *in vitro*, referred to as a 'gliding assay' has been extensively used to examine the fundamental nature of multi-molecular transport of actin and microtubule filaments by motors [12–15]. Recent studies have also used 'gliding assays' to address microtubule mechanics based on the bending of filaments while undergoing transport [16]. Kymography of cytoskeletal filaments *in vivo* has been used to follow actin contractility and microtubule buckling dynamics [17]. However in most cases the use of kymography has been limited to visualizing the time-series in a single-image, as a compact form of data representation. A general tool that could use this information to objectively extract the measures of motility would hence be of some use to these multiple applications.

The assembly of proteins by 'recruitment' to structures is fundamental in multi-protein complex formation. The assembly of vesicles by budding off membranes and their fusion is critical for cellular function. For the assembly of coated pits with clathrin for endocytosis the site of assembly [18], sequence of binding events [19] and interactions of other proteins [20] is considered to be critical. Microscopy of *in vitro* reconstituted membrane bilayers has become a powerful tool to study the dynamics of protein assembly during vesicle formation [21,22]. Proteins such as epsin, which were reported to accelerate clathrin 'recruitment' [23] have been examined using kymography of the fluorescently labelled clathrin and the effect of mutant epsins on the process [24]. While such an approach lends itself to high-content screening, the analysis of the kymograph has been manual. Many other such 'recruiment' dynamics studies could benefit from an automated routine to quantify the kinetics of assembly through intensity measurements coupled to kymography.

Neuronal vesicles are transported in axons by the action of molecular motors. Microscopy of *in vitro* reconstituted [25] and the *in vivo* transport in cultured cells [26,27] has provided insights into both the components and forces regulating transport. Recent technical developments have allowed whole animal *in vivo* microscopy of sub-cellular vesicle movements in neurons [28]. In this and comparable studies, quantitative statistics have been obtained using manual detection of kymographs. This is possibly due to the complex nature of the time-series with cross-overs and the crowded *in vivo* environment. An approach that uses objective

criteria and automates the process of quantification could provide valuable improvements to our understanding of fundamental nature of vesicle transport as well as aid in the process of modeling vesicle transport.

Here, we have developed a novel tool to automatically quantify kymographs from fluorescence image time-series. We proceed to demonstrate the utility of the automated multi-peak tracking kymography (AMTraK) tool by quantifying dynamics from diverse sub-cellular fluorescence microscopy data sets. These include bacterial genome-segregation, microtubule (MT) motility of 1D filaments and 2D radial asters, membrane protein assembly dynamics and vesicle transport in axons.

Algorithm and workflow

The automated multi-peak tracking kymography (AMTraK) is open source software based on an algorithm that combines peak detection and distance minimization based linking to quantify dynamics of fluorescence image time-series. The source code has been released with a GPL license and can be accessed from: http://www.iiserpune.ac.in/~cathale/SupplementaryMaterial/Amtrak.html and https://github.com/athale/AMTraK

The program has a GUI front-end and is accompanied by a detailed help file. The algorithmic workflow (Fig 1A) is divided broadly into three steps:

1. Making the kymograph
2. Peak detection and tracking
3. Statistics

These steps in the workflow are reflected in the graphical user interface (GUI) layout (Fig 1B). The functioning of each of these steps is briefly described as follows:

(a) Making the kymograph. The user chooses an input image time-series with the "Open File" button. Image time-series are assumed to be uncompressed, multi-page TIF files (independent of bit depth). The user can choose to process either the whole or a subset of frames using the "Frame nos." text box. For example entering "2:2:8" will now result in only frames 2, 4, 6 and 8 being processed for further analysis. The text box "Save as sub-folder" takes a number input (default "1") indicating where the outputs will be stored (e.g.: "./amtrak-1"). The drop-down menu "Apply LOI" allows the user to either choose a line of interest (LOI) using the mouse ("Interactive") or apply a pre-existing LOI on a different channel (color) of the image time-series ("From file"). Once an interactively drawn LOI is selected, it is stored in the output sub-folder as "LOIselection.txt" (S1 Data). This LOI can subsequently be applied, to another channel or the same region of another dataset (e.g.: microfluidics channels) using the "From file" mode. For this, the user is required to load a separate TIF time-series using "Open File" and change the sub-folder number in order to prevent overwriting old data. The "LOI width (pixels)" allows a user to choose the width of the LOI, to compensate for occasional drift of the object, in a direction orthogonal to the LOI orientation. The choice widths- 1, 3 and 5 pixels- is centered around the selected LOI pixels, similar to that implemented in the ImageJ Multi Kymograph plugin [2]. The drop-down menu "Units" allows the user to select distance and time units, and the text boxes "Scaling factor" and "Time interval" are used to provide conversion factors per pixel and frame respectively. This results in scaling the pixels and frame numbers to physical units. The button "Make Kymograph" produces a maximum intensity projection image of the input time-series, if the user had chosen the "Interactive" mode (default) in the "Apply LOI" menu. The user is required to select the line of interest by drag-

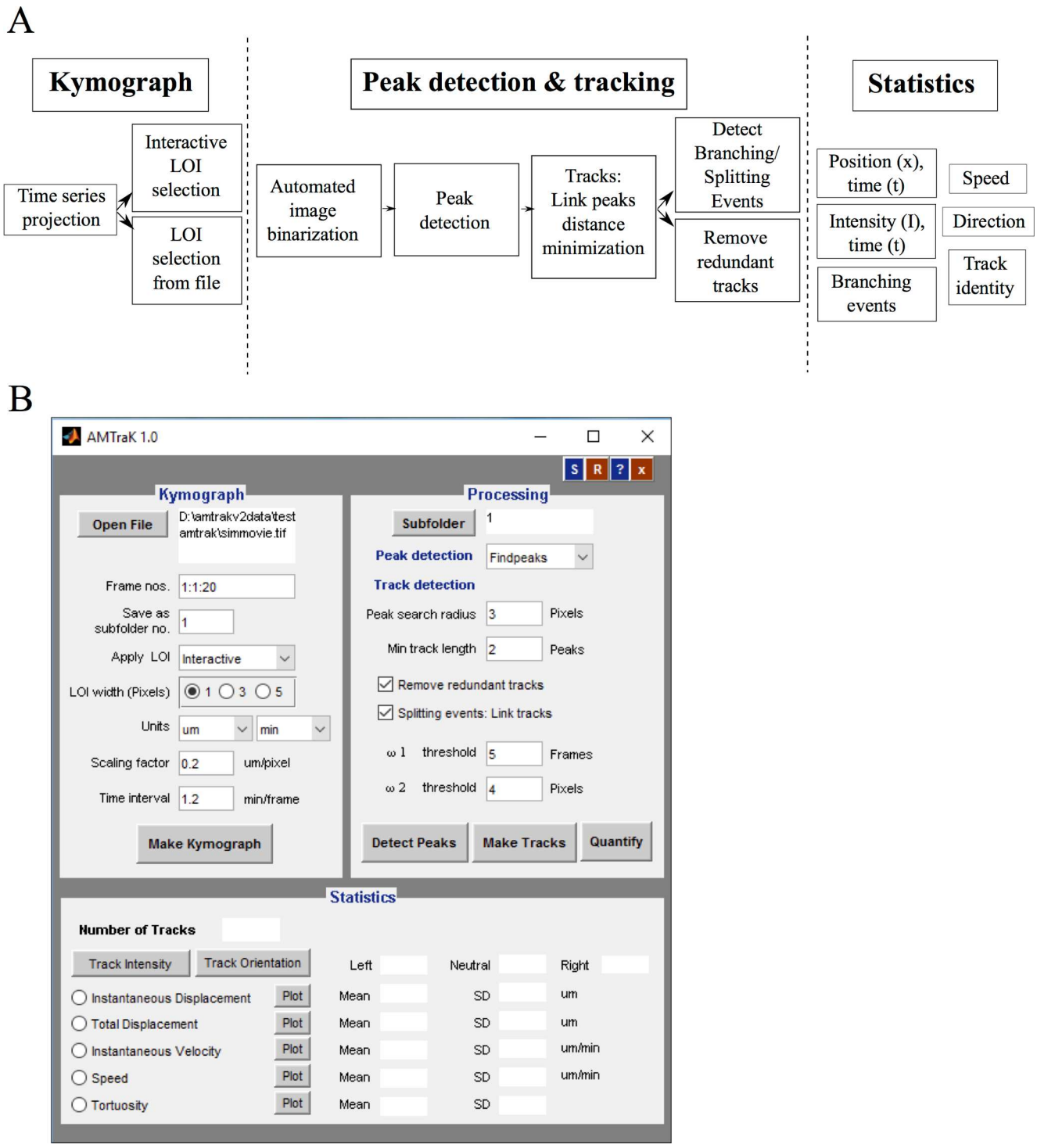

Fig 1. Algorithm workflow and user-interface. (A) The workflow of the algorithm involves three steps (1) kymograph generation, (2) peak detection and tracking and (3) quantification and the functions invoked by each part are elaborated. (B) The GUI is organized to reflect this workflow.

doi:10.1371/journal.pone.0167620.g001

clicking the mouse. Double-clicking ends the selection, and throws a dialog box, which prompts the user to choose to either select more LOIs or continue with the processing of the

one already selected. This generates file one or more "LOIselection.txt" files in the sub-folders. If the "From file" mode was selected, the program allows the user to select a pre-existing "LOI-selection.txt" from the directory structure. The program then generates kymographs based on these LOIs and stores the matrices corresponding to the LOIs in sub-folders numbered according to the sequence of LOI selection (e.g.: "/amtrak-1/", "/amtrak-2/" etc.).

(b) Peak detection and tracking. *Detecting peaks*: The button "Subfolder" allows the user to choose the kymographs to be processed using "Add", which adds the subfolders created earlier to the active list. Using this feature, a user can either process a single kymograph at a time, or process multiple kymographs using the same parameters. The kymograph is segmented row-wise using Otsu's method [29] and the resulting binary image is processed for "Peak detection". The user can choose between three alternative methods: (i) *findpeaks* [30] and (ii) watershed [31] to find central peaks, while (iii) Canny edge detection [32] is useful if the edge information is the most reliable descriptor of the dynamics. Typically *findpeaks* and watershed are ideal for spherical objects.

Linking: The list of peaks *P(t)* for each time point *t* is linked resulting in tracks, based on user input parameters of "Peak search radius" (λ_1) and "Min. track length" (λ_2). Peaks are linked if the minimal pair-wise distance dj(t,t+τ) between every j^{th} peak in successive rows (*t*, *t* +τ) satisfies the condition $\min(d_j(t, t+\tau)) \leq \lambda_1$, iteratively for the j^{th} peak in every subsequent time step (t+τ). If two or more peaks are equidistant, the peak that makes the largest angle (0 to π) with the existing track is chosen, similar to our previously developed branch detection method [33]. For the peaks in t = 1, the angle criterion does not hold true and equidistant peaks are resolved by user-input. Tracks are eliminated from further analysis if their number of peaks linked $\text{len}(P) \leq \lambda_2$, to avoid artifacts due to very short tracks.

Remove redundant: If the checkbox "Remove redundant tracks" is selected, each i^{th} track with η_i coordinates, is tested for intersections using the inbuilt *intersect* function. If the number of common coordinates η_c satisfies the condition $\eta_c \geq \eta_i/3$, it is eliminated as a redundant track.

Splitting and joining tracks: If the checkbox "Splitting events: Link tracks" is selected, events where two tracks merge are identified by a two-step process. First, all peaks (I(x,t)) are evaluated for the condition $I(x,t) = (d^te \leq \omega_1)$ AND $(d^xe \leq \omega_2)$, where d^te is the distance on the time-axis (t) and d^xe is the distance on the spatial (x) axis. Then, a peak with the minimal (Euclidean) distance is minimized for the distance to the end-point (e) coordinate J_m. The time and distance thresholds are set by the user in the text box for ω_1 (frames) and ω_2 (pixels) respectively.

The button "Detect Peaks" then outputs an image of the kymograph with the peaks overlaid in color, while invoking the button "Make tracks" links the peaks based on the input parameters. Lastly the button "Quantify" produces a text file corresponding to each track (S2 Data, S3 Data and S4 Data).

(c) Statistics. This section of the code produces both text-file outputs and plots of the dynamics estimated from the kymograph. The frequency distribution of "Instantaneous Displacement", "Total Displacement", "Instantaneous Velocity", "Speed" and "Tortuosity" (i.e. directionality) are plotted if the button "Plot" corresponding to these variables is pressed. Additionally the mean and standard deviation (s.d.) of these variables are also generated in the text boxes. Pressing the "Track Intensity" button plots the normalized (0–1) grey value intensity of each track as a function of the time. The button "Track orientation" triggers a recoloring the tracks in the kymograph based on the net direction of movement along the X-axis- blue (-ve, left), red (+ve, right) and green (stationary, neutral).

The outputs of the analysis are stored in multiple tab-delimited text files: "LOIselection.txt" with the LOI coordinates (S1 Data), "USER_TrackStats.txt" which reports track-wise mean

values (S2 Data), "USER_InstStats.txt" which reports the time-dependent statistics (S3 Data), "Tracklist.txt" which stores the grey-value intensities as a function of track number and time (S4 Data) and "Branchpoints.txt" which stores the position and time coordinates of detected branches (S5 Data). The user-inputs to AMTraK in terms of files, directories and parameters are all stored in "All_Parameters.txt" (S6 Data), to enable reproducible analysis.

Materials and Methods

Simulated test images

Simulated images of static beads were generated by creating 8 bit images with a black background (intensity: 0) with equally spaced single white pixels (intensity: 255) in MATLAB (MathWorks Inc., USA). To simulate bead motion, a simple 1D random-walk was implemented where each bead was moved randomly in each frame, with displacement drawn from a normally distributed random number with mean m = 0 and standard deviation (s). The standard deviation is a measure of the mean speed of motion. Both the static and mobile bead image time-series were filtered with a 5x5 disk filter and smoothed using a 3x3 averaging filter. The resulting convolved circular objects (S1A Fig) have intensity profiles that resemble point sources of fluorescence signal (S1B Fig). The time-series were saved as a multi-page TIF files. Noise was added to individual time-series in order to simulate increasing levels of image-noise using a Gaussian filter with increasing standard deviation (0–100) using ImageJ [34].

Bacterial growth and microscopy

E. coli MG1655 (CGSC, Yale, USA) expressing the pBAD24-hupA-GFP [35] were cultured in Luria Bertani (LB) medium (HiMedia, Mumbai, India) with 100 μg/ml Ampicillin (Sigma-Aldrich, Mumbai, India) at 37˚C with shaking at 170 rpm (Forma, ThermoScientific, USA). Nutrient 'agar-pads' with 0.2% arabinose (Sisco Research Labs, Mumbai, India) and 100 μg/ml ampicillin were imaged on a glass-bottomed Petri dish (Corning, NY, USA) at 37˚C using an inverted Zeiss LSM780 confocal microscope (Carl Zeiss, Germany) with a Plan Apochromat 63x (N.A. 1.40, oil) lens in DIC and fluorescence (excitation by 405 nm diode laser with a beam splitter MBS 405 and the emission collected between 487–582 nm) modes. Images were corrected for drift using the rigid body transformation in the StackReg plugin [36] for ImageJ.

Microtubule gliding assay

A 1:4 ratio of TRITC-labeled bovine and unlabeled porcine tubulin (Cytoskeleton Inc., USA) at a concentration of 20 μM were used to prepare taxol stabilized MT-filaments in general tubulin buffer as described by the supplier (Cytoskeleton Inc., USA). Into a double backed tape chamber, we sequentially flowed in 4.1 μg/μl of a 67 kDa recombinant human kinesin (Cytoskeleton Inc., USA), blocking buffer (5 mg/ml Casein) and MT filaments. The chamber was then washed with a casein-containing buffer and the reaction was started with 1 mM ATP with anti-fade mix (0.05 M glucose, 1% sucrose, 0.5 mg/ml catalase, 0.5 mg/ml glucose oxidase, 0.5% beta-mercaptoethanol (Cytoskeleton Inc., USA)). Time-series images were acquired every minute for 30 minutes on an upright epifluorescence microscope with a 40x (N.A. 0.75) EC Plan Neofluar lens mounted on a Zeiss Axio Imager.Z1 (Carl Zeiss, Germany) using filters for excitation (563 nm) and emission (581 nm) and an MRC camera (Carl Zeiss, Germany).

Image processing

The acquired time-series and movies taken from published data were converted to uncompressed TIF time-series using ImageJ (Schneider et al., 2012) and online converters for MOV

files. MT-gliding assay images were de-noised using a median filter in ImageJ. For manual analysis of kymographs of MT-gliding, a program was written in MATLAB (MathWorks Inc., USA) to generate a kymograph from the time-series, interactively draw a segmented line along the edges and extract coordinates to calculate velocities. The automated multi-peak tracking kymography (AMTraK) code was implemented in MATLAB R2014b (MathWorks Inc., USA) in combination with the Image Processing (ver. 7.0) and Statistics (ver. 7.3) Toolboxes and tested on Linux, Mac OSX and Windows7 platforms. Vesicle transport image time-series in *C. elegans* from supporting material of published work [28] were calibrated based on the width of the axon from the same report.

Data analysis

All data analysis and plotting was performed using MATLAB 2014b (MathWorks Inc., USA). Fitting of custom functions was performed using either the Levenberg-Marquardt non-linear least square routine or the Trust-Region method, implemented in the CurveFitting toolbox (ver. 3.5) of MATLAB.

Results

Accuracy of detection

To test the positional detection accuracy of the algorithm, we have created simulated image time-series of circular objects that represent typical fluorescence images of circular objects (Fig 2A), comparable to images of sub-cellular structures in pixels (S1A Fig). Since the time-series consists of the same image, the objects are perfectly static as seen in the resulting kymograph (Fig 2B) output from running AMTraK on the data. Intensity variations are a result of the noise from the spatial filter (s.d. 40). The difference between the position of the detected tracks (x_D) and the simulated position (x_S) is used as an estimate of the limit of accuracy in position detection, $\Delta x = |x_S - x_D|$. The normalized frequency distribution of Δx can be fit to an exponential decay function to obtain a mean accuracy $<\Delta x> = 1/b$ from the fit, in pixel units (Fig 2C). For all images with noise of s.d.< 40, the mean error (from fit) in detection $\langle \Delta x \rangle < 1$ pixel. For higher values appears to saturate between 2–3 pixels (Fig 2D). Using the arithmetic mean as an estimate of the accuracy for a given noise s.d. appears to result in an underestimate that does not change with increasing noise s.d. (Fig 2D), and hence the mean from the exponential decay of the frequency of Δx was taken to be more representative of the central tendency. To test if motility affected the positional accuracy, we also evaluated the positional accuracy of particles undergoing a random walk (as described in the Materials and Methods section) with a fixed image noise (noise s.d. 30). By increasing the s.d. of the random walk we estimated the effect of increasing velocity on Δx (Fig 3A). The accuracy of positional detection using both the arithmetic and exponential mean error ($<\Delta x>$) as before, is less than 1 pixel for the chosen range of velocities of the random walk (Fig 3B). At higher velocities, the tracking errors accumulate, suggesting image noise is the major limiting factor for the positional accuracy of detection, independent of particle motility. Thus, while AMTraK analysis can result in sub-pixel accuracy of position detection, it is essential that the input data have low-noise. We proceeded to test our method on the multiple experimental datasets to examine the utility of this program involving bacterial DNA segregation, microtubule motility and vesicle assembly and transport dynamics.

Detecting splitting events in bacterial DNA-segregation

A time-series of growing *E. coli* is acquired in fluorescence (Movie A in S1 Video) and DIC (Movie B in S1 Video) to follow the nucleoid segregation dynamics of HupA-GFP labeled

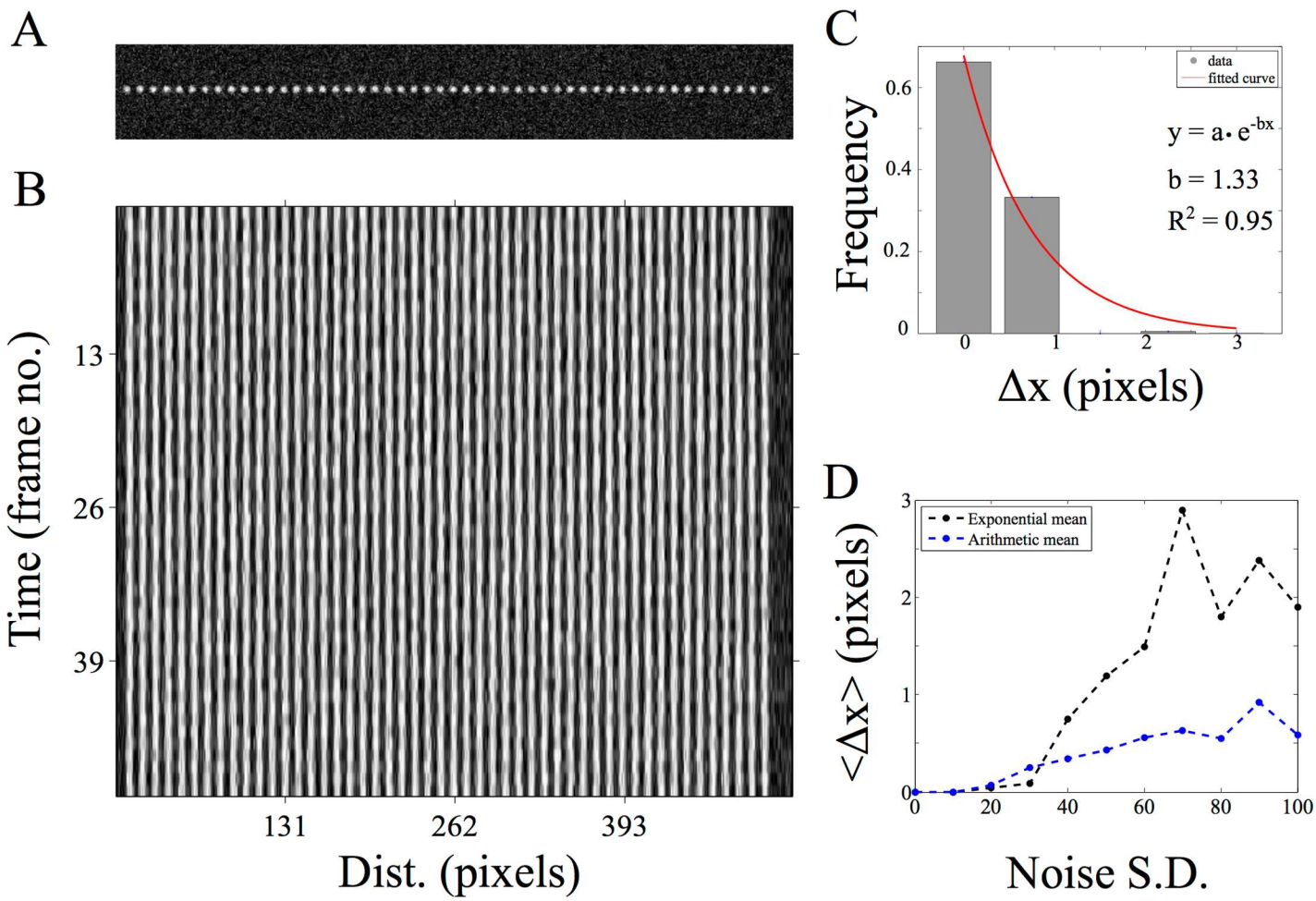

Fig 2. Estimating positional accuracy. (A) A single frame of a 2D image time-series of static spheres (with a peak intensity of 1) with Gaussian noise (mean = 0, s.d. = 40) is analyzed using AMTraK (B) resulting in a kymograph. (C) The frequency distribution of the error in position detection (Δx) by AMTraK (bars) is fit by an exponential decay (red). The mean error obtained is 0.75 pixels (goodness of fit $R^2 = 0.95$) for a representative time-series with noise s.d. = 40. (D) The mean error of detection (y-axis) from the exponential fit $\langle \Delta x \rangle = 1/b$ (black) is compared to the arithmetic mean (blue) in pixel units, plotted as a function of increasing noise s.d. (x-axis). The noise generates random intensities drawn from a Gaussian distribution with mean 0 and the specified s.d. being added to the image (based on the "Specified Noise" function in ImageJ).

doi:10.1371/journal.pone.0167620.g002

DNA (Fig 4A). Using the maximum intensity projection produced from AMTraK, the LOIs are chosen (Fig 4B) and used to generate and analyze two kymographs (Fig 4C and 4D). The segregation of the genome is captured by the branched structures of the tracks marked in the kymographs. Additionally we can evaluate both the instantaneous velocity for time-dependence (Fig 4E) and average statistics (Fig 4F). The mean nucleoid transport velocity is 0.103±0.12 μm/min (arithmetic mean ± standard deviation). Based on the form of the frequency distribution of instantaneous velocities, we also fit an exponential decay function to obtain the exponential mean velocity $v_{ex} = 0.104$ μm/min. These values of nucleoid movement speed from *E. coli* MG1655 (wild-type) cells are comparable to a previous report in which nucleoids were tracked in 3D over time [11]. While nucleoids form a diffraction-limited spot in microscopy images, un-branched cytoskeletal filaments form typical 1D structures and dynamics of transport on them and of the filaments themselves, are ideally suited for kymography.

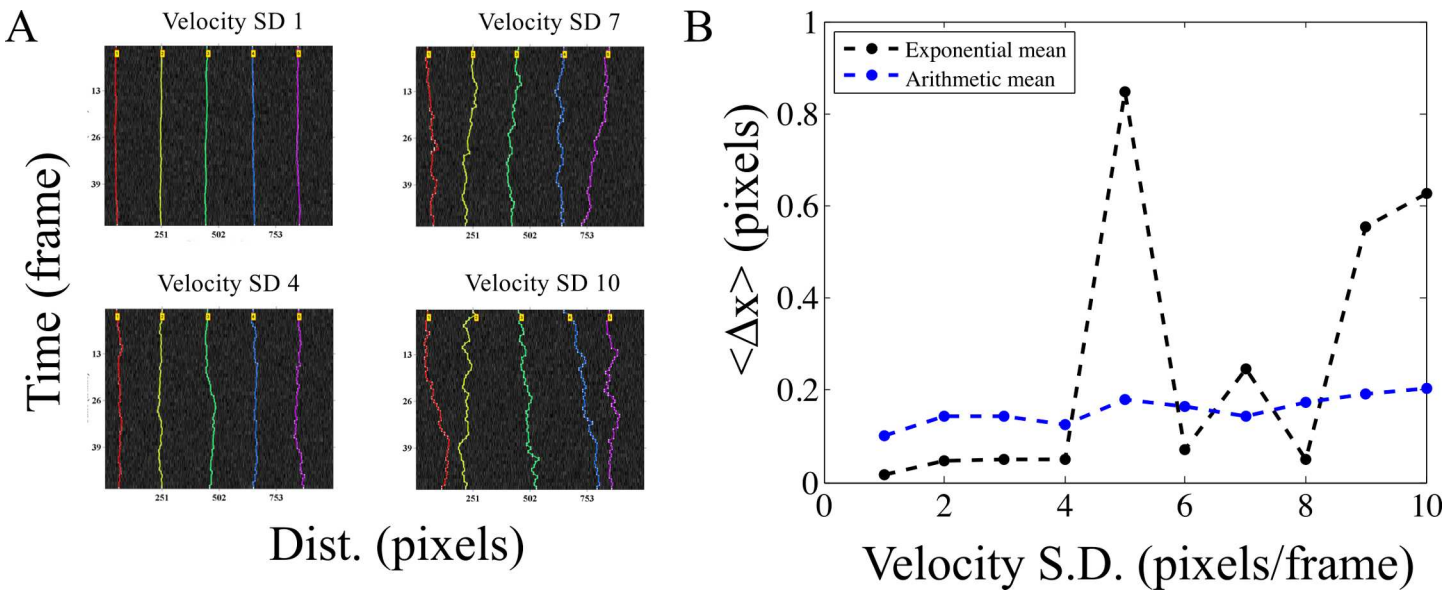

Fig 3. Positional accuracy of tracking simulated motility. (A) Kymographs of time-series of spheres undergoing a 1D random walk with Gaussian noise (s.d. = 30) were tracked. The colors indicate the detected tracks. (B) The arithmetic mean (blue) and exponential mean (black) of error in position detection (Δx) (y-axis) over 3 iterations of the time-series is plotted for increasing velocity of the random-walk (x-axis) as inferred from the standard deviation (s.d.).

doi:10.1371/journal.pone.0167620.g003

Microtubule transport: filament edges, centers and time-dependence of velocity

The transport of microtubule (MT) filaments by surface-immobilized molecular motors in the presence of ATP and buffers is referred to in the literature as 'gliding assay' or 'collective transport assay'. Here, we analyze the gliding motility of MT on kinesin, as described in the methods section, using AMTraK. The analysis of a representative kymograph using either peak- (Fig 5A) or edge-detection (Fig 5B) successful traces the centroids and edges respectively. The mean velocity estimates for collective motor transport show variations between individual filaments. The centroid and edge velocity estimates of multiple MT filaments (n = 10) are strongly correlated as evidenced by the straight line fit with slope ~ 1 (Fig 5C and 5D), as expected. However, the linear correlation of edge-based velocities has a slope of ~0.9 (Fig 5E), suggesting small deviations from the ideal slope, within the range of the average positional detection error (Fig 2C). While typical kymograph analysis of cytoskeletal transport averages the edge information (movement of the tips over time), correlating edge-velocities could potentially be used to estimate small alterations in the filament geometry such as bending and length change. The mean velocity of 0.5 μm/min obtained from our analysis of the assay (Fig 5F) is consistent with previous reports for the same construct [37,38]. While the transport of effectively 1D MT filaments lends itself to kymography, we proceeded to investigate if 2D radial MT structures or asters can also be analyzed by kymography.

Fusion of MT asters

In recent experiments by Foster et al. [39] they examined the spontaneous contraction dynamics of radial MT arrays or asters labeled with Alexa647-tagged tubulin, in *Xenopus* egg extracts. We have taken a time-series of such asters from published data (kindly shared by the author Peter J. Foster) and analyzed coalescence events using AMTraK (Fig 6A) The projection of the time-series for selecting the LOI enables us to reduce the complex movements of such 2D

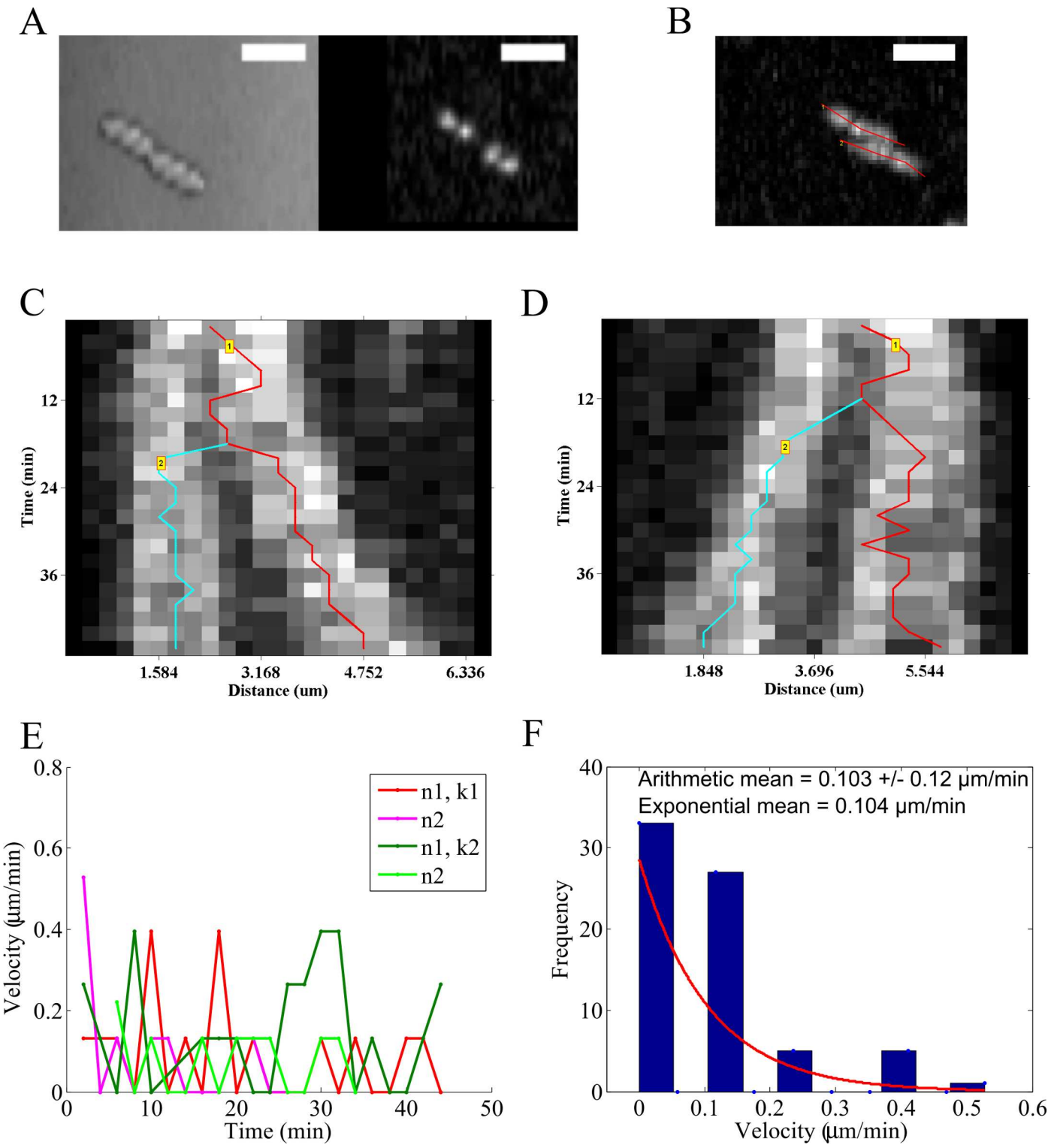

Fig 4. Nucleoid segregation dynamics of *E. coli*. (A) Image time-series of *E. coli* MG1655 grown on agar pads and imaged in DIC (left) and fluorescence based on HupA-GFP (right) are analyzed using AMTraK. (B) AMTraK generates a maximum intensity projection on the basis of which user-selected lines of interest (red lines) are used by the program to generate kymographs. The kymographs based on (C) LOI 1 (k1) and (D) LOI 2 (k2) were tracked resulting in branched tracks (colored lines). (E) The instantaneous velocities of nucleoids 1 and 2 (n1, n2) from kymographs 1 (k1) and 2 (k2) are plotted as a function of time (colors indicate nucleoids n1, n2 each from the kymographs k1, k2). (F) Mean velocities are estimated using both the arithmetic mean (±s.d.) and v_{ex}, the mean of the exponential decay ($y = e^{-1/vex}$) that was fit (red line) to the frequency distribution of instantaneous velocity (bars). Scale bar 4 µm.

doi:10.1371/journal.pone.0167620.g004

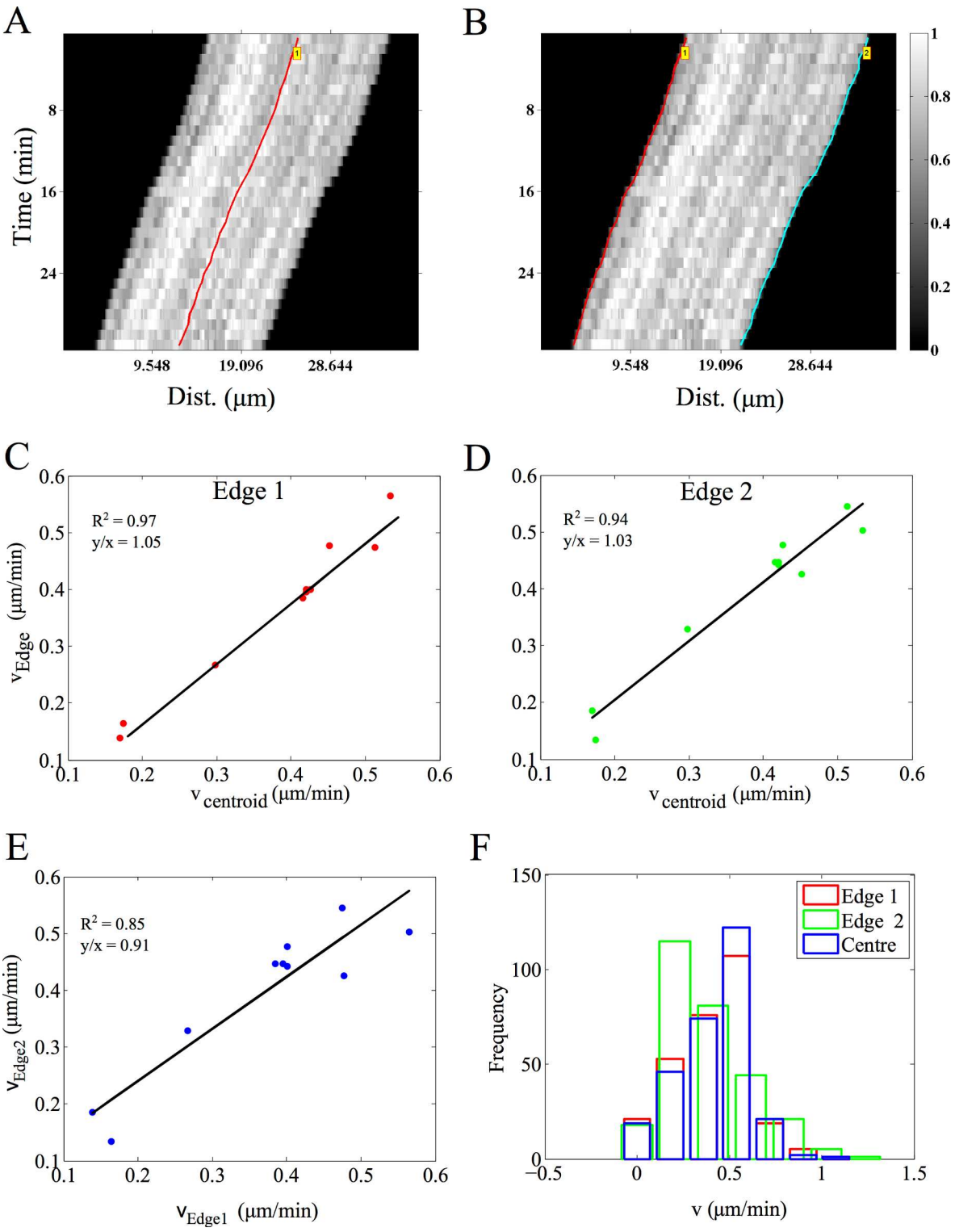

Fig 5. Microtubule (MT) gliding motility on kinesin motors. MTs gliding on kinesin (images acquired every 1 minute for 30 minutes) were analyzed using AMTraK by either detecting **(A)** the centerline (red) or **(B)** the two edges the filament, edge 1 (red) and 2 (cyan). Color bar: gray scale image intensity normalized by the maximal value for the bit-depth. **(C, D)** The velocity estimates from the centroid-based velocity estimates and the two edges and **(E)** the velocity estimated from each edge are correlated. **(F)** The frequency distribution of the instantaneous velocity estimates using the centroid (blue) is compared to edge-based estimates. r^2: goodness of fit, y/x: slope of the linear fit. Number of filaments analyzed, n = 10.

doi:10.1371/journal.pone.0167620.g005

structures to a 1D over time process. The movement of the smaller aster as it merges with the larger one is rapid. The fluorescence intensity following the merger fluctuates, but does not increase, which we interpret to mean tubulin density at the center of the new aster does not increase (Fig 6B). While the coalescence appears not to result in a compaction of the aster, it demonstrates the utility of the code for 2D MT array transport. On the other hand, intensity measurements are expected to change during processes such as molecular 'recruitment' of sub-cellular structures, so we proceed to test the tool on this process, which had previously been studied using manual kymography.

Kinetics of clathrin assembly during in vitro vesicle formation

We proceed to quantify the assembly kinetics of clathrin on membranes from an *in vitro* reconstitution assay of clathrin assembly on vesicle precursors reported previously by Holkar et al. [24]. This process has been analyzed using kymography due to its effectively 1D spatial extent and the multiple simultaneous events of assembly. The published time-series of fluorescently labeled clathrin assembly kinetics in the presence of wild-type epsin (supplementary movie 3 in [24]) and L6W mutant epsin (supplementary movie 5 in [24]) in the form of 16 bit TIF images were provided by the authors (Sachin Holkar, personal communication). AMTraK was used to analyze this data without any pre-processing, resulting in tracked kymographs of assembly kinetics with wild-type (Fig 7A) and mutant epsin (Fig 7B). The software outputs a text-file of grey-value intensities normalized by the bit-depth (maximum normalized, between 0–1) (S4 Data), which when multiplied by the bit-depth of the input images, produced intensity profiles of clathrin assembly in grey-values with time in the presence of wild-type (Fig 7C, S3A Fig) and mutant epsin (Fig 7D, S3B Fig). These intensity profiles were fit to a single phase exponential function $y = a+(b-a)^*(1-e^{-c^*t})$, where y is the intensity which increases with time t, and depends on three fit parameters, a, b and c, the same function as used by Holkar et al. [24]. A large proportion of the assembly events were successfully tracked and most showed

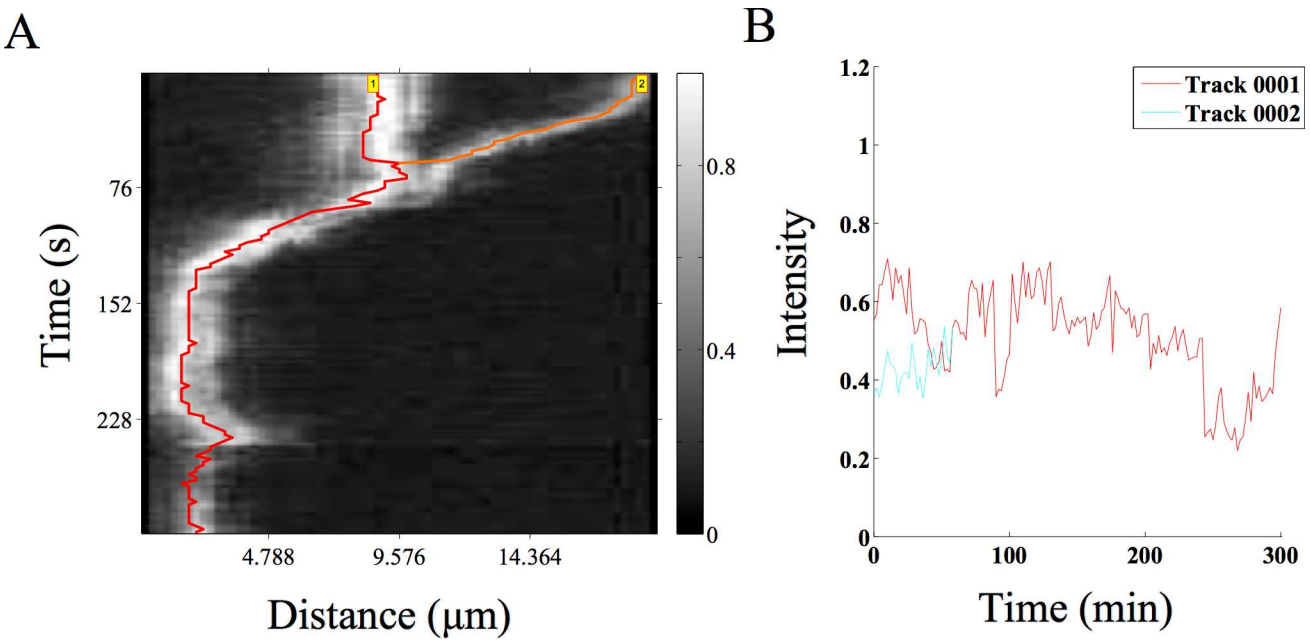

Fig 6. MT aster coalescence. (A) A time-series of MT asters undergoing fusion (time-series taken from previous work by Foster et al. [39]) was analyzed using AMTraK. The grey scale bar indicates normalized fluorescence intensity of Alexa-647 labeled tubulin. **(B)** The relative intensity over time of the two coalescing asters is plotted.

doi:10.1371/journal.pone.0167620.g006

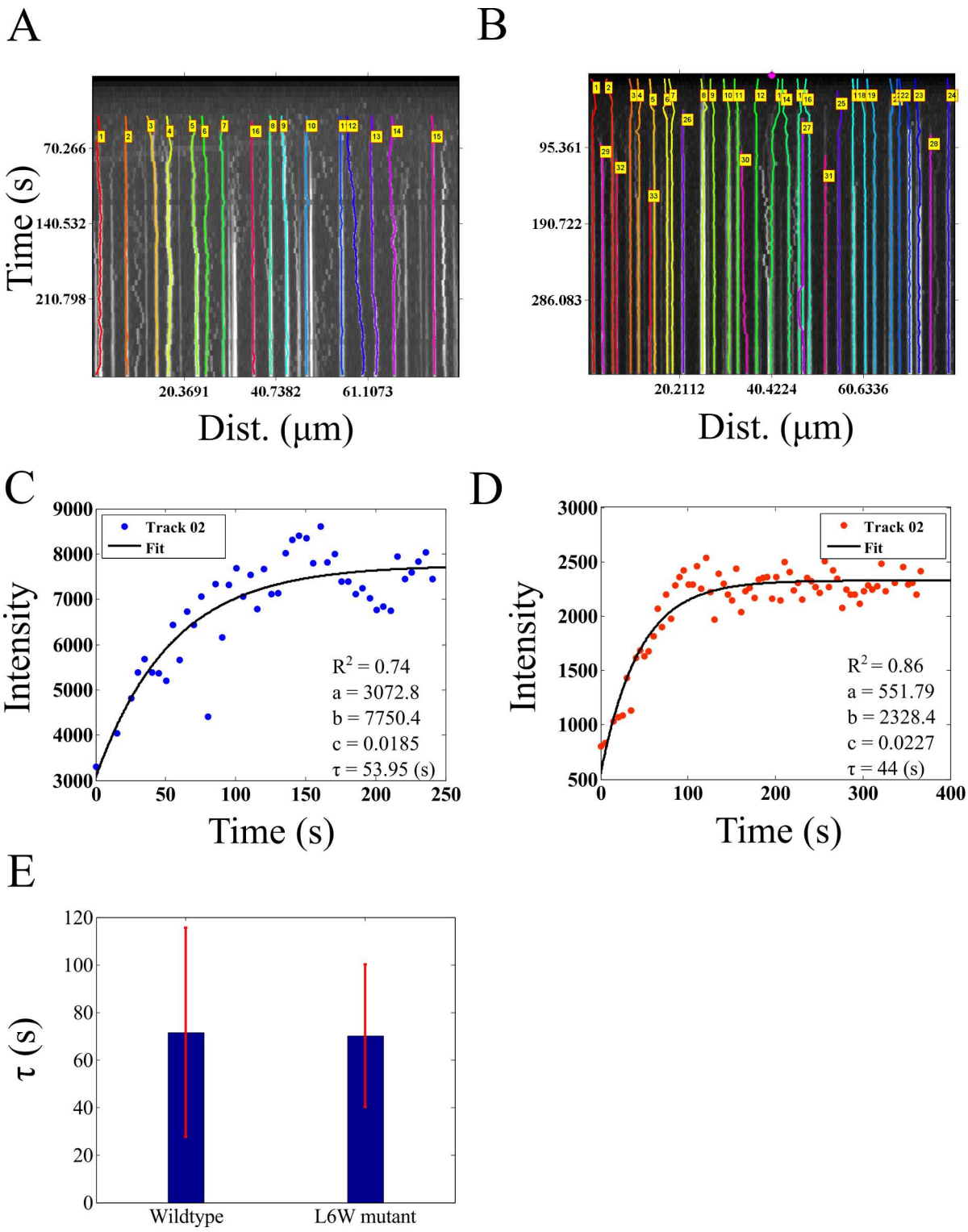

Fig 7. Dynamics of clathrin assembly. (A, B) Microscopy time-series taken from Holkar et al. [24] of fluorescently labeled clathrin assembly in the presence of **(A)** wild-type and **(B)** mutant epsin were analyzed using AMTraK. Colored lines in the kymographs indicate detected tracks. **(C, D)** The change in intensity as a function of time based on AMTraK detected tracks from **(C)** clathrin + w.t. epsin and **(D)** compared to clathrin + (L6W) mutant epsin. The intensity kinetics plots are fit to a single-phase exponential function, $y = a+(b-a)*(1-e^{-c*t})$ to obtain the time constant of assembly $\tau = 1/c$ (red). R^2: goodness of fit. **(D)** The mean values (error bar represents s.d.) of the time constant of assembly of clathrin (τ) in the presence of wild-type and mutant epsin are compared.

doi:10.1371/journal.pone.0167620.g007

saturation kinetics that were fit by curves with $R^2>0.7$ (S3 Fig). While the parameters *a* and *b* are scaling factors, *c* determines the characteristic clathrin polymerization time, $\tau = 1/c$. In our analysis the clathrin assembly time in presence of wild-type epsin is $<\tau> = 71.49\pm44.09$ s while with mutant epsin $<\tau> = 70.16\pm29.89$ s. In our estimate of the mutant assembly time is indistinguishable from wild-type, consistent with the previous report, which used manual quantification of the kymograph [24]. We proceed to examine if our tool, which appears to work successfully on *in vitro* data with low background noise, can also be used for the quantification of *in vivo* dynamics inside the crowded environment of an intact cell.

Axonal vesicle transport: Characterizing directional switching

Synaptic vesicles in *Caenorhabditis elegans* mechanoreceptor neurons labeled with GFP-Rab3 have been recently studied by Mondal et al. in a whole-animal microfluidics device, providing retrograde and anterograde vesicle transport statistics [28]. Such *in vivo* data is complex, involves multiple crossovers and has many objects close to each other. AMTraK based analysis of the published data could detect up to 17 different tracks (Fig 8A). Vesicles that were not detected have typically low intensity or were out of focus and were not segmented. The spread of the distribution of instantaneous velocities (left-ward: negative, anterograde; right-ward: positive, retrograde, non-motile: paused) shows that the GFP-Rab3 vesicles are equally likely to be anterograde and retrograde in their transport (Fig 8B). Based on the shape of the frequency distribution of the non-zero velocities in anterograde (Fig 8C) and retrograde (Fig 8D) directions, an exponential decay fit to the frequency distribution was used to estimate mean velocities (goodness of fit, $R^2 = 0.99$). To enable comparison with the arithmetic means reported in literature [28], we also estimate the average. The mean velocity from the exponential fits of anterograde transport is 0.625 μm/s (n = 425, arithmetic mean±s.d.: 0.77±0.53 μm/s) while the mean retrograde velocity is 0.714 μm/s (n = 540, arithmetic mean±s.d.: 0.854±0.67 μm/s). In this case, both means are comparable since only non-zero values were the analyzed. Velocities in both directions are of comparable order of magnitude to the published values obtained by manual detection [28], but 1.5-fold lower, due to a (non-zero) threshold velocity used by the authors to define pauses (as personally communicated by the author, Sudip Mondal). Thus, AMTraK can be reliably used to quantify transport and assembly dynamics from both *in vitro* and *in vivo* fluorescence microscopy data, as seen from the quantification, which is consistent with literature.

Discussion

In this report, we have described a novel tool for automatic detection and quantification of kymographs from fluorescence microscopy time-series. Using simulations we have demonstrated sub-pixel position detection accuracy of our proposed method, in conditions of low Gaussian noise. The program quantifies position, motility, and brightness intensity of fluorescence signal and fusion/splitting events. The utility of the code is tested on *in vitro* and *in vivo* fluorescence time-series ranging from *in vitro* assays of MT gliding assays with kinesin, coalescence dynamics of MT-asters, clathrin assembly kinetics on lipid tethers to *in vivo* axonal synaptic vesicle transport. The measures of average transport and kinetics of these diverse data types are consistent with published data and provides opportunities for improved statistics of individual events from a dynamic time-series, which were not as easily accessible with current methods.

Manual quantification of kymographs [2] depends typically on reliable edge detection. As a result, quantification varies between individuals and requires prior information or experience [40]. Yet, manual kymography is widely reported in cell-biological literature for the analysis of

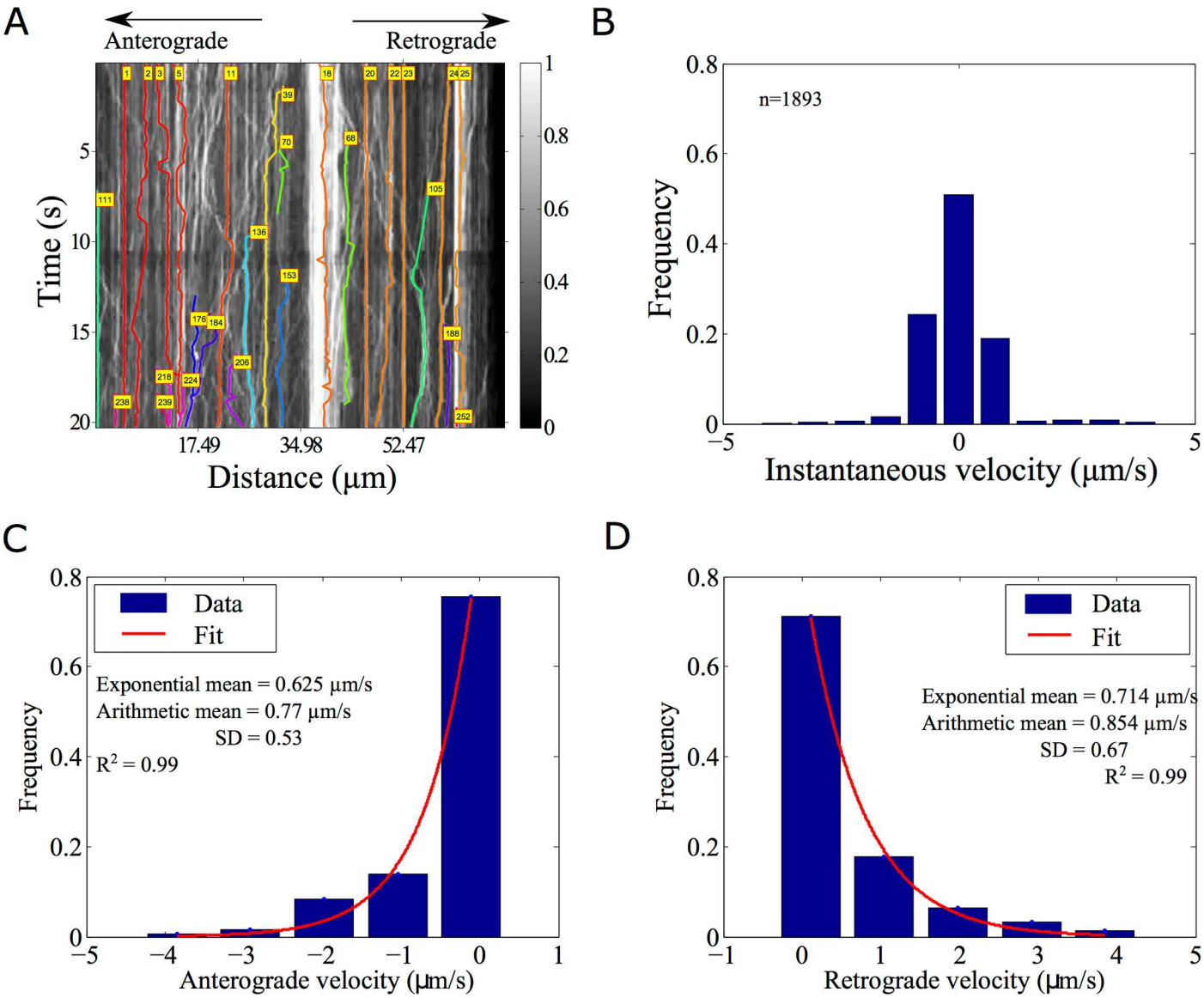

Fig 8. Analysis of synaptic vesicle transport. (A) GFP-Rab3 tagged vesicles from posterior touch cell neurons in *C. elegans* (experimental data from taken from supporting movie S1 Movie from [28]) were analyzed using AMTraK. Colored lines with index numbers indicate tracks. **(B)** The frequency distribution of instantaneous velocities of the vesicles (n = 1592) is plotted using AMTraK (mean: 0.49 µm/s, s.d. 0.88). **(C, D)** The frequency distribution of non-zero velocities are fit with an exponential decay function $y = A*e^{-x/m}$ (red line), where A: scaling factor and *m*: mean. **(C)** The mean anterograde velocity from the fit is 0.625 µm/s with arithmetic mean 0.77±0.53 µm/s (n = 425) and **(D)** the mean retrograde velocity from the fit is 0.714 µm/s with arithmetic mean 0.854±0.67 µm/s (n = 540). Arithmetic means are reported ± standard deviation (s.d.). R^2 indicates the goodness of the fit.

doi:10.1371/journal.pone.0167620.g008

dynamic processes, possibly due to the heterogeneity of the data types and the absence of a single standard method or even criterion, which to make the process less interactive. While developing AMTraK, we tested global (whole-image) methods of edge-segmentation (contour-, watershed- and gradient-based), but found them to be inadequate for the task. Possible reasons include the time-dependent brightness and contrast changes of the sample resulting from either bleaching or intrinsic dynamics. We find that for some applications such as vesicle transport and protein recruitment, the detecting and tracking peaks is ideal, while for microtubule gliding assays edge detection is better. As a result our code allows the user to choose

amongst three different methods of segmentation based on the nature of their data (a) peak detection by *findpeaks* and (b) watershed and (c) edge detection using the Canny edge detector.

Typical problems in peak or edge detection arise when the data has poor signal to noise. This is also seen in our error analysis with increasing noise amplitude (Fig 2D). One solution is to background subtract the image, which can be easily done in multiple tools. The occasional loss of some particles in a time-series such as synaptic vesicles (Fig 8A), despite being visible to the eye, results from a failure in detection or a 'pruning' step used to remove spurious and redundant tracks. Such pruning however was found to be necessary to ensure robustness of the code for handling multiple data types and is simple to trouble-shoot due to the limited number of adjustable parameters. While intensity matching did not improve the percentage vesicles tracked, in future additional features like those used in pattern-matching for tracking [41] could be used further improve the detection percentages. Our test with increasing Gaussian random image noise (Fig 2) also suggests that increases of fluorescently tagged proteins (for instance due to expression level increases *in vivo*), could result in reduced spatial contrast. Such data would then be difficult to automatically quantify using AMTraK. The data would require pre-processing with something similar to an anisotropic diffusion filter [42] to preserve edge information but reduce non-specific signal. In future, multiple data pre-processing routines could be implemented in a separate module, to add to the functionality of the program.

Our quantification of the frequency distribution of synaptic vesicle transport in anterograde and retrograde directions (Fig 8C and 8D) suggests the instantaneous velocities are exponentially distributed. While the arithmetic mean suffices for comparison with experimental reports [28], the quantification of the precise nature of the distribution of velocities could be used as a test of theoretical models. Such a comparison has been made in previous work on synaptic vesicle precursor trafficking [43]. Such models are relevant for both neurophysiology as well as understanding of collective effects in molecular-motor driven vesicle transport *in vivo* [44,45].

The collective motor velocity of human kinesin driven gliding of MTs has been well characterized in previous work [12,46,47]. Many of these studies have shown that the MT length and kinesin density do not affect the mean speed. However, the time-series of individual filaments show small time-dependent variations (Fig 4A and 4B), possibly a result of the local inhomogeneity of motor distributions. This information could be of some use when mixed-motor populations are used [48]. Recent studies of filament motility have used a filament-tracking approach based on a MATLAB program FIESTA [49], with a positional accuracy of 30 nm. We find the distribution of time-averaged velocity of gliding calculated using AMTraK match closely the distribution obtained from analysis using FIESTA (S2 Fig). This suggests that while complex transport dynamics in 2D are indeed better analyzed using tracking tools, for those data sets that are amenable to kymography analysis, AMTraK results are comparable to those obtained from tracking tools with sub-pixel accuracy.

While the dynamics of multiple particles can be simultaneously quantified using AMTraK, the selection of LOIs remains manual. However, once an LOI has been selected, the program can also be used in the "From file" mode to apply a pre-existing LOI to quantify kymographs in other channels (e.g.: bright field, fluorescence) and other fields of view with similar sample geometries. Potentially, LOIs could be generated independent of AMTraK too, provided they are compatible with the input format. The multiple bright-field and fluorescence correlative analysis tools for bacterial image analysis [10,33,50,51] are an example in case. More recent developments in image-analysis software to systematically extract data from microfluidics experiments automatically output channel information [52], which could also form the basis for the LOIs for multiple fields of view. These approaches could in future further increase the throughput our analysis tool.

Table 1. A comparison of features in kymography tools described in literature and commonly in use for cellular and sub-cellular scale images.

Feature / Tool	AMTraK	Multi-kymograph	Makekymograph	Icy-Kymograph Tracker	Kymomaker	Points from Kymograph	Kymograph mt2	KymographClear and KymographDirect
LOI selection	Manual	Manual	Semi-automated	Manual	Manual	No	Manual	Manual
Multiple LOIs	Yes	Yes	Yes	Yes	Yes	No	No	No
Automated track detection	Yes	No	No	Semi-automated	Yes	Semi-automated	No	Yes
Quantification	Yes	Separate	No	Separate	No	XY-coordinates	No	Separate
No. of adjustable parameters	8	1	1	7	13	-	-	-
Split and merge detection	Automatic	No	No	No	No	No	No	Manual
Open source	Yes	Yes	Yes	Yes	No	Yes	Yes	Yes
Programming language	MATLAB	ImageJ macro	Java (ImageJ plugin)	Plugin for Icy	-	Java (ImageJ plugin)	Java (ImageJ plugin)	ImageJ macro and LabView
Reference	This report	[57]	[58]	[5]	[4]	[59]	[60]	[53]

doi:10.1371/journal.pone.0167620.t001

Multiple software tools for kymography have been described in the recent past in literature and their features are summarized in Table 1 for comparison. While most tools including this one, require user inputs for the process of kymograph generation, only AMTraK and Kymograph Direct [53] automates the detection and connection. However, certain features of AMTraK make it unique, being absent in other comparable tools, such as automated branch-point detection, an integrated quantification module and sub-pixel positional accuracy accessible with an easy to use GUI front-end. In addition, since the code is open source and written in MATLAB, it is more likely to be used in an existing microscopy analysis workflow, due to the increasing spread of MATLAB as a data analysis platform in quantitative cell-biology research [54,55]. Thus, AMTraK could serve as a tool for the rapid quantification of image time-series of transport and assembly kinetics from microscopy. This has become particularly relevant in the context of high-content screening [56], where the spatial interaction patterns are becoming just as important as bulk kinetics measured in traditional high throughput screens.

We have developed an automated tool for the quantification of kymographs. Our approach detects peak and edge information and utilizes a distance minimization approach to link them. We demonstrate the wide utility of our tool by quantifying microtubule transport dynamics, clathrin polymerization kinetics and vesicle transport. Combined with a user-friendly interface, objective detection criteria and open source code, we believe AMTraK can be used to extract more and reproducible statistics from microscopy of sub-cellular dynamics.

Supporting Information

S1 Data. The LOI coordinates generated are stored in the file "LOIselection.txt" when the user chooses the "Interactive" mode of LOI selection at the stage of generating a kymograph. This provides the 2D image coordinates (X and Y) in pixel units, as indicated by the columns labels.
(TXT)

S2 Data. The average statistics for all trajectories are stored in a file "USER_TrackStats.txt". It reports in a column-wise manner the track number, time over which it is tracked (in

user-provided units), speed, net-velocity (displacement/time), tortuosity (displacement/path-length), average of instantaneous velocity and the standard deviation of the average instantaneous velocity. All column headers are labeled for clarity.
(TXT)

S3 Data. The instantaneous (time-dependent) statistics of each track are stored in "USER_InstStats.txt" with track number, time interval to the previous frame in units provided by the user, displacement magnitude, positive/negative displacement (leftwards: negative, rightwards: positive), instantaneous velocity (displacement/time interval), signed-velocity (leftwards: negative, rightwards: positive), and cumulative time (adding up time intervals in units provided by the user). All column headers are labeled for clarity.
(TXT)

S4 Data. The file "Tracklist.txt" stores the time-dependent intensity statistics of each track. This provides the track number, position in distance from the origin (upper-left corner) in pixels, time-frame (frame number), normalized grey-value intensity (divided by the bit-depth of the image) and normalized time-frame (setting the first time-frame to 0). All column headers are labeled for clarity.
(TXT)

S5 Data. The branch-points detected by the code are stored in a file "Branchpoints.txt" which is generated when the user chooses to detect "Splitting events" (check-box) with an appropriate parameter choice. It contains the track-number that splits off from or joins another track, the 1D distance (from the origin at the left edge) and it's time point both in terms of user-provided units. The column headers describe the variables.
(TXT)

S6 Data. User provided values are stored in "All_Parameters.txt". This includes the name and path of the input TIF image time-series, scaling factors (distance, time) and parameters for the detection, tracking and splitting-events.
(TXT)

S1 Fig. The simulated image. (A) The simulated bead image used to estimate the accuracy of the code. A profile through the image (yellow line) is used to generate **(B)** an intensity profile through the three beads.
(PDF)

S2 Fig. Comparing kymography to filament tracking. The frequency distribution of instantaneous velocities obtained after analyzing time-series of MTs gliding on kinesin using AMTraK (red bars) and the high-precision filament-tracking tool, FIESTA (blue bars) are plotted.
(PDF)

S3 Fig. Kinetics of clathrin endocytosis. The fluorescence intensity in grey values (colored circles) as a function of time in seconds estimated from multiple detected tracks after AMTraK analysis (Fig 7A and 7B) of clathrin assembly kinetics in the presence of **(A)** wild-type and **(B)** mutant (L6W) epsin (based on data from Holkar et al. [24]). A single-phase exponential function (the same as in Fig 7C and 7D) is used to fit the data (black line) and the parameters are listed for each fit, with τ indicating the time-constant of assembly in seconds.
(PDF)

S1 Video. Time-series of division and genome-segregation in *E. coli* MG1655 is followed **(A)** in fluorescence with nucleoids labeled by HupA-GFP (grey) and **(B)** DIC is used to follow cell

morphology. Scale bar: 4 μm. Time indicated in minutes.
(ZIP)

Acknowledgments

A grant from Dept. of Biotechnology, Govt. of India in Basic Biology (BT/PR1595/BRB/10/1043/2012) financed part of this work. ARC, KJ and MSG are supported by fellowships from the University Grants Commission (UGC) India (F.2-14/2011 (SA-1)), DST-Inspire Fellowship and Indian Council of Medical Research (ICMR) respectively. We are grateful to Peter J. Foster for sharing the original MT aster time-series data and Sachin Holkar for sharing the original image time-series data and calibration values for the Clathrin assembly kinetics. We are grateful to Sudip Mondal for an explanation of the vesicle transport analysis.

Author Contributions

Conceptualization: CAA ARC.

Data curation: ARC.

Formal analysis: ARC.

Funding acquisition: CAA.

Investigation: ARC KJ MSG.

Methodology: ARC KJ MSG.

Project administration: CAA.

Resources: CAA.

Software: ARC CAA.

Supervision: CAA.

Validation: CAA ARC KJ MSG.

Visualization: ARC CAA.

Writing – original draft: CAA.

Writing – review & editing: CAA ARC.

References

1. Pereira AJ, Maiato H (2010) Improved kymography tools and its applications to mitosis. Methods 51: 214–219. doi: 10.1016/j.ymeth.2010.01.016 PMID: 20085815
2. Rietdorf J, Seitz A (2008) Multi Kymograph. Available: http://fiji.sc/Multi_Kymograph.
3. Chetta J, Shah SB (2011) A novel algorithm to generate kymographs from dynamic axons for the quantitative analysis of axonal transport. J Neurosci Methods 199: 230–240. Available: http://www.ncbi.nlm.nih.gov/pubmed/21620890. doi: 10.1016/j.jneumeth.2011.05.013 PMID: 21620890
4. Chiba K, Shimada Y, Kinjo M, Suzuki T, Uchida S (2014) Simple and direct assembly of kymographs from movies using KYMOMAKER. Traffic 15: 1–11. doi: 10.1111/tra.12127 PMID: 24102769
5. Chenouard N, Buisson J, Bloch I, Bastin P, Olivo-Marin J-C (2010) Curvelet analysis of kymograph for tracking bi-directional particles in fluorescence microscopy images. IEEE International Conference on Image Processing (ICIP). http://icy.bioimageanalysis.org/plugin/KymographTracker.
6. Skarstad K, Steen HB, Boye E (1985) Escherichia coli DNA distributions measured by flow cytometry and compared with theoretical computer simulations. J Bacteriol 163: 661–668. PMID: 3894332

7. Nordström K, Dasgupta S (2006) Copy-number control of the Escherichia coli chromosome: a plasmidologist's view. EMBO Rep 7: 484–489. doi: 10.1038/sj.embor.7400681 PMID: 16670681
8. Nielsen HJ, Ottesen JR, Youngren B, Austin SJ, Hansen FG (2006) The Escherichia coli chromosome is organized with the left and right chromosome arms in separate cell halves. Mol Microbiol 62: 331–338. doi: 10.1111/j.1365-2958.2006.05346.x PMID: 17020576
9. Spahn C, Endesfelder U, Heilemann M (2014) Super-resolution imaging of Escherichia coli nucleoids reveals highly structured and asymmetric segregation during fast growth. J Struct Biol 185: 243–249. doi: 10.1016/j.jsb.2014.01.007 PMID: 24473063
10. Sliusarenko O, Heinritz J, Emonet T, Jacobs-Wagner C (2011) High-throughput, subpixel precision analysis of bacterial morphogenesis and intracellular spatio-temporal dynamics. Mol Microbiol 80: 612–627. doi: 10.1111/j.1365-2958.2011.07579.x PMID: 21414037
11. Fisher JK, Bourniquel A, Witz G, Weiner B, Prentiss M, et al. (2013) Four-Dimensional Imaging of E. coli Nucleoid Organization and Dynamics in Living Cells. Cell 153: 882–895. doi: 10.1016/j.cell.2013.04.006 PMID: 23623305
12. Howard J, Hudspeth AJ, Vale RD (1989) Movement of microtubules by single kinesin molecules. Nature 342: 154–158. doi: 10.1038/342154a0 PMID: 2530455
13. Nitzsche B, Bormuth V, Brauer C, Howard J, Ionov L, et al. (2010) {S}tudying kinesin motors by optical 3D-nanometry in gliding motility assays. Methods Cell Biol 95: 247–271. doi: 10.1016/S0091-679X(10)95014-0 PMID: 20466139
14. Leduc C, Ruhnow F, Howard J, Diez S (2007) Detection of fractional steps in cargo movement by the collective operation of kinesin-1 motors. Proc Natl Acad Sci U S A 104: 10847–10852. doi: 10.1073/pnas.0701864104 PMID: 17569782
15. Toyoshima YY, Kron SJ, McNally EM, Niebling KR, Toyoshima C, et al. (1987) Myosin subfragment-1 is sufficient to move actin filaments in vitro. Nature 328: 536–539. doi: 10.1038/328536a0 PMID: 2956522
16. Martin DS (2013) Measuring microtubule persistence length using a microtubule gliding assay. Methods Cell Biol 115: 13–25. doi: 10.1016/B978-0-12-407757-7.00002-5 PMID: 23973063
17. Bicek AD, Tuzel E, Demtchouk A, Uppalapati M, Hancock WO, et al. (2009) Anterograde microtubule transport drives microtubule bending in LLC-PK1 epithelial cells. Mol Biol Cell 20: 2943–2953. doi: 10.1091/mbc.E08-09-0909 PMID: 19403700
18. Ungewickell E, Branton D (1981) Assembly units of clathrin coats. Nature 289: 420–422. PMID: 7464911
19. Avinoam O, Schorb M, Beese CJ, Briggs JA, Kaksonen M (2015) Endocytosis. Endocytic sites mature by continuous bending and remodeling of the clathrin coat. Science 348: 1369–1372. doi: 10.1126/science.aaa9555 PMID: 26089517
20. Skruzny M, Desfosses A, Prinz S, Dodonova SO, Gieras A, et al. (2015) An organized co-assembly of clathrin adaptors is essential for endocytosis. Dev Cell 33: 150–162. doi: 10.1016/j.devcel.2015.02.023 PMID: 25898165
21. Pucadyil TJ, Schmid SL (2010) Supported bilayers with excess membrane reservoir: a template for reconstituting membrane budding and fission. Biophys J 99: 517–525. doi: 10.1016/j.bpj.2010.04.036 PMID: 20643070
22. Neumann S, Pucadyil TJ, Schmid SL (2013) Analyzing membrane remodeling and fission using supported bilayers with excess membrane reservoir. Nat Protoc 8: 213–222. doi: 10.1038/nprot.2012.152 PMID: 23288321
23. Kalthoff C, Alves J, Urbanke C, Knorr R, Ungewickell EJ (2002) Unusual structural organization of the endocytic proteins AP180 and epsin 1. J Biol Chem 277: 8209–8216. doi: 10.1074/jbc.M111587200 PMID: 11756460
24. Holkar SS, Kamerkar SC, Pucadyil TJ (2015) Spatial Control of Epsin-induced Clathrin Assembly by Membrane Curvature. J Biol Chem 290: 14267–14276. doi: 10.1074/jbc.M115.653394 PMID: 25837255
25. Allan VJ, Vale RD (1991) Control of Microtubule-based Membrane Transport and Tubule Formation In Vitro. J Cell Biol 113: 347–359. PMID: 2010466
26. Welzel O, Knörr J, Stroebel AM, Kornhuber J, Groemer TW (2011) A fast and robust method for automated analysis of axonal transport. Eur Biophys J 40: 1061–1069. doi: 10.1007/s00249-011-0722-3 PMID: 21695534
27. Hill DB, Plaza MJ, Bonin K, Holzwarth G (2004) Fast vesicle transport in PC12 neurites: velocities and forces. Eur Biophys J 33: 623–632. doi: 10.1007/s00249-004-0403-6 PMID: 15071760

28. Mondal S, Ahlawat S, Rau K, Venkataraman V, Koushika SP (2011) Imaging in vivo Neuronal Transport in Genetic Model Organisms Using Microfluidic Devices. Traffic 12: 372–385. doi: 10.1111/j.1600-0854.2010.01157.x PMID: 21199219

29. Otsu N (1979) A Threshold Selection Method from Gray-Level Histograms. IEEE Trans Syst Man Cybern SMC-9: 62–66.

30. Brookes, Mike (2005) Voicebox. http://www.ee.ic.ac.uk/hp/staff/dmb/voicebox/voicebox.html.

31. Meyer F (1994) Topographic distance and watershed lines. Signal Processing 38: 113–125.

32. Canny J (1986) A Computational Approach to Edge Detection. IEEE Trans Patt Analy Mach Int 8: 679–698.

33. Athale CA, Chaudhari H (2011) Population length variability and nucleoid numbers in Escherichia coli. Bioinformatics 27: 2944–2948. doi: 10.1093/bioinformatics/btr501 PMID: 21930671

34. Schneider CA, Rasband WS, Eliceiri KW (2012) NIH Image to ImageJ: 25 years of image analysis. Nat Methods 9: 671–675. PMID: 22930834

35. Wery M, Woldringh CL, Rouviere-Yaniv J (2001) HU-GFP and DAPI co-localize on the Escherichia coli nucleoid. Biochimie 83: 193–200. PMID: 11278069

36. Thévenaz P, U.E. R, Unser M (1998) Thévenaz P1, Ruttimann UE, Unser M. IEEE Trans Image Process 7: 27–41.

37. Cytoskeleton (2005) Kinesin Motility Assay Biochem Kit BK027. Denver, CO, USA.

38. Stewart RJ, Thaler JP, Goldsteint LSB (1993) Direction of microtubule movement is an intrinsic property of the motor domains of kinesin heavy chain and Drosophila ncd protein. Proc Nat Acad Sci USA 90: 5209–5213. PMID: 8506368

39. Foster PJ, Fürthauer S, Shelley MJ, Needleman DJ (2015) Active contraction of microtubule networks Active Contraction of Microtubule Networks. Elife 4:e10837: 1–21. doi: 10.7554/eLife.10837 PMID: 26701905

40. Welzel O, Boening D, Stroebel A, Reulbach U, Klingauf J, et al. (2009) Determination of axonal transport velocities via image cross- and autocorrelation. Eur Biophys J 38: 883–889. doi: 10.1007/s00249-009-0458-5 PMID: 19404633

41. Miura K (2005) Tracking Movement in Cell Biology. In: Rietdorf J, editor. Adv. Biochem. Engin/Biotechnol. Springer Berlin / Heidelberg. pp. 267–295.

42. Perona P, Malik J (1990) Scale-space and edge detection using anisotropic diffusion. IEEE Trans Pattern Anal Mach Intell 12: 629–639.

43. Maeder CI, San-Miguel A, Wu EY, Lu H, Shen K (2014) In vivo neuron-wide analysis of synaptic vesicle precursor trafficking. Traffic 15: 273–291. doi: 10.1111/tra.12142 PMID: 24320232

44. Bridgman PC (1999) Myosin Va movements in normal and dilute-lethal axons provide support for a dual filament motor complex. J Cell Biol 146: 1045–1060. PMID: 10477758

45. Hendricks AG, Perlson E, Ross JL, Schroeder HW, Tokito M, et al. (2010) {M}otor coordination via a tug-of-war mechanism drives bidirectional vesicle transport. Curr Biol 20: 697–702. doi: 10.1016/j.cub.2010.02.058 PMID: 20399099

46. Howard J (2001) Mechanics of Motor Proteins and the Cytoskeleton. Sunderland: Sinauer Associates.

47. Gibbons F, Chauwin JF, Despósito M, José J V (2001) A dynamical model of kinesin-microtubule motility assays. Biophys J 80: 2515–2526. doi: 10.1016/S0006-3495(01)76223-6 PMID: 11371430

48. Ikuta J, Kamisetty NK, Shintaku H, Kotera H, Kon T, et al. (2014) Tug-of-war of microtubule filaments at the boundary of a kinesin- and dynein-patterned surface. Sci Reports 4: 5281.

49. Ruhnow F, Zwicker D, Diez S (2011) Tracking Single Particles and Elongated Filaments with Nanometer Precision. Biophys J 100: 2820–2828. doi: 10.1016/j.bpj.2011.04.023 PMID: 21641328

50. Guberman JM, Fay A, Dworkin J, Wingreen NS, Gitai Z (2008) PSICIC: noise and asymmetry in bacterial division revealed by computational image analysis at sub-pixel resolution. PLoS Comp Biol 4: e1000233.

51. Ducret A, Quardokus EM, Brun Y V (2016) MicrobeJ, a high throughput tool for quantitative bacterial cell detection and analysis. Nat Microbiol 1: 1–7.

52. Sachs CC, Grünberger A, Helfrich S, Probst C, Wiechert W, et al. (2016) Image-Based Single Cell Profiling: High- Throughput Processing of Mother Machine Experiments. PLoS One 11: e0163453. doi: 10.1371/journal.pone.0163453 PMID: 27661996

53. Mangeol P, Prevo B, Peterman EJG (2016) KymographClear and KymographDirect: two tools for the automated quantitative analysis of molecular and cellular dynamics using kymographs. Mol Biol Cell 27: 1948–1957. doi: 10.1091/mbc.E15-06-0404 PMID: 27099372

54. Shekhar S, Zhu L, Mazutis L, Sgro AE, Fai TG, et al. (2014) Quantitative biology: where modern biology meets physical sciences. Mol Biol Cell 25: 3482–3485. doi: 10.1091/mbc.E14-08-1286 PMID: 25368426

55. Howard J (2014) Quantitative cell biology: the essential role of theory. Mol Biol Cell 25: 3438–3440. doi: 10.1091/mbc.E14-02-0715 PMID: 25368416

56. Zanella F, Lorens JB, Link W (2010) High content screening: seeing is believing. Trends Biotechnol 28: 237–245. doi: 10.1016/j.tibtech.2010.02.005 PMID: 20346526

57. Rietdorf, Jens (FMI B, Seitz A (EMBL H (2008) Kymograph (time space plot) Plugin for ImageJ. http://www.embl.de/eamnet/html/body_kymograph.html.

58. Hallman S (2007) Make_Kymograph plugin. http://www.ics.uci.edu/~fowlkes/sam_hallman/doc/

59. Das M, Drake T, Wiley DJ, Buchwald P, Vavylonis D, et al. (2012) Oscillatory dynamics of Cdc42 GTPase in the control of polarized growth. Science (80-) 337: 239–243.

60. Siebrasse JP, Kaminski T, Kubitscheck U (2012) Nuclear export of single native mRNA molecules observed by light sheet fluorescence microscopy. Proc Natl Acad Sci USA 109: 9426–9431. doi: 10.1073/pnas.1201781109 PMID: 22615357